Developing a Viable Process Window for Alloys Based on the Mg-Zn-Nd-Y System

Andrew Williams

Department of Materials Science and Engineering

The University of Sheffield

Thesis submitted for the degree of Doctor of Philosophy

February 2014

Abstract

In recent years there has been an increased demand for light-weight alloys from the aerospace and automotive industries. One particular challenge is producing cost-effective alloys for automotive applications. In response to this demand, Magnesium Elektron North America Inc. have produced three novel alloys based on the Mg-Zn-Nd-Y system. Although these alloys cost less to produce than their aerospace counterparts, it is necessary for them to provide good levels of formability for wrought applications, while retaining a high strength to weight ratio.

The three alloys have been tested with hot axisymmetric compression. A matrix of tests was carried out between 425 and 450 ºC with strain rates ranging from 0.5 to 5/s. The narrow range of the test conditions was due to the narrow process window exhibited by the alloys. Tests outside of this range failed due to incipient melting at higher temperatures or brittle fracture at lower temperatures. The limited ductility of the alloys was due to a significant volume fraction of a eutectic phase that existed at grain boundaries. The phase was identified with differential scanning calorimetry (DSC) and transmission electron microscopy to be the W-phase. The W-phase is deleterious to the tensile properties of Mg-Zn-RE alloys. The Zn/RE ratio was identified as being a controlling factor in the formation of the brittle eutectic compound. Changes in the alloy composition have been recommended in order to expand the process window.

The deformed microstructures exhibited extensive dynamic recrystallisation (DRX) when examined with electron backscattered diffraction (EBSD). The dominant active mechanism of DRX was believed to be a function of the Zener-Hollomon parameter. Continuous dynamic rotation recrystallisation (CDRRX) was the only mechanism of DRX to significantly weaken the otherwise strong basal texture that developed after deformation.

A complementary study showed that the alloys age harden with the β_1 and β_1' precipitates being identified as possible strengthening phases.

Acknowledgements

Firstly, I would like to give sincere thanks to my academic supervisor, Prof. Mark Rainforth. Quite simply this work would not have been completed without his constant advice, direction and, most importantly, endless patience. He has guided me throughout this project and given me a kick when motivation was needed. I will always be grateful for the support that he has provided. I would also like to extend thanks to my secondary academic supervisor, Dr. Brad Wynne, who has provided support and advice along the way.

This project would not have been possible without generous financial support from the Engineering and Physical Sciences Research Council (EPSRC). Further financial assistance was provided by Magnesium Elektron North America Inc. From Magnesium Elektron, I would like to thank my industrial supervisor, Dr. Bruce Davis, who provided the opportunity for working on these new alloys and supplied the materials necessary to carry out the work. Also at Magnesium Elektron, I would like to thank Dr. Dave Randman and Dr. Mark Turski who have provided invaluable suggestions and advice throughout the duration of my Ph.D.

I am grateful to the technical staff in the Department of Materials Science and Engineering (MSE) for their help and support over the years. I particularly appreciated their (twisted) humour that always gave me a smile, even on the darker days. Staff at the Sorby centre exhibited unbelievable patience with my endless questions about microscopy. Special thanks go to Dr. Peng Zeng and Dr. Cheryl Shaw for putting up with me.

My sanity is, fortunately, still intact (just). This is primarily due to the excellent group of people that I had the fortune to call friends over the last four years. In particular, members of D1 and H6 research offices, past and present, provided endless entertainment throughout my time at Sheffield. Thanks to all of you.

Finally, I can never quite believe the support that my family has given me over my (rather lengthy) time in academia. Their patience truly knows no bounds. Anything that I may achieve during my life is due to their endless love. Thank you.

Contents

Abstract i

Acknowledgements ii

Contents iii

Nomenclature ix

Chapter 1 Introduction 1

1.1 Background 1

1.2 Mode of Work 1

1.3 Project Objectives 2

Chapter 2 Literature Review 4

2.1 Introduction 4

2.2 Magnesium Alloys 5

2.2.1 Background 5

2.2.2 Alloy Designations 6

2.2.3 Modern Alloy Additions 6

2.2.4 Rare Earth Additions 8

2.2.5 Zinc Additions 10

2.2.6 Zirconium Additions 11

2.2.7 Miller-Bravais Notation 11

2.2.8 Precipitation 12

2.2.8.1 Mg-RE System 12

2.2.8.1.1 Mg-Nd 14

2.2.8.1.2 Mg-Y 15

2.2.8.2 Mg-Zn System 15

2.2.8.3 Mg-Zn-RE System 16

2.3 Crystallography and Deformation Mechanisms 17

2.3.1 Slip Systems 17

2.3.2 Twinning Systems 17
2.3.3 Grain Boundary Sliding 18
2.3.4 High Temperature Deformation 20
2.3.5 Restoration Mechanisms 21
2.3.5.1 Stacking Fault Energy 22
2.3.5.2 Dynamic Recovery 22
2.3.5.3 Dynamic Recrystallisation 23
2.3.5.3.1 Discontinuous Dynamic Recrystallisation 23
2.3.5.3.2 Continuous Dynamic Recrystallisation 24
2.3.5.3.3 Twinning-induced Continuous Dynamic Recrystallisation 25
2.3.5.3.4 Continuous Dynamic Rotation Recrystallisation 26
2.3.5.3.5 Mode of Recrystallisation 27
2.3.5.3.6 Grain Size and Grain Growth 27
2.3.6 Deformation Texture 28
2.3.7 Flow Behaviour 29
2.3.7.1 Modelling the Flow Behaviour 31

Chapter 3 Experimental Method 33

3.1 Material 33
3.2 Hot Axisymmetric Compression Testing 34
3.2.1 Specimen Description 34
3.2.2 Test Outline and Equipment 34
3.2.3 Testing Procedure 37
3.2.4 Friction Testing 38
3.2.5 Summary of Hot Axisymmetric Compression Testing 39
3.2.6 Analysis of Raw Data 41

3.2.7 Calculation of Equivalent Strain and Equivalent Flow Stress 42
3.2.8 Strain Rate Corrections 44
3.3 Isothermal Age Hardening 45
3.3.1 Procedure 45
3.3.2 Vickers Hardness Testing 46
3.4 Microscopy 46
3.4.1 Sample Preparation Route 46
3.4.1.1 Introduction 46
3.4.1.2 Common Problems Encountered 46
3.4.1.2.1 Oxidation 47
3.4.1.2.2 Pull-Out of Second Phase and Large Particles 47
3.4.1.2.3 Sensitivity to Methanol 48
3.4.1.2.4 Cleaning Samples after a Colloidal Silica Polish 48
3.4.1.3 Sectioning 49
3.4.1.4 Optical and Scanning Electron Microscopy 50
3.4.1.4.1 Etching 51
3.4.1.5 Electron Backscattered Diffraction 51
3.4.1.6 Transmission Electron Microscopy 52
3.4.2 Optical Microscopy 53
3.4.3 Electron Backscattered Diffraction 53
3.4.3.1 Procedure 54
3.4.3.2 Presentation and Analysis of EBSD Data 55
3.4.3.2.1 Noise Reduction 55
3.4.3.2.2 Inverse Pole Figure Coloured Orientation Imaging Maps 56
3.4.3.2.3 Pole Figures 57
3.4.4 Transmission Electron Microscopy 58
3.4.4.1 Procedure 58
3.5 Differential Scanning Calorimetry 58

Chapter 4 Results and Discussion I 59

4.1 As-received Material 59
4.1.1 Chemistry 59
4.1.2 Microstructure 60
4.1.2.1 Volume Fraction of Second Phase 62
4.2 Solution Heat Treatment 62
4.3 Pre-deformation Microstructures 65
4.4 Flow Characteristics 67
4.4.1 Introduction 67
4.4.2 Uncorrected Flow Data 67
4.4.3 Flow Curve Corrections 69
4.4.3.1 Coefficient of Friction 69
4.4.3.2 Strain Rate Sensitivity 72
4.4.3.3 Activation Energy of Deformation (Qdef) 74
4.4.3.4 Calculation of β 76
4.4.3.5 Fully Corrected Flow Curves 78
4.4.4 Process Window 80
4.4.5 Rolling Trial 83
4.5 Post-deformation Microstructures 87
4.5.1 Introduction 87
4.5.2 Variation of Microstructure with Different Deformation Conditions 87
4.5.3 Recrystallised Fraction 91
4.5.3.1 Recrystallised Grain Size 92
4.5.4 Subgrain Formation 94
4.5.5 Texture 96
4.5.5.1 Variation of Texture with Processing Conditions 96
4.5.5.2 Influence of Dynamic Recrystallisation on Texture 98
4.5.5.2.1 Randomisation of Texture by Dynamic Recrystallisation 101

4.6 Discussion
4.6.1 Introduction 104
4.6.2 Flow Characteristics 104
4.6.2.1 Variation of Flow Characteristics with Alloy Chemistry 106
4.6.2.2 Variation of Flow Characteristics with Processing Conditions 107
4.6.2.2.1 Onset of Flow Softening 107
4.6.2.3 Activation Energy of Deformation (Qdef) 108
4.6.2.3.1 Constitutive Behaviour 110
4.6.2.4 Process Window 111
4.6.3 Post-deformation Microstructures 113
4.6.3.1 Dynamic Recovery and Dynamic Recrystallisation 114
4.6.3.2 Recrystallised Fraction 121
4.6.3.2.1 Recrystallised Grain Size 122
4.6.3.3 Texture 123
4.7 Summary 124

Chapter 5 Results and Discussion II 126

5.1 Analysis of the Second Phase 126
5.1.1 Introduction 126
5.1.2 Energy Dispersive X-ray Spectroscopy 127
5.1.3 Differential Scanning Calorimetry 128
5.1.4 Software-based Analysis of Phase Transformations 130
5.1.5 Discussion 132
5.1.5.1 Phase Reactions in Mg-Zn-Y Alloys 132
5.1.5.2 Neodymium Additions to the Mg-Zn-Y System 133
5.1.5.3 Characterisation of the Second Phase 133
5.1.5.4 Improving the Current Alloys 138
5.2 Isothermal Age Hardening 141
5.2.1 Introduction 141

5.2.2 Isothermal Ageing Response 141
5.2.3 Precipitation Reactions in the Peak Aged Condition 142
5.2.4 Discussion 146
5.2.4.1 Age Hardening Response 146
5.2.4.2 Precipitation Reactions 146
5.3 Summary 149

Chapter 6 Conclusions 151

6.1 Initial Microstructure 151
6.2 Flow Behaviour 151
6.3 Post-deformation Microstructure 153
6.4 Analysis of the Second Phase 154
6.5 Artificial Age Hardening 155

Chapter 7 Future Work 156

Chapter 8 References 159

Nomenclature

SEM	scanning electron microscope
FEGSEM	field emission gun scanning electron microscope
TEM	transmission electron microscope
LaB_6	lanthanum hexaboride
EDX	energy dispersive X-ray spectroscopy
EBSD	electron backscattered diffraction
IPF	inverse pole figure
OIM	orientation imaging map
MUD	multiples of uniform density
MD	misorientation distribution
DSC	differential scanning calorimetry
TMC	thermo-mechanical compression
HCP	hexagonal close packed
FCC	face-centred cubic
BCC	body-centred cubic

BCO	body-centred orthorhombic
BCM	base-centred monoclinic
[xyuz]	direction in the Miller-Bravais indexing notation
<xyuz>	family of directions in the Miller-Bravais indexing notation
(xyuz)	plane in the Miller-Bravais indexing notation
{xyuz}	family of planes in the Miller-Bravais indexing notation
DRV	dynamic recovery
DRX	dynamic recrystallisation
CDRX	continuous dynamic recrystallisation
CDRRX	continuous dynamic rotation recrystallisation
DDRX	discontinuous dynamic recrystallisation
PSN	particle-stimulated nucleation
a, c	atomic lattice parameters
SSSS	super-saturated solid solution
GP zone	Guinier-Preston zone
RE	rare earth

MM	mischmetal
$\beta, \beta', \beta'', \beta_1, \beta_1', \beta_2'$	precipitate phases existing in Mg-RE and Mg-Zn-RE alloys
CRSS (τ)	critical resolved shear stress
SFE	stacking fault energy
UTS	ultimate tensile strength
ε	strain
$\dot{\varepsilon}$	strain rate
$\dot{\varepsilon}_1$	instantaneous strain rate
$\dot{\varepsilon}_2$	nominal strain rate
σ	stress
R	universal gas constant
T	temperature
T_0	original temperature
T_1	instantaneous temperature
T_2	nominal temperature
Z	Zener-Hollomon parameter

Q_{def}	activation energy of deformation
h	instantaneous height
h_0	original height
h_c	cold height
d_p	measured displacement
d	diameter
F	instantaneous load
A	instantaneous cross sectional area
A_0	original cross sectional area
μ	coefficient of friction
E_0	accelerating voltage
ρ	density

1. Introduction

1.1 Background

Although magnesium alloys have existed for some time, their production and use has been extremely limited when compared to other structural materials such as aluminium alloys. Of the magnesium alloys that have been developed, over 90% are casting alloys[1]. In recent years attention has turned to producing structural materials that can offer greater fuel efficiency through reduced density/weight than the currently available products. In particular, the aerospace and automotive industries are leading the way in development of light materials, especially for wrought applications.

To date, the greatest interest in wrought magnesium alloys has been from the aerospace sector. This has led to the development of high-end alloys such as Elektron WE43 (Mg-4.0wt%Y-3.3wt%RE-0.5wt%Zr). However, the production of such alloys is expensive. The automotive sector has also started to show interest in magnesium alloys for car body parts. For this reason, it is necessary to develop highly formable alloys that can compete in terms of performance and cost with the current automotive-based materials. The rare earth-based magnesium alloys that have been produced for aerospace have excellent structural properties, while remaining extremely light. However, alloys such as WE43 with high rare earth contents are not easily formable and are expensive relative to other magnesium alloys. The main thrust of the current project was to develop new alloys, with lower rare earth additions, which are consequently cheaper and, hopefully, more formable.

1.2 Mode of Work

The first step in assessing the formability of the new alloys was to carry out a range of deformation tests at various strain rates and temperatures. The thermo mechanical compression (TMC) machine offers the ability to deform materials under uniaxial or plane strain conditions while accurately measuring the temperature, load and displacement. This information can then be used to model the deformation behaviour of the material. Due to the

limited amount of material available during the current project, hot axisymmetric compression testing was selected as the optimal technique for collecting compression data while minimising the material used. To analyse the resultant deformed microstructures, electron backscattered diffraction (EBSD) was used. The technique can be used to quantitatively assess the microstructure and texture formed after deformation.

Mg-Zn-RE-based alloys often contain residual eutectic and peritectic phases after solution heat treatment. The current work has used differential scanning calorimetry (DSC) to study the solidus temperature of the eutectic with energy dispersive X-ray (EDX) spectroscopy being used to analyse the composition. Furthermore, transmission electron microscopy (TEM) has been employed to investigate the structure and morphology of the second phase.

TEM was also used to investigate the microstructure after artificial ageing. Precipitation reactions that took place were documented with visual assessment as well as selected area diffraction (SAD) patterns.

1.3 Project Objectives

In reference to sections 1.1 and 1.2, the aims of the current project are as follows:

- Develop a suitable solution heat treatment for the alloys.
- Carry out a series of hot axisymmetric compression tests through a range of temperatures and strain rates.
- Use the resultant data to assess the formability of the novel alloys.
- With the knowledge of the deformation behaviour, carry out a series of rolling experiments with an experimental rolling mill.
- Carry out a detailed investigation into the deformed microstructures and mechanisms of plastic deformation.

- Investigate the mode of dynamic recrystallisation as a function of the Zener-Hollomon parameter.

- Analyse any residual second phases.

- Carry out a complementary investigation into the age hardening response of the alloys.

2. Literature Review

2.1 Introduction

In recent years there has been an increased interest in fuel efficiency, both in the automotive and aerospace industries. In light of this, manufacturers are constantly looking at ways of improving alloy design to reduce overall weight without losing material properties. As far as structural metals go, magnesium holds great promise with the lowest density; approximately one fifth that of steel[1-3]. Magnesium offers an impressive strength to weight ratio, even when compared to most aluminium alloys[4].

Magnesium is an abundant and readily available element. It is the fourth most abundant element in the Earth, after oxygen, silicon and iron[1]. However, the availability of magnesium is even greater in seawater, where it is the second most abundant metal after sodium[1]. Commonly, electrolytic extraction and thermal reduction processes are employed to extract magnesium from seawater and the Earth's crust respectively[5]. At the beginning of the twentieth century, magnesium-based casting alloys were developed containing additions of aluminium and zinc. These early alloys suffered from substantial corrosion in wet and chloride-rich environments. The introduction of manganese to the system in small amounts (0.2 wt %) served to transform impurities, such as iron, into reasonably harmless intermetallics[5]. Grain size also proved to be a problem with earlier alloys. Large, inconsistent grain sizes led to poor mechanical properties. By the time of the Second World War, metallurgists in Germany had discovered that zirconium additions dramatically refined grain sizes, consequently improving the mechanical properties of the alloys[3]. Post-wartime saw a significant drop in the use of magnesium-based alloys that would not recover for the next 30 years[1, 2].

2.2 Magnesium Alloys

2.2.1 Background

Magnesium is the lightest metal that is currently used for commercial and industrial applications[1]. Other properties include: machinability, vibration dampening and electromagnetic wave shielding[3]. As such, magnesium has moved on from being a fringe material to being a genuine alternative to the current popular structural metals such as steel and aluminium. The main impetus for magnesium development has been the recent weight-saving trend in transport design. Currently there are strict quotas in place to reduce CO_2 emissions globally. As such, many automotive and aerospace manufacturers are investigating ways to expand the application of magnesium in their designs. One area that magnesium alloys have been particularly successful is in consumer electronics. Several manufacturers of portable laptops and mobile phones use magnesium alloys as light-weight chassis' for their goods. More exotic potential applications include the next generation of supersonic aircraft where magnesium is desired for its low weight, stiffness, dampening properties, strength and low thermal conductivity[6]. To truly capitalise on the benefits of magnesium, several issues need to be resolved. Many applications in automotive and aerospace design require wrought products. Magnesium is notoriously difficult to deform at room temperature. Therefore, it is necessary to produce wrought products at elevated temperatures. This fact increases the production costs dramatically[3]. Magnesium also has a high affinity with oxygen and severe corrosion susceptibility in the presence of other metals. To counteract these problems, it is necessary to surface treat magnesium alloys before use[1].

The current work is aimed at developing magnesium alloys that are attractive to the automotive industry in particular. The objective is to eventually produce a light-weight alloy that exhibits strength and dampening properties suitable for automotive design. However, to be truly attractive to the automotive industry, the alloy must be produced in a cost-effective manner. To do this, the material must be readily formable at a wide range of temperatures to reduce production costs. The alloys for the current work contain dilute amounts of rare earth additions (yttrium and neodymium) with zinc and zirconium. Rare earths have been used extensively in magnesium alloy design to provide strengthening and ductility as well as creep

and heat resistance. Zinc is also widely used for its increased workability as well as solid solution and precipitation strengthening[1, 3, 5]. Zirconium is commonly used in trace amounts for its potent grain refining effect[1, 3, 5]. The following sections will focus primarily on the additions added to the current alloys as well as outlining some additions used in other magnesium-based alloys.

2.2.2 Alloy Designations

Although there is some commercial variation in the naming of magnesium alloys, most manufacturers accept the nomenclature proposed by the American Society for Testing and Materials (ASTM). This designation method typically consists of two letters followed by two numbers which are sometimes followed with a third letter. The first two letters indicate the two major alloying additions. The following numerals indicate the quantity of the respective additions to the nearest weight per cent. When added, the third letter indicates a variation on the composition within the primary range. The third letter will be one of the following: A – First composition, B – Second composition, C – Third composition registered by ASTM, D – high-purity and E – High corrosion resistance[7]. Table 2.1 gives the major alloying additions with their respective naming designation. Once the alloys have been produced, they are thermally treated. The ASTM temper designation for magnesium alloys is the same as that used for aluminium alloys. Table 2.2 shows the range of tempers used to treat magnesium alloys along with the relevant ASTM temper designation. As an example, WE54 T6 is a magnesium-based alloy containing approximately 5wt% yttrium, 4wt% rare earths (Nd, Yb, Er, Dy, and Gd) that has been solution heat treated and artificially aged.

2.2.3 Modern Alloy Additions

Many of the modern alloys are based on the Mg-Al-Z system. Common alloys such as AZ31 and AZ61 (Mg-3Al-1Zn-0.3Mn and Mg-6.5Al-1Zn-0.3Mn respectively) are used for wrought applications in the form of sheet, extrusions and forgings. These cost-effective alloys offer reasonable strength with good formability and are readily weldable. Aluminium provides improved casting properties and solid solution hardening whereas zinc improves strength through precipitation[5]. Thorium was used with great success in magnesium alloys such as

Table 2.1 – Major ASTM alloy designations[7].

Letter Designation	Alloy Addition	Letter Designation	Alloy Addition
A	Aluminium	N	Nickel
C	Copper	P	Lead
D	Cadmium	Q	Silver
E	Rare Earths	R	Chromium
F	Iron	S	Silicon
H	Thorium	T	Tin
K	Zirconium	W	Yttrium
L	Lithium	Y	Antimony
M	Manganese	Z	Zinc

Table 2.2 – Major ASTM temper designations[7].

ASTM Code	Temper	ASTM Code	Temper
F	As fabricated	3	Solution heat treated, cold worked
O	Annealed, recrystallised	T4	Solution heat treated
H	Strain hardened	T5	Cooled, artificially aged
W	Solution heat treated	T6	Solution heat treated, artificially aged
H2	Strain hardened, partially annealed (wrought products)	T7	Solution heat treated, stabilised
H3	Strain hardened, stabilised (wrought products)	T8	Solution heat treated, cold worked, artificially aged
T1	Cooled, naturally aged	T9	Solution heat treated, artificially aged, cold worked
T2	Annealed (castings)	T10	Cooled, artificially aged, cold worked

ZH62 and HZ32, providing strength at elevated temperatures, improved creep resistance and excellent weldability[1, 3, 8]. However, in recent years, the radioactive nature of thorium has led to these alloys being phased out[3].

2.2.4 Rare Earth Additions

The rare earths consist of the lanthanide series (elements 57-71 of the periodic table), yttrium (atomic number 39) and scandium (atomic number 21). These elements are divided into two main subgroups. The cerium subgroup consists of elements from lanthanum to europium (atomic numbers 57-63) and the yttrium subgroup which consists of yttrium and the elements gadolinium up to lutetium (atomic numbers 64-71)[9]. The cerium group decompose quickly from the supersaturated solid solution to form Guinier-Preston (GP) zones that cause rapid solid solution hardening[8, 10]. The yttrium group generally show a good age-hardening response when added to magnesium alloys. The precipitates formed upon age hardening prove to be stable at elevated temperatures making the yttrium group of rare earth elements useful in alloys designed for high temperature operation[9]. Neodymium is used to great effect with yttrium in magnesium alloys (See Figures 2.1 and 2.2 for phase diagrams[9]) such as WE43 (Mg-4.0wt%Y-3.3wt%RE-0.5wt%Zr) and WE54 (Mg-5.1wt%Y-3.3wt%RE-0.5wt%Zr). These alloys are strengthened upon ageing by precipitates lying on prismatic planes that impede dislocation motion[11-14].

In the earlier half of the 20th century, rare earth metals were usually used in their naturally occurring form of mischmetal. Mischmetal contains a mix of rare earths with cerium making up the majority (~50wt%)[9]. Although mischmetal was primarily used in lighter and torch flints it found some favour when alloyed with magnesium, providing strengthening and improved high temperature performance. Leontis[15-18] later investigated the properties of individual rare earths and led the way in developing neodymium-based magnesium alloys that exhibited greater strength the mischmetal equivalent. By the 1960s, yttrium-based magnesium alloys were demonstrated to improve the strength properties even further[9]. This sparked numerous investigations into magnesium alloyed with other rare earth metals[9].

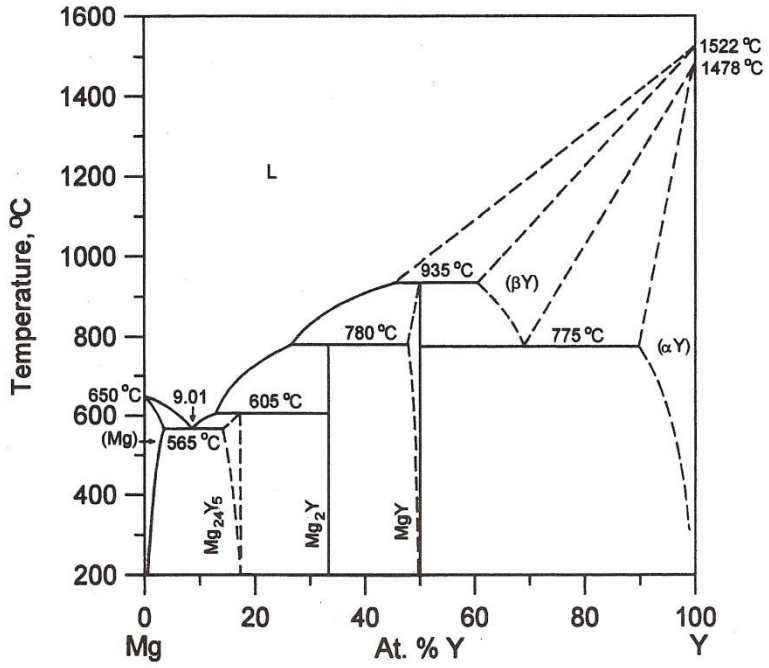

Figure 2.1 – Binary phase diagram for the Mg-Y system[9].

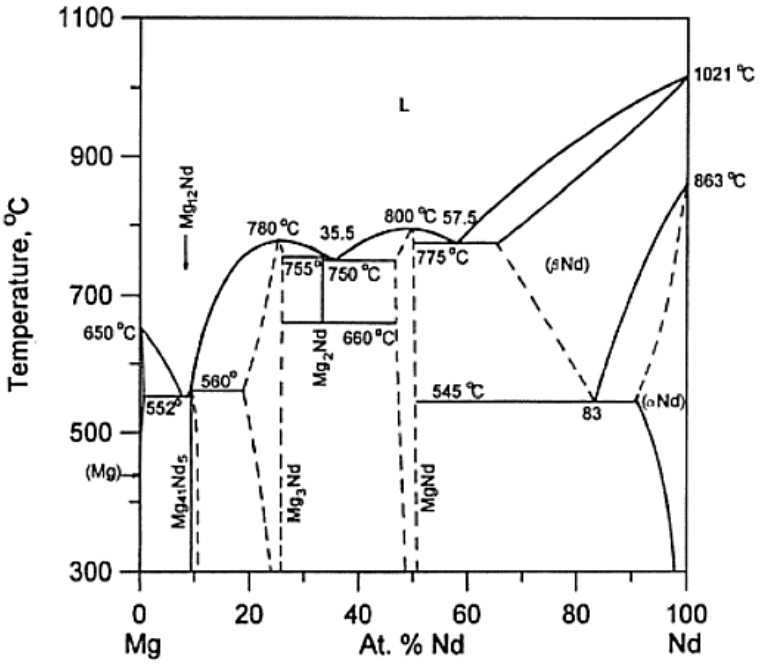

Figure 2.2 – Binary phase diagram for the Mg-Nd system[9].

2.2.5 Zinc Additions

Zinc is one of the most common alloy additions in magnesium alloys. The tensile properties of the binary system are not particularly impressive with limited elongation and poor ultimate tensile stress (UTS)[1]. Figure 2.3 shows the binary Mg-Zn phase diagram[19]. However, zinc does produce beneficial precipitation upon artificial ageing, increasing the hardness of the system[20]. When zinc is alloyed in magnesium along with rare earth elements, a drastic improvement in the tensile properties is observed. The formation of plate-like precipitates on the basal planes retards dislocation motion and reduces the occurrence of basal slip and cross-slip[21, 22]. However, recent work has suggested that the ratio of zinc to rare earths, particularly yttrium and neodymium, has a distinct effect on the formation of eutectic and peritectic second phases. Several studies[23-27] concluded that low Zn/RE weight ratios promote the formation of the W-phase ($Mg_3Zn_3Y_2$). The W-phase is a face-centred cubic (FCC) structure that severely limits the process window of wrought alloys due to its brittle nature and low melting point[23]. However, when the Zn/RE weight ratio is increased, the quasicrystalline I-phase (Mg_3Zn_6Y) can form. The I-phase is an icosahedral structure that disperses as beneficial, strengthening precipitates upon deformation[28]. Increasing the zinc content always decreases the solidus temperature, within the compositional ranges typically used in magnesium alloys[9].

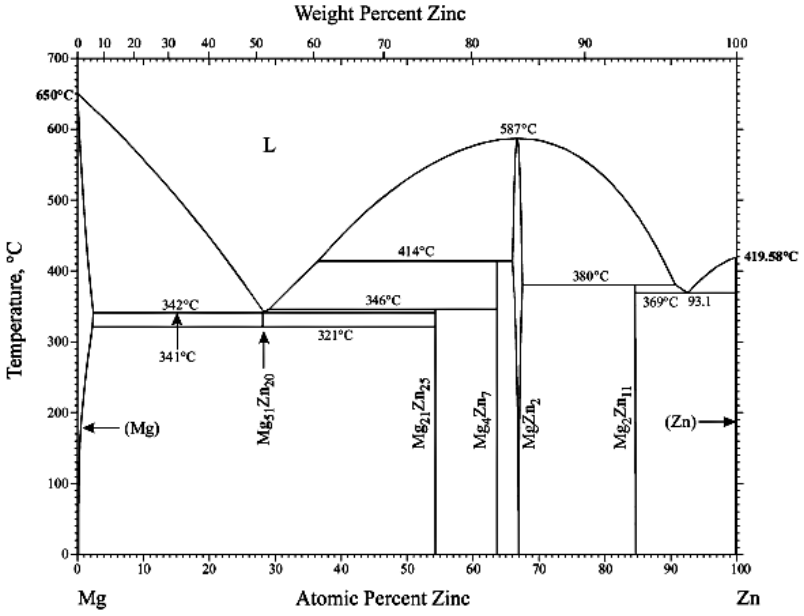

Figure 2.3 – Binary phase diagram for the Mg-Zn system[19].

2.2.6 Zirconium Additions

Zirconium has been used extensively in magnesium alloys for many years due to its potent grain refining properties[1]. The effect was first observed by the German metallurgist Sauerwald in the 1940s[29]. The grain refinement exhibited by zirconium is far greater than that of other popular grain refiners such as: aluminium, strontium, calcium and silicon[30]. The peritectic reaction between magnesium and zirconium occurs at around 654 ºC with over 0.58wt% zirconium[31]. However, grain refinement is also observed at much lower concentrations. This would suggest that the grain refining effect is due to undissolved particles of zirconium or compounds that form with zirconium and other elements[30, 31]. Zirconium-rich, dendritic coring is often observed in magnesium alloys[31-33], either at the grain centres or at grain boundaries. It is thought that these dendrites act to pin grain boundaries, helping to refine the final grain size[31-33]. Unfortunately, zirconium forms high melting point intermetallics with many other elements such as manganese, silicon and, in particular, aluminium[31]. This effect severely retards the grain refining properties of zirconium, thereby limiting the alloy systems that it can be used in. Fortunately, there are no such incompatibility issues with rare earth metals.

2.2.7 Miller-Bravais Notation

Magnesium has a hexagonally close packed (HCP) atomic structure. Unlike cubic materials, that are described with the three-figure Miller indexing notation, hexagonal structures contain more complex symmetry relationsh If the same, three figure, notation was used in HCP materials, similar crystal planes would, incorrectly, be described by different indices. In the case of HCP atomic structure, the Miller-Bravais indexing notation is used. In this system there are four indices [xyuz]. The first three indices, x, y and u, lie on the basal plane at an angle of 120º from each other. See Figure 2.4 for a schematic of the hexagonal unit cell. The third index is always the negative of the sum of x and y. If x = 1 and y = 1 then u = -2. If z = 0 then the complete indexing would be $[11\bar{2}0]$[34].

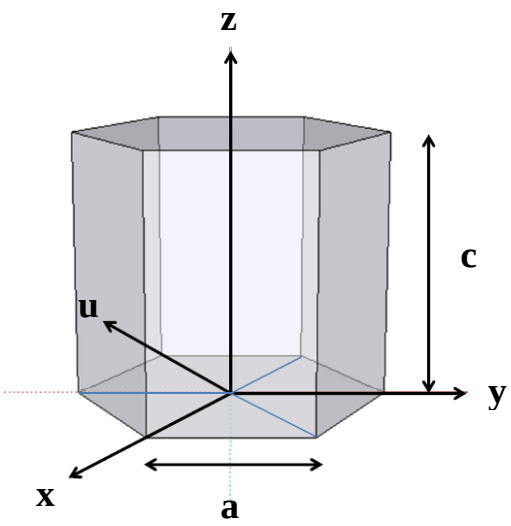

Figure 2.4 – Hexagonal unit cell including the four Miller-Bravais indices and the lattice parameters a and c.

2.2.8 Precipitation

2.2.8.1 Mg-RE System

Mg-RE alloys systems are readily hardened by stable precipitates forming upon artificial ageing. The precipitation sequence can be split into two groups; the yttrium subgroup and the cerium subgroup of rare earths (see section 2.2.4)[9]. The yttrium group tend to follow the precipitation sequence of:

SSSS → β'' → β' → β

The cerium subgroup follows a similar sequence but with the inclusion of Guinier-Preston zones (GP zones)[9]:

SSSS → GP zone → β'' → β' → β

Having two rare earths in the alloy from the same subgroup will develop intermediate properties of the two elements. By combining rare earths from both subgroups, the final alloy properties can be significantly improved[9].

Two popular rare earth alloys currently in use are WE43 (Mg-4.0wt%Y-3.3wt%RE-0.5wt%Zr) and WE54 (Mg-5.1wt%Y-3.3wt%RE-0.5wt%Zr). These alloys are strengthened upon ageing by precipitates lying on prismatic planes that impede dislocation motion[11-14]. The precipitation sequence upon ageing has been reported by several authors[8, 11-14, 35] to be:

$$SSSS \rightarrow \beta'' \rightarrow \beta' \rightarrow \beta$$

The metastable β'' phase has a $D0_{19}$ crystal structure with hexagonal lattice parameters of a=0.642 nm and c=0.521 nm and a habit plane of $\{11\bar{2}0\}_{Mg}$[5, 36]. The intermediate β' phase has a body-centred orthorhombic (BCO) structure with lattice parameters of a=0.640 nm, b=2.223 nm and c=0.521 nm. Finally the equilibrium β phase ($Mg_{14}Nd_2Y$) is FCC with a lattice parameter of a=2.223 nm[12]. Nie and Muddle[12-14] have also observed a precursor to the equilibrium β phase. The β_1 phase was observed to nucleate between β' precipitates upon ageing (see Figure 2.5). Upon further ageing the β' phase decomposes while the β_1 phase was observed to transform 'in-situ' to the equilibrium β phase. Some disagreement exists over the morphology of the intermediate β' phase. Several authors[37, 38] state that the β' phase forms as plates on $\{1\bar{1}00\}_{Mg}$ planes while others observed the β' phase as irregularly faceted, globular particles[12, 13].

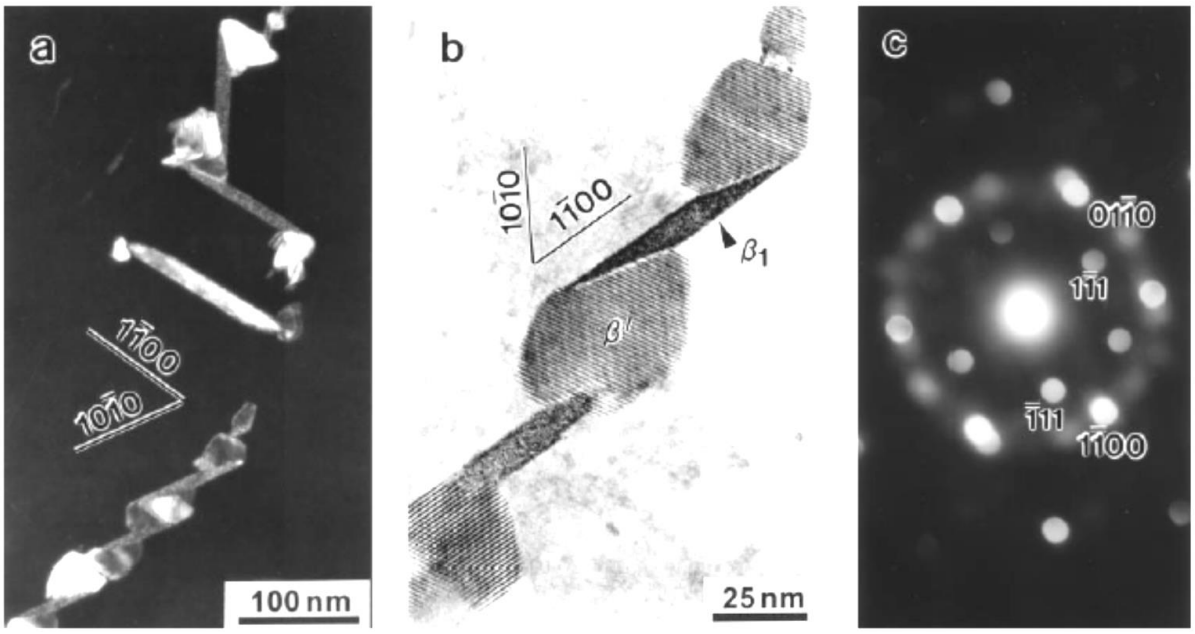

Figure 2.5 – a) Centred dark field, and b) bright field $[0001]_{Mg}$ micrographs showing irregular, faceted-shaped particles of β' and $\{1\bar{1}00\}_{Mg}$ plates of β_1 in samples aged for 48 h at 250°C; c) [110] Electron microdiffraction pattern recorded from β_1. a) was obtained using precipitate reflections at $1/2\{1\bar{1}00\}_{Mg}$ in a $[0001]_{Mg}$ SAED pattern[12].

2.2.8.1.1 Mg-Nd

With neodymium additions to magnesium, the precipitation sequence has been reported to be:

SSSS → GP zones → β'' → β' → β

The sequence was observed for a Mg-2.9wt%Nd alloy that was aged to 320 ºC[39]. The initial GP zones were reported as needle like structures growing along the $[0001]_{Mg}$ axis and existing at temperatures up to 180 ºC. The β'' phase occurred at temperatures from 180–260 ºC possessing a DO_{19} superlattice structure[39]. At higher temperatures of 200–320 ºC the β' precipitate nucleated, possessing a plate-like morphology, with $\{10\bar{1}0\}_{Mg}$ habit planes. The precipitate was hexagonal with lattice parameters of a=0.52 nm and c=1.3 nm[39]. At over 330 ºC the incoherent β phase formed ($Mg_{12}Nd$) with a body-centred tetragonal (BCT)

structure and lattice parameters of a=1.031 nm and c=0.593nm[39]. Both the β' and β'' precipitates are believed to be responsible for the age hardening observed in this system[40].

2.2.7.8.2 Mg-Y

In a Mg-10wt%Y alloy the precipitation sequence was observed to be[41]:

SSSS → β'' → β' → β

Both the β' and β'' precipitates were observed to have a body-centred orthorhombic (BCO) structure, while the β ($Mg_{24}Y_5$) precipitate exhibited a base-centred cubic (BCC) atomic structure[41]. Mizer and Peters[42] believed that a primitive monoclinic structure developed prior to the intermediate phases in a Mg-8.7wt%Y alloy. This coherent precipitate had the lattice parameters: a=0.64 nm, b=0.52 nm, c=1.155 nm and β=73.9°[42]. The phase dissolved at temperatures over 260 ºC followed by the formation of the intermediate and equilibrium precipitates.

2.2.8.2 Mg-Zn System

Magnesium alloys with additions of zinc form stable precipitates upon artificial ageing. Early work[43] on the binary system observed a β' precipitate ($MgZn_2$) with a hexagonal laves-type structure and lattice parameters of a=0.52 nm and c=0.85 nm. It was believed that the β' precipitate transformed into the equilibrium β precipitate upon further ageing[20]. The β' precipitate was later referred to as β_1' by Umezurike[44] in a Mg-6wt%Zn alloy, occurring after 24 hours ageing at 150 ºC. The precipitation sequence was:

SSSS → β_1' → β_2' → β

Two variants of the β_2' precipitate were observed; plate-like precipitates existing parallel to the basal plane and rod-like structures existing on the $(0001)_{Mg}$ plane and growing in $<11\bar{2}0>$ directions. The lattice parameters were reported to be the same as the β_1' precipitate[44].

Although there is general agreement on the structure and morphology of the β_1' precipitate[5, 11, 43, 45-48], more recent work by Gao and Nie[49] has demonstrated that the β_1' precipitate in a Mg-8wt%Zn alloy aged at 200 ºC possessed a base-centred monoclinic (BCM) structure similar to a Mg_4Zn_7 compound with lattice parameters of: a=2.596 nm, b=1.428 nm, c=0.524 nm and β=102.5º. Singh and Tsai[50, 51] agreed with Gao and Nie[49] that the β_1' precipitate had a BCM structure, adding that the structure was a complex one existing as several variants with different orientation relationships with the matrix. Both authors[49, 51] agreed with previous work[44, 45, 47] that the β_2' was hexagonal in nature and existed as plates and laths on the basal plane.

2.2.8.3 Mg-Zn-RE System

When rare earths are added to the binary Mg-Zn alloy, similar precipitates form, enhancing the strength and creep resistance[11, 21, 47]. Studies of Mg-Zn alloyed with mischmetal[47] (Mg-4wt%Zn-1.5wt%MM and Mg-8wt%Zn-1.5wt%MM) observed hardening by rod-like precipitates upon ageing. The precipitates were referred to as β_1' and grew along the $[0001]_{Mg}$ direction. After over-ageing, the β_2' developed with a plate-like morphology and an HCP structure[47]. It has been noted[52-54] that the plate-like precipitates have less interaction with dislocations than rods that grow along the $[0001]_{Mg}$ direction and, therefore, are less effective strengtheners.

Nie et al.[21] examined the effect of varying the zinc content of a Mg-6wt%Gd-0.6wt%Zr alloy. The ageing response was enhanced when the zinc content was greater than 1wt% as a result of plate-like precipitates existing on the basal plane. Similarly, Wilson et al.[55] observed plate like precipitates forming on the basal planes of a Mg-3wt%Nd-*x*Zn alloy after ageing. A modest increase in the peak hardness was measured when the alloy contained a zinc content of 1.35wt%. However, the peak hardness was found to be greater when the alloy only contained a zinc content of 0.5wt%. It was also noted that the addition of zinc to the Mg-Nd binary alloy, increased the ageing time required to reach peak hardness.

2.3 Crystallography and Deformation Mechanisms

2.3.1 Slip Systems

As with all HCP metals, magnesium exhibits poor formability at room temperature[1, 11, 35, 56]. However, once the working temperature is slightly elevated, ductility is increased, making the metal readily formable. Magnesium's atomic unit cell has axial lattice parameters of c=5.199 and a=3.202 Å, giving a c/a ratio of 1.624. As the theoretical axial ratio for an incompressible sphere is 1.633, magnesium is very near to being ideally close packed[1]. This close packed structure limits the modes of deformation available at lower temperatures (≤ 225 °C) when compared to cubic metals. At these temperatures deformation is primarily by slip along the basal plane (0001)[35]. The von Mises criterion states that for a material to plastically deform uniformly without failure, five independent slip systems must be active[57]. Slip is considered to be independent when it changes the crystal shape in a unique way that would not be possible through any other combination of slip systems[58]. While slip is primarily along the basal plane, only two independent systems of slip are available.

For full, uniform plasticity, slip on other planes must be made possible. Slip on the prismatic $\{10\bar{1}0\}$ and primary pyramidal $\{10\bar{1}1\}$ planes is in the <a> $<\bar{1}2\bar{1}0>$ direction offers only two more independent slip systems[58]. However, the <c+a> $<\bar{1}\bar{1}23>$ type direction along the second-order pyramidal $\{11\bar{2}2\}$ planes can offer the remaining slip systems for full plasticity[59-61]. Although five independent slip systems allow for full plasticity, a small amount of ductility can still be observed with a lower number of slip systems[62]. A schematic of the most common slip planes is depicted in Figure 2.6[35].

2.3.2 Twinning Systems

At lower temperatures plastic deformation is assisted by mechanical twinning. When the material is subject to an external shear stress, part of the crystal lattice can reorientate to give a mirror image of the adjacent atoms[63]. This process is known as mechanical twinning. Some strain is accommodated by the formation of twins and the process occurs rapidly[64]. Twins generally have a lenticular morphology. This shape is caused by the variation in speed

at which the different zones of the twin form. In the shear direction, the atomic matrix reorders into a mirror image at a velocity approaching the speed of sound[60, 65]. However, atomic reordering in other directions occurs more slowly. The width of these lenticular structures is greater in twins undergoing less shear[65-67]. Twinning dominates over slip in materials undergoing deformation at higher strain rates[68, 69].

Twinning occurs most frequently on the pyramidal planes $\{10\bar{1}2\}$ with secondary twining occurring on the $\{10\bar{1}1\}$ and $\{10\bar{1}3\}$ planes. $\{10\bar{1}2\}$ twinning accommodates strain under c-axis extension[61, 70]. Less common is twinning of the primary planes with the secondary planes to give $\{10\bar{1}1\}$-$\{10\bar{1}2\}$ and $\{10\bar{1}3\}$-$\{10\bar{1}2\}$ double twins. Double twinning can occur when the c-axis is under compression leading to a preferential alignment of the basal planes for slip. The preferential mechanism for slip can lead to work softening and strain localisation causing failure[71]. This work softening and failure has been observed in magnesium single crystals and polycrystals [72, 73]. Nave and Barnett[72] have studied the misorientation angles of common twins with the matrix in pure magnesium and collated the results of several studies as displayed in Table 2.3. It may appear that twinning provides the avenues of slip on pyramidal planes that offer full plasticity at room temperature. However, twinning only allows shear in one direction, unlike dislocation slip, so cannot be thought of as an independent mechanism of deformation[35]. Once the working temperature is raised above approximately 200 °C (depending on alloy composition), twinning is replaced by non-basal slip as further slip systems are activated[1-3].

The occurrence of twinning is strongly influenced by the average grain size of the sample. In general, larger grain sizes promote twinning while small grain sizes will promote deformation through slip[73-76]. As the number of grain boundaries increases, so does the critical stress required for the formation of twins[77].

2.3.3 Grain Boundary Sliding

Another possible deformation mechanism in magnesium is grain boundary sliding[73, 78-83]. Grain boundaries can slide in any direction through the sample during deformation and therefore offer compression in the c-axis direction. The occurrence of grain boundary sliding

will increase as the number of grains increase and temperature rises. Therefore, the phenomenon is more prevalent in samples with a smaller grain size (~<10 μm) being deformed at high temperature[73, 78-80, 84].

Table 2.3 – Misorientations between the matrix and primary or secondary twins commonly observed in Mg[72].

Type of Twin	Misorientation Angle (°)	Misorientation Axis
$\{10\bar{1}1\}$	56	$<1\bar{2}10>$
$\{10\bar{1}2\}$	86	$<1\bar{2}10>$
$\{10\bar{1}3\}$	64	$<1\bar{2}10>$
$\{10\bar{1}1\}$-$\{10\bar{1}2\}$	38	$<1\bar{2}10>$
$\{10\bar{1}3\}$-$\{10\bar{1}2\}$	22	$<1\bar{2}10>$

The various types of slip and twinning require a certain level of shear stress to be present. The critical resolved shear stress (CRSS) is the amount of stress, resolved to a particular slip plane, necessary to initiate the slip. For single crystals, this stress is constant for a given temperature[85]. For uniaxial compression conditions, the CRSS (τ) required for dislocations to move along a particular slip plane in a particular direction, is given by equation 2.1.

$$\tau = \sigma \cos\phi \cos\lambda \tag{2.1}$$

Where σ is the applied tensile stress, ϕ is the angle between the slip plane normal and the direction of compression and λ is the angle between the direction of slip and the direction of compression. The critical stress required to initiate slip is a function of the Schmid factor given in equation 3.2.

$$Schmid\ factor = \cos\phi \cos\lambda \tag{2.2}$$

The Schmid factor can be seen as the ease of slip occurring in a given direction for an applied stress[85]. Typically, the Schmid factor ranges up to 0.5, for polycrystalline metals. Grains with a higher Schmid factor value will be more favourably aligned for slip to occur.

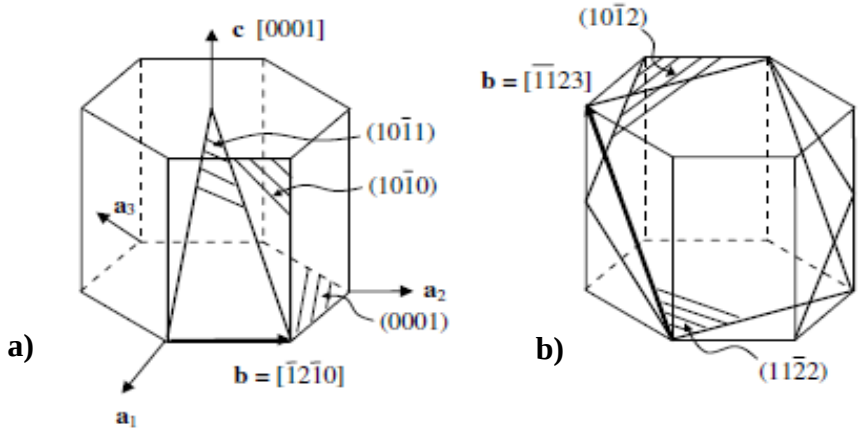

Figure 2.6 – Hexagonal close packed crystal planes and directions relevant to: a) slip of dislocations with the <a> type Burgers vector and b) slip of dislocations with the <c+a> type Burgers vector and one of the $\{10\bar{1}2\}$ habit planes of the most common twinning mode[35].

2.3.4 High Temperature Deformation

As previously mentioned, magnesium alloys become much more ductile at raised temperatures (>200 °C), due to a greater number of slip systems becoming active. The temperature can be considered with the strain rate to give the Zener-Hollomon parameter (Z) as shown in equation 2.3.

$$Z = \dot{\varepsilon} \exp\left(\frac{Q_{def}}{RT}\right) \tag{2.3}$$

Where $\dot{\varepsilon}$ is the strain rate, Q_{def} is the activation energy of deformation (see section 4.4.3.3), R is the universal gas constant and T is the temperature in Kelvin[86]. Lower values of Z make activation of prismatic and pyramidal slip systems possible. This can be achieved by either increasing the working temperature or decreasing the strain rate[3, 59].

The effect of temperature on the CRSS for various slip systems to be activated has been studied for various magnesium-based alloys[61, 87-95]. The general consensus is that the CRSS for each mode of slip decreases as the temperature rises. The various studies on the effect of temperature variation have been collated by Barnett[59] and displayed in Figure 2.7. An estimated line is included on the figure to show the CRSS required for the activation of twinning. As can be seen, the CRSS for the onset of twinning is not affected by the increasing temperature. However, as temperature increases, other slip systems are activated that will accommodate strain preferentially over twinning[59].

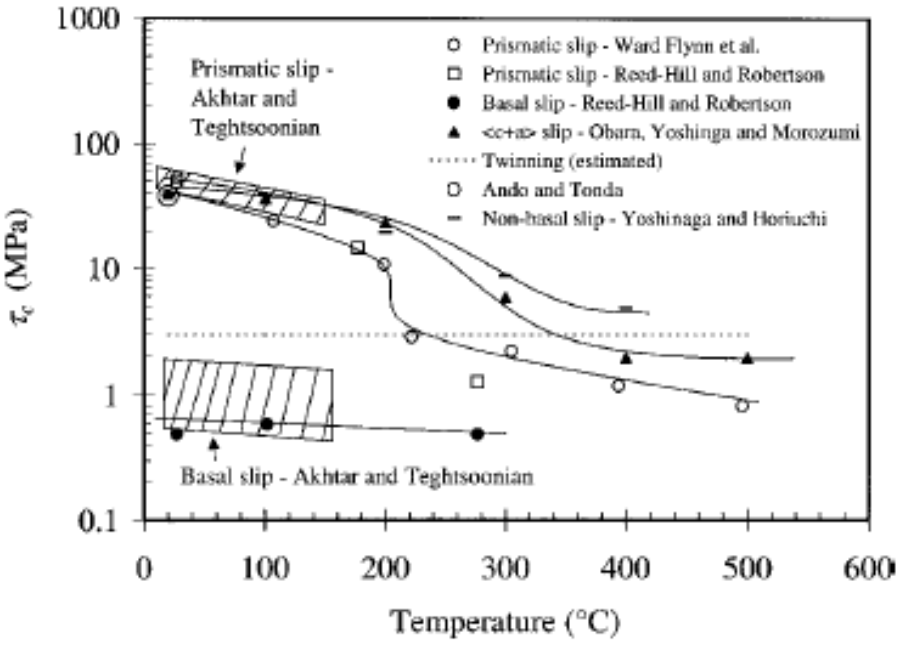

Figure 2.7 – Influence of deformation temperature on the critical resolved shear stress (CRSS) reported in several studies[89-95] and collated by Barnett[59].

2.3.5 Restoration Mechanisms

Deformation can lead to a build-up of stored energy or residual stress within a material. Structural defects, such as dislocations, build up at grain and twin boundaries leading to a significant amount of work hardening. However, this stored energy can be reduced by the onset restoration mechanisms. In particular, recovery and recrystallisation act to soften the

material which is clearly apparent when examining a stress-strain curve. When these recovery and recrystallisation mechanisms occur during deformation, they are considered to be dynamic processes. Conversely, when they occur after deformation, in an annealing process, they are considered to be static[56]. Both dynamic recrystallisation and dynamic recovery are of relevance to hot deformation processes such as hot rolling, extrusion and forging. Only dynamic processes are studied during the current project.

2.3.5.1 Stacking Fault Energy

The stacking fault energy (SFE) is a material property and affects the type of restoration mechanism taking place during deformation. In materials with a high SFE, climb and cross-slip occur more readily. When the stored energy is accommodated by climb and cross-slip in this way, recrystallisation is less likely to occur. When the SFE of a material is lower, climb and cross-slip become more difficult which favours recrystallisation over recovery[56, 96]. The SFE of magnesium alloys varies greatly with alloy composition. The SFE energy reported for magnesium alloys varies greatly through the literature with values ranging from low SFE to high SFE[97-99]. As there is such variation in the alloy compositions and SFE values, it is not possible to predict the active restoration mode by SFE alone.

2.3.5.2 Dynamic Recovery

Dynamic recovery (DRV) helps to relieve some of the residual stresses present during deformation. The primary reason for this residual stress is the build-up of dislocations at sites such as grain and twin boundaries. During DRV, these dislocations move through glide, climb or cross-slip[56]. The stress from the deformation process as well as from the surrounding microstructure will push dislocations in a given direction. When opposing dislocations on the same plane meet, they will combine and annihilate. If the opposing dislocations are on an adjacent slip plane they will not annihilate in the same manner, but create a dislocation dipole. This dislocation dipole will have much less energy than the two original dislocations. By further dislocation climb, the dipole can be annihilated completely[100]. A schematic showing the effect of these dislocation rearrangements is shown in figure 2.8[85]. The effect of this rearrangement is a net reduction of dislocations and,

therefore, of residual stress. The remaining dislocations will move to an arrangement that leaves them in a low-energy state. Through further rearrangement they will commonly form low-angle grain or subgrain boundaries.

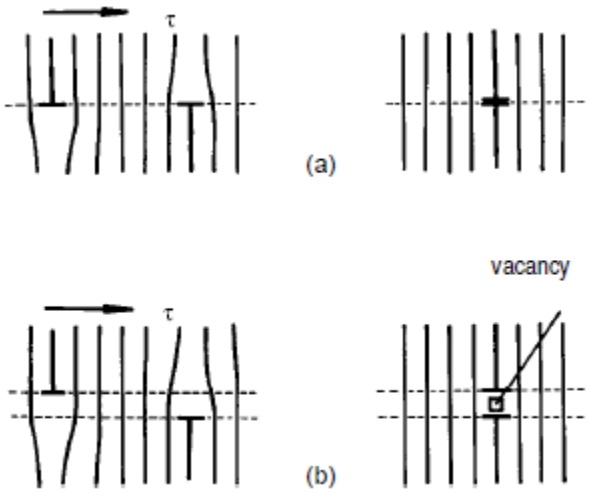

Figure 2.8 – Illustration of the principle of: a) annihilation and b) dipole generation by edge dislocations[85].

2.3.5.3 Dynamic Recrystallisation

2.3.5.3.1 Discontinuous Dynamic Recrystallisation

Another way in which a material may reduce the amount of residual stress present during deformation is through a process of dynamic recrystallisation (DRX). This process leads to completely new grains forming within the deformed microstructure. The most common example of DRX observed is that of discontinuous dynamic recrystallisation (DDRX). At higher temperatures (~300 °C) DDRX generally initiates at twin or grain boundaries with the new grains growing into the original grain[56]. It is generally accepted[101-103] that dislocation build-up at grain and twin boundaries leads to an increased amount of strain. Once the strain reaches a certain critical value, DRX initiates. Galiyev et al.[102, 104] concluded that, at temperatures in the region of 300 °C, dislocation climb leads to the formation of low-angle

boundaries that trap moving dislocations. Eventually, as dislocations build up, the low-angle boundaries become true, high-angle grain boundaries. A schematic of this process is displayed in Figure 2.9[102]. Once the new recrystallised grains nucleate, they will grow into the original grain until the stored energy is reduced and the growth will stop. The new recrystallised grains will deform more readily than the original grain, forming a soft mantle that will repeatedly recrystallise[101, 105].

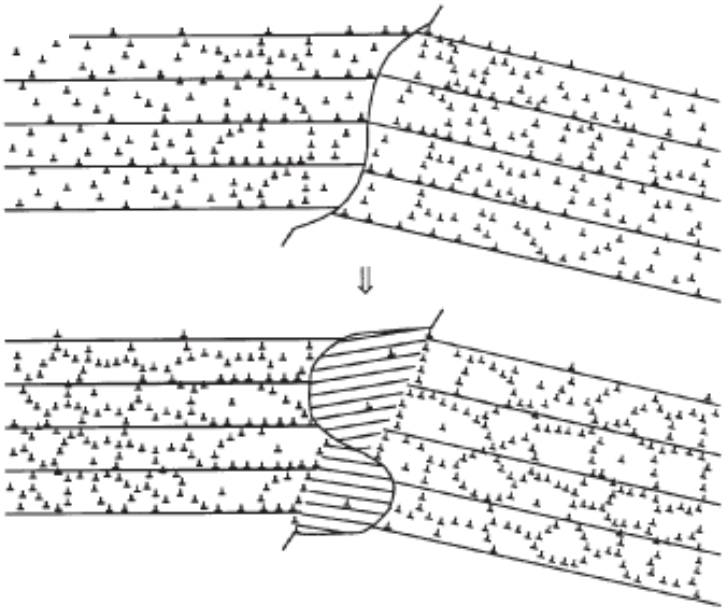

Figure 2.9 – Sketches of the nucleation process at 300 °C[102].

2.3.5.3.2 Continuous Dynamic Recrystallisation

At lower temperatures or higher strain rates a mechanism of continuous dynamic recrystallisation (CDRX) dominates the restoration process[56]. Strictly speaking, CDRX is a recovery mechanism, as the phenomenon is started by the rearrangement of dislocations into cells and subgrains. However, as CDRX creates entirely new grains, it is grouped together with the other DRX mechanisms. Dislocations rearrange in the vicinity of grain boundaries by means of cross-slip and climb to form low-angle boundaries. Further, moving dislocations are absorbed into this array of low-angle boundaries, causing the region to rotate into new, recrystallised grains around the original grain[60, 102]. A schematic of this process is displayed

in Figure 2.10[102]. The type of recrystallisation that occurs is dependent on either the temperature or strain rate. Galiyev et al.[102] concluded that CDRX is most common at lower temperatures (or higher strain rates) below 250 °C with DDRX becoming prevalent at higher temperatures (or lower strain rates) above 300 °C although there is some crossover between the types of mechanism.

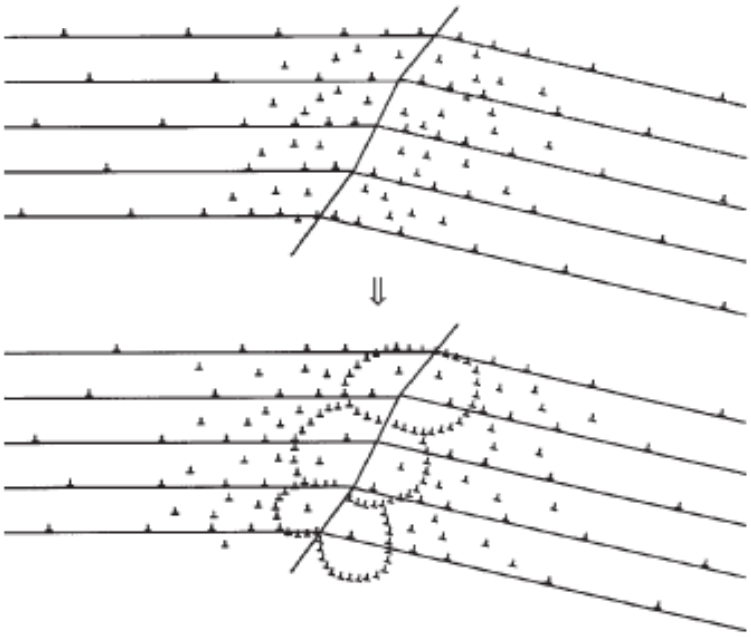

Figure 2.10 – Sketches of the nucleation process at 250 °C[102].

2.3.5.3.3 Twinning-induced Continuous Dynamic Recrystallisation

Twins can act as nucleation sites for DRX. Twinning-induced CDRX occurs in the same way as standard CDRX but the twin becomes the nucleation point for the occurrence. Dislocation pile-up occurs in and around the twinned material. The boundaries and intersections of twins act as stress concentration points, allowing further slip systems to activate. New cells and subgrains are formed as the dislocation density increases. Eventually, fully recrystallised grains are created[106-108].

The twinning-induced CDRX phenomenon can be exploited to produce a more desirable final microstructure. By carrying out a cold-forging pre-treatment, Park et al.[108] maximised the nucleation sites for CDRX upon further deformation, producing a finer resultant grain size

with a slightly weaker texture. Twinning-induced CDRX can be promoted by using high strain rates and strains with low temperatures during deformation[108].

It was noted in section 2.3.2 that twins can be uniquely identified by their misorientation angle with the grain matrix. As twinning-induced CDRX makes little difference to the original twin orientation, the same technique can be employed to identify the original twin type. By examining a misorientation plot of the CDRX region, characteristic peaks will exist at known twin orientations[72, 100, 107].

2.3.5.3.4 Continuous Dynamic Rotation Recrystallisation

Once the temperature is raised higher, twinning-induced CDRX becomes less prevalent. However, stress build-up in the grain boundary regions helps to activate non-basal slip. This activity is the precursor to continuous dynamic rotation recrystallisation (CDRRX)[60, 109]. Figure 2.11 displays a schematic of the mechanism[110]. The grain boundary is viewed as a soft mantle region surrounding the non-deforming grain centre. When stress builds up due to deformation, a shear will exist parallel to the grain boundary. Frictional effects in the grain boundary region cause the atomic lattice to rotate creating a build-up of dislocations. The dislocations will reconfigure into low-energy forms, leading to the development of cells and subgrains. As the strain continues, the rotation will continue until entirely new grains exist in a 'necklace' formation around the original grain[60, 102, 111, 112].

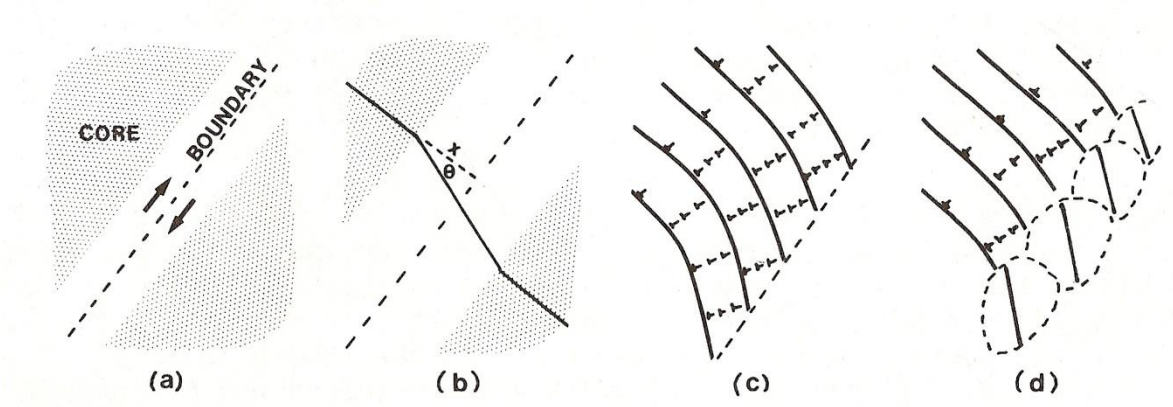

Figure 2.11 – Schematic of rotational recrystallisation developing in the mantle[110].

2.3.5.3.5 Mode of Recrystallisation

The prevalent type of DRX is heavily influenced by the conditions that the sample is deformed under. Previous studies[102, 113] have investigated the dominant DRX mechanism as a function of deformation conditions. At lower temperatures, twinning dominates the deformation in the early stages leading to twinning-induced CDRX in the later stages. As the temperature is increased slightly, dislocation slip and dislocation pile-up become more common at grain boundaries. These conditions lead to the common CDRX-type mechanism occurring. When the temperature is much higher, movement of the grain boundaries becomes more common and DDRX becomes the dominant DRX mechanism[113, 114]. Although a particular type of DRX mechanism may dominate at particular deformation conditions, it does not mean that it is the only mechanism active. Other mechanisms can also be active, but at a lesser rate.

2.3.5.3.6 Grain Size and Grain Growth

The final grain size after DRX is dependent on the deformation conditions of the test and , by extension, the dominant mechanism of DRX. When CDRX is active, the grain size tends to stay constant throughout the test[60]. Conversely, when DDRX is active, the initial grains are very small and then coarsen as the test continues. Once the DRX grains start to recrystallise again, a steady state is reached and the average grain size becomes constant[60]. A general, inverse relationship can be found between the Zener-Hollomon parameter and the final grain size. The smallest final grain size is produced when the sample is deformed at low temperatures with a high strain rate (high Z value)[60, 100, 102, 113, 115]. The final grain size can be approximated with equation 2.4[74, 115, 116].

$$Z = kd^{-N} \tag{2.4}$$

Where Z is the Zener-Hollomon parameter, d is the DRX grain size and k and N are constants.

2.3.6 Deformation Texture

The deformation texture developed in HCP metals upon rolling is largely dependent on the slip and twinning modes present and the c/a ratio[117]. For HCP metals with a c/a ratio $< \sqrt{3}$, such as magnesium, the primary $\{10\bar{1}2\}$ twin is activated by extension of the c-axis[117]. Under plane-strain conditions such as rolling, grains with the c-axis perpendicular to the compression axis will be favourably aligned for $\{10\bar{1}2\}$ twinning which will reorient the twin's c-axis close to the compression axis, leading to a near-basal texture[117]. It might be expected that magnesium should develop a near perfect basal texture due to its near perfect c/a ratio. However, observed microstructures often show a slightly off-basal texture with the basal plane being $\approx \pm 10\%$ from the expected plane[118]. Unfortunately, this strong basal texture leads to anisotropy in the properties of the material, especially when considering plastic deformation of magnesium alloy sheet. It has been found that random textures within AZ31 lead to greater formability however, due to the nature of industrial rolling, basal texture is inevitable[119]. However, there have been some studies of magnesium alloys with rare earth additions (yttrium and neodymium) that show a more random texture developing after deformation[120-122]. It has been inferred that this randomisation of texture is due to a particle-stimulated growth nucleation (PSN) mechanism of recrystallisation[121, 122]. Although the consequence of such PSN in magnesium alloys is attractive in the sense of improved secondary formability, caution must be taken. The studies of PSN in magnesium alloys are very limited to date and the controlling mechanism of texture randomisation has yet to be agreed on. Ball and Prangnell[122] suggested that large (>1 μm) particles within commercial WE alloys acted as sites for recrystallisation and a subsequent randomisation of texture. However other studies have shown that the presence of rare earth additions alone is enough to promote a change in texture without the formation of particles inducing PSN[120, 123]. To avoid the complications of matrix solute elements that may interfere with deformation, Robson et al. deformed three simple Mg-Mn alloys in an attempt to stimulate PSN[124]. The study concluded that although PSN was observed, it faced intense competition from standard dynamic recrystallisation events within the grain-mantle region, which dominated the final microstructure.

2.3.7 Flow Behaviour

For wrought metals to be designed, for any particular application, it is essential that the deformation behaviour is understood and modelled. When it comes to the modelling of industrial rolling, two popular types of test exist; plane strain compression and axisymmetric compression. Both of these tests usually involve compressing a heated sample between two platens at various temperatures and strain rates while recording the temperature, instantaneous load and displacement[125, 126]. From this data, stress-strain curves can be plotted for investigation. An example of typical flow curves of AZ31 under uniaxial compression from Barnett's work[68] is displayed in Figure 2.12. For magnesium alloys it is common to see a linear, elastic region followed by a period of work hardening that rises to a peak stress followed by a transition to work softening or failure at lower temperatures (< ~250 °C)[1]. This work softening is due to restoration events such as DRX and DRV[56]. As the temperature is increased or the strain rate reduced, the amount of work hardening reduces, as does the peak stress reached[1, 68, 127]. If the work hardening and work softening reach a point of equilibrium, then this will show as a steady-state, horizontal region on the stress-strain curve. This steady-state region will generally be reached at higher temperatures and/or lower strain rates[1, 56, 60, 68, 128]. This inverse relationship between temperature and strain rate, as discussed in section 2.3.4, can be combined using the Zener-Hollomon parameter. Beladi and Barnett[128] also carried out a uniaxial compression study of the rare earth based magnesium alloy, WE54 (5–5.5% Y, 1.5–2% Nd, 1.5–2% RE and 0.45% Zr). The results of one of the tests are displayed in Figure 2.13. The samples tested at lower temperatures (<300 °C) failed by shearing and the higher temperature tests showed a negligible amount of work hardening with a small amount of work softening before reaching a steady-state.

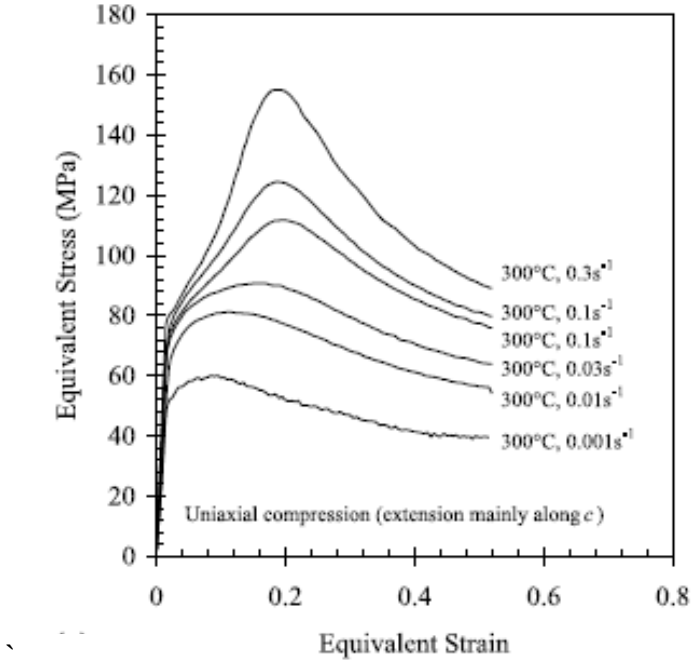

Figure 2.12 – Stress-strain data obtained using uniaxial compression[68].

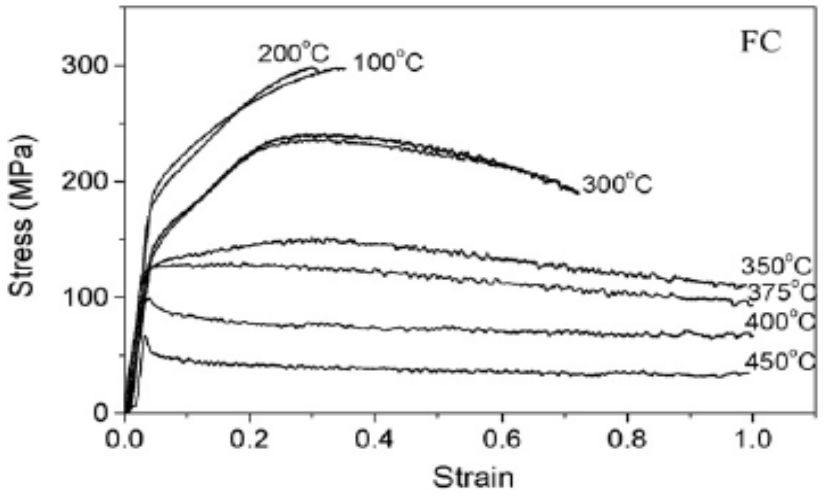

Figure 2.13 – True stress-strain curves of WE54 deformed under uniaxial compression at a strain rate of $0.01.s^{-1}$[128].

2.3.7.1 Modelling the Flow Behaviour

Davenport et al.[125] have presented a method of modelling the flow behaviour of steel under plane strain compression conditions to produce a set of constitutive equations. To derive the first set of equations, several discreet points on the flow curve need to be identified as shown in Figure 2.14.

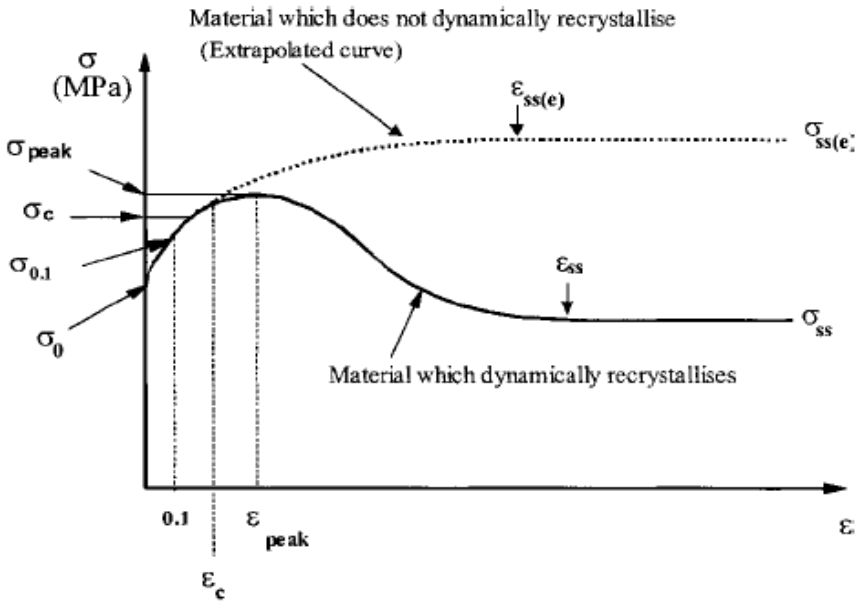

Figure 2.14 – Characteristic points on the flow stress curve for material that recrystallises dynamically[125].

The activation energy of deformation (Q_{def}) must also be calculated by following the following procedure:

A plot of the natural logarithm against stress is made for tests of at least three temperatures. Lines of best fit are placed between the data and vertical lines at set true stresses are added as shown in Figure 2.15 and the intercepts of these lines recorded. The natural logarithm of the strain rate at these points is plotted against $1/T_{inst}$ as shown in Figure 2.16. The gradient of these lines is $-\frac{Q_{def}}{R}$, where R is the universal gas constant. If the gradients of these lines remains reasonably constant then, so too, does $Q_{def.}$

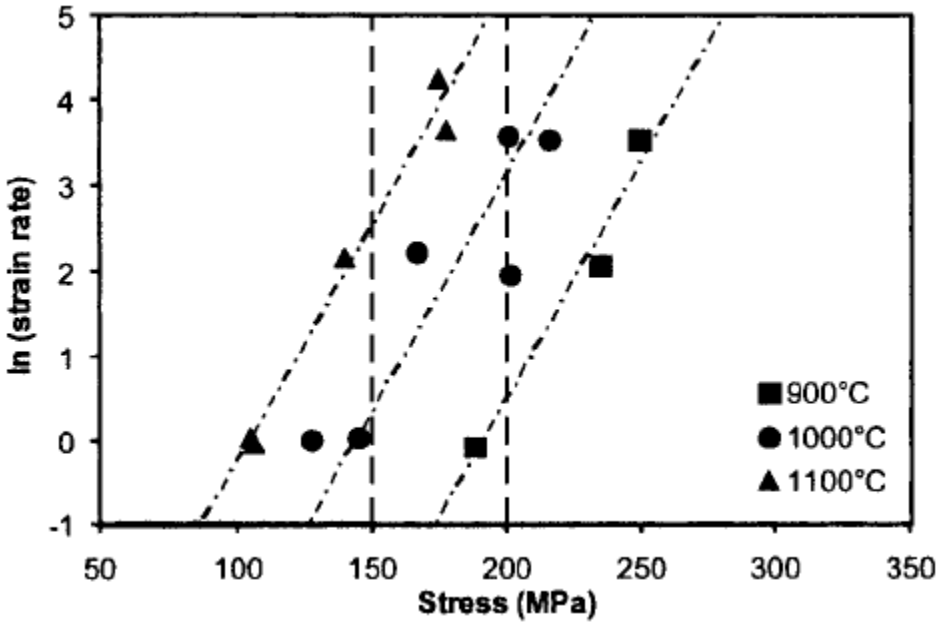

Figure 2.15 – Instantaneous values for ln-strain rate versus stress at a strain (ε) of 0.3[125].

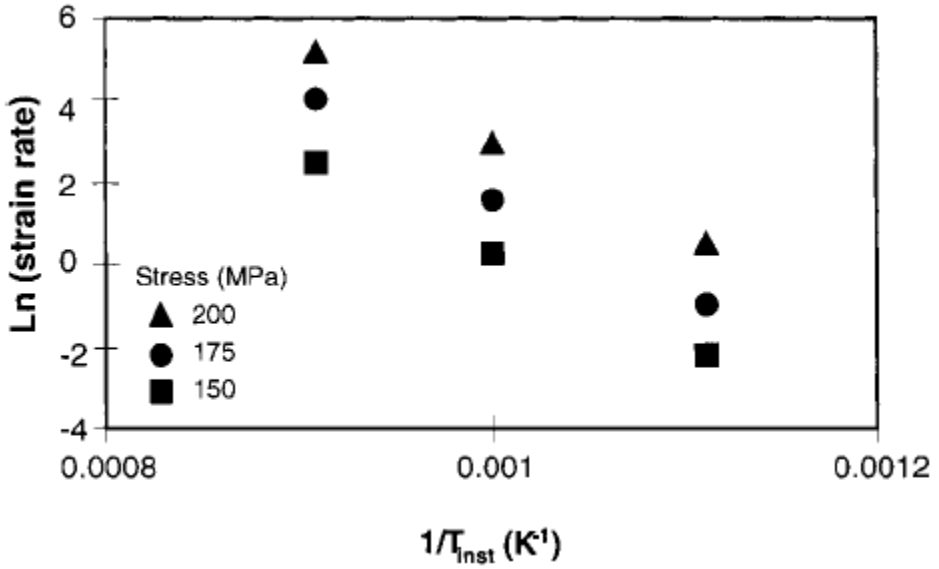

Figure 2.16 – Interpolated values of ln-strain rate versus inverse temperature taken from Fig. 2.8[125].

With the first stage of equations set out by Davenport et al.[125], the stress can be calculated at a given value of strain. The second stage of equations can then be used to predict a flow curve. Although the procedure was developed for steels, if has also been used successfully for magnesium alloys[109, 129, 130].

3. Experimental Method

3.1 Material

Four alloys were provided by Magnesium Elektron North America Inc: A base level alloy, AZ31b (Mg - 3% Al, 1% Zn, 0.5% Mn) and three experimental alloys based on the magnesium-zinc-yttrium-neodymium system. Containing relatively low amounts of rare-earth additions, the experimental alloys are intended to be a cost-effective solution for wrought applications in the automotive industry. As the new alloys are yet to receive official designations, for the purpose of this study, they have simply been referred to as alloys 93, 94 and 95. AZ31b is a standard alloy, common in low-end applications and has been supplied as a comparison to the new alloys. Billets of 200x150x40mm were sand-cast at Magneisum Elektron and the AZ31b was subsequently solution heat treated at 525 °C for 16 hours. The experimental alloys were supplied in their as-cast state and subsequently solution heat-treated at 525 °C for 6 hours at the university to homogenise the microstructure.

Although the composition of the experimental alloys is commercially sensitive, it is useful to differentiate the chemistries in terms of the weight ratio of major alloy additions (Zn, Y and Nd). Table 3.1 shows the ratio of the major alloying additions when considered without the magnesium majority.

Table 3.1 – Ratio of major alloy additions in terms of weight.

	Weight Ratio		
Alloy	Zn	Y	Nd
93	3	2	3
94	3	2	5
95	3	4	5

3.2 Hot Axisymmetric Compression Testing

To examine the flow behaviour of a material under hot deformation the axisymmetric compression test offers a reliable test method while using a minimal amount of test material. Due to the novel nature of the current alloys, a relatively small amount of the material was cast. For this reason it was crucial to minimise the amount of material used while maximising the available data. Although the test material is not compressed under plane strain conditions, the flow behaviour is still representative of other deformation processes such as hot rolling.

3.2.1 Specimen Description

Specimens were machined and tested in accordance with the UK National Physics Laboratory Good Practice Guide for Hot Axisymmetric Testing[126]. Cylinders of 12mm diameter and 15mm height were machined by Ashmark UK. A small lip was added at each end of the specimen to aid in the retention of lubricant during testing. Each specimen included a 1.1mm diameter hole at the mid-point of the cylinder to insert a thermocouple for flow analysis. Figure 3.1 gives a schematic of the specimen alongside an image for comparison. As required by the Good Practice Guide, all samples were machined in such a way as to minimise any residual stress or microstructural changes.

Lubrication is required at the points of contact between the sample and the tools to minimise frictional effects. As the testing was carried out at relatively low temperatures (420–465 ºC), an aqueous graphite solution was used, applied immediately before each test. The viscosity of the lubricant ensures that an even coating adheres to both the top and bottom of the sample.

3.2.2 Test Outline and Equipment

The compression testing was carried out using a Servotest Ltd. thermomechanical compression machine (TMC) in The Department of Materials Science and Engineering at The University of Sheffield. The testing rig was designed in accordance to the university's specification and commissioned in 2002. The relevant components of the TMC are three furnaces (preheating, testing and annealing), the fast thermal treatment unit (FTTU), the

robotic arm for controlling the position of the test specimen, the working tools and the ram. An image of the TMC and a schematic of the relevant components are displayed in Figures 3.2 and 3.3 respectively. The bottom tool is held in a stationary position on top of a post at the bottom of the test furnace. The upper tool is attached to the ram which is controlled, very precisely, by several actuators. The sample is initially held in position between the upper and lower tools by the robot arm. The ram moves downward causing the upper tool to make contact with the specimen and deformation occurs. For the current work, the testing was carried out in the form of constant strain rate. Therefore the velocity of the ram is a function of the instantaneous specimen height. The ram can achieve a maximum force of 500 kN. However, during tests carried out for this work, maximum forces of 15–25 kN were typical.

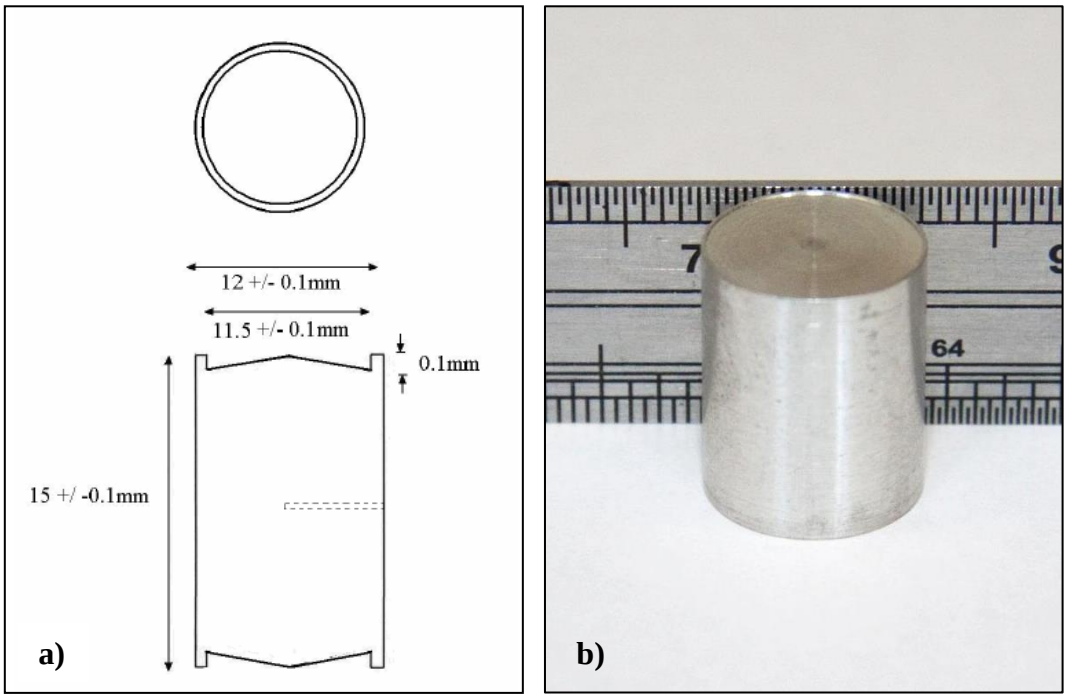

Figure 3.1 – a) Schematic of an axisymmetric compression test piece[131]. b) Image showing a test piece before deformation.

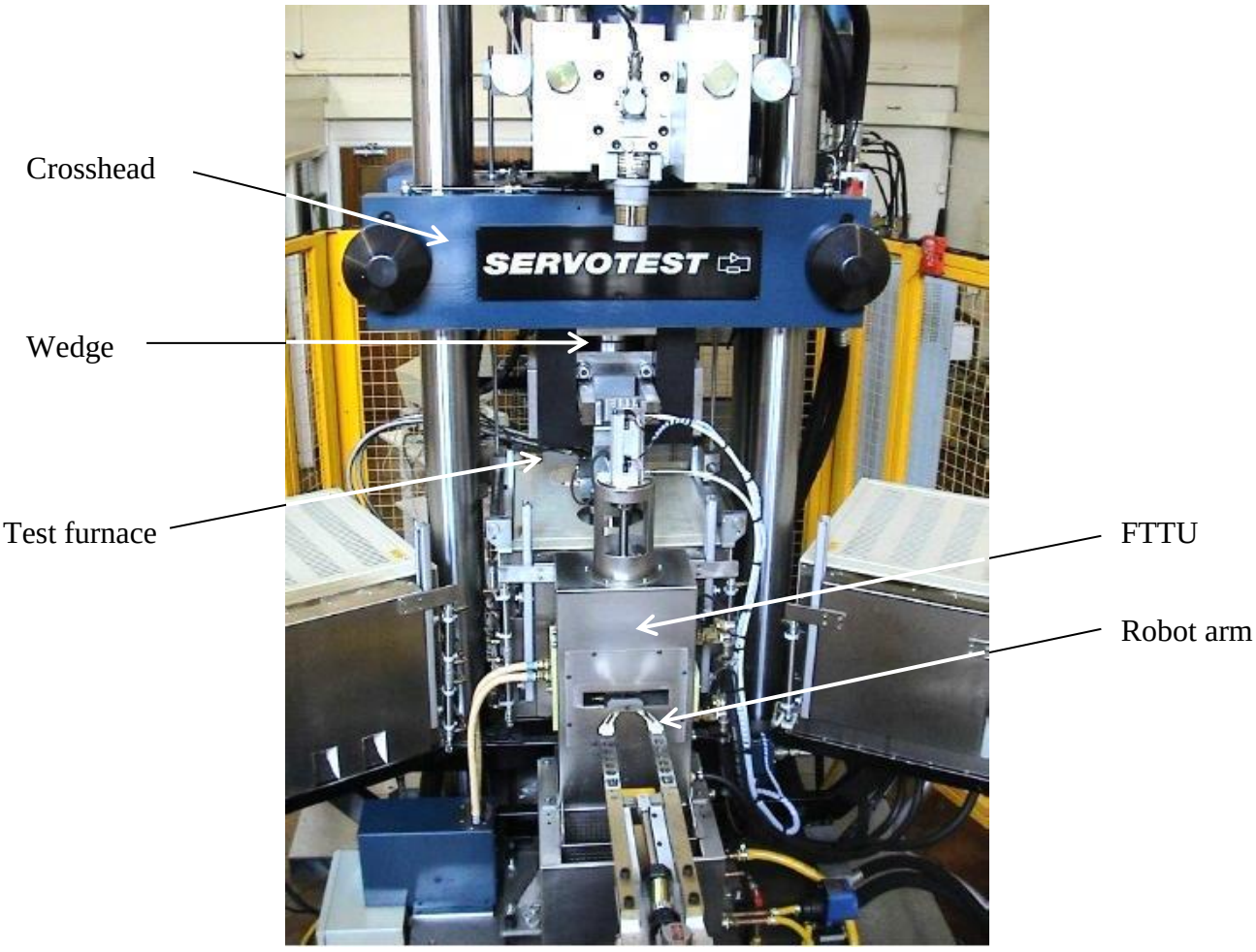

Figure 3.2 – The Servotest thermomechanical compression machine.

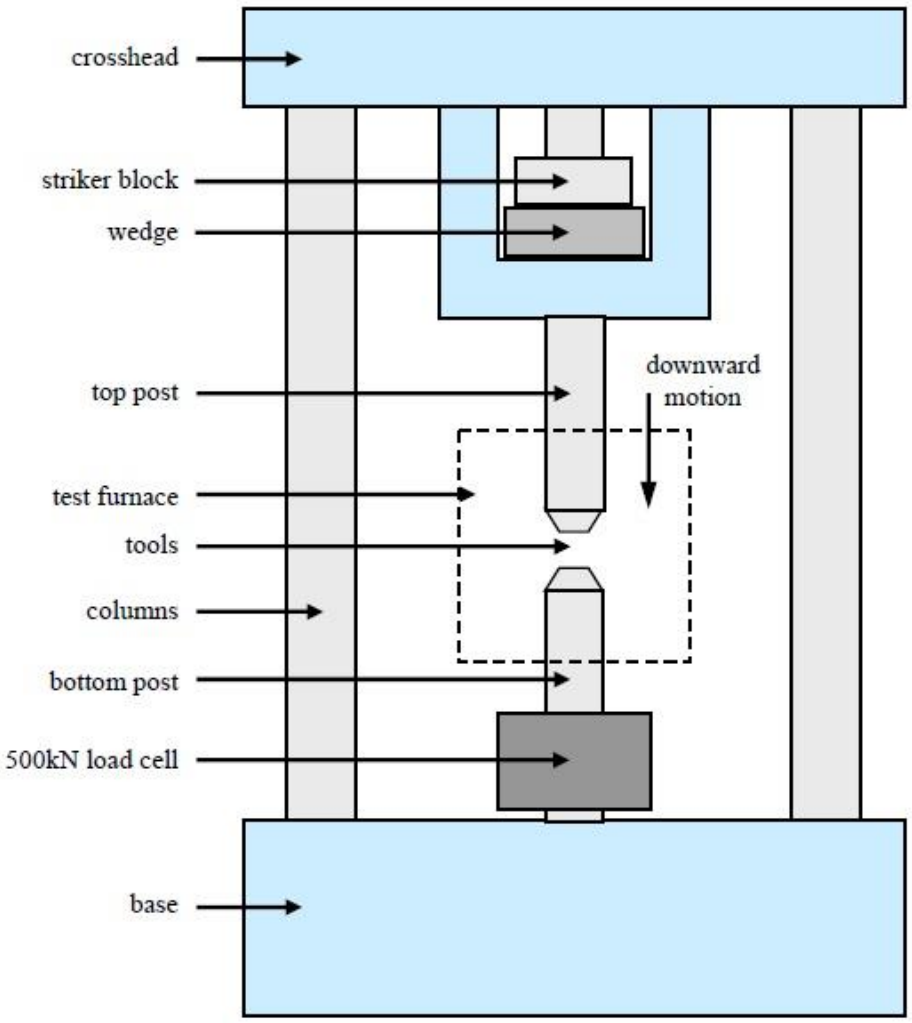

Figure 3.3 – Schematic of the TMC machine illustrating the relevant components[132].

3.2.3 Testing Procedure

At the start of a test, the sample was fitted with a thermocouple and placed between the robot arms. As the sample was held in place by friction, it is essential to ensure that nothing can displace the sample as it is moved into the FTTU, and eventually, the test furnace. Prior to the test the robot arm was manually rolled into the furnace with the sample in place. By doing this it was possible to check that there was enough clearance between the lower tool and sample. The height of the robot arm can be manually adjusted at this point to ensure that the sample does not strike the lower tool while being transferred during the test. A gap of ~ 2 mm

between the sample and lower tool is usually sufficient, allowing for any vibrational effects during transfer, to prevent any such collision.

Once the robot arm height had been adjusted the contact surfaces of the sample were given a thin layer of lubricant before commencing with the test. The relevant test parameters were input into the control computer, including preheat profile, test temperature, strain and strain rate. The preheating was carried out in the FTTU unit. The FTTU uses induction to quickly heat the sample to the test temperature and hold it at that temperature for a specified time. Before deformation, each sample was raised in temperature by 2 ºC per second to the desired testing temperature. Once at the deformation temperature, the sample was held for 300 s to 'soak', ensuring and even temperature was reached across the whole test piece. After 300 s soaking the sample was transferred rapidly by the robot arm to the test furnace for deformation. The test furnace was held at a slightly higher temperature to ensure that the tools were at the desired testing temperature. The sample was deformed at the required strain rate to a strain of 0.6 and subsequently water quenched to retain the deformation microstructure. A schematic of the deformation profile is displayed in Figure 3.4.

During the test, the temperature was recorded precisely by an N-type thermocouple inserted into the sample within the deformation zone and recorded by the control computer. As well as temperature; load, displacement and velocity information was also collected. Typically, the temperature was recorded at intervals of approximately 1000–10,000/s depending on strain rate. Accurate recording of the temperature during the test was essential to correct for deformational heating when carrying out further analysis. Once the test had been completed, the final dimensions of the deformed sample were accurately measured and recorded in accordance with the Good Practice Guide[126].

3.2.4 Friction Testing

It is important to consider the effects of friction as the sample deforms and slides against the work tools. For this reason, a simple method of assessing the coefficient of friction was carried out[133]. Three samples were machined to different heights and deformed at a temperature of 450 ºC and a strain rate of 1/s. Once the data from the tests had been collected,

and incorporated into stress-strain curves, the correct coefficient of friction could be assessed. Regardless of the sample height, the stress-strain curves should be very similar if the test has been carried out under the same conditions. Therefore, by trial and error, the correct coefficient of friction can be found by fitting a range of values to the data until the stress-strain curves closely match. For the further information regarding this method and the necessary calculations, refer to section 4.4.3.1.

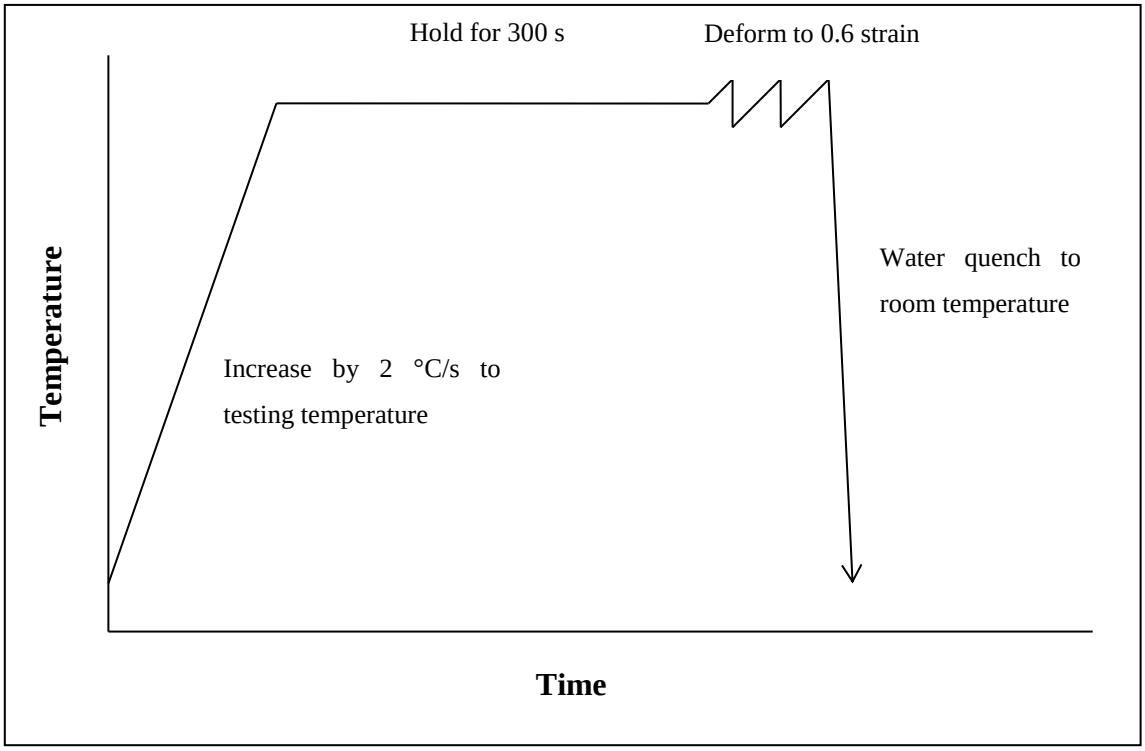

Figure 3.4 – Schematic of the deformation test process.

3.2.5 Summary of Hot Axisymmetric Compression Testing

Compression tests at a range of temperatures and strain rates were carried out. However, due to the limited process window of the three alloys, only a narrow range of the tests could be used for further, in-depth analysis. The tests used for analysis are listed in Table 3.2. The coefficient of friction calculations were based on the three tests listed in Table 3.3.

Table 3.2 – Hot axisymmetric compression tests carried out to a strain of 0.6.

Alloy/Test number	Strain Rate (s^{-1})	Temperature (ºC)
93 – 1	0.5	425
93 – 2	1	425
93 – 3	5	425
93 – 4	0.5	435
93 – 5	1	435
93 – 6	5	435
93 – 7	0.5	450
93 – 8	1	450
93 – 9	5	450
94 – 1	0.5	425
94 – 2	1	425
94 – 3	5	425
94 – 4	0.5	435
94 – 5	1	435
94 – 6	5	435
94 – 7	0.5	450
94 – 8	1	450
94 – 9	5	450
95 – 1	0.5	425
95 – 2	1	425
95 – 3	5	425
95 – 4	0.5	435
95 – 5	1	435
95 – 6	5	435
95 – 7	0.5	450
95 – 8	1	450
95 – 9	5	450

Table 3.3 – Tests carried out to assess the coefficient of friction.

Alloy/Test Number	Strain Rate (s^{-1})	Temperature (ºC)	Sample Height (mm)
94 – 1	1	450	10
94 – 2	1	450	12.5
94 – 3	1	450	15

3.2.6 Analysis of Raw Data

The TMC gives raw data in the form of load (kN) and displacement (mm). Once this data is plotted, a number of corrections are required. In theory, the tools should make contact with the sample at zero displacement. However, variations in the sample height, due to the lubricant thickness, and machine drift cause discrepancies in this reading. To correct for these discrepancies, the linear region of the load-displacement curve is extrapolated to the x-axis. The intercept on the x-axis is then subtracted from the displacement data so that the extrapolated linear region passes through the origin. Figure 3.5 shows this zero-corrected curve next to the raw curve.

Further errors are introduced due to machine compliance and slight elastic deformation of the sample during the test. The combination of these two factors is represented on the load-displacement curve as the linear region discussed above. The gradient of the linear region is calculated and subsequently subtracted from the data. The final correction is in the discrepancy between the final measured height of the sample and the overall displacement measured by the TMC. Once this has been subtracted from the data the yield point, signifying the start of plastic deformation, should occur at zero displacement. The final, corrected curve is depicted in Figure 3.5 as the solid line.

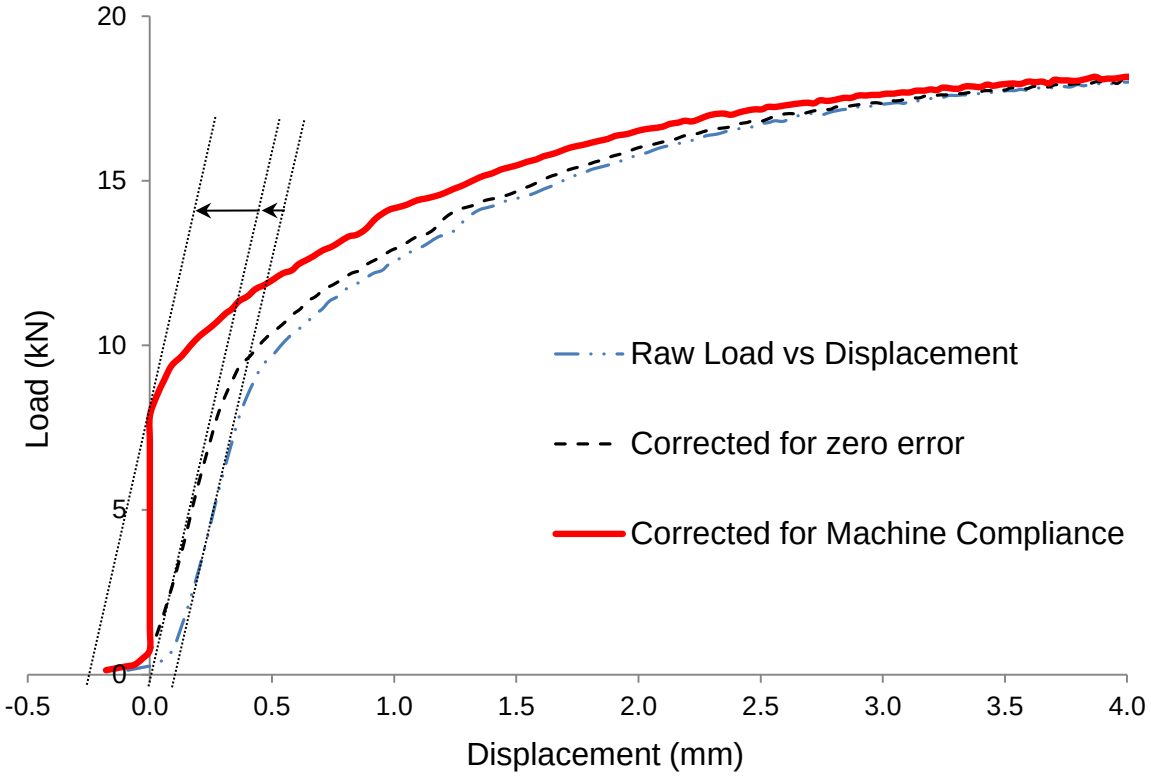

Figure 3.5 – Zero error and machine compliance corrections.

3.2.7 Calculation of Equivalent Strain and Equivalent Flow Stress

Once the load-displacement data has been corrected it is used along with time, temperature and velocity to produce the stress-strain curves. First equivalent strain is calculated using equation 3.1.

$$\varepsilon = \ln\left(\frac{h}{h_0}\right) \tag{3.1}$$

Where ε is the equivalent strain, h is the instantaneous height and h_0 is the initial height of the work piece.

To calculate equivalent stress equation 3.2 is used.

$$\sigma = \frac{F}{A} \tag{3.2}$$

Where σ is the stress, F is the instantaneous load and A is the instantaneous cross sectional area of the work piece, calculated with equation 3.3.

$$A = A_0 \times \exp(\varepsilon) \tag{3.3}$$

Where A is the instantaneous cross sectional area of the work piece, A_0 is the original cross sectional area and ε is the instantaneous strain.

To calculate the instantaneous height it is necessary to adjust the measured specimen dimensions for thermal expansion. Using the cold height measurement (h_c) it is possible to calculate the initial height (h_0) at the testing temperature with equation 3.4:

$$h_0 = h_c + \alpha_t h_c (T - T_0) \tag{3.4}$$

Where α_t is the coefficient of thermal expansion for AZ31 at 26.8×10^{-6} K^{-1} as supplied by Magnesium Elektron, T is the test temperature and T_0 is the instantaneous temperature. The instantaneous height (h) is then calculated with equation 3.5:

$$h = d_p - h_0 \tag{3.5}$$

Where d_p is the measured displacement of the TMC Crosshead.

Once the stress has been calculated, it is important to factor in the effects of friction and correct the value for true stress accordingly. For the initial tests, a coefficient of friction (μ) of 0.2 was used. This value was determined experimentally and detailed in section 4.3.3.1. Equation 3.6 has been adapted from Dieter[134] to give a friction-corrected value of true stress.

$$R = \frac{2\sigma}{\left[\frac{h}{\mu d}\right]^2\left[\exp\left[\frac{\mu d}{h}\right] - \frac{\mu d}{h} - 1\right]} \tag{3.6}$$

Where R is the friction-corrected true stress, σ is the stress calculated from equation 3.1, h is the sample height, d is the sample diameter and μ is the coefficient of friction.

3.2.8 Strain Rate Corrections

The instantaneous strain rate has a profound effect on the measured flow stress. During the test the velocity of the ram will vary due to changes in pressure as the deformation occurs. When these variations are incorporated into the flow stress calculations they are exaggerated further, thereby, causing noise in the final flow curve. For accurate flow stress it is necessary to clean up the strain rate measurements. Tukey[135] has detailed a method of smoothing large ranges of data. Figure 3.6 shows an example of this smoothing function with the raw, noisy data and the smoothed strain rate superimposed (dashed line).

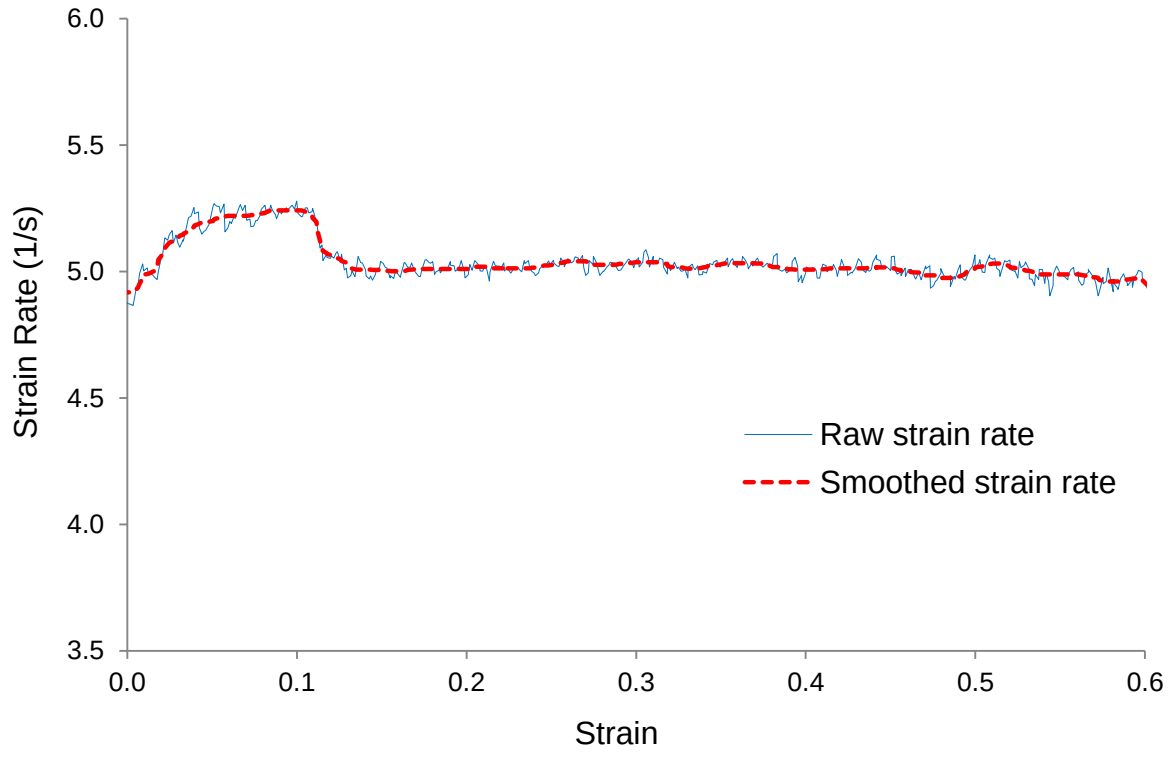

Figure 3.6 – Smoothing of strain rate data.

Once the strain rate data has been smoothed it is necessary to correct the measured flow stress accordingly. Equation 3.7 is used to correct the flow stress data of every test to give true iso-strain rate flow curves.

$$\sigma_2 = \sigma_1 \left(\frac{\dot{\varepsilon}_2}{\dot{\varepsilon}_1} \right)^{1/n} \tag{3.7}$$

Where σ_2 is the corrected, nominal stress, σ_1 is the measured stress, $\dot{\varepsilon}_2$ is the nominal strain rate at which the test was set, $\dot{\varepsilon}_1$ is the measured strain rate and *n* is a constant calculated in section 4.3.3.2.

Temperature variations during the test also affect the flow stress significantly. These variations are caused by deformational heating and differences in the tool temperatures as they make contact with the sample. In order to present the flow curves isothermally the data from each test is corrected using equation 3.8

$$\sigma_2 = \sigma_1 + \frac{Q_{def}}{\beta R} \left(\frac{1}{T_2} - \frac{1}{T_1} \right) \tag{3.8}$$

Where Q_{def} is the activation energy of deformation, calculated in section 4.3.3.3, β is a constant calculated in section 4.3.3.4, R is the universal gas constant, T_1 is the measured temperature and T_2 is nominal temperature at which the test was set.

3.3 Isothermal Age Hardening

3.3.1 Procedure

A number of tests were carried out to assess the isothermal ageing response of the three alloys. A number of uniform pieces, measuring 30x20x10 mm, were sectioned from the test alloys after the solution heat treatment stage. A Lenton chamber furnace was used to carry out a simple ageing treatment. All of the treatments were carried out at 225 ºC for times

ranging from 1 to 100 hours and subsequently cooled in air. A protective atmosphere was not required.

3.3.2 Vickers Hardness Testing

A Mitutoyo Vickers hardness tester was used to investigate the ageing profile of the test pieces. After each sample had been subjected to isothermal ageing, the top surface was ground with silicon carbide paper up to 2500 grit and polished with an alcohol-based 1μm diamond solution. Due to the relatively large grain size of the material in this condition, it was essential to ensure that the hardness measurements were taken from similar areas within each sample. For each age condition, a series of 20 measurements were taken from grain centres, taking care to avoid grain boundaries or any second phase material.

3.4 Microscopy

3.4.1 Sample Preparation Route

3.4.1.1 Introduction

The preparation of magnesium alloys for analysis with optical and electron microscopy is notoriously difficult, with each type of alloy presenting its own, unique problems. This section gives an overview of the preparation methods used for each analysis technique. Problems encountered during the project have been given special attention along with details of the proposed solution. It is hoped that future magnesium researchers will find the following pages useful in their own work.

3.4.1.2 Common Problems Encountered

With the current alloys, several issues arose during the sample preparation. This section lists some of the generic problems encountered with the later sections listing the more technique-specific problems.

3.4.1.2.1 Oxidation

Most magnesium-based alloys are affected by oxidation. In the example of the current alloys, oxidation of the sample surface occurs very quickly after preparation. A number of steps were taken to reduce the onset of an oxide layer. During the initial grinding stages, it is difficult to avoid the use of water as a lubricant. However, alternatives can be used during the final polishing stages. For polishing, alcohol-based diamond solutions and lubricants were used. When cleaning samples between stages, it was found that a quick blast of high-pressure water with soap followed by a thorough rinse with isopropyl alcohol was sufficient to clean any debris from the surface without forming an oxide layer.

When transporting samples to a microscope they were kept under high-purity isopropyl alcohol or ethanol to slow the rate of oxidation. It is prudent to prepare samples as soon as possible before analysis. Even in the relatively high vacuum environment of an SEM chamber, after long (3 day) EBSD scans, a visible oxide layer developed.

3.4.1.2.2 Pull-Out of Second Phase and Large Particles

When a large volume fraction of second phase material or large particles are present in a sample, pull-out can occur during the polishing stage. Second phases will often have a different hardness and ductility to the matrix. For this reason the wear rate during grinding and polishing will vary. When the second phase is harder and more brittle than the matrix, relief can occur during grinding with the second phase standing proud from the matrix. Combined with the high friction of some polishing cloths, the second phase can shear, causing pull-out. Once pull-out occurs, the polishing cloth will become contaminated and the sample surface will become scratched. In order to minimise pull-out it is necessary to minimise relief during the grinding steps and friction during polishing.

Over-grinding is a common cause of excess relief. The current alloys are very soft (40–70 HV) with material removal during grinding occurring extremely quickly. Therefore, in terms of minimising relief, better results were produced with shorter grinding times. Typically, depending on the sample preparation route being used, course grinding on silicon carbide

paper (400–800 grit) was carried out for less than 30 seconds with fine grinding (2500–4000 grit) taking around 90–120 seconds.

To reduce frictional effects during polishing it is important to use a suitable lubricant and an appropriate polishing surface. The napped-type cloths, commonly used for polishing during the 1μm diamond stage, were found to cause too much friction and therefore pull out with the experimental alloys. To avoid this problem, a non-woven textile cloth was used for polishing with 1 and 0.25 μm diamond along with an alcohol-based lubricant. When a final polish with colloidal silica was required, a neoprene polishing cloth was used.

3.4.1.2.3 Sensitivity to Methanol

During the project it was found that the current alloys were particularly reactive in the presence of methanol. This effect was most apparent when placing thin foils for TEM into lab-grade methanol. The samples would visibly react with the solvent and would completely dissolve within several minutes. However, when the methanol was mixed with other chemicals, such as an electrolytic polishing solution, the effect was reduced. As a general rule, ethanol or isopropyl alcohol were used as alternative solvents when cleaning or storing samples.

3.4.1.2.4 Cleaning Samples after a Colloidal Silica Polish

When colloidal silica has been used as a final polish it is common to use an ultrasonic bath to remove traces of the solution from the sample surface. However, some magnesium alloys, including those studied during this project, suffer from severe pitting when placed in an ultrasonic bath. Another approach is to use cotton wool soaked in a solvent such as isopropyl alcohol or ethanol, but this method can leave fine scratches on the highly polished surface. Although water can cause problems with oxidation, it was found to be the most effective solvent when removing the fine residue left by the colloidal silica polish. As long as the exposure to water was kept to a minimum, oxidation did not cause any problems. The method used to clean the samples after the final polish is detailed in section 3.5.1.5.

3.4.1.3 Sectioning

When considering which plane to investigate in an axisymmetric compression sample, it is important to consider which features of the material are of most interest. When hexagonal materials, such as magnesium, are deformed by compression, grains will usually align themselves with the basal plane perpendicular to the compression axis. Under the right conditions of strain rate and temperature, the grains will undergo dynamic recrystallisation. Once recrystallised, a desirable microstructure of fine, randomly orientated grains will be produced. For this project it was the variation in texture, away from the basal plan, that proved most interesting. For this reason, samples were sectioned perpendicular to the compression axis. By doing so, the variation of recrystallised grains away from the basal plane, could be visualised and studied with EBSD.

A schematic of how axisymmetric compression samples were sectioned is shown in Figure 3.6. A Struers gravity-fed Minitom cut-off saw with a silicon carbide blade was used to section compression samples. This type of cut-off saw makes very precise cuts with the minimum of material deformation. The first cut made was through the centre of the sample, perpendicular to the compression axis (see Figure 3.6a). A deformational dead zone exists at the contact surface of the sample due to frictional effects[136]. Further to this, the centre of the sample contains a region of high deformational heating. For these reasons, the optimal plane to examine exists at 25% of the total height of the sample. When the sample is ground and polished after sectioning, the visible plane will be at approximately 25% of the total height (shown as a dotted, red line in Figure 3.6a). The next cuts to be made were to create a sample that is compatible with the dimensions of the EBSD sample holder (10 x 10 x 5 mm). Two cuts were made to remove the ‘shoulders’ of the sample followed by a single cut to slice the sample in half. This produces two equivalent samples for further investigation.

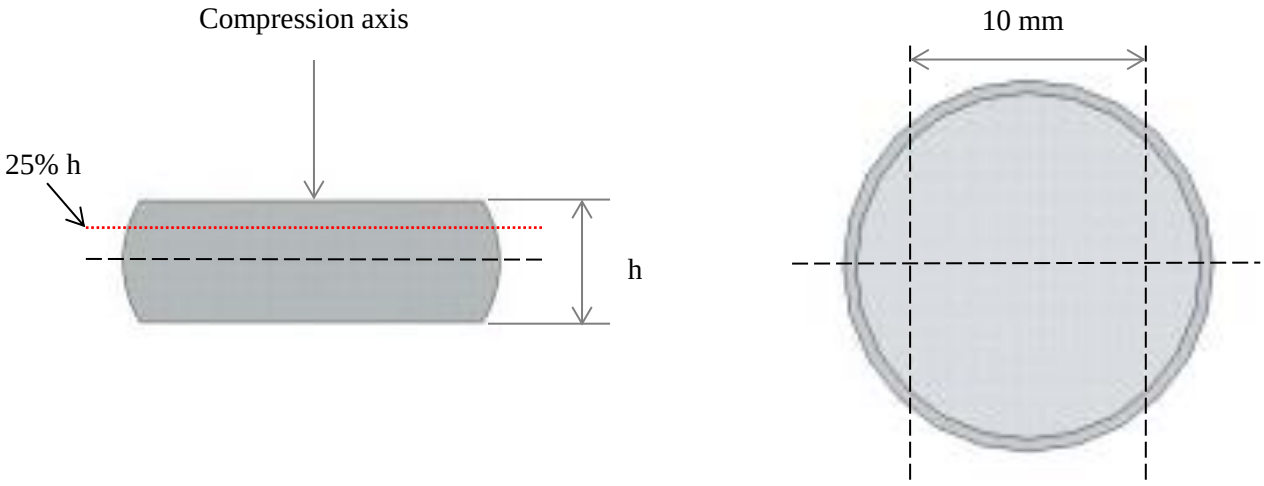

Figure 3.6 – Schematic of axisymmetric compression sample sectioning. a) Initial section perpendicular to the compression axis to expose plane of interest with dotted red line showing the 25% height plane reached after grinding and polishing. b) Further sections made, parallel to the compression axis.

3.4.1.4 Optical and Scanning Electron Microscopy

For individual samples that were to be studied by optical microscopy or SEM, a simple, manual method of sample preparation was followed. The samples were mounted in conductive Bakelite and an initial, plane grind was made with 800 grit silicon carbide (SiC) paper using water as a lubricant. Typically, 30 seconds was long enough to produce a flat surface. Further grinding was carried out on increasingly fine SiC paper from 1200–4000 grit with slightly longer times for each step. At the 4000 grit stage 90–120 seconds was usually long enough to remove any traces of the previous step. Between each step, the sample was sprayed with soap, quickly flushed with water and rinsed with isopropyl alcohol before drying under a blast of warm air.

Polishing consisted of two steps; 1 and ¼ μm diamond. To minimise the exposure to water, alcohol-based diamond solutions were used with an alcohol-based lubricant. The same type of non-woven textile cloth was used for both polishing stages to minimise frictional effects and pull-out. Again, the sample was cleaned thoroughly between steps, as above. When polishing, it was important to gauge the correct pressure to apply to the sample. Enough force must be applied to optimise the polishing effect of the diamond. However, with too much

pressure, deformational defects, such as mechanical twinning, can occur. With manual polishing, the correct force was rather subjective. For that reason, it was necessary to use a trial and error approach with spare material to perfect the polishing method.

3.4.1.4.1 Etching

For optical microscopy, samples were etched after the final polish. To enhance the polarised light response of the samples, a picric acid-based etchant was used. The etchant consists of:

4.5 g picric acid
10 ml glacial acetic acid
70 ml isopropyl alcohol
10 ml distilled water

This etchant contains slightly more picric acid than the common etchants used for magnesium alloys. It was found that this produced a better response to polarised light. However care must be taken as the etchant acts very quickly. The sample was held in the etchant for approximately 2-3 seconds and then quickly flushed with water followed by isopropyl alcohol and then dried in a stream of warm air.

3.4.1.5 Electron Backscattered Diffraction

For samples prepared for EBSD it is essential to produce a flat surface with the best possible finish, free from scratches with minimal oxidation. For consistent results a Struers Abramin semi-automatic grinding and polishing machine was used. The machine has a centrally loaded head capable of holding up to 6 samples. It was found that the best results were when the head was loaded with 3 samples, spaced equally, to keep the load balanced. A total load of approximately 100 N was applied to the 3 samples when grinding, increasing to approximately 150 N when polishing. An initial, planar grind was carried out for 30 seconds with 500 grit SiC paper followed by 60 seconds grinding with 1200 grit. Water was used as the lubricant during grinding. The next step was a coarse polish with a 9 μm alcohol-based diamond solution on a Struers Largo, honeycomb polishing disc. The coarse polish was

carried out for 7 minutes using an alcohol-based lubricant. A dose of the diamond solution and a spray of lubricant were added to the pad every minute during polishing. The final polishing step was colloidal silica (0.05 μm particle size) mixed 50/50 with isopropyl alcohol on a neoprene polishing pad. This final step was carried out for 20 minutes with approximately 5 ml of the colloidal silica solution added to the centre of the neoprene pad every minute. Finally the neoprene pad was flushed with water to remove any colloidal silica residue from the sample surface for one minute (see section 3.5.1.2.4). Once the cleaning was completed, the sample was removed from the holder and kept in a bath of isopropyl alcohol until needed for analysis.

3.4.1.6 Transmission Electron Microscopy

Samples for investigation by TEM require electropolishing until the centre of the sample is electron-transparent. The first step was to section the sample so that the area of interest can be studied. A Struers Minitom gravity-fed cut off saw with a SiC blade was used to cut thin sections of the sample of approximately 1 mm in thickness. Once a thin section had been cut, it was mounted on to a steel block of approximately 30 x 20 x 15 mm to aid in the grinding process. To mount the sections, Agar Crystalbond resin was used. The steel block was heated on a hot stage until the resin could melt. The section was then placed centrally on the block and cooled in water. The mounted section was then ground using 4000 grit SiC paper with water as a lubricant to approximately 200 μm. To remove the mounted sample, the block was placed on the hot stage again until the resin melted and the sample could be removed with tweezers. Acetone was used to remove any remaining resin. 3 mm discs were then punched from the sample and further thinned using a grinding jig until they were approximately 75 μm in thickness.

The electrolyte for polishing consists of:

185 ml methanol
35 ml butoxyethanol
1.94 g lithium chloride
4.09 g magnesium perchlorate

A Metalthin twin-jet electropolishing unit was used for the final thinning process. The electrolyte was cooled to -45 ºC with liquid nitrogen and polishing was carried out at 30 mA. The other variables to consider are the sensitivity of the light sensor and the flow rate of the electrolyte. As these vary between polishing units a trial and error approach was required until satisfactory results were obtained. Ideally, at the end of polishing, there will be a small hole at the centre of the sample with a flat, thin area for observation. During this project it was found that it was essential to keep the temperature during polishing constantly low. The polishing process is exothermic and increases the temperature of the solution. To keep the temperature constant, the flow rate of the coolant had to be increased during polishing. If the solution temperature raised by 5 ºC or more the resultant sample would usually have an uneven thin area with signs of pitting. Once the samples were completed, they were stored in ethanol or isopropyl alcohol until required.

3.4.2 Optical Microscopy

For optical observation an Olympus Polyvar with crossed polariser was used. This technique was used when assessing the volume fraction of second phase and recrystallised material as well as grain size. Point counting was used when investigating volume fractions with the mean linear intercept method employed to measure grain size.

3.4.3 Electron Backscattered Diffraction

EBSD was used to investigate the crystallographic texture of the deformed samples. EBSD is the preferred technique when analysing the texture of bulk samples due to the combination of spatial resolution and speed at which it can index the orientation of each grain. When an incident electron beam interacts with a sample, backscattered electrons escape the sample. When the exiting electrons satisfy the Bragg condition, they will diffract with the atomic lattice planes of the sample. For each set of atomic planes, pair of diffraction lines are formed. When a number of planes exist, as they do in crystalline materials, these sets of lines will form a Kikuchi diffraction pattern. The Kikuchi diffraction pattern can be used to measure the orientation of a given grain from a known zone axis. To detect and measure the Kikuchi diffraction patterns the SEM contains a phosphor screen and a high resolution CCD

camera (see Figure 3.7). The detected patterns can then be compared to recorded information about known atomic lattice parameters and subsequently indexed. This system is fully automated, with the electron beam moving across the sample in a raster, and recording the orientation information of every point analysed.

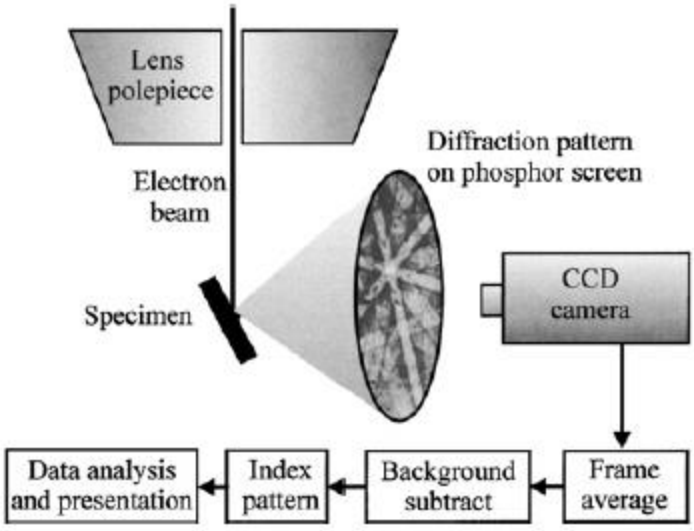

Figure 3.7 – Schematic of EBSD system[137].

3.4.3.1 Procedure

For this project a FEI Sirion field emission gun SEM (FEGSEM) was used for EBSD analysis. The microscope is equipped with an Oxford Instruments HKL Nordlys F EBSD detector. To process the acquired data, the HKL Channel 5 Flamenco software was used. The polished sample was fitted into the correct holder and mounted onto the microscope stage. Initially, the standard procedure was followed in obtaining a secondary electron image. Once the beam was corrected, the sample was tilted to an angle of 70º. At this angle the EBSD detector is in the optimal position to receive backscattered electrons. The relevant parameters are defined within the Flamenco software (see Table 3.4) and the area to be scanned is input. Once started, the microscope can be left for the duration of the run.

It is worth noting that an important factor when acquiring EBSD maps is the accelerating voltage of the electron beam, as the interaction volume of the beam must be considered. The depth of penetration of the beam (x) is described by equation 3.9. Low-density materials,

such as magnesium, will have a large penetration depth; typically 1–5 μm. For small grain sizes, such as those in recrystallised material, interference will be apparent in the resultant EBSD pattern. For this reason it is necessary to reduce the accelerating voltage, thereby, reducing the interaction volume. For the study of the current alloys, an accelerating voltage of 15 keV was found to produce strong Kikuchi patterns with little interference.

$$x(\mu m) = \frac{0.1E_0^{1.5}}{\rho} \tag{3.9}$$

Where E_0 = accelerating voltage (keV) and ρ = density (g/cm^3).

Table 3.4 – EBSD parameters for the Sirion FEGSEM.

Parameter	Value
Magnification	200x
Beam Voltage (keV)	15
Spot Size	5
No. of Background Frames	64
No. of Averaged Frames	5 – 6
Step Size (μm)	0.3 – 1
Acquisition Rate (s^{-1})	10 – 50
Camera Binning	4x4

3.4.3.2 Presentation and Analysis of EBSD Data

3.4.3.2.1 Noise Reduction

Before the collected data can be analysed, it needs to be cleaned for any noise present. Several factors exist to cause noise in the resultant EBSD map. Frequently, imperfections on the sample surface, such as contamination or scratches, reduce the quality of the Kikuchi pattern. When this occurs, the software can misinterpret the pattern, resulting in incorrect

indexing. These misindexed points reduce the overall accuracy of the EBSD map. If the pattern cannot be indexed at all, it is simply recorded as a blank, non-indexed pixel. Another issue that occurs is pseudosymmetry. Sometimes the software fails to distinguish between two symmetrically similar rotation axes[138].

The HKL Channel 5 Tango software includes a range of noise-reduction features. Firstly, any pixels that are clearly different to the surrounding materials (wild spikes) are removed. Next, any non- or misindexed points are removed by extrapolating information from the surrounding pixels. The software analyses the surrounding 'neighbours' and uses an iterative method to fill in the blank, non-indexed pixels. This method depends heavily on the percentage of non-indexed points to start with. If a high percentage of points are missing from the map, the process of extrapolating based on nearest neighbours can lead to unusual artefacts (e.g. perfectly square grains) in the resultant map. Ideally, for good quality maps, an initial indexing rate of 80% or higher is required. Finally, a Kuwahara filter can be employed to remove occurrences of pseudosymmetry.

3.4.3.2.2 Inverse Pole Figure Coloured Orientation Imaging Maps

For the majority of texture work carried out, inverse pole figure (IPF) colouring was used. This system uses a range of colours for the orientation of each grain in relation to the reference direction. This provides a texture map that is easy to interpret. The [0001] direction was chosen as the reference direction (coloured red) as the orientation in respect of the basal plane (0001) was of most interest. Figure 3.8 displays the colour scheme used with presenting IPF maps.

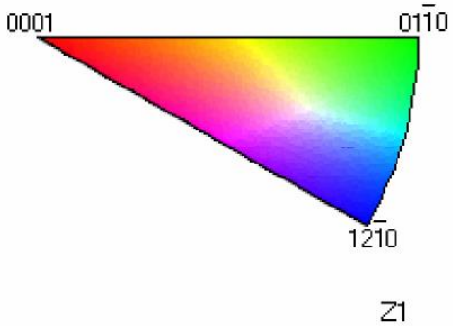

Figure 3.8 – Legend of the colour scheme used with IPF texture maps.

The IPF colouring system only relates the orientation of grains with one direction and does not describe rotation around this direction. Therefore, it cannot be used describe the texture in full. However, due to the predominately basal texture of deformed HCP metals, it is mainly the orientation in relation to the c-axis that is of interest. For this reason, IPF colouring was deemed suitable for texture analysis of the current alloys.

3.4.3.2.3 Pole Figures

To further understand the texture of a material, a pole figure can be used. The pole figure displays the poles of each grain within a sample as a point on a stereographic projection of a given pole. The information can either be displayed as individual data points or as a coloured contouring showing the multiples of uniform density (MUD). In Figure 3.9 the 0002 and $10\bar{1}0$ poles are displayed with the higher intensity colouring (red) depicting the higher MUD value. With this colouring system a MUD of 1 would indicate randomly orientated grains. A MUD significantly higher than 1 would represent a preferred texture. The 0002 pole is parallel to the compression axis while the $10\bar{1}0$ pole perpendicular to the compression axis. These two poles are sufficient to describe the texture within an axisymmetric compression sample. For pole figures to be statistically viable, a large area needs to be scanned from each sample. Typically areas of 1–2 mm^2 were analysed for texture determination.

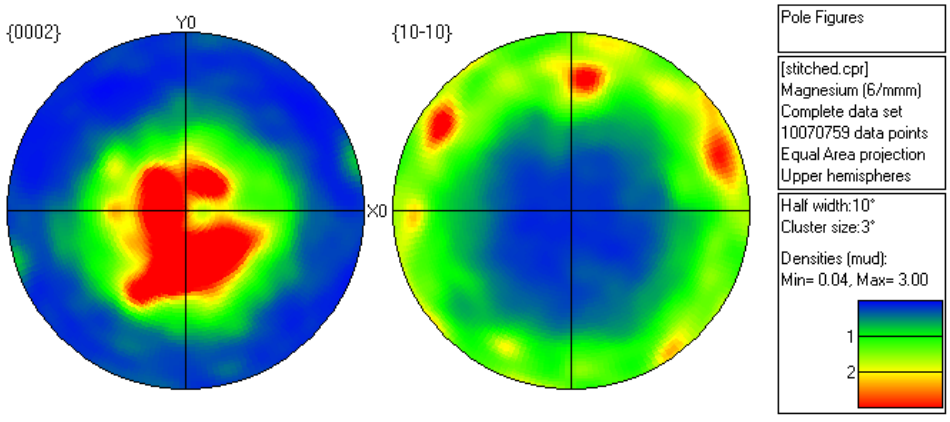

Figure 3.9 – Contoured pole figure displaying the 0002 and $10\bar{1}0$ poles.

3.4.4 Transmission Electron Microscopy

A small number of TEM micrographs were taken during this project. These were mostly to investigate the density of strengthening precipitates during isothermal ageing. Two microscopes were used during this work. A Philips 420 TEM operating at 200 kV with a tungsten filament and an FEI Tecnai 20 TEM operating at 200 kV with a LaB_6 filament.

3.4.4.1 Procedure

After insertion into the microscope the hole at the centre of the sample was located. The areas around the hole were investigated until a suitably large, thin area was found. For bright field imaging, a diffraction pattern was first produced. The objective aperture was introduced into the column and moved to the central spot of the pattern. Bright field produces good contrast when examining the general microstructure. For the majority of the ageing work, the precipitates of interest were β^1 and β_1'. The plate-shaped β^1 precipitate is known to lie in the basal plane while the rod-like β_1' precipitate is known to grow along the [0001] direction. Therefore, the sample was tilted so that the beam was parallel to the [0001] and $[1\bar{2}10]$ directions so that the precipitates could be viewed 'edge-on' and 'end-on'. Kikuchi diffraction was used to tilt the sample to the [0001] zone axis.

3.5 Differential Scanning Calorimetry

A Perkin-Elmer twin furnace differential scanning calorimeter (DSC) with the Pyris Software package was used to assess the solidus temperature of each alloy. Small samples, weighing ~3 mg, were used for each analysis. The sample was placed within an alumina pan into one of the furnaces. An empty pan was placed into the remaining furnace as a reference. The sample and reference pan were heated at a rate of 10 ºC/min up to 650 ºC. The Pyris software monitored the heat flow in mW into the furnaces and recorded any variations. Changes in state due to a phase melting were recorded on a temperature vs heat flow curve. The scans were repeated in triplicate with the average being recorded for the final analysis.

4. Results and Discussion I

4.1 As-received Material

4.1.1 Chemistry

The composition of the three new alloys studied in this work is commercially sensitive. However, due to various problems with the microstructures, it has become necessary to analyse the chemistry in detail. Tables 4.1a shows the nominal compositions, in weight per cent terms, as supplied by Magnesium Elektron. Table 4.1b gives the compositions, in atomic per cent terms, extrapolated from the data in Table 4.1.

Table 4.1a – Weight percentage of major alloying additions. Possible variation in brackets.

	Alloy Additions (Weight %)			
Alloy	**Zn**	**Y**	**Nd**	**Zr**
93	1.5 (±0.25)	1 (±0.25)	1.5 (±0.25)	0.4
94	1.5 (±0.25)	1 (±0.25)	2.5 (±0.25)	0.4
95	1.5 (±0.25)	2 (±0.25)	2.5 (±0.25)	0.4

Table 4.1b – Approximate atomic percentage of major alloying additions. Extrapolated from the data in Table 4.1.

	Alloy Additions (Atomic %)			
Alloy	**Zn**	**Y**	**Nd**	**Zr**
93	0.62	0.31	0.31	0.12
94	0.62	0.32	0.52	0.16
95	0.66	0.68	0.55	0.13

4.1.2 Microstructure

Figures 4.1–4.3 show polarised optical micrographs of the three alloys in their as-received condition.

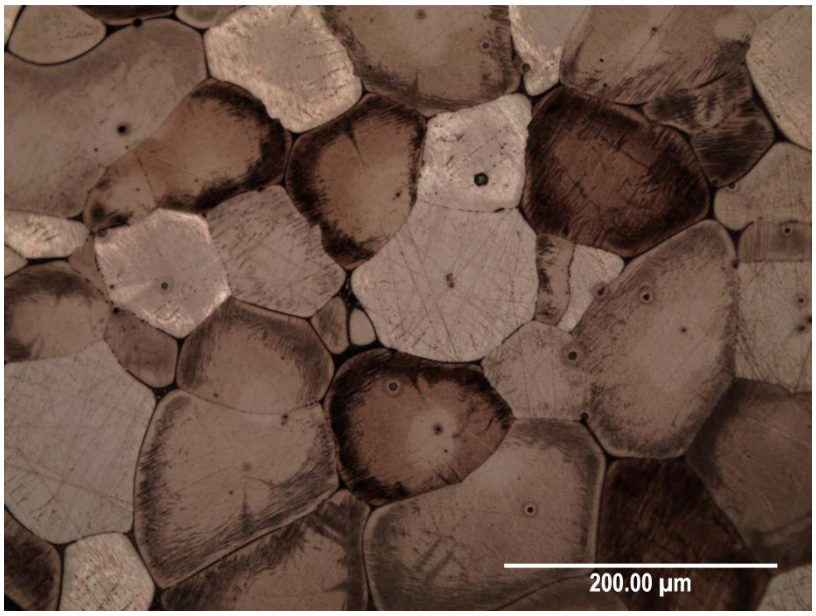

Figure 4.1 – Polarised optical micrograph of alloy 93 in the as-received condition.

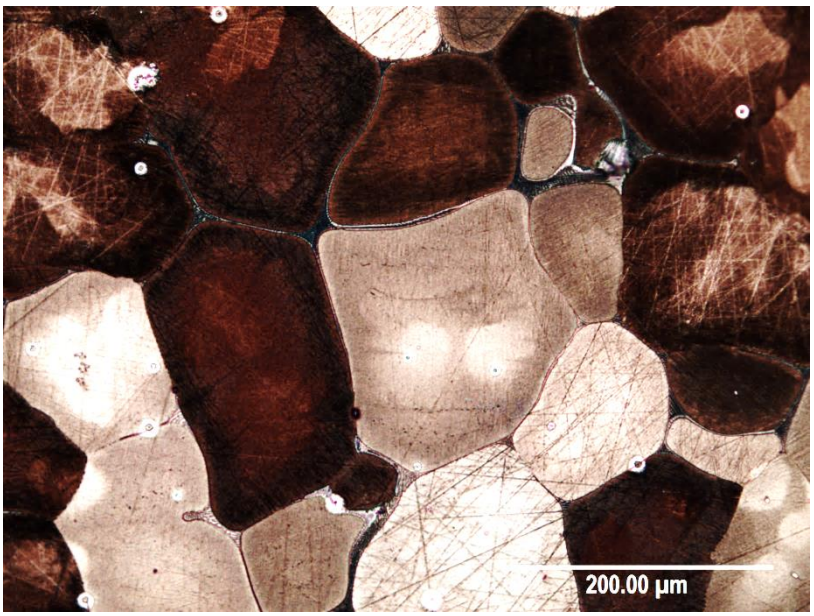

Figure 4.2 – Polarised optical micrograph of alloy 94 in the as-received condition.

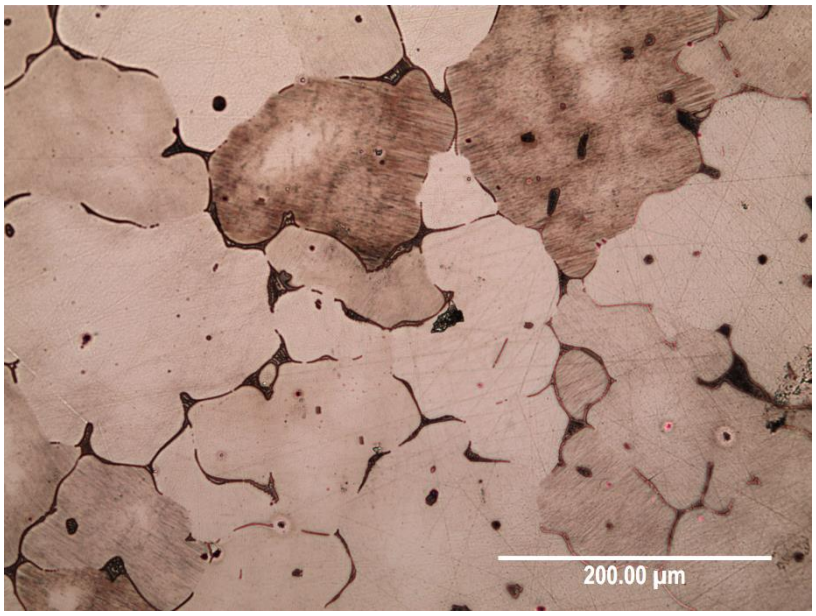

Figure 4.3 – Polarised optical micrograph of alloy 95 in the as-received condition.

Each alloy had generally equiaxed grains with a significant volume fraction of a eutectic at grain boundaries and triple points. The eutectic had a lamellar morphology, as expected. The mean linear intercept method[139] was used to calculate the average grain size with the results presented in table 4.2. Alloys 94 and 95 had similar grain sizes that are notably larger than alloy 93.

Table 4.2 – Mean grain size of the three novel alloys in the as-received condition.

Alloy	Mean Grain Size (µm)	95% Confidence Limit (µm)
93	87.7	±3.9
94	111.3	±3.5
95	115.1	±4.2

4.1.2.1 Volume Fraction of Second Phase

The volume fraction of the eutectic was calculated using the point counting method[140]. As the volume fraction of this second phase is relatively low, a high number of points are required to give an acceptable level of accuracy. For each alloy, ten micrographs were used, totalling over 3300 points. Table 4.3 shows the volume fraction of the second phase present in each alloy in the as-received condition.

Table 4.3 – Volume fraction of the second phase present in the three novel alloys in the as-received condition.

Alloy	Volume Fraction of Second Phase	95% Confidence Limit
93	0.0149	±0.005
94	0.0327	±0.010
95	0.0565	±0.017

4.2 Solution Heat Treatment

Prior to any deformation it was necessary to solution heat treat the three alloys to homogenise the microstructure. Initially a solution treatment similar to that used with other rare earth containing magnesium alloys, such as WE43 and WE54, was carried out. The alloys were heated in a Lenton chamber furnace to 525 ºC and held for 6 hours before quenching in water. However, the sudden thermal shock from the quench caused visible cracking throughout the material. Figure 4.4 shows a polarised optical micrograph of alloy 93 after the initial solution heat treatment with a water quench. Although there is a clear reduction in the second phase, when compared to Figure 4.1, a large intergranular fracture is clearly visible. Another notable difference is the large volume of mechanical twins throughout the microstructure. These mechanical twins are a product of the high residual stresses remaining in the material after a water quench.

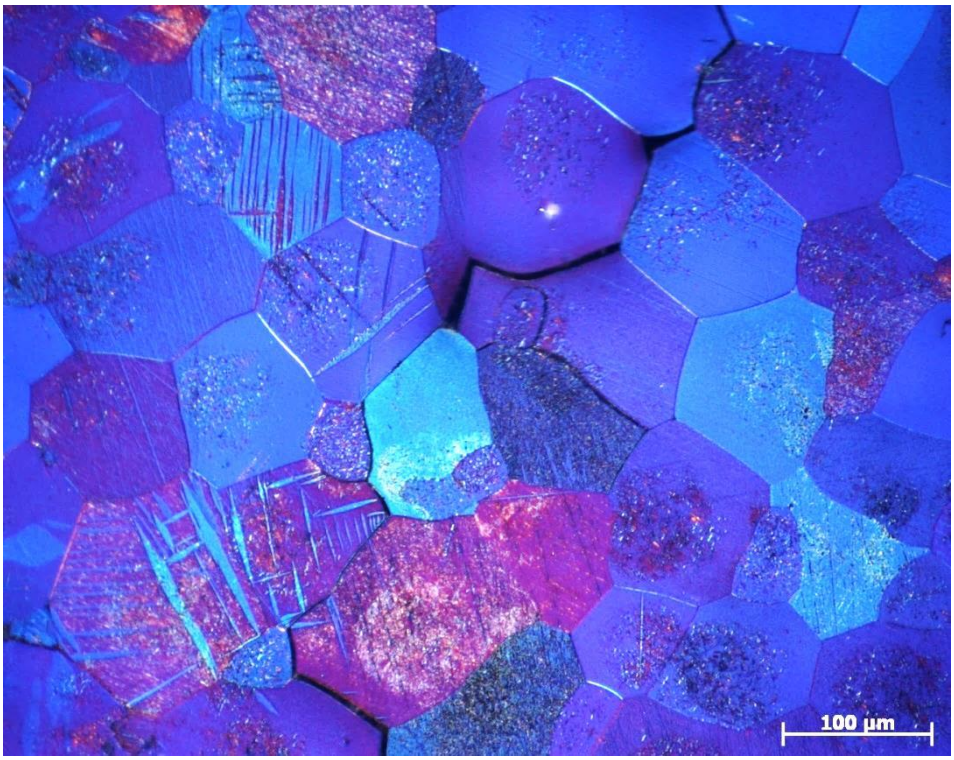

Figure 4.4 – Polarised optical micrograph of alloy 93 after solution heat treatment with a water quench.

To reduce the thermal shock after solution heat treatment an oil quench was used instead. This reduced the cooling rate after heat treatment and as a result there was no apparent cracking with any of the alloys. Figure 4.5 shows a polarised optical micrograph of alloy 94 after a solution heat treatment with an oil quench. There is no visible fracturing but a large volume of mechanical twins still exists. A large volume fraction of second phase also exists at grain boundaries and triple points.

A series of further solution heat treatments were carried out to minimise the amount second phase at grain boundaries. To compare the effect of time on the microstructure, two solution heat treatments of 8 and 10 hours were carried out at the same temperature of 525 ºC. Tables 4.4 and 4.5 show the volume fraction of second phase in each alloy after solution heat treatments of 8 and 10 hours respectively. Compared to the as-received material (see Table 4.3), there is a significant decrease in the volume fraction of second phase after the solution heat treatment of 8 hours. However no further reduction was apparent after 10 hours.

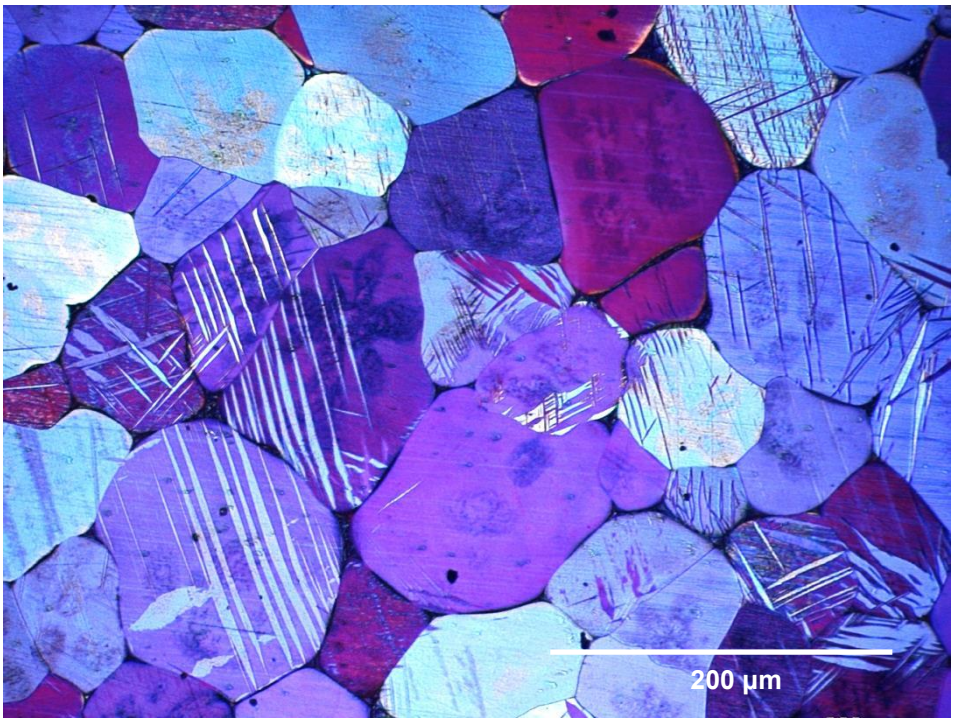

Figure 4.5 – Polarised optical micrograph of alloy 94 after solution heat treatment with an oil quench.

Table 4.4 – Volume fraction of the second phase present in the three novel alloys after a solution heat treatment at 525 ºC for 8 hours.

Alloy	Volume Fraction of Second Phase	95% Confidence Limit
93	0.0050	±0.002
94	0.0127	±0.004
95	0.0381	±0.012

Table 4.5 – Volume fraction of the second phase present in the three novel alloys after a solution heat treatment at 525 ºC for 10 hours.

Alloy	Volume Fraction of Second Phase	95% Confidence Limit
93	0.0052	±0.002
94	0.0133	±0.005
95	0.0392	±0.014

Since a significant volume fraction of second phase still existed in the three alloys after this prolonged heat treatment, it was clear that no improvement was to be gained by prolonging the solution heat treatment. In addition, solution heat treatments of magnesium alloys aimed at low-end applications are typically no longer than 8 hours. It is therefore desirable to keep the heat treatment time to a minimum in the interest of keeping production costs down. Therefore, the deformation study was carried out with the alloys in this condition. A further investigation into solidus of the second phase is conducted in section 5.1.

4.3 Pre-deformation Microstructures

Once the three alloys were solution heat treated, they were machined into samples for hot axisymmetric compression testing (see section 3.2.2). Before compression testing commenced the pre-deformation microstructures and texture were analysed with EBSD. Other than the volume fraction of the second phase, there were no discernible differences between the starting microstructures of each alloy. Therefore, the figures below give representative results for all three alloys.

Figure 4.6 shows an EBSD map (IPF colouring) of alloy 93 prior to deformation. The grain structure was equiaxed with random orientations. To further investigate the starting texture, Figure 4.7 shows pole figures of the same sample. A scan area of approximately 4 mm^2 was used to ensure that a statistically viable number of grains were captured. The pole figures indicate a completely random texture with no favoured orientation. Each alloy had the same random texture after the solution heat treatment. Therefore, the figures below represent the microstructures of the novel alloys prior to deformation.

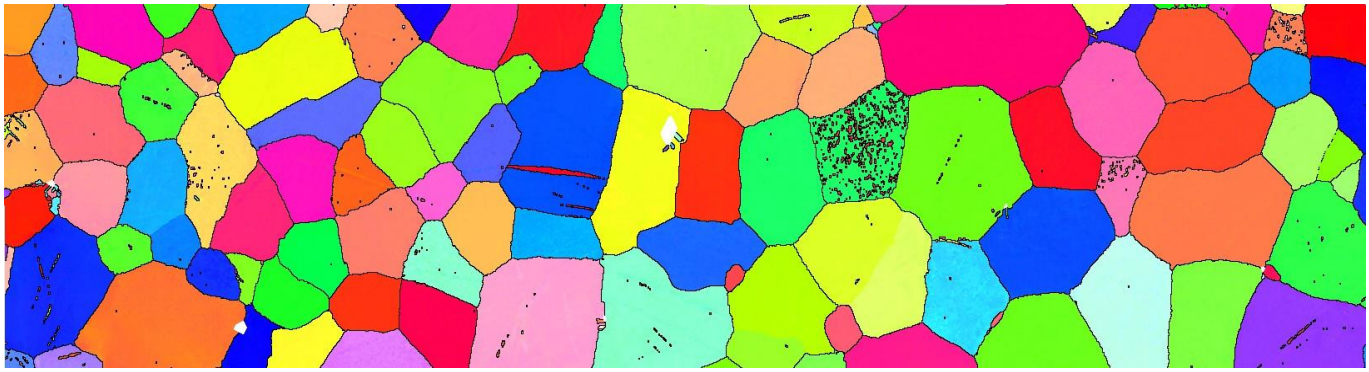

Figure 4.6 – EBSD map (IPF colouring) of alloy 93 after solution heat treatment, prior to deformation.

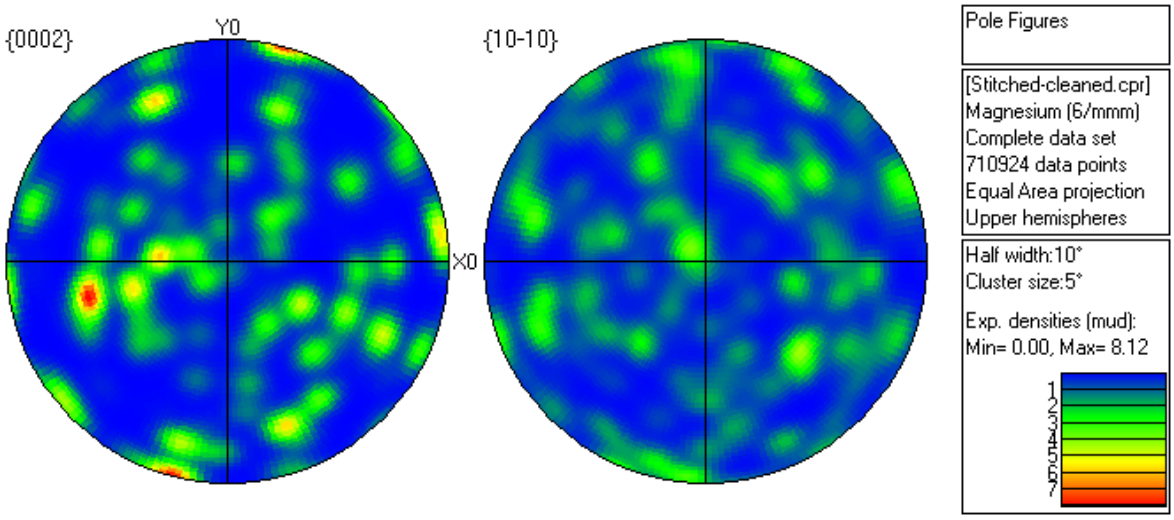

Figure 4.7 – Pole figures of alloy 93 showing the random texture prior to deformation.

4.4 Flow Characteristics

4.4.1 Introduction

As the new alloys are intended for wrought applications, it is essential to first assess their deformation and flow characteristics under vigorous experimental conditions. The following section describes the range of hot axisymmetric compression tests carried out using the TMC machine. The primary objective of the testing was to prove the suitability of the alloys for industrial rolling to sheet form. It is desirable that wrought alloys can be deformed under a wide range of strain, strain rate and temperature conditions, suitable for industrial conditions. The work carried out in this section aims to describe the potential process window and demonstrate its application using an experimental-scale rolling mill.

4.4.2 Uncorrected Flow Data

A matrix of deformation tests was carried out for each new alloy (see Table 3.2). To summarise: three strain rates (0.5, 1 and 5/s) at three temperatures (425, 435 and 450 ºC) were tested for each alloy. Initially tests at temperatures and strain rates outside of this range were also undertaken. However, due to issues with shearing and incipient melting, a narrower matrix of tests was used for the final analysis. From each test a raw stress-strain flow curve was produced. From the raw data a series of corrections were made to compensate for friction, adiabatic heating, and strain rate variations. The procedure for these corrections was described in section 4.3.3 with the fully corrected flow curves presented later in the chapter. Figures 4.1–4.3 show representative flow curves from each alloy before any corrections had been made.

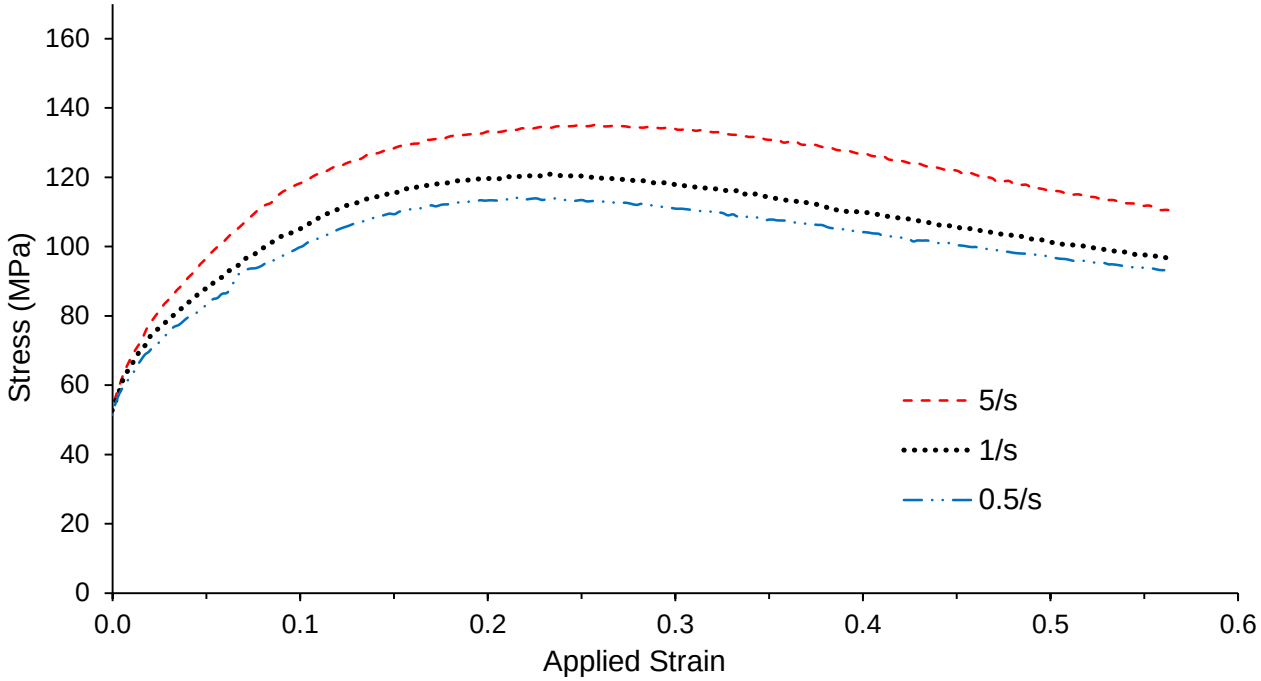

Figure 4.1 – Uncorrected flow curves for axisymmetric compression tests of alloy 93 carried out at 435 ºC and three strain rates.

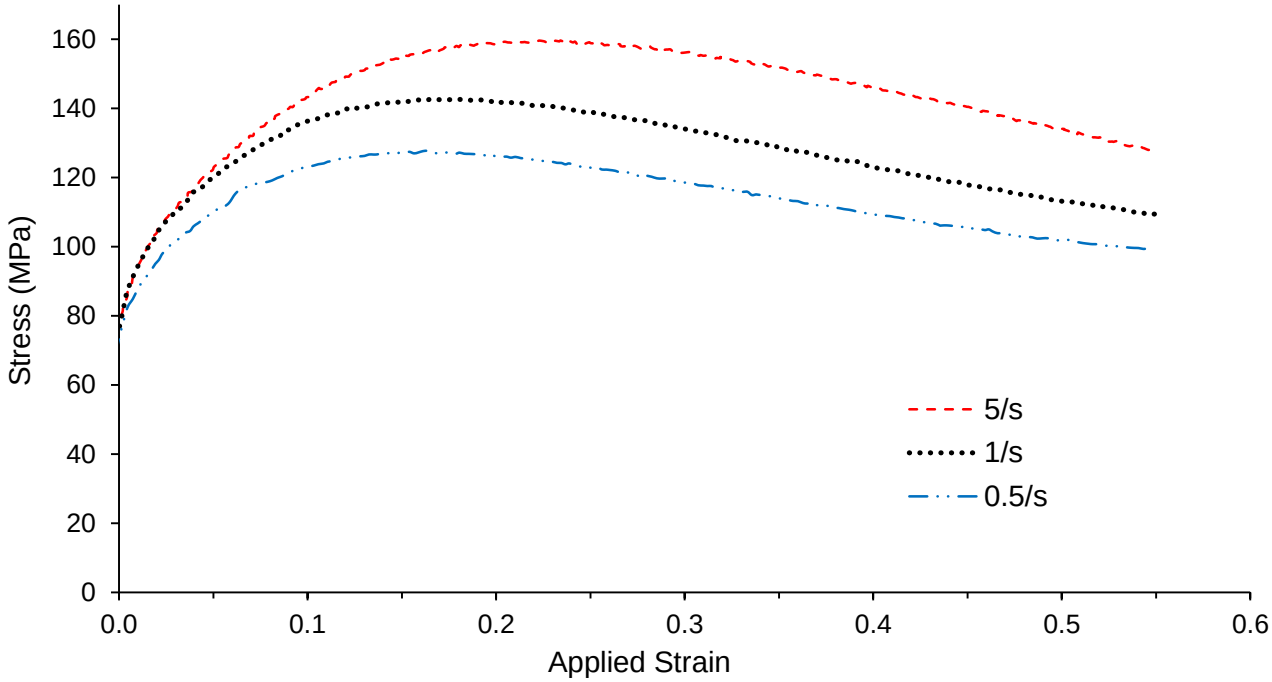

Figure 4.2 – Uncorrected flow curves for axisymmetric compression tests of alloy 94 carried out at 435 ºC and three strain rates.

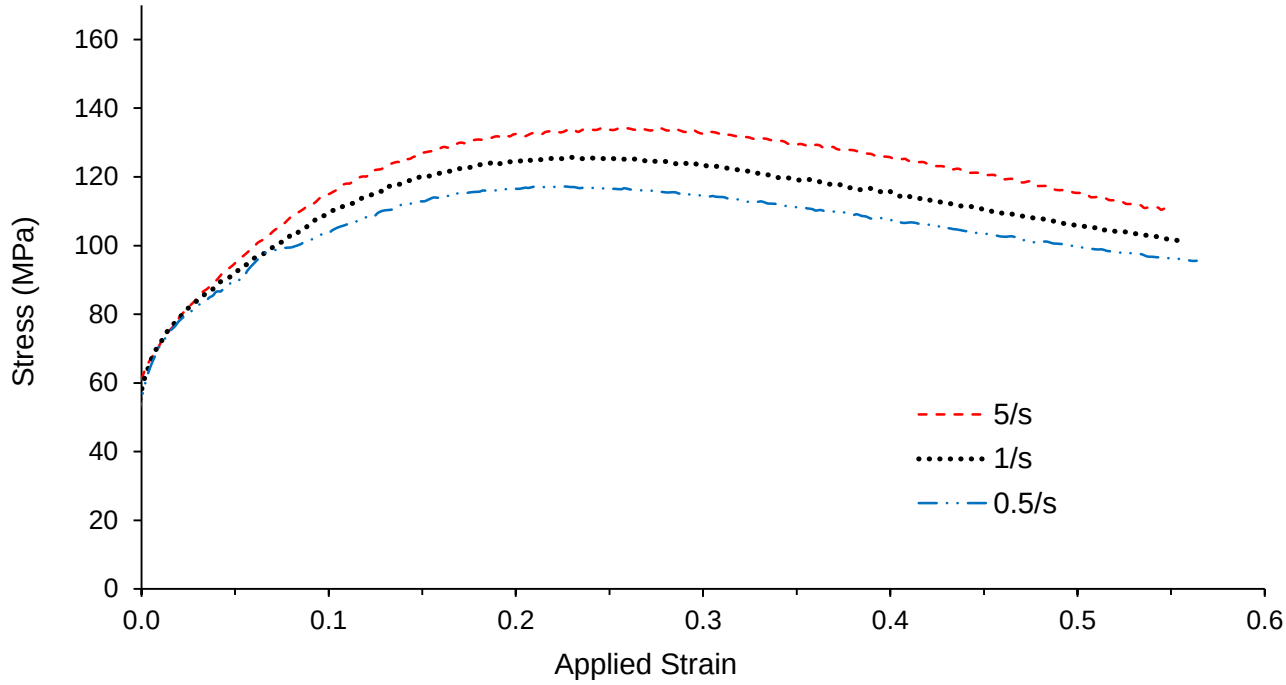

Figure 4.3 – Uncorrected flow curves for axisymmetric compression tests of alloy 95 carried out at 435 ºC and three strain rates.

4.4.3 Flow Curve Corrections

4.4.3.1 Coefficient of Friction

As discussed in section 3.2.4 three samples of different heights were used to assess the coefficient of friction, μ, of the new alloys under uniaxial compression. Regardless of sample height, the stress-strain curve should be very similar if the deformation conditions are identical. The three samples used were the standard axisymmetric compression sample with a height of 15 mm and two samples milled down to a height of 12.5 mm and 10 mm. Compression was carried out at 450 ºC with a strain rate of 1/s. In terms of Z (see section 2.3.4 for definition) this is approximately in the middle of the range of tests. The strain rate of 1/s ensures a smooth deformation without the risk of shearing that can occur at higher strain rates. A trial and error approach was employed to correct each flow curve until a coefficient of friction had been found that gave the closest fit between each test. To save on material,

only alloy (94) was used for the friction testing. This was seen as sufficient due to the similar chemistries of each alloy and the same lubricant (graphite) being used across the range of tests. Equation 3.6 in section 3.2.7 was used to correct the raw flow curves and produce Figures 4.4–4.7 using different values of μ.

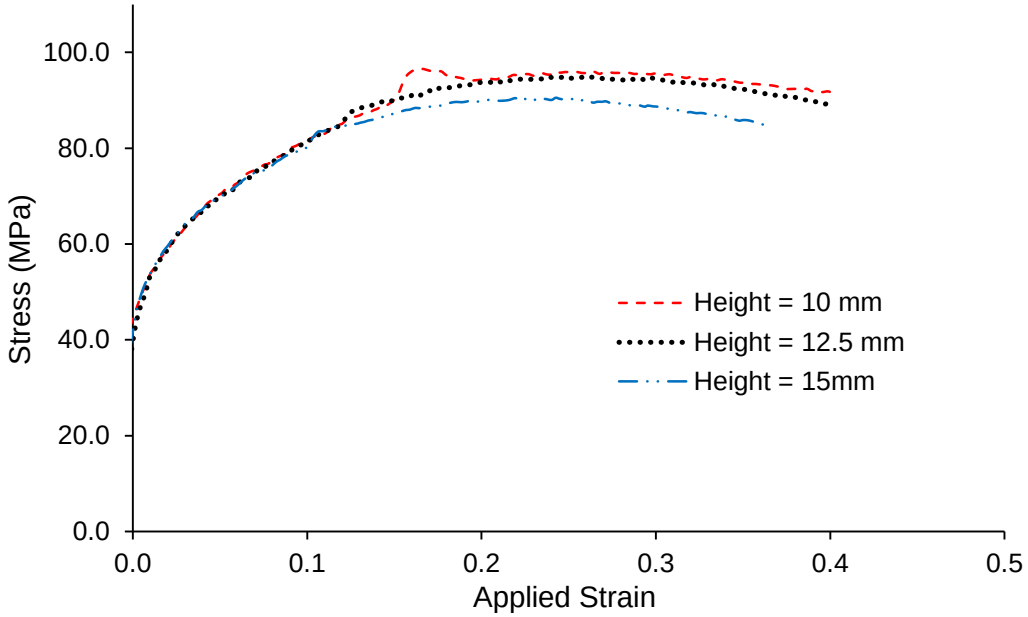

Figure 4.4 – Friction corrected flow curves when μ = 0.1.

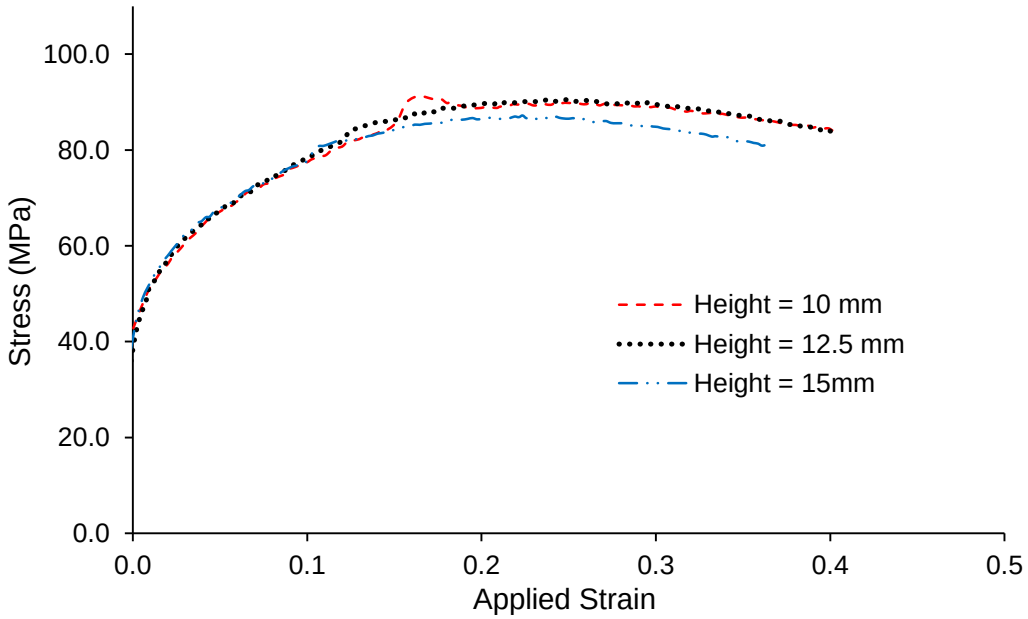

Figure 4.5 – Friction corrected flow curves when μ = 0.15.

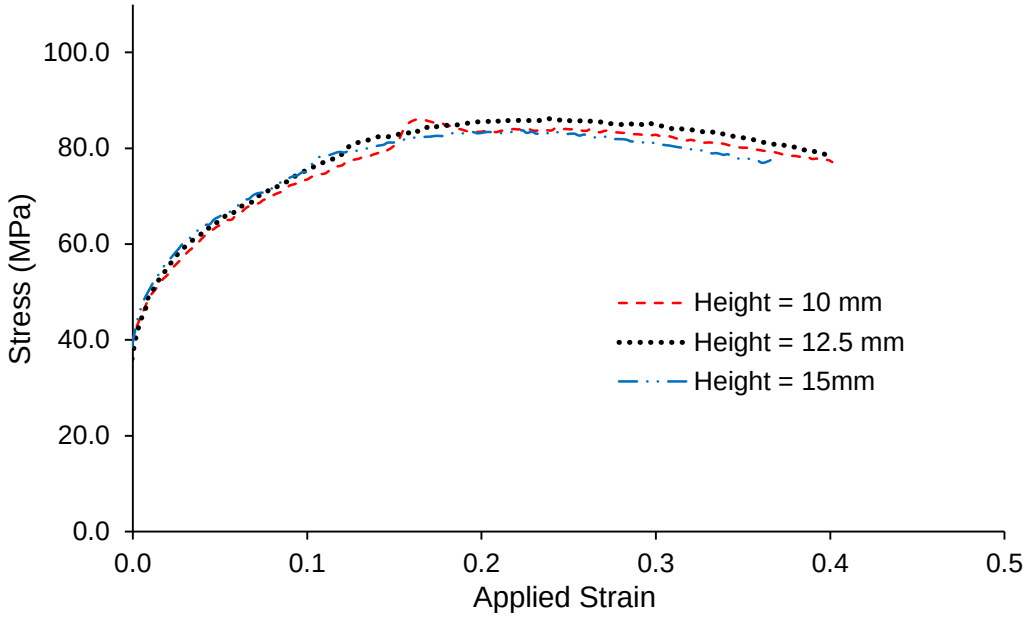

Figure 4.6 – Friction corrected flow curves when μ = 0.2.

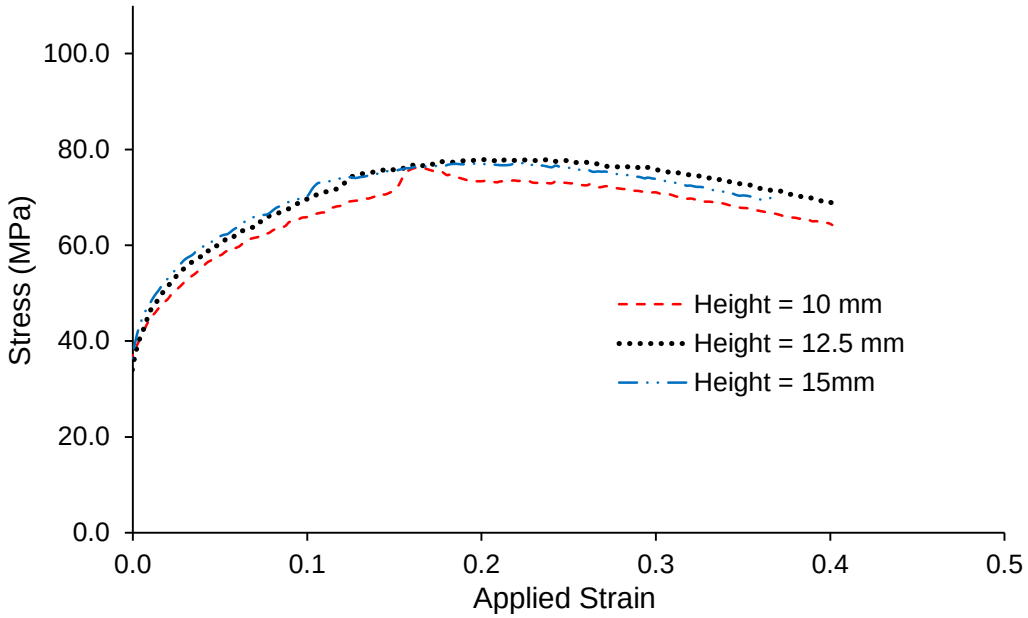

Figure 4.7 – Friction corrected flow curves when μ = 0.25.

The closest fit between the three flow curves is when a μ value of 0.2 is used. This value was used to correct all further flow curve data. Figure 4.8 shows the original flow curves from

Figure 4.1 (dotted and dashed lines) compared to the friction corrected flow curves when μ = 0.2. Compared to the original data, it can be seen that incorporating friction into the flow curves reduced the peak stress significantly, by approximately 20 MPa in this instance.

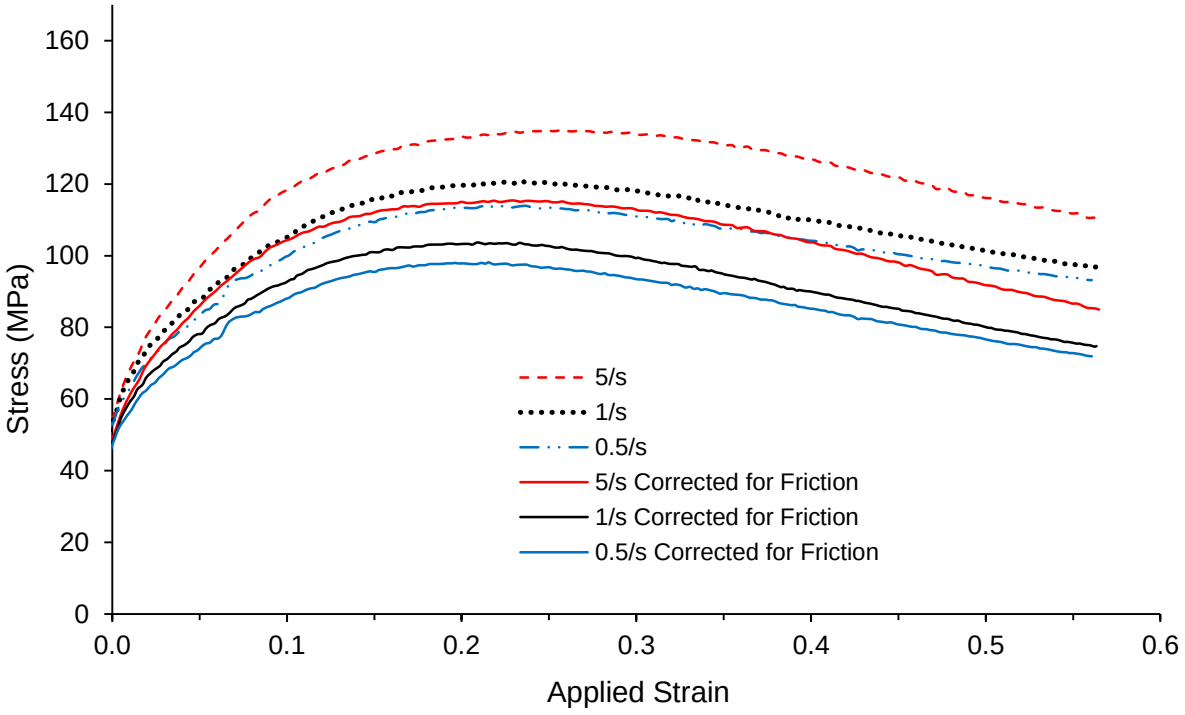

Figure 4.8 – Comparison of friction corrected flow curves (solid lines) with uncorrected flow curves (dotted and dashed lines) for axisymmetric compression tests of alloy 93 carried out at 435 ºC with three strain rates.

4.4.3.2 Strain Rate Sensitivity

During deformation the strain rate can be seen to change due to material variables and inconsistencies with the TMC. It is necessary to correct the stress in respect of the instantaneous strain rate at any given point. The method was described in section 3.2.8 with the relevant equation being repeated below.

$$\sigma_2 = \sigma_1 \left(\frac{\dot{\varepsilon}_2}{\dot{\varepsilon}_1} \right)^{1/n} \tag{4.1}$$

Where σ_2 is the corrected, nominal stress, σ_1 is the measured stress, $\dot{\varepsilon}_2$ is the nominal strain rate at which the test was set, $\dot{\varepsilon}_1$ is the measured strain rate and *n* is the strain rate sensitivity constant. The strain rate sensitivity constant, *n*, is found by taking the gradient of a ln Z vs ln σ plot for a for a range of strains from each deformation throughout the test matrix. Plots were taken from a starting strain of 0.2 and then at increments of 0.1 up to a maximum of 0.6. The gradients of each plot were then averaged to give a single value of *n* for each alloy. Figure 4.9 shows a representative plot of a ln Z vs σ plot for alloy 94 at a strain of 0.4. Table 4.6 lists the average values of *n* calculated for each alloy.

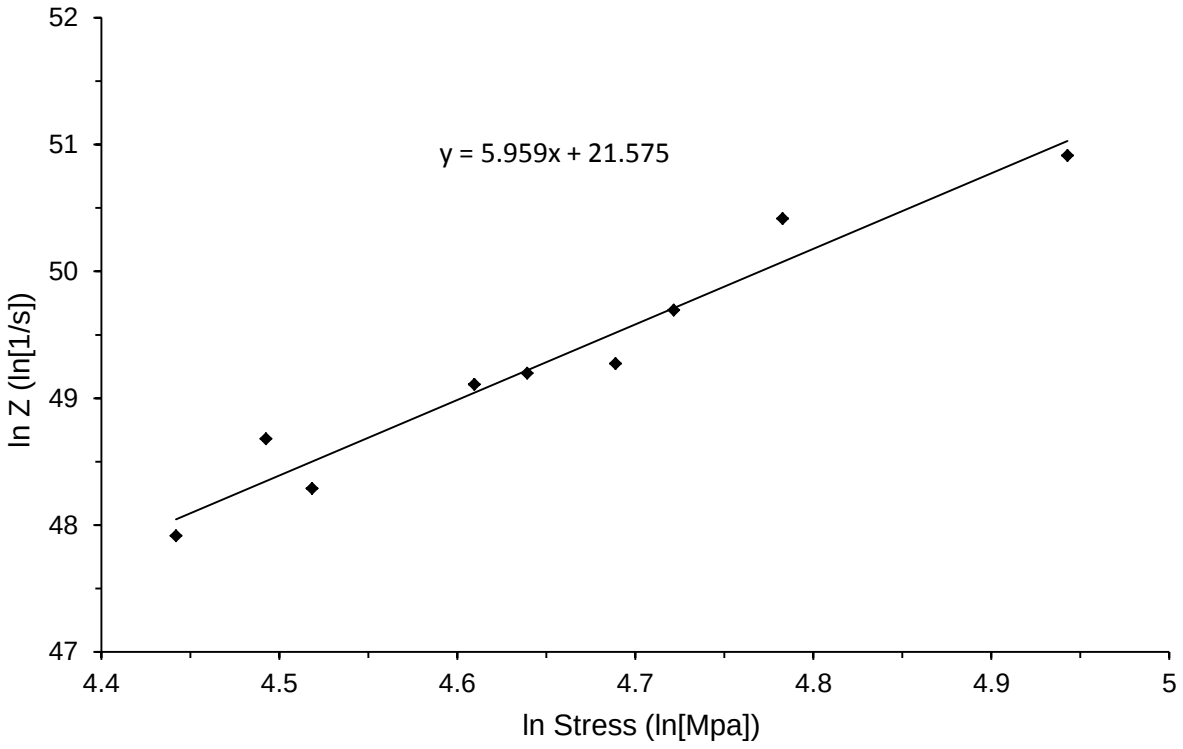

Figure 4.9 – Example of an ln Z vs ln Stress plot for alloy 94 at a strain of 0.4.

Table 4.6 – Strain rate sensitivity of each novel alloy.

Alloy	***n***
93	6.23
94	7.83
95	9.32

4.4.3.3 Activation Energy of Deformation (Q_{def})

For the flow curves to be used in further analysis, such as the development of constitutive behaviour, every point on the curve needs to be accurately corrected for thermal variations. Such variations are caused by adiabatic heating and the unavoidable transfer of heat from the tools to the sample. To fully correct the data for thermal variations equation 4.2 is used.

$$\sigma_2 = \sigma_1 + \frac{Q_{def}}{\beta R}\left(\frac{1}{T_2} - \frac{1}{T_1}\right) \tag{4.2}$$

Where Q_{def} is the activation energy of deformation, β is a constant, R is the universal gas constant, T_1 is the measured temperature and T_2 is nominal temperature at which the test was set. Firstly the material constant, Q_{def}, needs to be calculated. Davenport et al.[125] set out the procedure for calculating Q_{def}. For each test, at every 0.1 increment of strain, the instantaneous stress is extracted and tabulated. A graph of ln (nominal strain rate) vs instantaneous true stress is constructed (see Figure 4.10). Lines of best fit were added to the graphs and vertical lines were fitted at increments of 10 MPa stress. The strain rates where the lines intersect are extracted and plotted against $1/T_2$. Again, lines of best fit were added and the gradient of each of these lines equals: $-\frac{Q_{def}}{R}$ where R is the universal gas constant (see Figure 4.11). Q_{def} is calculated for each line's gradient and averaged over the whole range to give one value of Q_{def} for each test. The values from each test were then averaged to give a value of Q_{def} for the material as a whole. Table 4.7 shows the values of Q_{def} calculated for each of the alloys.

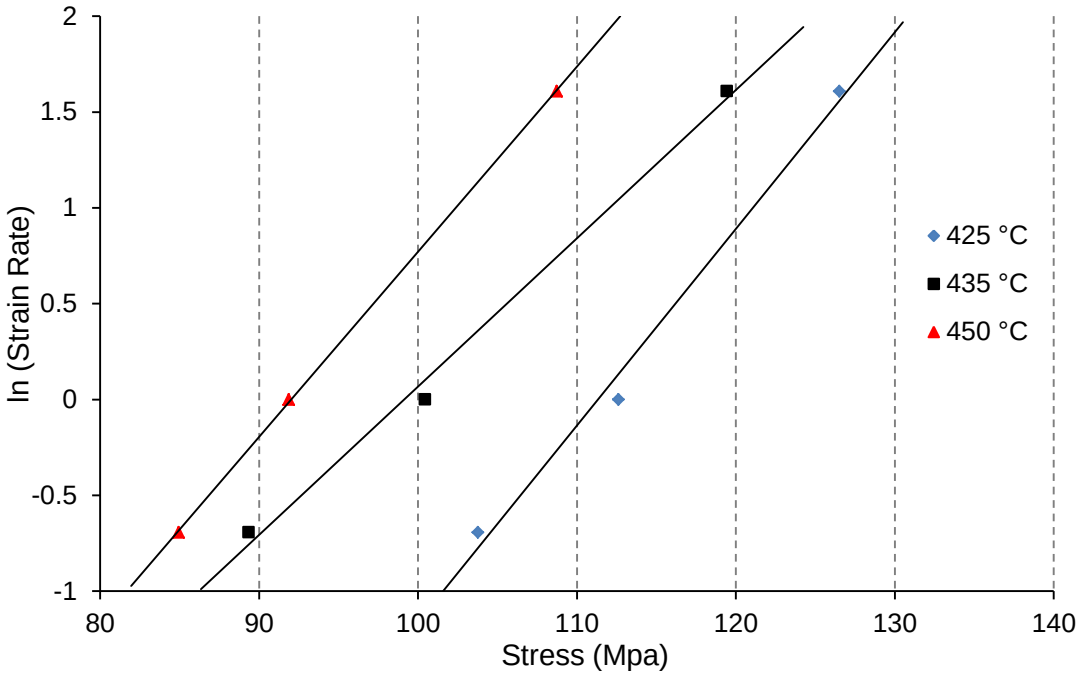

Figure 4.10 – ln (strain rate) vs stress plot for alloy 94 at a strain of 0.4 and three temperatures.

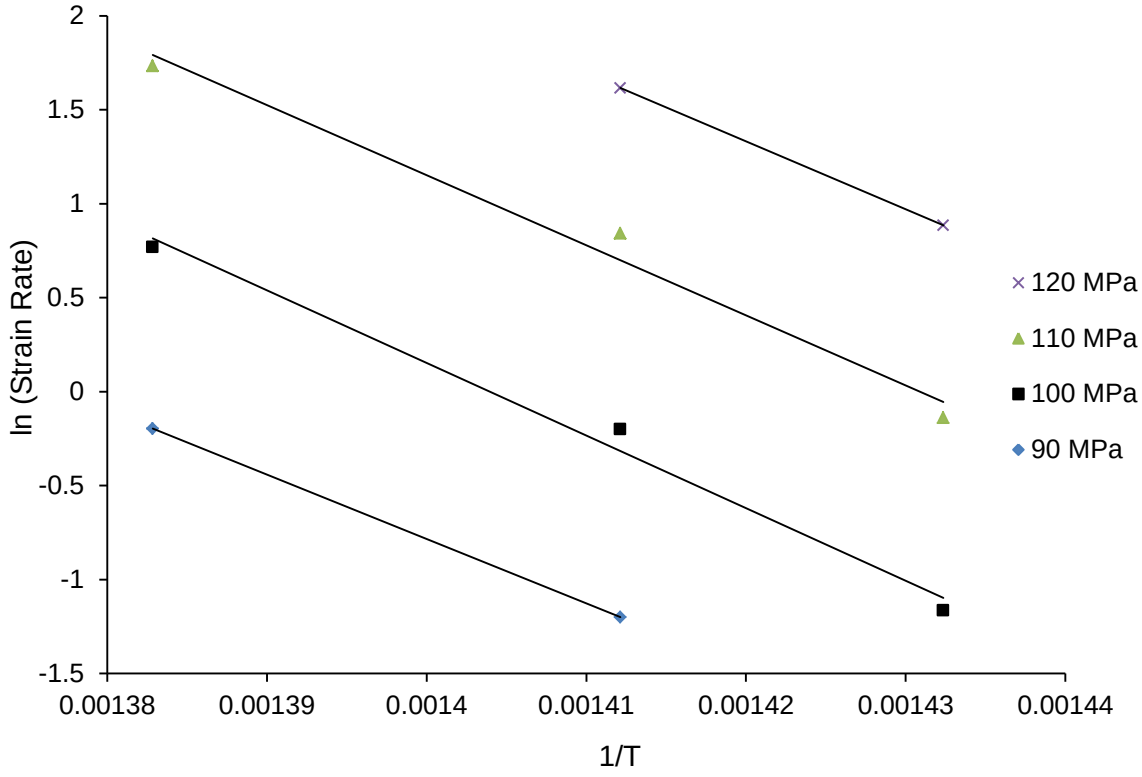

Figure 4.11 – ln (strain rate) vs $1/T$ plot for alloy 94 at a strain of 0.4.

Table 4.7 – Values of Q_{def} calculated for the three novel alloys.

Alloy	Q_{def} (kJ.mol^{-1})
93	196.8
94	250.5
95	150.8

4.4.3.4 Calculation of β

The final material constant to calculate before the flow curves can be fully corrected is the constant β from equation 4.2. So that the curves can be corrected for each data point, it is necessary to develop an equation for β that can be applied across the whole matrix of tests for each alloy. The first step is to plot the stress vs ln Z for individual values of strain at increments of 0.02 and add a line of best fit (see Figure 4.12). The gradient of this line is equal to β for the relevant value of strain. This procedure was repeated for values of strain up to 0.5, with the β value being recorded. These β values were then plotted against their relevant values of strain as displayed in Figure 4.13. A fifth order polynomial is fitted to the curve, producing an expression to calculate β at any given strain for each alloy (see equations 4.3–4.5).

$$\beta = -3.0345\varepsilon^5 + 12.995\varepsilon^4 - 15.076\varepsilon^3 + 7.4036\varepsilon^2 - 1.656\varepsilon + 0.187 \quad (4.3)$$

$$\beta = -7.7989\varepsilon^5 + 17.351\varepsilon^4 - 15.892\varepsilon^3 + 7.8291\varepsilon^2 - 2.1383\varepsilon + 0.3235 \quad (4.4)$$

$$\beta = 52.149\varepsilon^5 - 70.499\varepsilon^4 + 35.054\varepsilon^3 - 8.2368\varepsilon^2 + 1.0995\varepsilon - 0.0161 \quad (4.5)$$

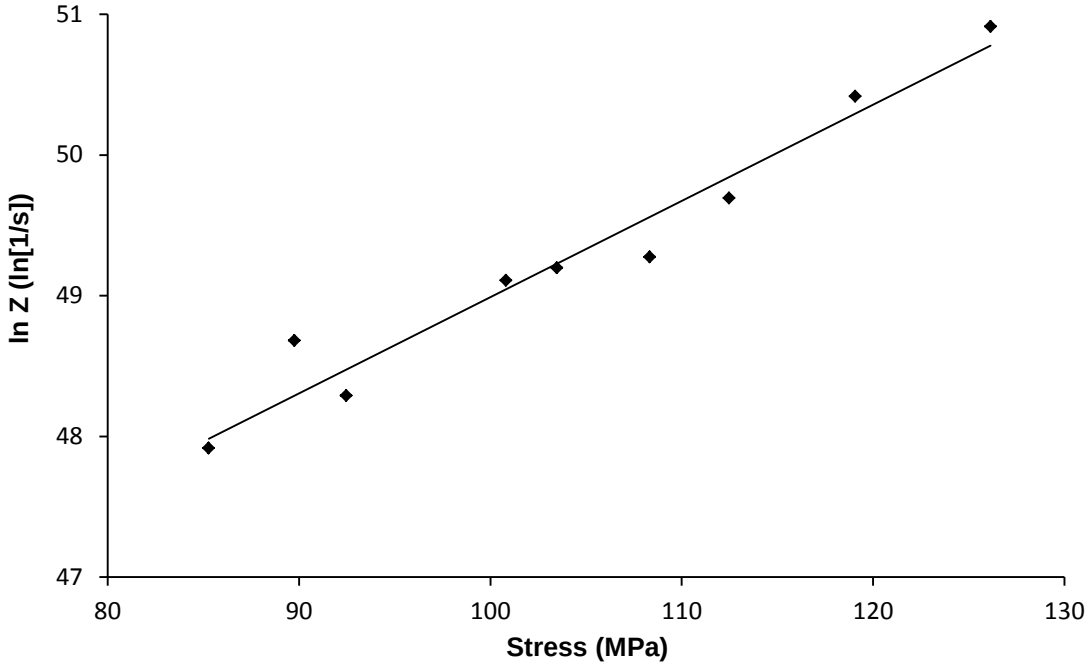

Figure 4.12 – Plot of ln Z vs stress at a strain of 0.4 for alloy 94.

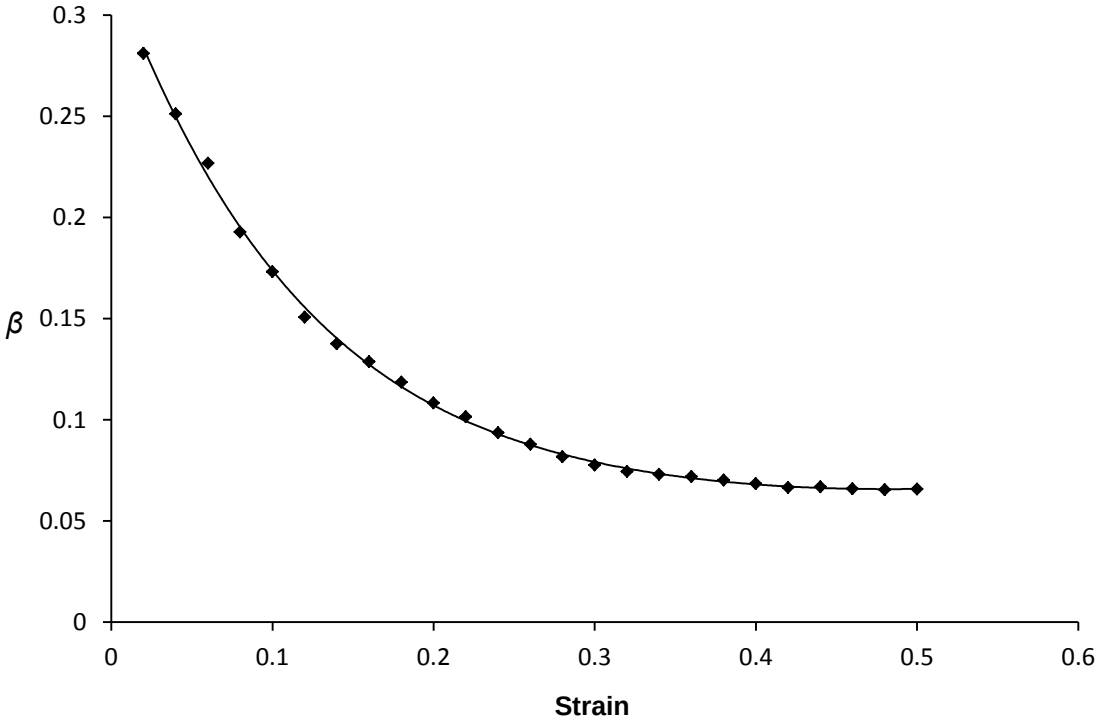

Figure 4.13 – Plot of β vs strain for alloy 94.

4.4.3.5 Fully Corrected Flow Curves

Once the corrections have been incorporated into the data, true isothermal, iso-strain rate flow curves can be plotted. Figures 4.14–4.16 show representative flow curves for each alloy corrected for the effects of friction, strain rate and deformational heating. The original, uncorrected curves are superimposed for comparison (dotted and dashed lines). The three alloys exhibit similar deformation characteristics. The measured stress rises gradually until a peak stress is reached. A slow transition into flow softening follows, caused predominately by dynamic recrystallisation.

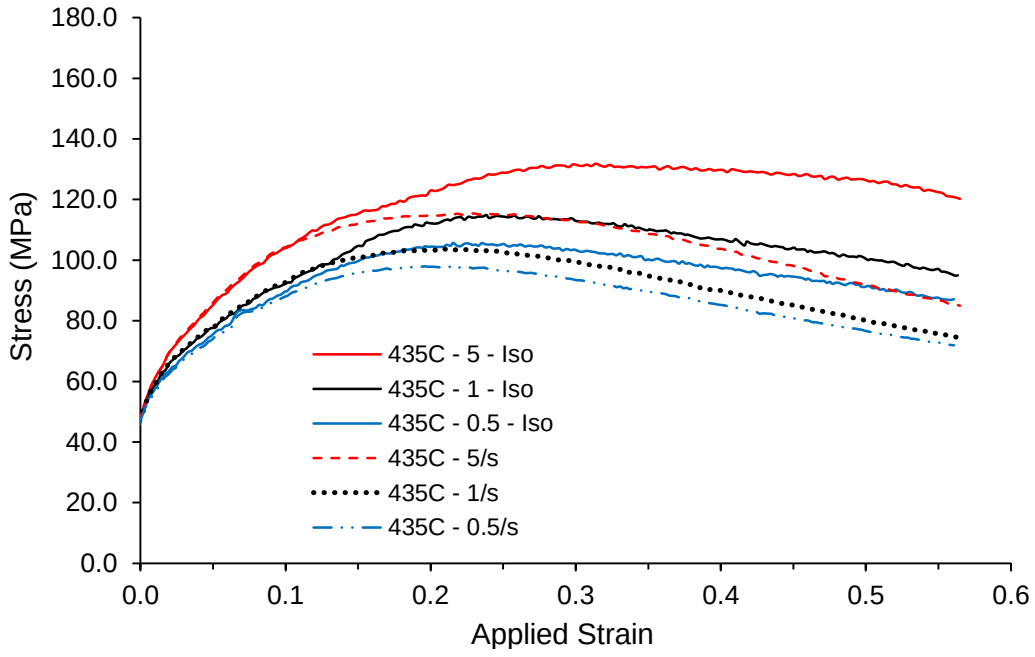

Figure 4.14 – Isothermal, iso-strain rate flow curves for three samples of alloy 93 tested at 435 ºC. Original, uncorrected flow curves are superimposed for comparison (dotted and dashed lines).

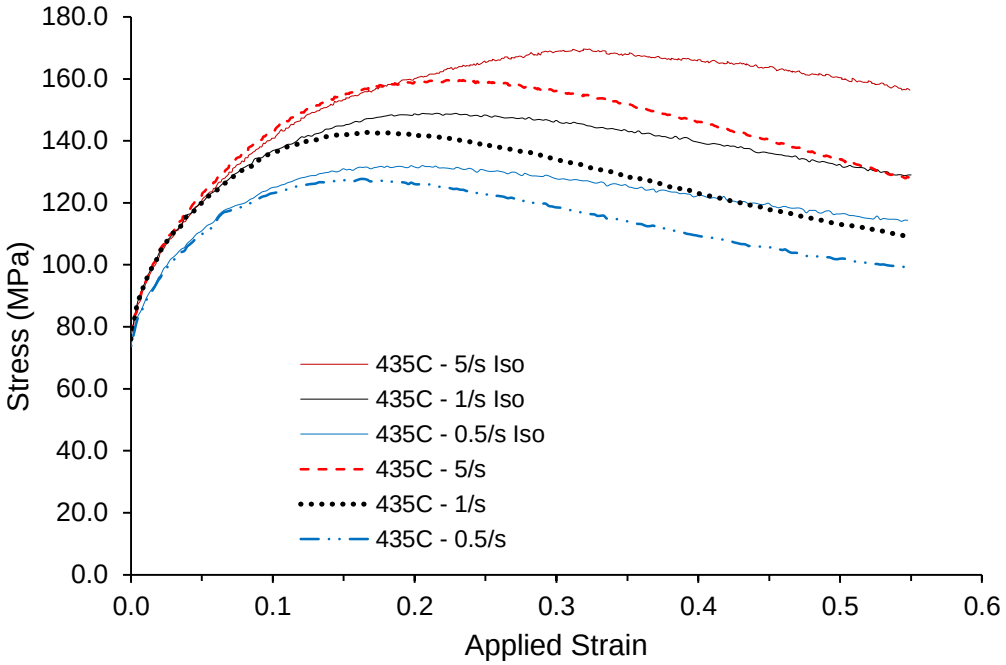

Figure 4.15 – Isothermal, iso-strain rate flow curves for three samples of alloy 94 tested at 435 ºC. Original, uncorrected flow curves are superimposed for comparison (dotted and dashed lines).

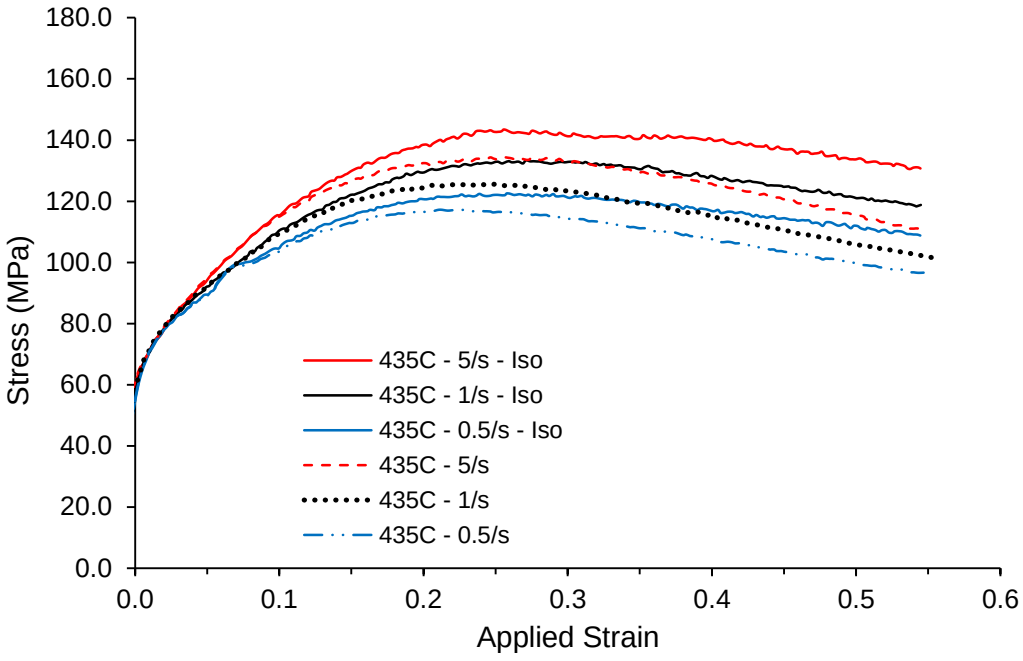

Figure 4.16 – Isothermal, iso-strain rate flow curves for three samples of alloy 95 tested at 435 ºC. Original, uncorrected flow curves are superimposed for comparison (dotted and dashed lines).

4.4.4 Process Window

Defining the limits of ductility for new alloys is an essential step when assessing their suitability for industrial forming processes. The process window gives a visual indication of these limits. A relatively narrow range of tests has been presented in the previous sections. Initially a much wider range of axisymmetric tests were carried out. However, it quickly became apparent that the range of possible conditions the alloys could be deformed under was very limited. Depending on the magnitude of strain rate, incipient melting was frequently observed at higher temperatures ($\geq$465 ºC). Conversely, at lower temperatures ($\leq$425 ºC), shear fracture was commonplace at modest strain rates ($\geq$1/s). Table 4.8 shows the original matrix of test carried out with each of the novel alloys.

Table 4.8 – Original hot axisymmetric test matrix.

Temperature (ºC)	Strain Rate (1/s)
350	1
400	0.5 1 5 10
425	0.5 1 5 10
450	0.5 1 5 10
475	0.5 1 5 10
500	1

Figures 4.17–4.19 show 3 samples of alloy 94. The conditions of each test yielded different outcomes. The first image shows a sample deformed at a strain rate of 1/s and a temperature of 450 ºC. The sample is uniformly deformed with no apparent failure. Figure 4.18 shows a sample deformed at a strain rate of 5/s and a temperature of 425 ºC. Clearly the sample has completely failed due to a shear fracture occurring at approximately 45º to the compression axis. Figure 4.19 shows a sample deformed at a strain rate of 5/s and a temperature of 475 ºC. In this case the sample has completely failed due to incipient melting.

The conditions under which each alloy exhibited either incipient melting or shear fracture were identical. Therefore a single process window can be used to describe the deformation limits of all three alloys. Figure 4.20 shows a plot of ln (strain rate) vs 1/T. This process window was employed to design the final matrix of tests used for analysis in section 4.3.3.

Figure 4.17 – Example of a well deformed sample. Alloy 94 deformed at 450 ºC with a strain rate of 1/s.

Figure 4.18 – Example of a failure due to shear fracture. Alloy 94 deformed at 425 ºC with a strain rate of 5/s.

Figure 4.19 – Example of a failure due to incipient melting. Alloy 94 deformed at 475 ºC with a strain rate of 5/s.

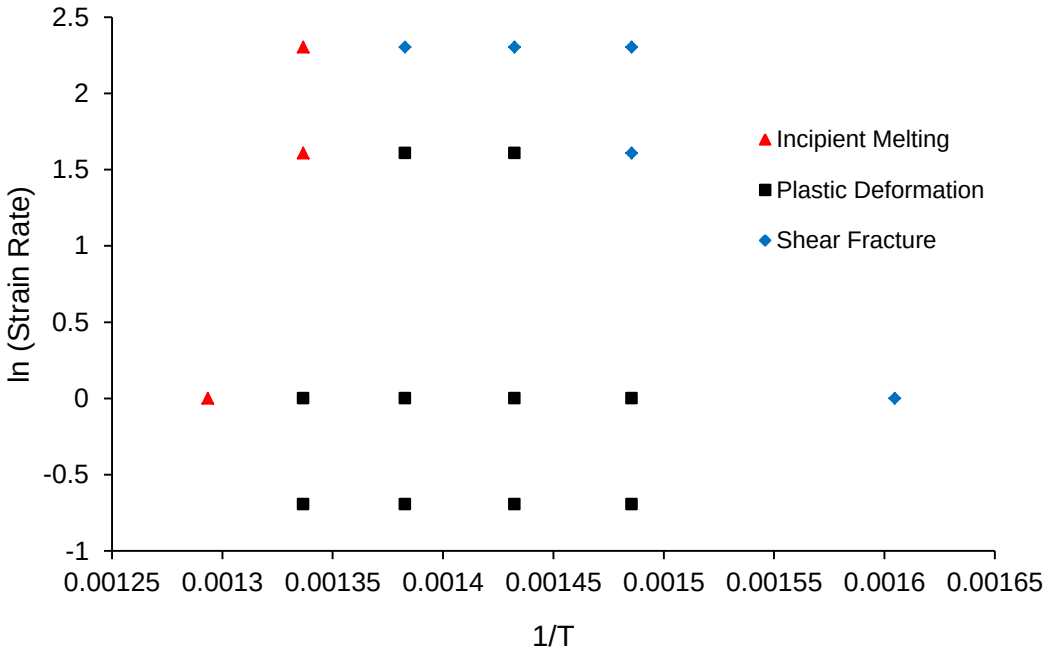

Figure 4.20 – Process window representing all three novel alloys.

4.4.5 Rolling Trial

Although the hot axisymmetric testing was carried out under isothermal conditions, industrial rolling practices are usually carried out with cold tools. Typically, the operating temperature of industrial rolls is approximately 70–120 ºC[1]. To investigate the behaviour of the three novel alloys under a typical industrial rolling regime, a Hille 50 experimental rolling mill was used. Each alloy was sectioned to bars measuring 40x50x100 mm with a 1 mm hole drilled at the centre for a thermocouple to be inserted (see Figure 4.21).

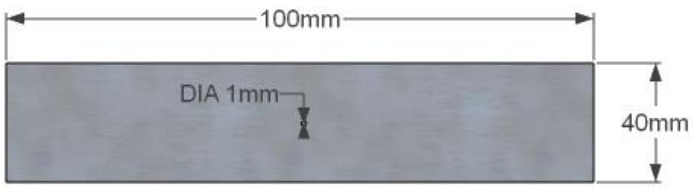

Figure 4.21 – Schematic of novel alloy rolling bar (side view).

Before the novel alloys were rolled, a series of trial rolls were carried out to test the rolling equipment and to warm the rolls to a typical operating temperature. For the trial rolling, a standard magnesium alloy, AZ31B, was used. The billet measured 200x150x40mm prior to deformation. Preheating was carried out in a chamber furnace with the billet being soaked at 420 ºC for 2 hours. A thermocouple was inserted into the centre of the billet to monitor the temperature at all stages. The billet would be approximately 400 ºC by the time it was removed from the furnace and placed into the rolling mill. When the temperature of the rolled billet dropped below 380 ºC it was reheated to 420 ºC and held for 30 minutes before further rolling commenced. A total of 7 passes were made, reducing the billet height in total by 95%, to 2 mm. The roll velocity was 0.8 $m.s^{-1}$. Other than some minor cracking at the very edges of the rolled sheet, there were no apparent defects upon visual inspection. Figure 4.22 shows an optical micrograph of AZ31B after a 95% reduction in height. The microstructure is nearly fully recrystallised with a fine grain size of 3.9 ± 0.26 μm.

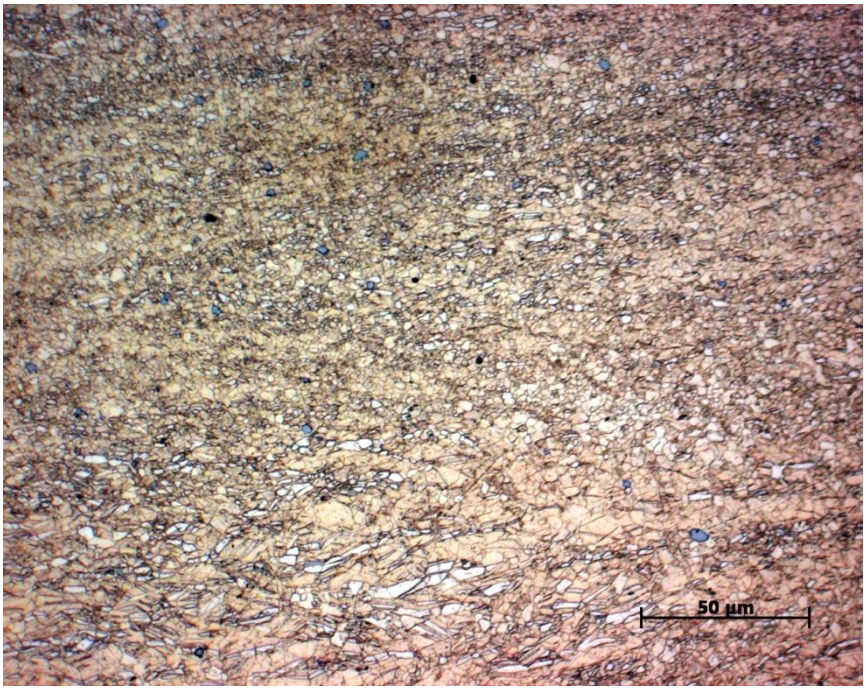

Figure 4.22 – AZ31B after a 95% height reduction with a 7 pass rolling regime at 400 ºC.

The three experimental alloys were rolled immediately after the AZ31B trial to make the most of the residual heat in the rolls. Using the results from the hot axisymmetric study as a starting point, the sectioned bars were preheated to 450 ºC and held for 2 hours to soak. This meant that the temperature at the start of rolling would be approximately 430–435 ºC after allowing for heat loss. The planned rolling schedule was to be a 5% height reduction with each pass, using a roll velocity of 0.8 $m.s^{-1}$, to a total height reduction of 95%. The bars were to be reheated to 450 ºC after each pass. However, all three alloys failed in the early stages of rolling. Alloy 93 failed after two passes of 5%, while alloys 93 and 94 failed after the first pass. Figures 4.23–4.25 show photographs of the failed bars after rolling. Visual inspection showed that the nature of failure was two-fold. At the contact edges of the bars the failure mode was brittle fracture. At the centre of the bars there was clear evidence of incipient melting. The temperature gradient through the rolled bar was significant due to the cooler temperature of the rolls. It should be noted that the volume fraction of second phase within alloys 94 and 95 was significantly higher than that of 93 (see Table 4.4). These two alloys crumbled during the first roll while alloy 93 survived the first pass before splitting into a classic ‘alligator’ during the second pass. The role of the second phase during deformation will be discussed further throughout section 4.6.

Figure 4.23 – Failure of novel alloys upon rolling at 435 ºC.

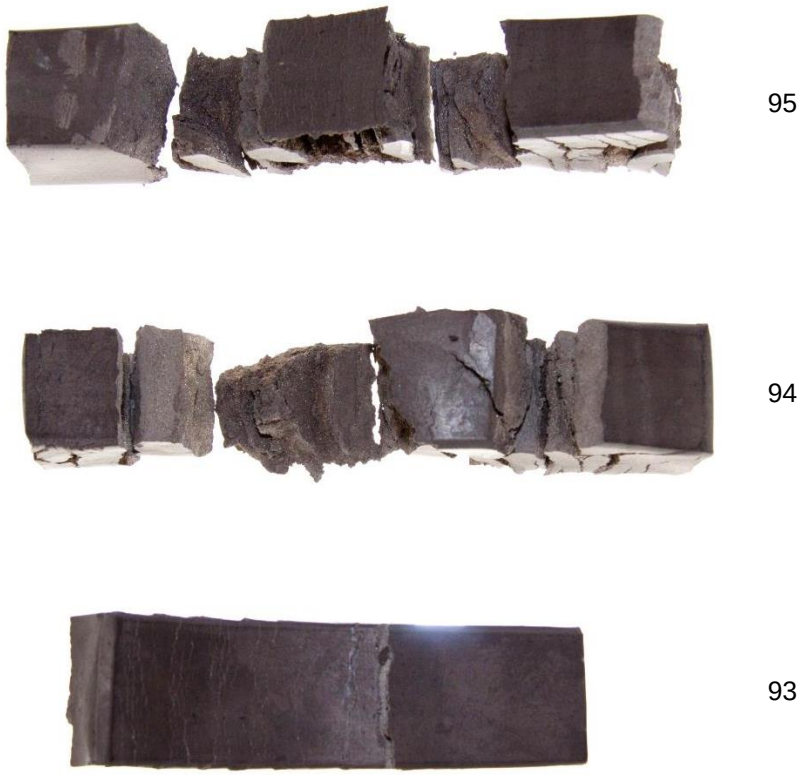

Figure 4.24 – Failure of novel alloys upon rolling at 435 ºC (plan view).

Figure 4.25 – Close up of alloy 93 after rolling at 435 ºC.

4.5 Post-deformation Microstructures

4.5.1 Introduction

Each of the hot axisymmetric compression test samples were analysed by both optical microscopy and EBSD. It is important to investigate and understand the various deformation mechanisms at work with different processing conditions. The main points of interest during this project were the effects of twinning, recovery and dynamic recrystallisation (DRX) on the final texture. After EBSD maps had been produced, the HKL Channel 5 software was used to analyse the data in a variety of ways. The methods used for analysis are discussed in the relevant sections of this chapter. In general, the microstructures of the three alloys appeared to be very similar under the same processing conditions. For that reason, representative figures have been used for the alloys as a whole, where suitable. Where there have been variations between the alloys, independent figures and data have been presented.

4.5.2 Variation of Microstructure with Different Deformation Conditions

The change in microstructure during deformation is affected by both temperature and strain rate. For this reason a temperature compensated strain rate known as the Zener–Hollomon parameter (Z) is used[86]. To calculate Z equation 4.6 is used (repeated from section 2.3.4).

$$Z = \dot{\varepsilon} \exp\left(\frac{Q_{def}}{RT}\right) \tag{4.6}$$

Where $\dot{\varepsilon}$ is the strain rate, Q_{def} is the activation energy of deformation, R is the universal gas constant and T is the temperature in Kelvin.

The following EBSD maps are presented for the lower values of Z, in respect of the particular alloy. Figure 4.26 depicts an IPF coloured EBSD map of alloy 93 deformed at 465 ºC at a strain rate of 0.5 (low Z). As expected, the majority of the map is coloured red, indicating a strong basal texture. Some of the larger, un-recrystallised grains show a distinct change in colour across their area. This is due to variations in the orientation across the grain as it

undergoes deformation. The large rotations across the grain cause dislocations to pile up, particularly at microstructural features such as grain, twin or phase boundaries. On further deformation these areas of high dislocation density develop into sub-grain boundaries with low misorientations (~1–10º). Eventually the sub-grain boundaries fully recrystallise into new grains with distinct, high-angle boundaries and low a dislocation density. At this relatively low strain rate, DRX is predominately visible on grain boundaries, forming a 'necklace' structure around the large parent grains. The white areas, mainly visible at triple points, are the second phase. As the structure of the second phase was unknown to the EBSD software, the areas were simply left as white, non-indexed points.

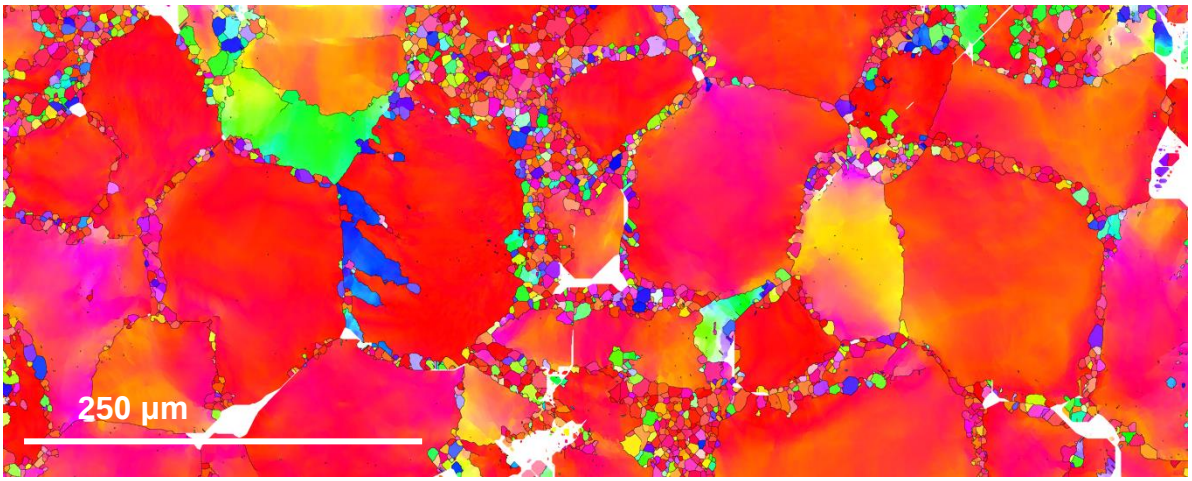

Figure 4.26 – EBSD map (IPF Colouring) of alloy 93 deformed at 465 ºC at a strain rate of 0.5/s.

Figure 4.27 shows an EBSD map of alloy 94 deformed at 450 ºC and a strain rate of 0.5/s. Similar to Figure 4.26, there are large, un-recrystallised grains that show significant variations in orientation across their area. DRX grains are generally formed, once again, in a 'necklace' formation around large parent grains. The major noticeable difference in this sample is a large area of DRX grains to the left of the image. Another interesting feature is the remains of twins that have formed early in the deformation process and then deformed further without recrystallising. The white arrow in the figure indicates an example of a deformed, un-recrystallised twin. Again, areas of second phase are apparent at grain boundaries and triple points.

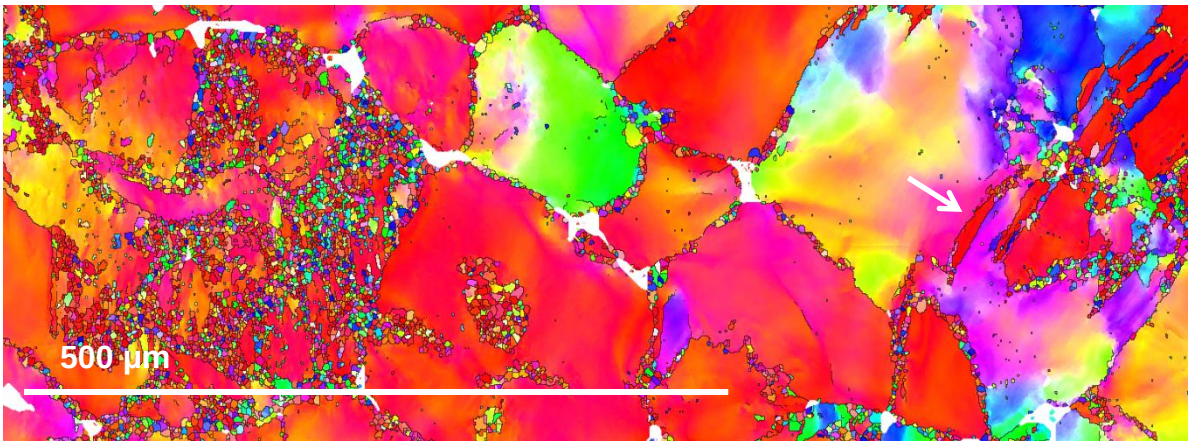

Figure 4.27 – EBSD map (IPF Colouring) of alloy 94 deformed at 450 ºC at a strain rate of 0.5/s.

Figure 4.28 shows an example of a specimen deformed at 450 ºC and a strain rate of 5/s. This is the higher end of the process window in terms of temperature and strain rate and towards the top end of the test matrix in terms of Z. Samples deformed under these conditions showed large, fully recrystallised areas of randomly orientated grains. The most desirable microstructure for each alloy was achieved under this testing regime. The recrystallised fraction and randomisation of texture will be discussed further in sections 4.5.3 and 4.5.5.2.1 respectively.

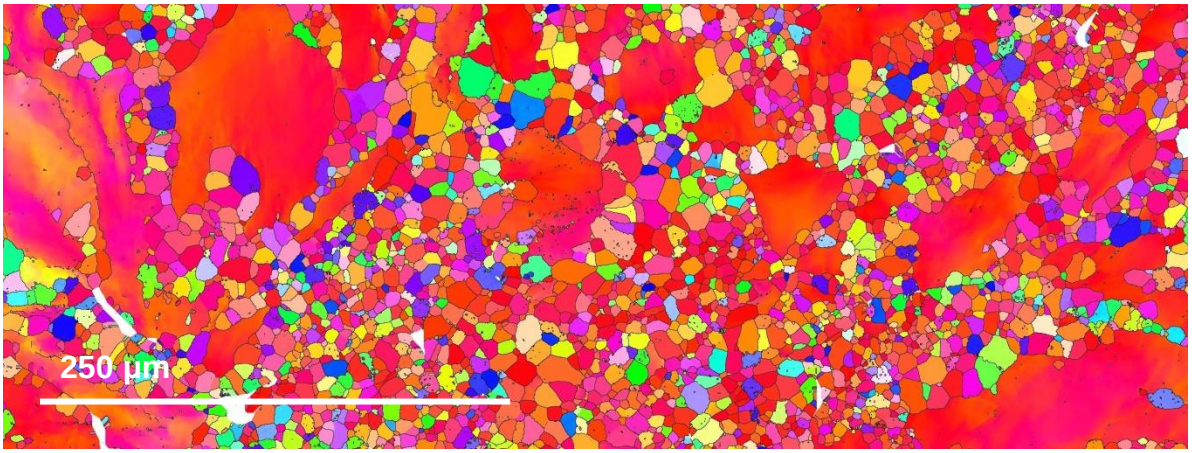

Figure 4.28 – EBSD map (IPF Colouring) of alloy 95 deformed at 450 ºC at a strain rate of 5/s.

At slightly higher values of Z (lower temperatures, high strain rates), a larger volume of DRX twins were apparent in the microstructures analysed. Figure 4.29 depicts a sample of alloy 94 deformed at 435 ºC and a strain rate of 5/s. Recrystallised twins are easily identified by their long, string-like structure, spanning the width of larger, un-recrystallised grains. Examples of dynamically recrystallised twins have been highlighted with white arrows.

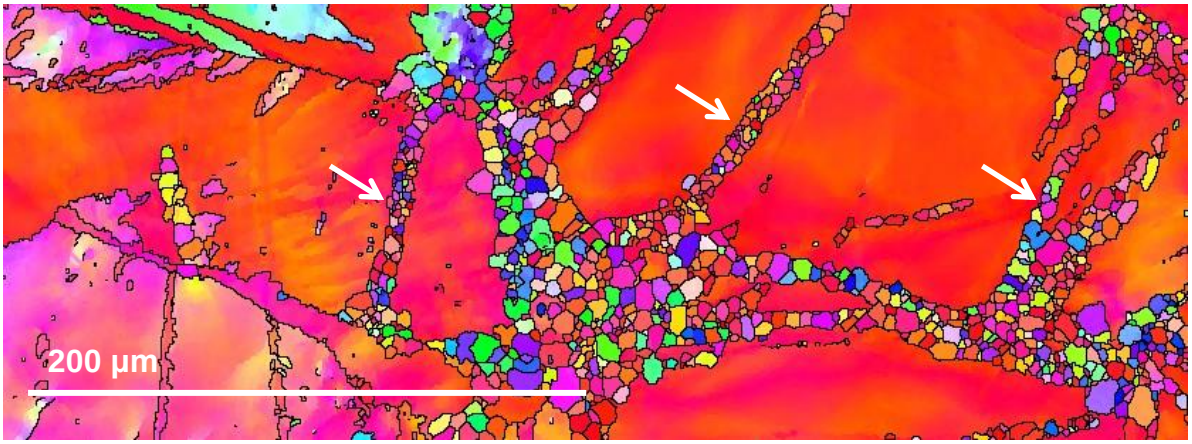

Figure 4.29 – EBSD map (IPF Colouring) of alloy 94 deformed at 435 ºC at a strain rate of 5/s.

At the highest values of Z (low temperature, high strain rate) the volume of DRX twins increases. Figure 4.30 shows a sample of alloy 94 deformed at 425ºC with a strain rate of 5/s. Again, white arrows are used to indicate examples of the DRX twins. Twins became a major nucleation site for DRX in all three alloys tested under these conditions.

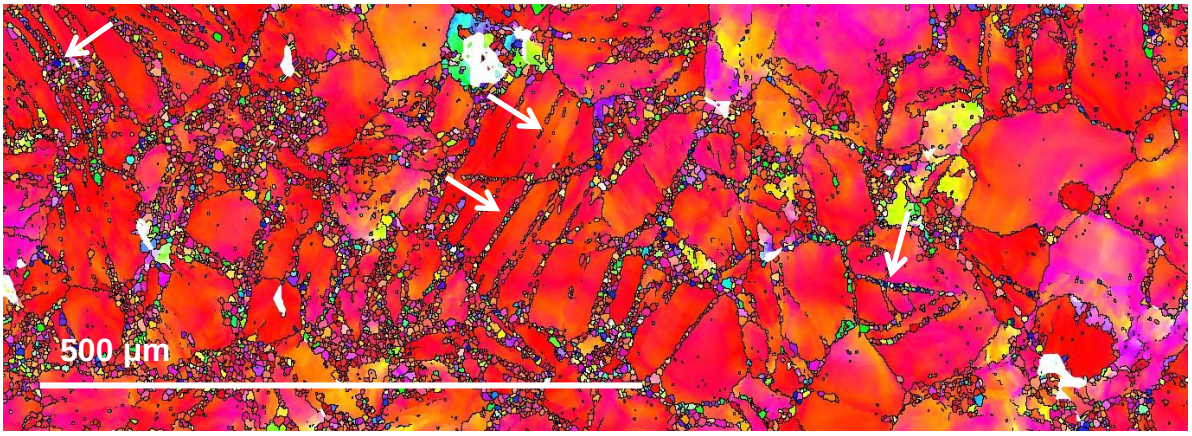

Figure 4.30 – EBSD map (IPF Colouring) of alloy 94 deformed at 425 ºC at a strain rate of 5/s.

4.5.3 Recrystallised Fraction

Although the deformation mechanisms were similar for each alloy, the recrystallised fraction varied significantly. Manual point counting was used to calculate the recrystallised fraction for all of the deformed samples. Large EBSD maps (~2 mm^2) from a range of areas were used for each sample. Optical micrographs of larger areas were also used to corroborate the results from the EBSD maps.

Figure 4.31 shows the recrystallised fraction of alloy 95 compared to the natural logarithm of Z. The error bars indicate the 95% confidence limit. The data have been grouped into test temperatures and exponential lines of best fit have been added. It can be seen that there is a strong relationship for each group. For all three alloys, the recrystallised fraction increased with an increase of temperature and/or strain rate.

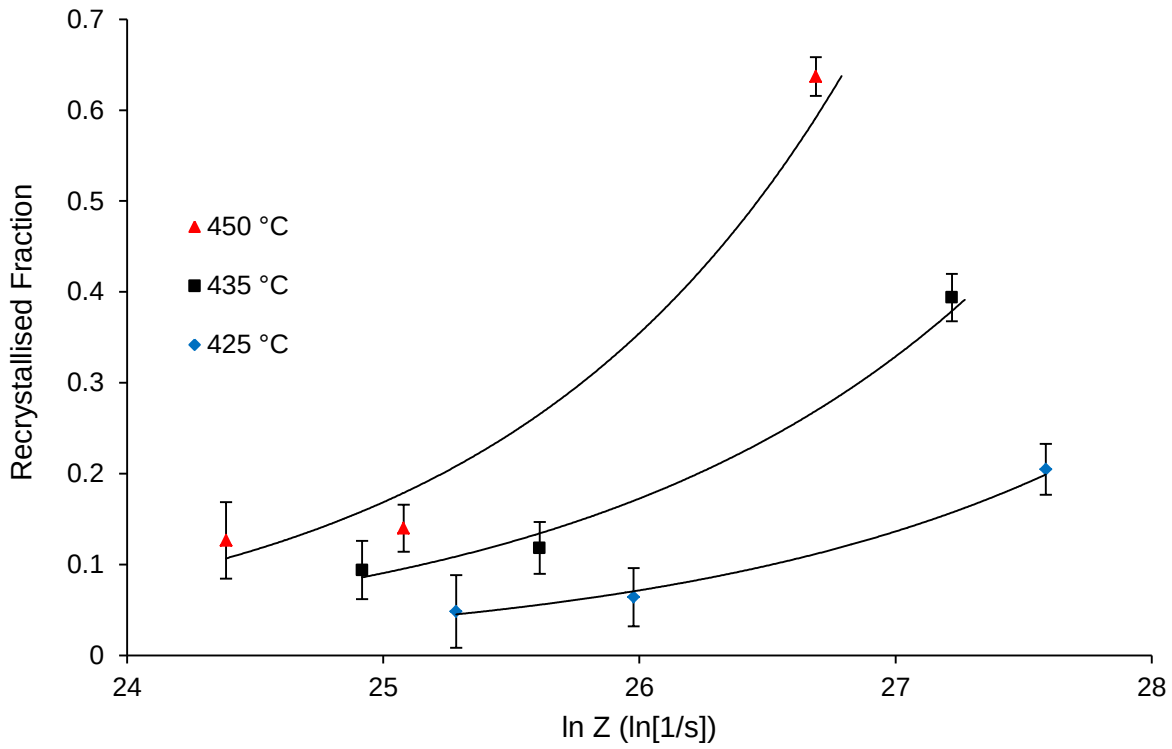

Figure 4.31 – Plot of recrystallised fraction vs ln Z for alloy 95.

Although the relationship was true for each alloy, the total recrystallised fraction varied significantly. Table 4.9 shows the recrystallised fraction for the three alloys at a strain rate of 5/s and a temperature of 450 ºC. As previously mentioned, these deformation conditions produced the highest level of dynamic recrystallisation in each of the alloys.

Table 4.9 – Recrystallised fraction of each alloy deformed at 450 ºC and a strain rate of 5/s.

Alloy	Recrystallised Fraction	95% Confidence Limit
93	0.248	±0.02
94	0.193	±0.02
95	0.637	±0.03

4.5.3.1 Recrystallised Grain Size

The average grain size of dynamically recrystallised material varied according to the processing conditions. Figure 4.32 shows the average DRX grain size vs the natural logarithm of Z for alloy 93. There is a strong linear trend of the average DRX grain size reducing as Z increases. The higher values of Z relate to higher temperatures and slower strain rates. The higher temperatures increase grain boundary mobility with the slower strain rates allowing more time for grain growth. The same trend was observed for each alloy. Table 4.10 compares the average DRX grain size for each alloy after deformation at 450 ºC and a strain rate of 0.5/s. For comparison, Table 4.11 shows the average DRX grain size for each alloy after deformation at 425 ºC and a strain rate of 5/s.

Table 4.10 – Average DRX grain size for each alloy deformed at 450 ºC and a strain rate of 0.5/s (low Z).

Alloy	Average DRX Grain Size (µm)	95% Confidence Limit
93	7.89	±0.65
94	7.23	±0.52
95	7.44	±0.81

Table 4.11 – Average DRX grain size for each alloy deformed at 425 ºC and a strain rate of 5/s (high Z).

Alloy	Average DRX Grain Size (µm)	95% Confidence Limit
93	4.39	±0.38
94	3.45	±0.30
95	3.22	±0.41

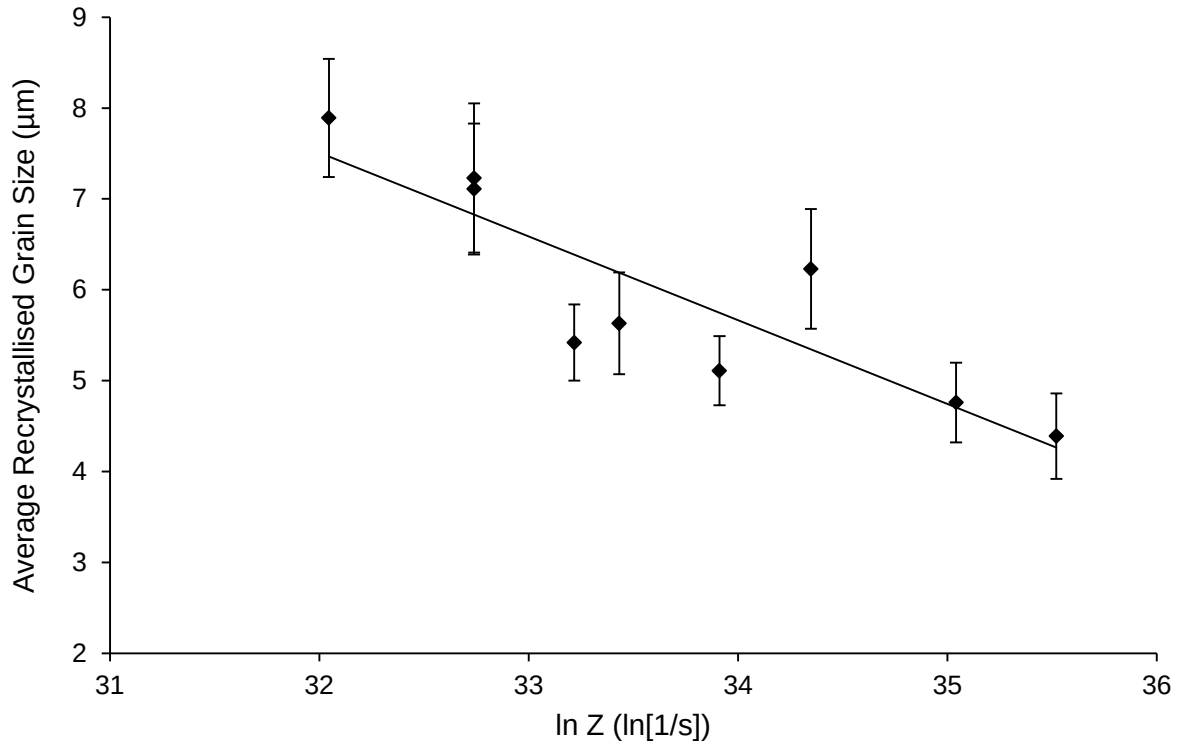

Figure 4.32 – Plot of average DRX Grain size vs ln Z for alloy 93.

4.5.4 Subgrain Formation

The HKL Channel 5 software was also used to investigate the development of substructure during deformation. Usually grain boundaries are identified as distinct changes in orientation of over 10º. To examine substructure, the software was set to also identify areas that contained lower changes in orientation of 2º or more. By doing this, features such as subgrain boundaries and areas of high dislocation density could be examined. Figure 4.33 shows a sample deformed at a high value of Z (high strain rate and low temperature). Features with lower angles of misorientation are coloured white to distinguish them from standard grain boundaries. Subgrain boundaries can be clearly seen in the proximity of dynamically recrystallised grains and close to grain boundaries. In some of the large, un-recrystallised grains, tangles of dislocations form random, low angle substructures. At these lower temperatures and high strain rates, areas of high dislocation density have little time to recover into lower energy configurations.

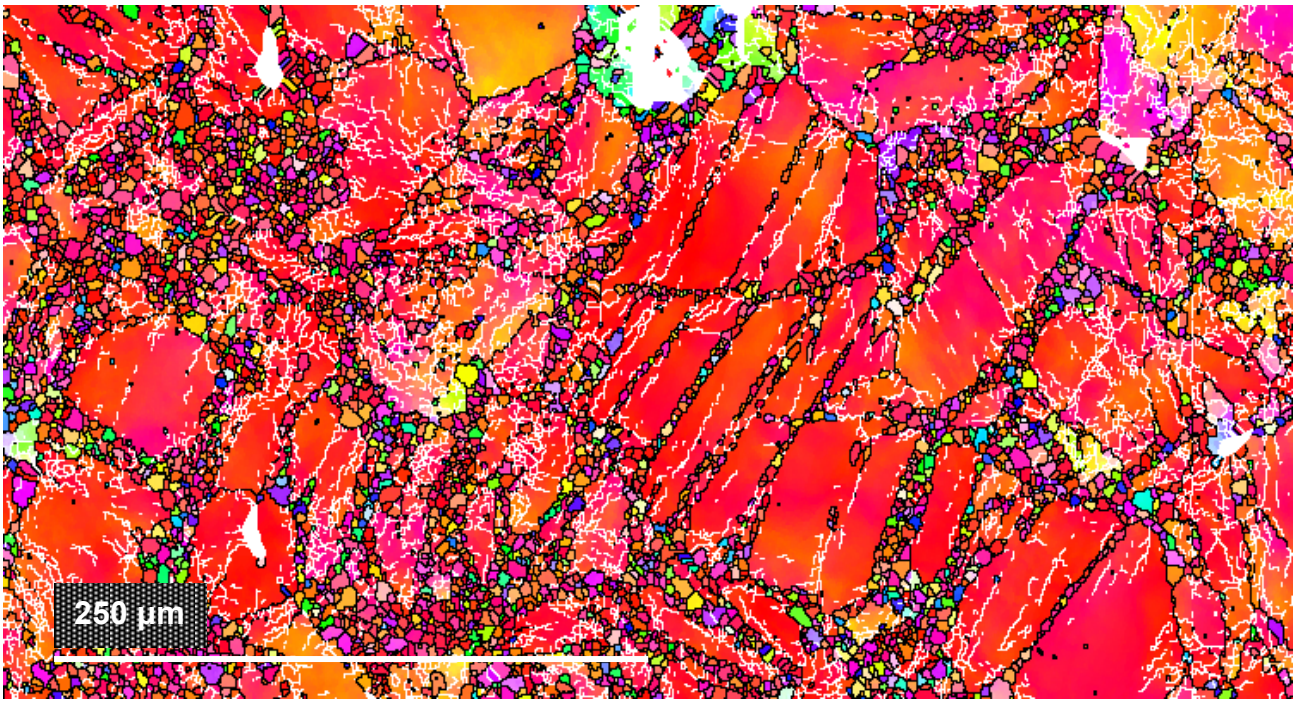

Figure 4.33 – EBSD map (IPF colouring) of alloy 94 deformed at 425 ºC and a strain rate of 5/s with subgrain structure between 2 and 10º coloured in white.

At lower values of Z (high temperature and low strain rate) dislocations become more mobile with time to recover into more ordered substructures. Figure 4.34 shows a sample deformed at 465 ºC and a strain rate of 0.5/s. The majority of visible substructure is along grain boundaries and close to areas of DRX. The dislocations have re-ordered into lower energy forms such as cells and subgrain boundaries. There are visibly far less networks of dislocations in the larger, un-recrystallised grains. Around the areas of DRX, ordered subgrain boundaries have formed.

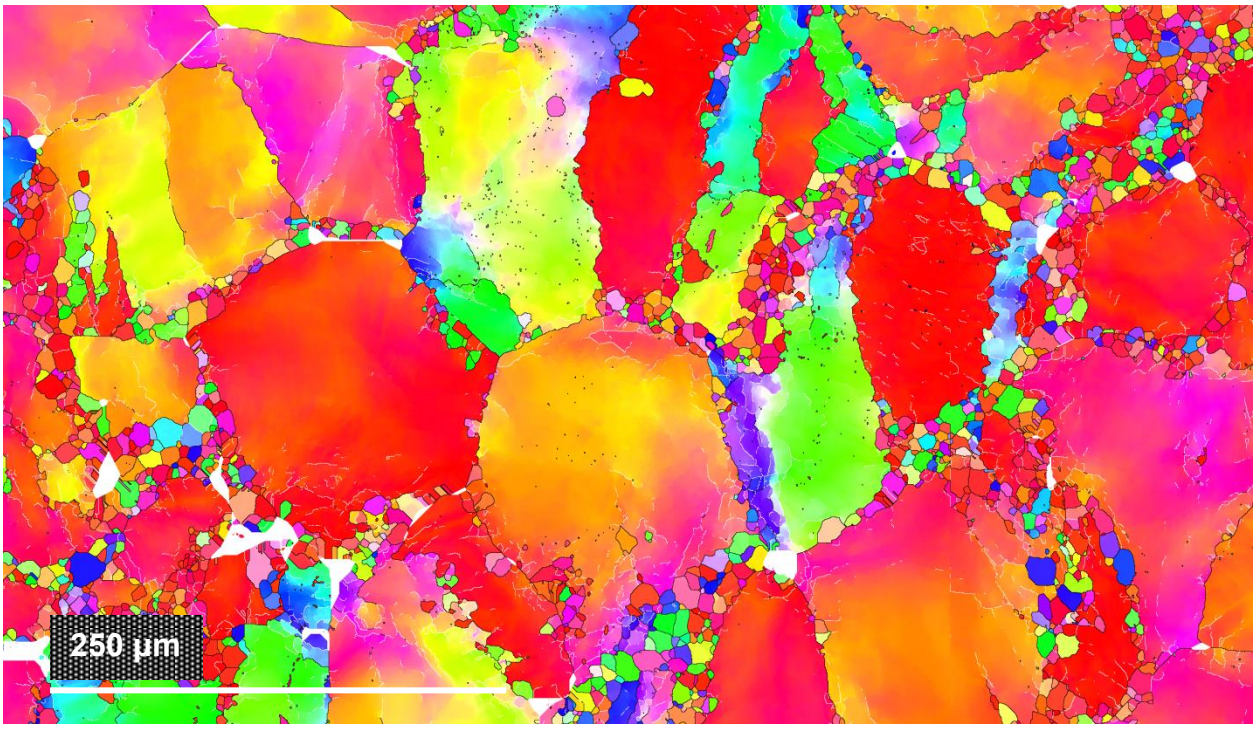

Figure 4.34 – EBSD map (IPF colouring) of alloy 93 deformed at 465 ºC and a strain rate of 0.5/s with subgrain structure between 2 and 10º coloured in white.

In samples with high levels of dynamic recrystallisation (high temperature and high strain rate), very little substructure remained. Many of the subgrains had fully recrystallised into new grains. Figure 4.35 shows a sample deformed at 450 ºC with a strain rate of 5/s. The majority of the substructure occurs at the edges of the un-recrystallised grains forming subgrain boundaries. There is also evidence of subgrain boundaries forming within DRX grains.

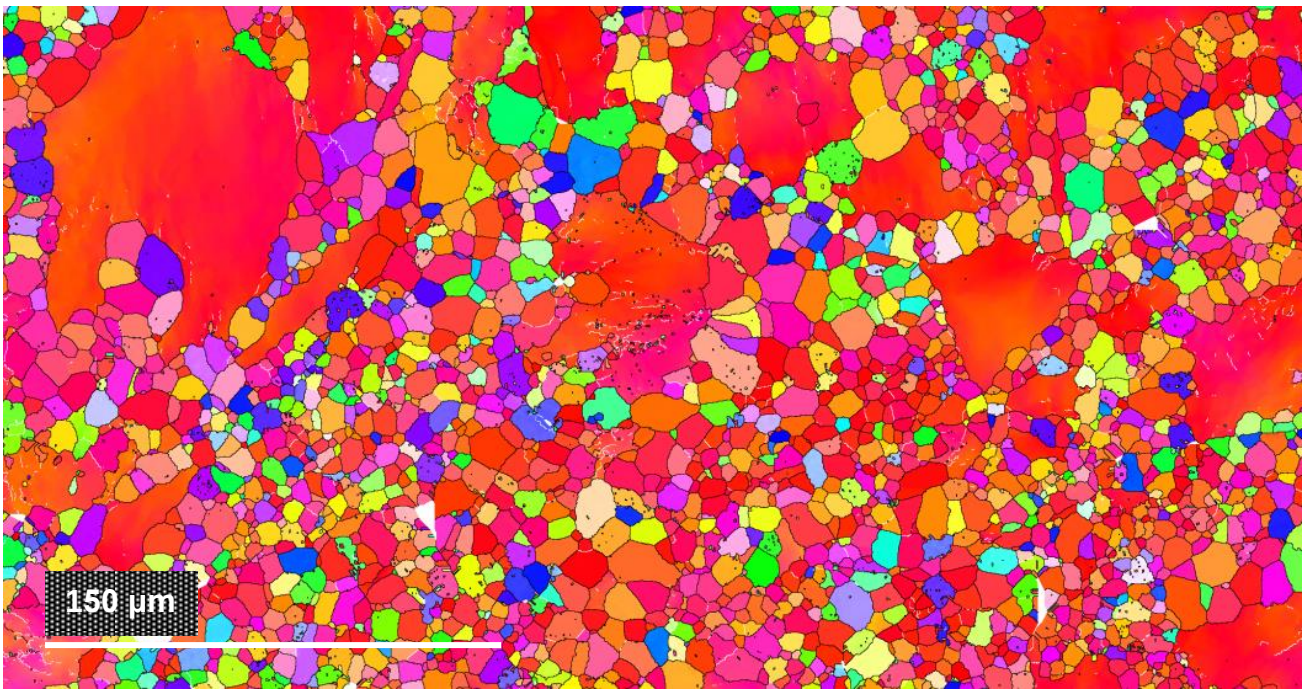

Figure 4.35 – EBSD map (IPF colouring) of alloy 95 deformed at 450 ºC and a strain rate of 5/s with subgrain structure between 2 and 10º coloured in white.

4.5.5 Texture

4.5.5.1 Variation of Texture with Processing Conditions

The HKL Channel 5 software was used to produce a series of pole figures to compare the deformed textures to the starting texture (see Figure 4.7). There were no notable variations in texture between the three alloys under equivalent processing conditions. Figure 4.36 shows three pole figures for alloy 94 through a range of Z values. There is little variation between the three samples. All samples show a strong basal texture with a slight split from the 0002 pole. The split from the pole reduces slightly with increasing Z from approximately 34º to 22º. It must be noted that these pole figures are taken from relatively small areas (typically 1.5–2.5 mm^2) and cannot, therefore, give a true indication of the global texture of the samples. However, it is clear that a strong basal texture exists in each alloy across the full range of processing conditions.

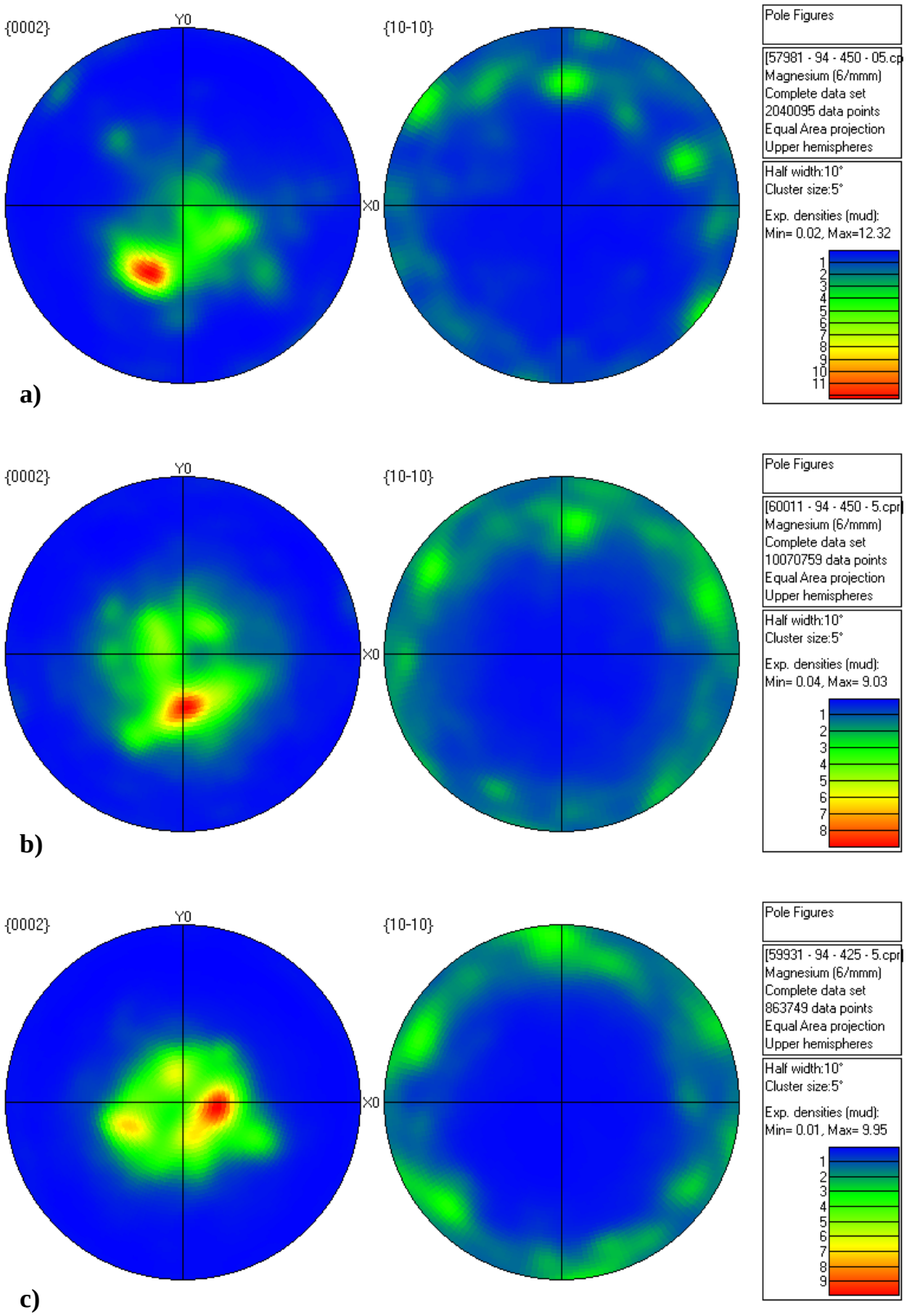

Figure 4.36 – Pole figures of alloy 94 deformed at: a) 450 ºC and 0.5/s ($Z = 6.180x10^{17}$), b) 450 ºC and 5/s ($Z = 6.180x10^{18}$) and c) 425 and 5/s ($Z = 2.747x10^{19}$).

4.5.5.2 Influence of Dynamic Recrystallisation on Texture

To investigate the effect of dynamic recrystallisation on the final texture, Channel 5 was used to isolate the DRX grains in each sample. Pole figures of the DRX grains were then produced for comparison with the general deformed textures. Figure 4.37 shows the same three samples as Figure 4.36 with only the DRX grains included. There is a very weak basal texture for each sample with no clear variation in the strength of the texture with varying values of Z. The multiples of uniform density (MUD) range from 2.98 to 3.55. With the relatively small areas examined, this range of MUD is not statistically significant. All three alloys exhibited the same weak basal texture when analysing the DRX grain only.

For comparison, Figure 4.38 shows the same three samples with only the non-dynamically recrystallised grains included. The pole figures look similar to the pole figures of the general texture in Figure 4.35. However, there is a notable increase in the MUD values. The magnitude of the increase in MUD correlates well with the recrystallised fraction of each sample (see Figure 4.31). The samples with a higher recrystallised fraction have a greater increase in MUD when the DRX grains are removed from the pole figures. Table 4.12 compares the change in MUD to the DRX fraction for the three samples from Figure 4.36 when considered with and without DRX grains. This shows that an increase in DRX fraction significantly weakens the general texture of the sample. The same pattern was observed for all three alloys.

Table 4.12 – Comparison of DRX fraction to change in MUD value when considered with and without DRX grains.

Sample	DRX Fraction	MUD Value (General)	MUD Value (Without DRX Grains)
94 – 450 ºC – 0.5/s	0.04	12.32	12.80
94 – 450 ºC – 5/s	0.19	9.03	16.51
94 – 425 ºC – 5/s	0.08	9.95	12.27

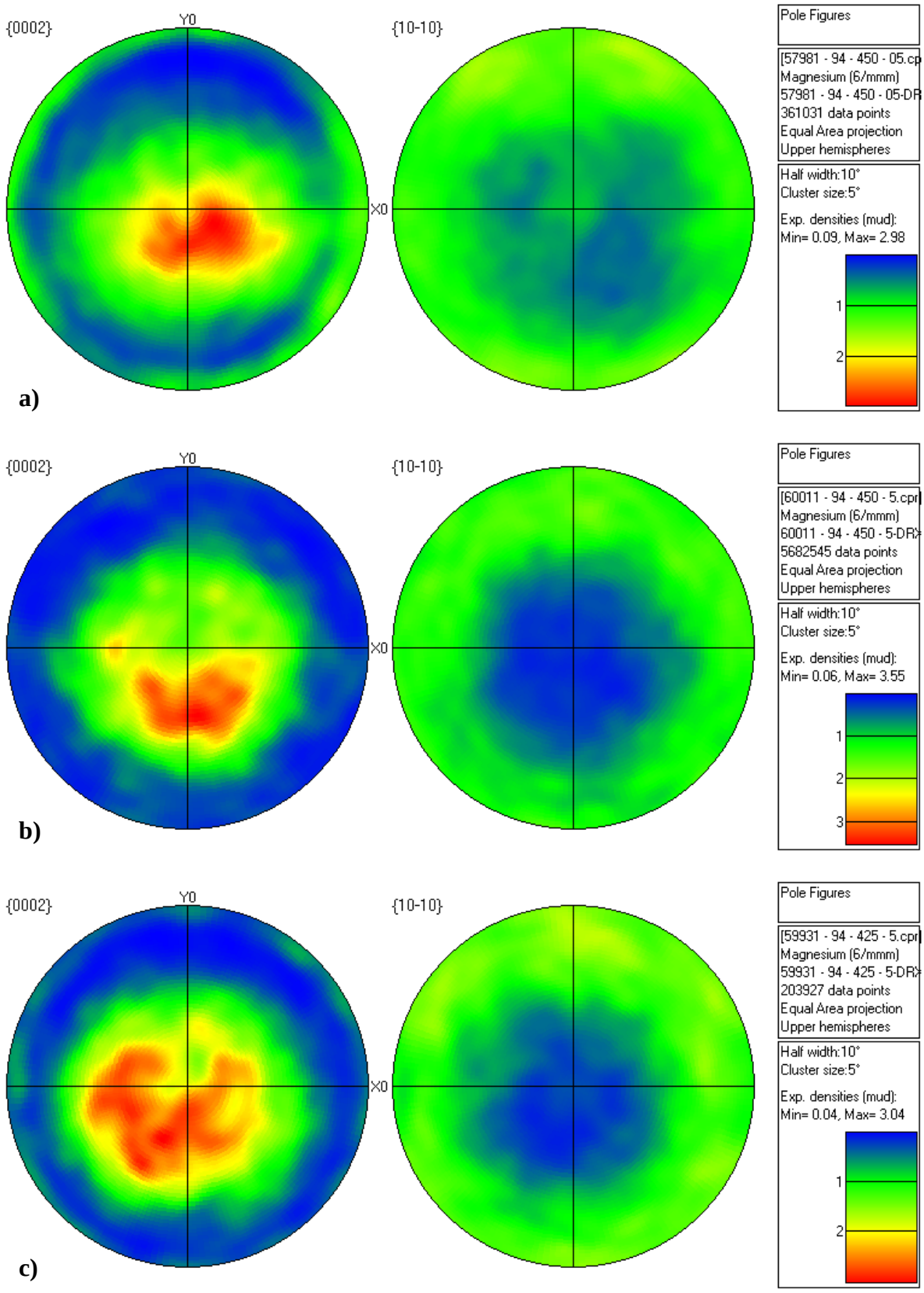

Figure 4.37 – Pole figures of DRX grains only in alloy 94 deformed at: a) 450 ºC and 0.5/s ($Z = 6.180x10^{17}$), b) 450 ºC and 5/s ($Z = 6.180x10^{18}$) and c) 425 and 5/s ($Z = 2.747x10^{19}$).

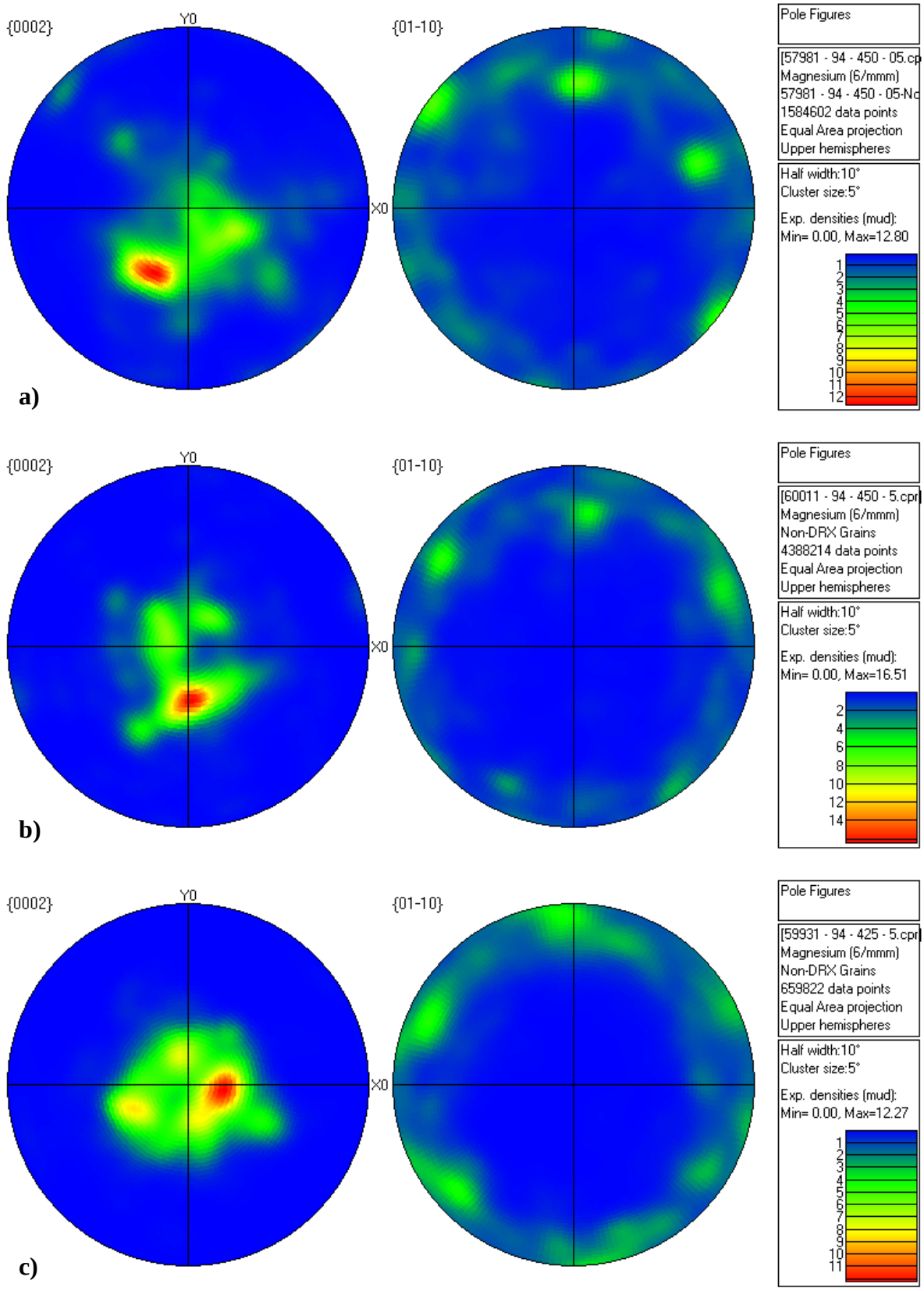

Figure 4.38 – Pole figures of non-DRX grains only in alloy 94 deformed at: a) 450 ºC and 0.5/s ($Z = 6.180x10^{17}$), b) 450 ºC and 5/s ($Z = 6.180x10^{18}$) and c) 425 and 5/s ($Z = 2.747x10^{19}$).

4.5.5.2.1 Randomisation of Texture by Dynamic Recrystallisation

A series of misorientation distribution (MD) plots were produced to investigate the weakening of basal texture by DRX grains. Channel 5 measures the misorientation between random pairs of pixels throughout the entire data set. The relative frequency is then calculated and displayed in a bar chart. Figure 4.39 gives an example of a MD plot for the non-recrystallised grains of alloy 95 deformed at 450 ºC with a strain rate of 5/s. This sample was chosen due to its high recrystallised fraction of 0.64. The black line shows a Mackenzie plot of the theoretical random MD[141]. There are a high number of angles in the region of 30º. The reason for this is that there are high levels of deformation across the un-recrystallised grains. Figure 4.40 shows a typical misorientation profile measured across a single un-recrystallised grain in the same sample. Rotations of over 30º are frequently observed in the un-recrystallised grains. This leads to a peak in the MD profile around 30º as the misorientation pixel pairs are selected at random across the whole sample.

Figure 4.41 shows the MD for the DRX grains only, within the same sample. There is a strong correlation with the theoretical random MD. Figure 4.42 shows the general MD for the entire sample. Although there is still a high frequency of misorientations within the 30-40º range, the DRX grains shift the distribution closer to the theoretical random. Every deformed sample exhibited the same shift, by varying degrees, towards a random misorientation distribution. The magnitude of this shift was a function of the recrystallised fraction. Samples with a higher recrystallised fraction had a more random overall texture.

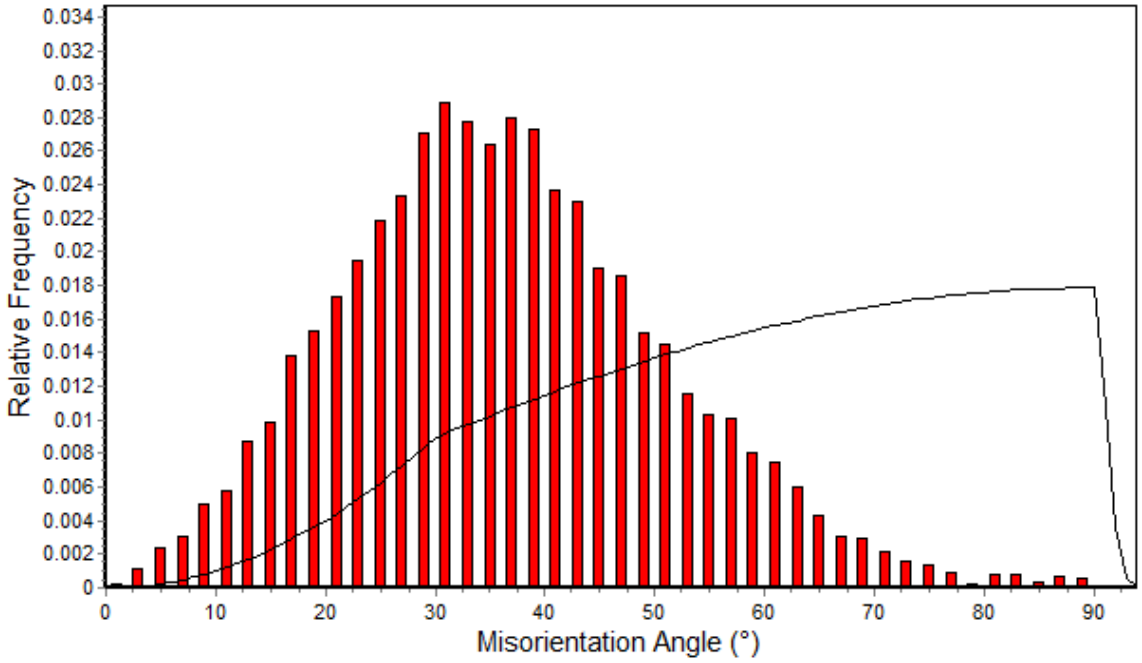

Figure 4.39 – Misorientation distribution plot of un-recrystallised grains within a sample of alloy 95 deformed at 450 ºC with a strain rate of 5/s. Black line indicates the theoretical random distribution.

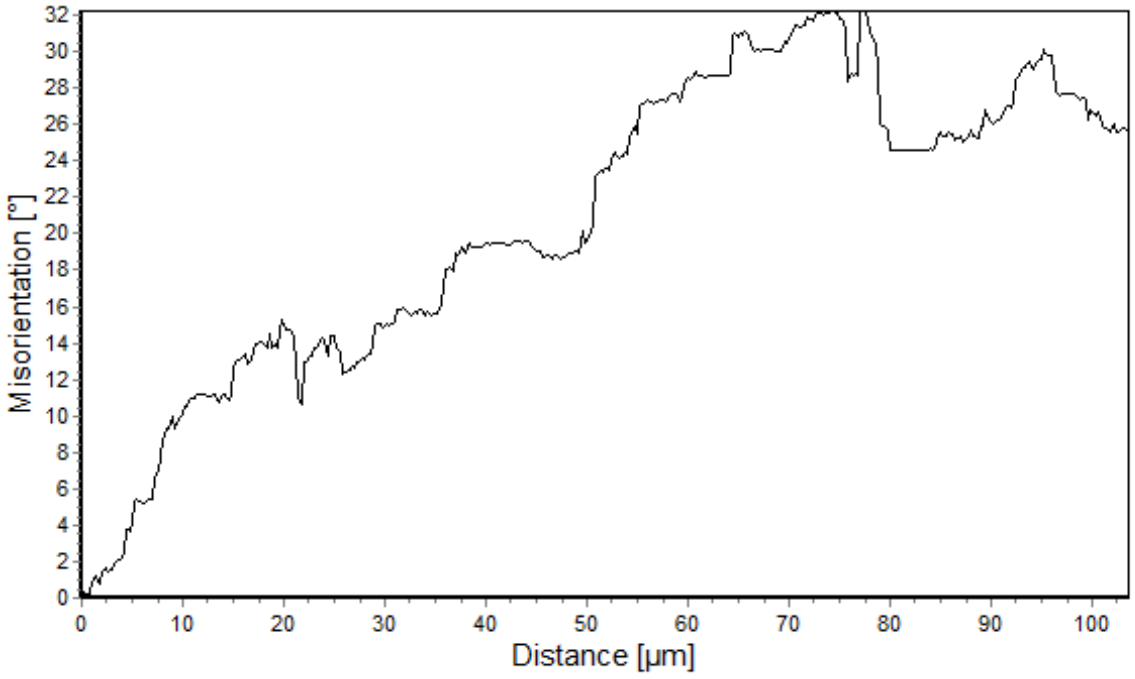

Figure 4.40 – Misorientation profile taken across a single, un-recrystallised grain within a sample of alloy 95 deformed at 450 ºC with a strain rate of 5/s.

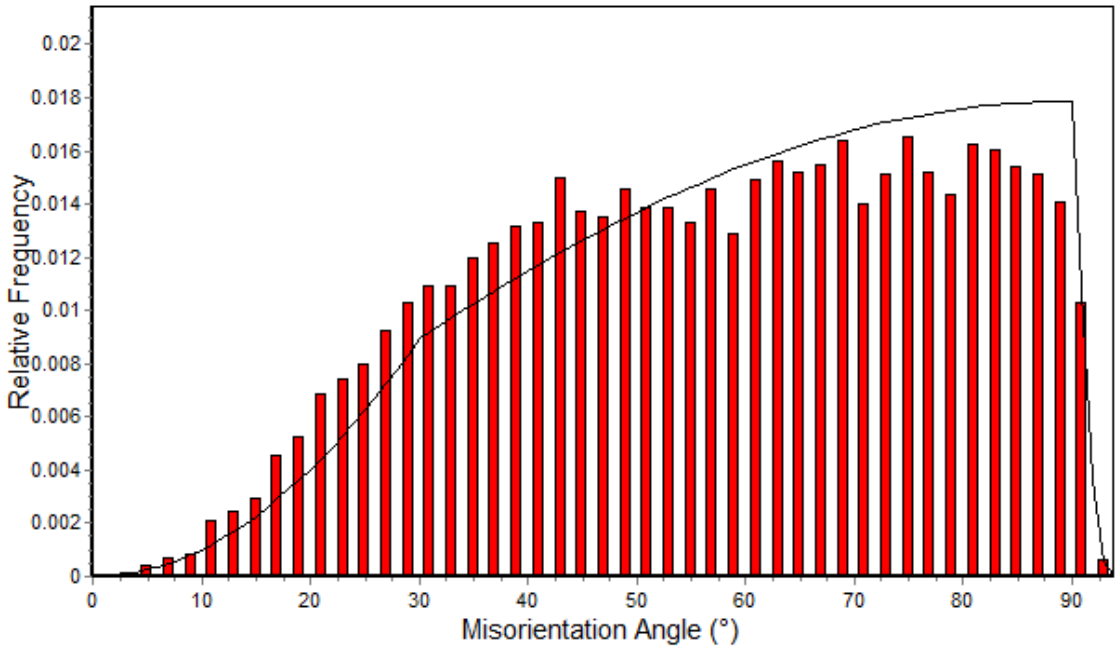

Figure 4.41 – Misorientation distribution plot of dynamically recrystallised grains within a sample of alloy 95 deformed at 450 ºC with a strain rate of 5/s. Black line indicates the theoretical random.

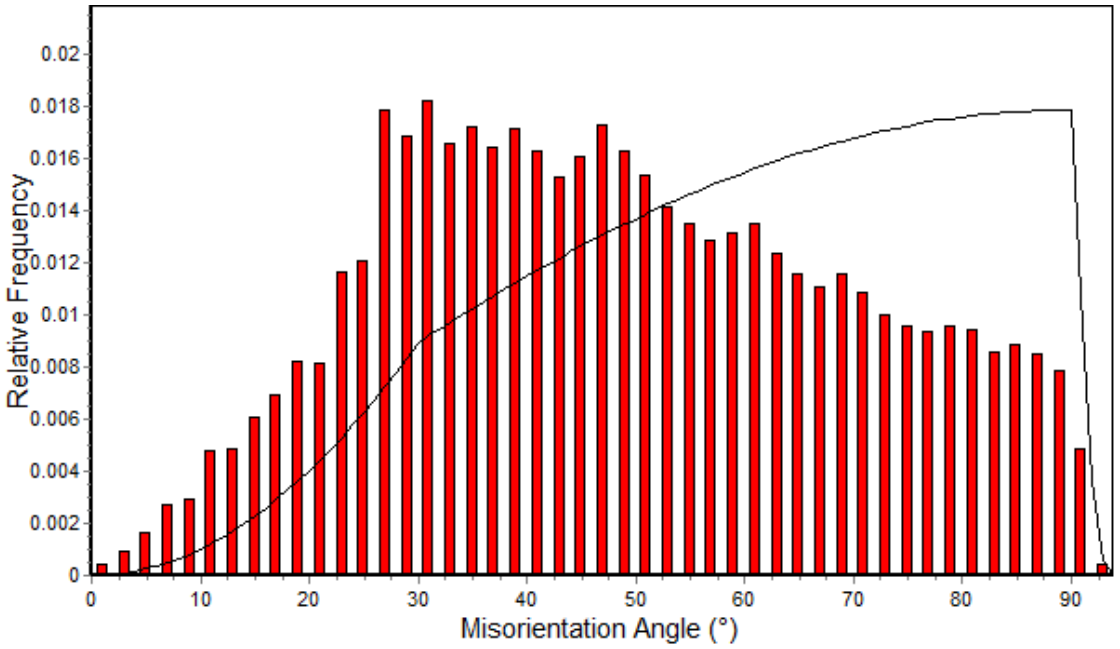

Figure 4.42 – Misorientation distribution plot of all grains within a sample of alloy 95 deformed at 450 ºC with a strain rate of 5/s. Black line indicates the theoretical random distribution.

4.6 Discussion

4.6.1 Introduction

This section will summarise and discuss the majority of results from Chapter 4. Particular attention is given to the flow behaviour including the shape of the flow curves and the mechanisms involved in work hardening and flow softening. The texture variation with processing conditions is also discussed in detail. A separate discussion section in Chapter 5 will analyse the chemistry of the alloys including the important contribution of the second phase to the deformation characteristics.

4.6.2 Flow Characteristics

The corrected flow curves can be viewed in section 4.4.3.5. All of the tests carried out on the three alloys exhibited the same general trend under hot deformation. Figure 4.43 shows a representative flow curve of alloy 94 compressed at 435 ºC with a strain rate of 0.5/s. After the yield point, there is a period of work hardening caused predominately by slip, mechanical twinning and dislocation pile up. All of the tests produced a convex shape during the work hardening part of the flow curve. This shape would suggest that slip is the dominant mechanism during work hardening. Previous investigations into the deformation behaviour of magnesium alloys have exhibited concave shaped work hardening regions[60, 61, 72, 78, 142-147]. These concave shaped curves usually occur when mechanical twinning is the dominant work hardening mechanism. The curve reaches a peak stress and then a prolonged period of flow softening occurs. In line with other magnesium alloys, the period of softening is attributed primarily to dynamic recrystallisation. The general shape of the flow curves is similar to most previous studies carried out with magnesium alloys[68, 109, 148-152]. A notable feature of the current work is that the flow curves do not reach a steady state when tested to a strain of 0.6. Such a steady state would indicate that the sample has fully recrystallised and any further plastic deformation occurs uniformly. Referring to section 4.5.3 it can be seen that the highest volume fraction of DRX was observed in alloy 95 at 450 ºC with a strain rate of 5/s. Under these conditions, DRX accounted for approximately 64% of the final microstructure. It is probable that if the test continued to a higher strain, then a steady state would be achieved.

However, preliminary tests carried out to higher strains generally caused the samples to fail due to incipient melting at the higher temperatures or fracture at the lower temperatures. Additionally, the graphite lubricant used starts to separate when the sample spreads under deformation. Upon visual inspection of the samples after higher strain tests (0.7) it was clear that relatively large areas of the sample surface were left without lubricant. Breaks in the lubrication of this nature were deemed unacceptable for reliable, repeatable testing.

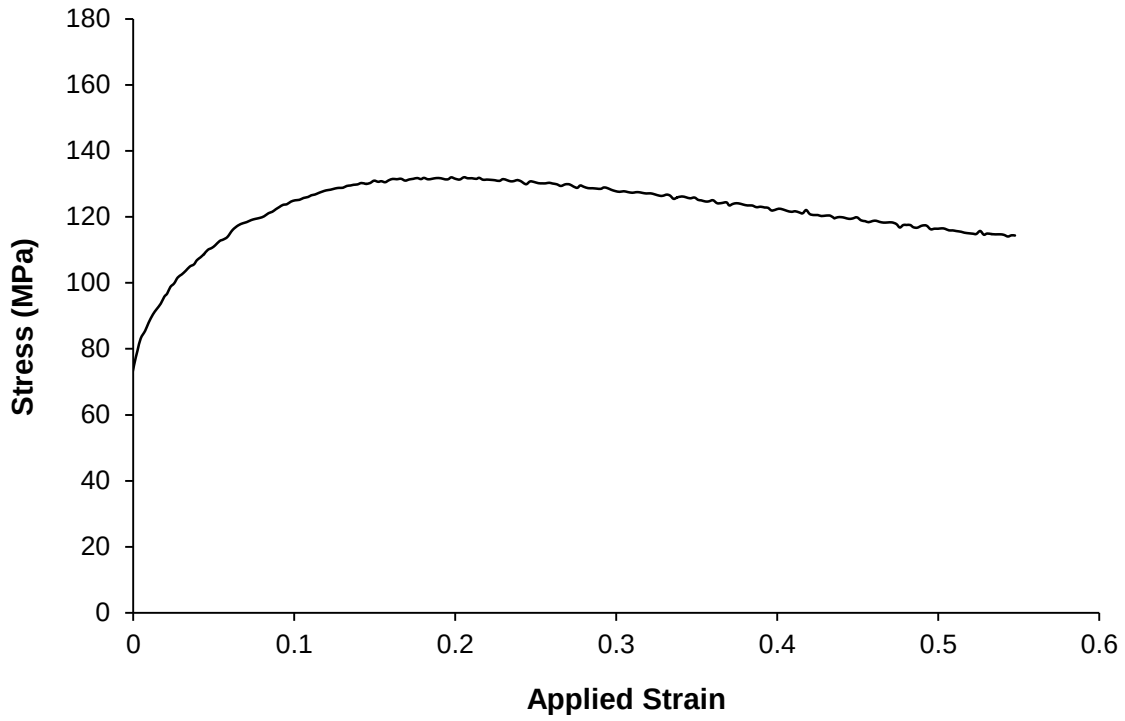

Figure 4.43 – Isothermal, iso-strain rate flow curve of alloy 94 deformed at 435 ºC with a strain rate of 0.5/s.

Alloys 93 and 94 exhibited lower volumes of DRX of 25 and 19% respectively at 450 ºC with a strain rate of 5/s. This suggests that the kinetics of DRX are particularly slow in these two alloys. For a steady state to be achieved, high levels of strain would be necessary. Such high strains are beyond the capabilities of hot axisymmetric compression testing with the current alloys.

4.6.2.1 Variation of Flow Characteristics with Alloy Chemistry

Although the general shape of the flow curves was similar for each alloy, there are distinct variations between each of the chemistries. For comparison Figure 4.44 shows flow curves of each of the alloys when deformed at 435 ºC with a strain rate of 5/s. At this temperature and strain rate alloy 94 had the highest peak stress of approximately 169 MPa and took the longest to reach this peak at around 0.31 strain. Alloy 93 reached a peak stress of approximately 131 MPa at ~0.3 strain.

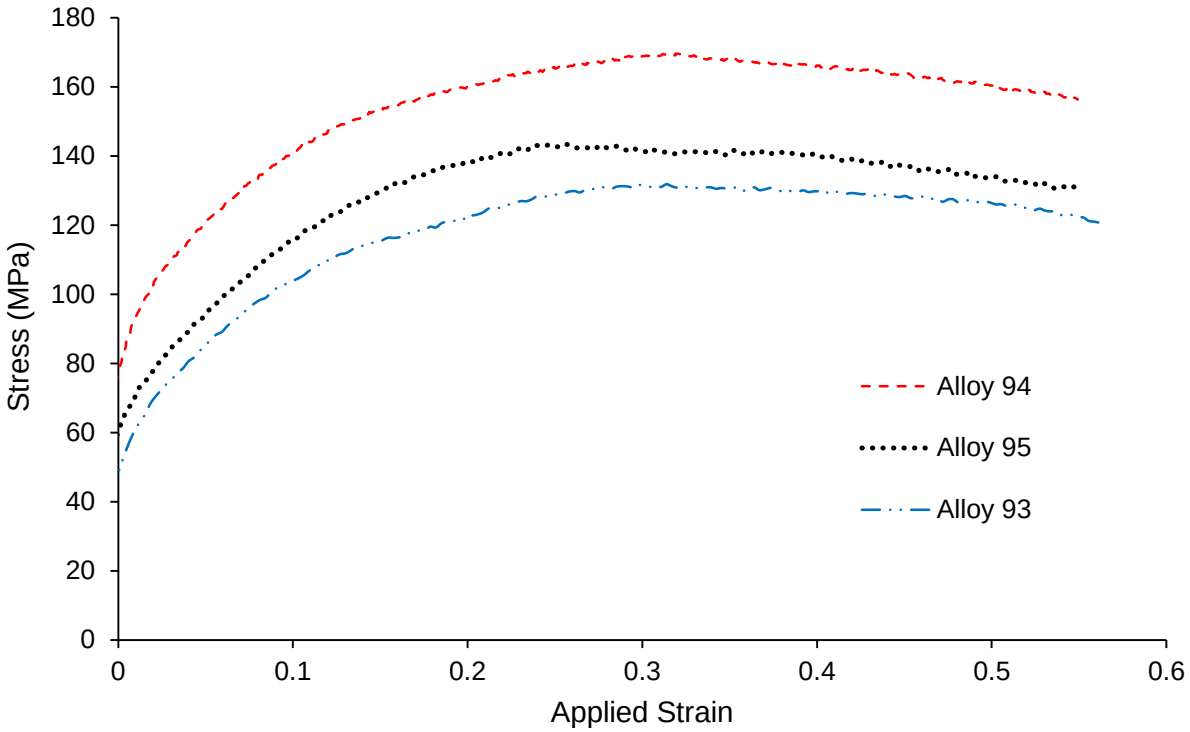

Figure 4.44 – Isothermal, iso-strain rate flow curves of the three novel alloys deformed at 435 ºC with a strain rate of 5/s.

4.6.2.2 Variation of Flow Characteristics with Processing Conditions

Temperature and strain rate have a great effect on the deformation characteristics for each of the alloys. For each alloy the low temperature and higher strain rate tests (high Zener-Hollomon parameter) displayed the greatest amount of work hardening at the start of the test and the highest peak stress. The strain at which the peak stress was reached also increased with increasing Z. Conversely, tests at low Z values reached peak stress at a lower value of strain. Therefore, the onset of flow softening started earlier and allowed for a longer period of dynamic recovery and recrystallisation.

4.6.2.2.1 Onset of Flow Softening

The peak stress represents the point at which hardening mechanisms, such as dislocation pile-up, and softening mechanisms, such as DRX coincide. However, Galiyev et al.[102] note that the peak stress does not occur at exactly the same point as the onset of DRX, but at a point slightly below. Poliak and Jonas[153] state that the onset of DRX occurs at a point on the flow curve where the stored energy is at a maximum and the dissipation rate is at a minimum. This location on the flow curve is defined by a point of inflection on a $\theta - \sigma$ plot ($\theta \equiv d\sigma / d\varepsilon$). To define the onset of flow softening in such a way requires the precise identification of certain points on the flow curve. Unfortunately, the current testing methods present too much noise in the data to identify such points accurately. However, the general trend in the onset of flow softening as a function of testing temperature and strain rate can be observed by simply identifying the approximate strain at which the peak stress occurs. Figure 4.45 shows a plot of the peak strain vs ln Z for each test carried out on alloy 94. It can be seen that there is a linear trend with the strain at which peak stress occurred increasing with increasing Z value. In line with previous studies[60, 154-157] this shows the dependence of the onset of DRX on time and temperature.

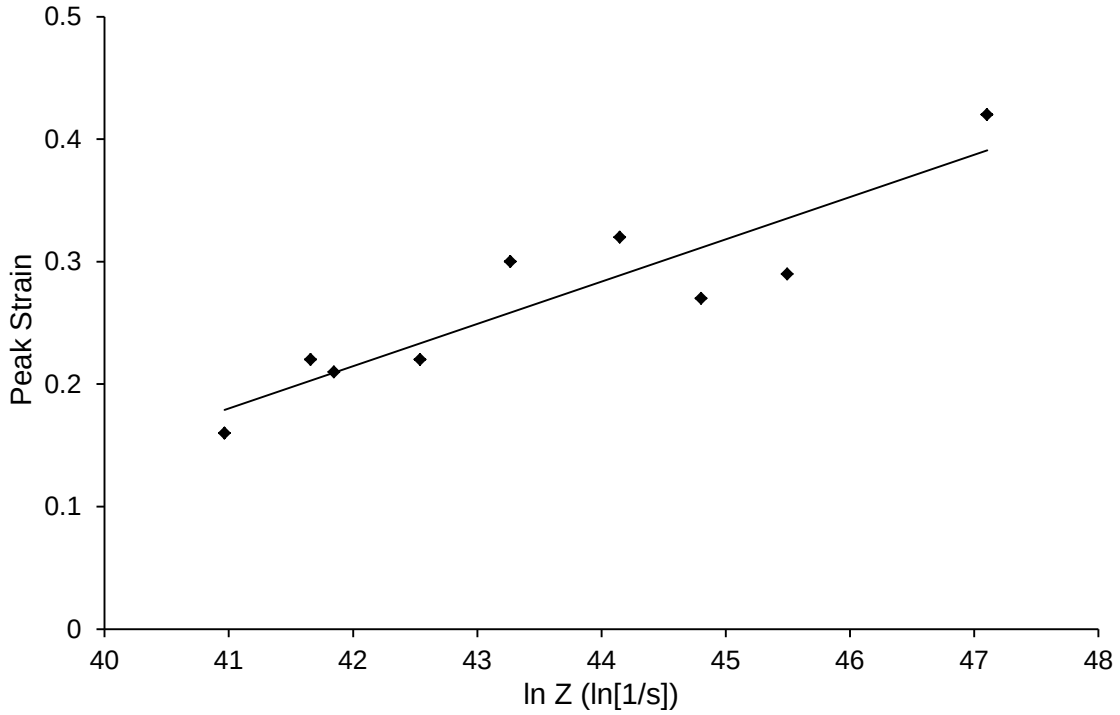

Figure 4.45 – Plot of ln Z vs the strain at which peak stress was reached for all tests carried out on alloy 94.

4.6.2.3 Activation Energy of Deformation (Q_{def})

The activation energy of deformation (Q_{def}) was calculated for each alloy in section 4.4.3.3 and the results are repeated in Table 4.13.

Table 4.13 – Values of Q_{def} calculated for the three novel alloys. Repeated from Section 4.4.3.3.

Alloy	**Q_{def} (kJ.mol^{-1})**
93	196.8
94	250.5
95	150.8

It can be seen that there is a large variation between each alloy. Values of Q_{def} in dilute magnesium alloys tend to be rather low. Similar values to the activation energy of self-

diffusion (134 kJ.mol^{-1})[2] are usually quoted. For base level alloys, such as AZ31, values of Q_{def} ranging from 112 to 175 kJ.mol^{-1} are reported in the literature[68, 129, 158-161]. Usually the value of Q_{def} would be expected to rise with increasing solute content[109, 162, 163]. For magnesium alloys with a high rare earth content, much higher values of Q_{def} have been observed. This is mainly attributed to the large atomic size difference between the rare earth elements and the magnesium matrix making diffusion of the solute atoms difficult. For example, Randman reported a Q_{def} value of 217 kJ.mol^{-1} for Elektron 675, a rare earth based magnesium alloy for high-end applications[109]. However, it is unusual for Q_{def} to be much higher than this figure in magnesium alloys.

The figures of Q_{def} reported in this study do not reflect the trend seen in previous work. Alloy 95 contains the highest level of alloy additions yet exhibits the lowest value of Q_{def} at 151 kJ.mol^{-1}. Alloy 94 exhibits an extremely high value for Q_{def} at 251 kJ.mol^{-1}, which is much higher than similar alloys studied in the literature. There are a number of issues arising when calculating Q_{def} using Davenport's method[125]. Firstly, the technique relies on the value of Q_{def} being constant throughout the test. For the current alloys the value of Q_{def} varied for each value of strain. The average of these figures was reported as the material's global value of Q_{def}. As an example, Figure 4.46 shows the variation of Q_{def} for alloy 93 across the full test matrix.

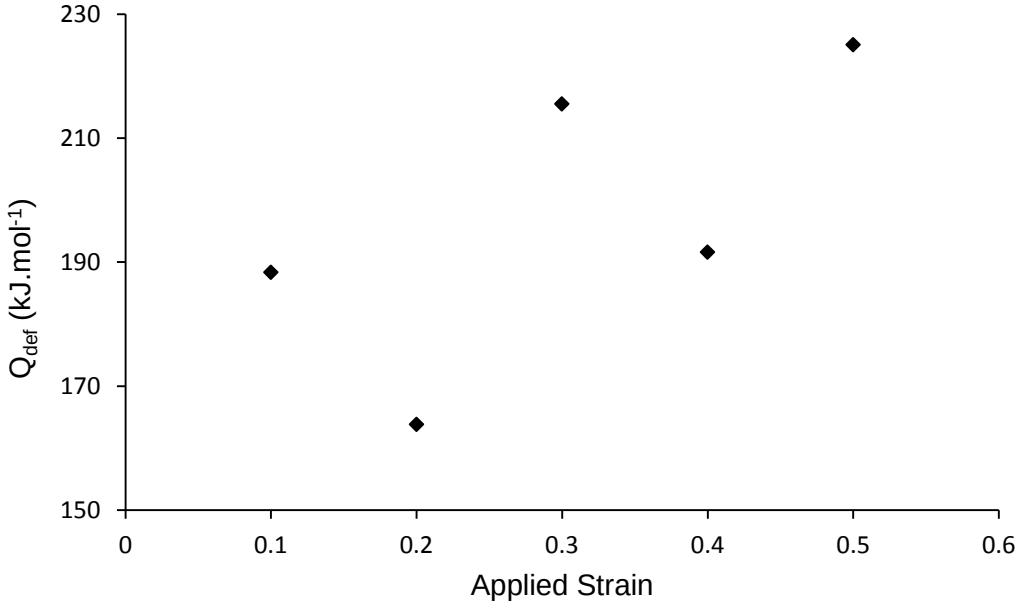

Figure 4.46 – Variation of Q_{def} for alloy 93 across the full test matrix.

The variation in activation energy suggests that different mechanisms of deformation are influencing the recorded figure. Another important point is that a significant volume fraction of second phase exists in each alloy. It will be recalled from section 4.1.2.1 that the volume fraction for alloy 95 is as high as 0.06. Little is known about the deformation behaviour of this brittle, eutectic phase. Ideally, Q_{def} should account for all of the deformation mechanisms active during the compression test. However, the current alloys should be considered as dual-phase materials. As such, the deformation characteristics of the two phases will be different with separate values of Q_{def}. It is also believed that the second phase has a significantly lower melting point than the matrix. Again, this will have a detrimental effect on the deformation behaviour as a whole. The second phase will be discussed further in Chapter 5.

It is clear that there are several mechanisms affecting the deformation behaviour during the compression tests that are not currently accounted for. Further work would be required to fully understand the effect of the second phase on the deformation behaviour of the current alloys. By extension, it should be noted, that the Davenport method[125] for calculating Q_{def} does not account for any significant second phases in a material. For this reason it would be necessary to incorporate the second phase deformation characteristics into the classic calculation. Only then could the material's value of $Q_{def,}$ be considered completely reliable.

4.6.2.3.1 Constitutive Behaviour

Originally it was planned to use the axisymmetric compression data to produce a series of constitutive equations to model the flow behaviour of each alloy. However, for the standard approach a broad range of tests is required. That is, a wide range of strain rates tested at a wide range of temperatures. It was shown in figure 4.20 that the process window of all three alloys was extremely narrow, particularly in terms of temperature. Table 4.8 shows the test matrix that was originally intended. However, the temperature range had to be severely reduced for the alloys to deform without failure. The final test matrix had a variation of just 25 ºC. It was also necessary to reduce the maximum strain rate of the tests to 5/s. Any constitutive behaviour produced with such a narrow range of data would be unreliable for modelling industrial processes. Testing at a wider range of temperatures may be possible by vastly reducing the strain rates. Unfortunately, the data produced by the TMC machine

becomes less reliable at very low strain rates due to significant noise. Potential future work could investigate the behaviour of the alloys deformed at strain rates within the creep regime.

As discussed in section 4.6.2.3 the values of Q_{def} cannot be entirely relied upon while the impact of the second phase is not fully understood. An accurate value of Q_{def} is essential for reliable constitutive behaviour development. Q_{def} is also used to correct the flow curves for temperature variations so that they can be used for constitutive behaviour. However, the uncertainty surrounding the current values of the activation energy of deformation calls into question the validity of such corrections.

4.6.2.4 Process Window

The limits of ductility were examined in section 4.4.4 by developing a process window. This visual representation clearly outlines the limited range of operation for the alloys. In terms of temperature, the lower limit of testing was 425 ºC. Tests carried out below this temperature generally failed due to shear fracture. The nucleation point for this fracture was always the thermocouple hole with cracks propagating at a 45º angle across the sample, as can be seen in Figure 4.18. The upper limit in terms of temperature was 450 ºC, with tests carried out above this limit showing signs of incipient melting, illustrated in Figure 4.19. The final test matrix was designed to stay well within these constraints for safety reasons. Consideration has to be given to the effects of adiabatic heating during the test with higher strain rates exhibiting a temperature increase of up to 45 ºC.

There is limited data on the process window of other magnesium alloys in the literature. AZ31 has been demonstrated to deform well within a temperature range from 350–550 ºC and strain rates from 0.0003–0.3/s[127]. Early tests on AZ31 during this project showed that deformation could be carried out up to 550 ºC with strain rates of 20/s without incident. Bhattacharya carried out plane strain compression testing on AZ31 with similar results while showing the lower limits of ductility to be as low as 350 ºC using strain rates up to 10/s[129].

Randman[109] showed that Elektron 675 had a more limited process window with the upper limits of testing being around 520 ºC at strain rates of up to 10/s. The lower temperature limit

for successful testing was observed to be at 400 ºC with strain rates of 1/s or below. It was suggested that the high rare earth content, compared to the AZ series of alloys, increased the strength of the material. This increase in strength prevented slip from occurring at lower temperatures. Although the current alloys also contain rare earths, they are at much more dilute levels than in Elektron 675. Therefore, the limits of ductility observed in these alloys must occur for different reasons. Slooff et al.[149] investigated the processing limits of several AZ series alloys. It was noted that as the aluminium content was increased, the upper temperature limit of testing decreased. This was due to a significant volume fraction of a β phase existing in the alloys of higher solute content. It was observed that the β phase had a lower melting point than the matrix material. It is believed that a similar effect is operating in the current novel alloys. The second phase softens and melts at much lower temperatures than the matrix. The second phase is also brittle at lower temperatures, thereby lowering the overall ductility of the alloys. These effects severely retard the viable processing conditions for all three alloys.

Section 4.4.5 demonstrates the effect the limited process window had when attempting a typical industrial rolling regime. It is highly unusual for industrial rolling to be carried out isothermally. The testing in the current work relied on residual heat being contained in the rolls after carrying out rolling of AZ31 billets. Typically, the temperatures of the rolls in an industrial setting would be in the range of 70–120 ºC[1]. Although the novel alloys were heated to the optimal temperature of 450 ºC, so that they would be approximately 430–435 ºC when reaching the rolls, the temperature difference of the rolls proved to be too great. Figures 4.23–4.25 show the catastrophic failure of each of the alloys under these conditions. It is interesting to note that the alloys with the higher volume fraction of second phase, 94 and 95, crumbled completely. Alloy 93, with its lower volume fraction of second phase, produced a textbook ‘alligator’ rolling defect after the second pass at a 5% reduction. The cause of the failures can be inferred by a simple visual inspection of the rolled pieces. At the outside edges of the rolled material, the failure mode was brittle fracture. This was caused by the sudden drop in temperature at the contact edges cooling the local material. The second phase in this region, present at grain boundaries and triple points, became brittle and intergranular cracking occurred. The mode of failure at the centre of the rolled pieces changed to ductile fracture and incipient melting. The deformation at the centre of the material causes adiabatic

heating, raising the temperature enough to cause the second phase in this region to melt. Frictional forces act tangentially where the outer edge of the sample is in contact with the rolls. This causes tensional stress at the centre of the piece as it exits the rolling mill. The combination of soft matrix material and melted second phase cause the rolled piece to tear apart causing the alligator effect observed in alloy 93. In alloys 94 and 95 the higher volume fraction of second phase aids the crack propagation at the outer contact surface of the rolled material. The brittle fracture continues to propagate causing complete failure, with the sample crumbling as they exit the rolling mill.

Originally it was intended to compare the deformation behaviour of the novel alloys with the base-level AZ31 alloy. However, the constraints in the process window mean that any direct comparison is meaningless. Figure 4.22 illustrates how well AZ31 performs when rolled to a 2 mm thick sheet. The material was rolled at a temperature of 400 ºC with cold rolls. After several passes a desirable, fully recrystallised microstructure was realised. The only way of achieving the same results with the novel alloys would be to roll isothermally. This would involve rolling within a furnace capable of maintaining a constant temperature within the range of 425–450 ºC. Any such rolling regime would be prohibitively expensive, which would conflict with the intended cost-effectiveness of the alloys. It is common practice to keep the strain rate high when rolling magnesium alloys to minimise the contact time and therefore heat loss, with the rolls. However, the bimodal failure observed would prevent such measures being useful. The increased strain rate would only increase the adiabatic heating at the centre of the sample causing melting of the second phase.

4.6.3 Post-deformation Microstructures

Section 4.5.2 details the development of the microstructures with varying processing conditions. It was demonstrated that the final microstructure varies considerably under different strain rates and temperatures (varying Zener-Hollomon parameter) with different types of dynamic recovery and recrystallisation being observed. This shows that the processing condition directly controls which mechanism dominates during plastic deformation. Generally speaking, the volume fraction of dynamically recrystallised (DRX) grains increased with decreasing Z. However, the largest volume fraction of recrystallised

grains occurred at the highest temperature and strain rate of the standard test matrix (450 ºC with a strain rate of 5/s). With higher volume fractions of DRX, the global texture of the sample became more random, weakening the otherwise strong basal texture. It was also shown that the processing condition strongly affected the final recrystallised grain size. A strong linear trend existed with the DRX grain size decreasing with increasing Z. The following section will discuss the various mechanisms of recovery and recrystallisation in operation. The volume fraction of DRX grains, DRX grain size and effect on final texture will also be explored. The main forms of DRX in magnesium alloys fall into two categories: discontinuous DRX (DDRX) and continuous DRX (CDRX). Of these two categories, several variations in mechanism exist and will be discussed in the following section. The three alloys exhibited the same general mechanisms of DRX at any given value of Z. Therefore, representative data, for all of the alloys, is given where appropriate.

4.6.3.1 Dynamic Recovery and Dynamic Recrystallisation

Several types of restoration mechanism were observed during this study. In line with section 4.5.2 the mechanisms will be discussed in terms of Z value, with the lower values first. Figure 4.26 showed a sample of alloy 93 deformed at 465 ºC with a strain rate of 0.5/s. Although this is outside of the standard test matrix used for the flow behaviour analysis, it is useful for studying restoration at a very low value of Z. At these conditions there is evidence of discontinuous dynamic recrystallisation (DDRX) being active. Figure 4.47 shows a different area of the same sample. White arrows indicate grain boundaries that exhibit serration and bulging. This phenomenon has been observed by many authors and believed to be an initiation point for DDRX[74, 100, 102, 106, 114, 116, 164, 165]. New grains nucleate and grow with high angle grain boundaries. Pre-existing high angle grain boundaries typically act as nucleation points for DDRX. This discontinuous recrystallisation mechanism is often observed in magnesium alloys with a coarse grain size, leading to a ‘necklace-like’ structure surrounding parent grains. DDRX can only activate when the grain size is large enough to allow for heterogeneous slip. Migration of original grain boundaries, marked by the tell-tale bulging, reduces the dislocation density in the grain boundary region. The effect of this reduction is a distinct peak in the flow curve followed by flow softening. Furthermore, the DRX grains observed in this sample had relatively similar orientations to the parent grains.

This indicates that a standard DRX mechanism is at work. According the literature most standard forms of DRX (DDRX and CDRX) have little effect on the texture of HCP metals[112, 166-169]. However, the pole figures in 4.37 suggest that the deformed samples do exhibit a slight randomisation in texture due to DRX.

Figure 4.34 shows the same sample with subgrain boundaries added to the EBSD map in white. The existence of these subgrain boundaries would indicate that CDRX is also active. CDRX is, strictly speaking, a recovery mechanism, as the initiation of the phenomenon is caused by the rearrangement of dislocations into cells and subgrains. Eventually the subgrains will rotate to form high angle boundaries, creating fully recrystallised grains. The formation of CDRX grains is progressive unlike DDRX that requires nucleation sites along pre-existing grain boundaries. Unlike DDRX, CDRX causes little in the way of grain boundary migration and therefore dislocation density is not significantly reduced[170]. For this reason the flow curve does not experience the same amount of flow softening as with DDRX.

The flow curve for this sample (Figure 4.48) does not show the same distinct peak observed in previous studies where DDRX has been the dominant mechanism of recrystallisation[170-172]. However there is still a distinct period of flow softening. The evidence suggests that both DDRX and CDRX are active mechanisms at this temperature and strain rate.

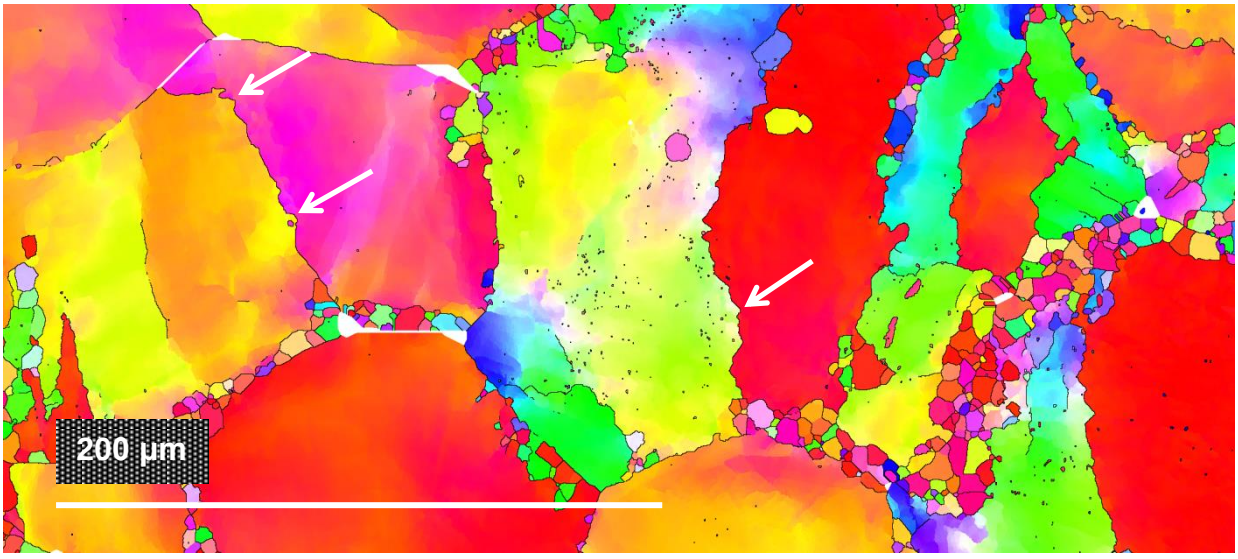

Figure 4.47 – EBSD map (IPF colouring) showing a sample of alloy 93 deformed at 465 ºC with a strain rate of 0.5/s. White arrows indicate the presence of grain boundary bulging.

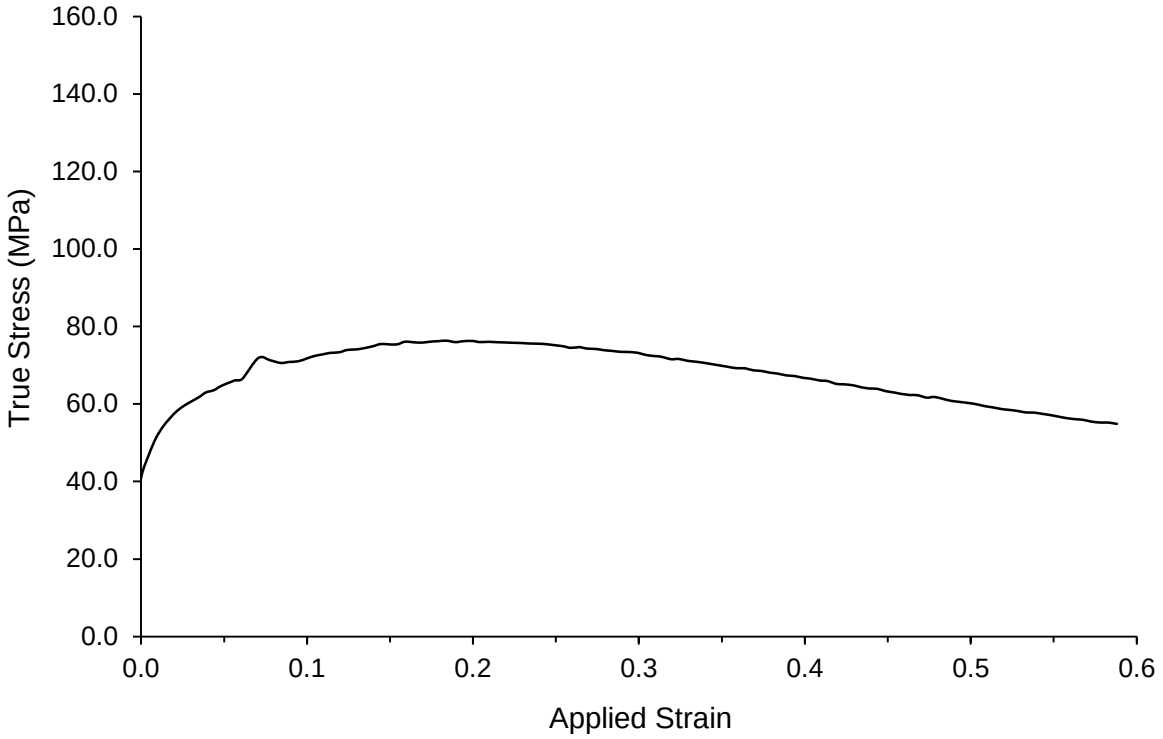

Figure 4.48 – Flow curve of alloy 93 deformed at 465 ºC with a strain rate of 0.5/s.

Figure 4.27 gives an example of alloy 94 deformed at 450 ºC with a strain rate of 0.5/s. The sample exhibits similar recrystallisation characteristics. Again, several boundaries show evidence of bulging and serration suggesting that DDRX is in operation. Adding subgrain boundaries to the image (Figure 4.49) it can be seen that there is a higher amount of subgrain activity. At these processing conditions, subgrain formation spreads throughout the parent grains and is especially active in areas of high DRX. Qualitatively, it can be inferred that CDRX is more active than DDRX at this lower temperature (higher value of Z). Similar subgrain formation was observed in each of the alloys under the same processing conditions.

Figure 4.28 depicts an EBSD map of alloy 95 deformed at 450 ºC with a strain rate of 5/s (middle of the test matrix in terms of Z). At these conditions the sample appears to be nearly fully recrystallised. This is the highest level of DRX observed in the current work. The sample exhibited little evidence of grain boundary bulging associated with DDRX. Figure 4.35 shows that there is also very little subgrain formation in the unrecrystallised parent grains suggesting that CDRX activity was minimal. The misorientation distribution displayed

in Figure 4.42 shows that, at these conditions, a distinct randomisation of texture was observed. Figure 4.41 shows the DRX grains only within the sample. There is a strong correlation to the theoretical random. The weakening of the basal texture to such an extent would be unlikely if only standard forms of DDRX and CRDX were operating. As previously mentioned only a slight weakening of the basal texture would be expected with these mechanisms of recrystallisation. Previous authors have reported that the only significant DRX mechanism to affect texture is continuous dynamic rotation recrystallisation (CDRRX)[60, 102, 109, 111, 112]. CDRRX was described in section 5.3.5.3.4 as the formation of dislocations caused by a rotation of the material adjacent to the grain boundary. As the crystal structure rotates under deformation, cells, subgrains and eventually fully recrystallised grains form[60]. CDRRX is unique due its potent effect in weakening texture. The high level of randomisation caused at these deformation conditions would suggest that CDRRX is the dominant DRX mechanism active.

Figure 4.49 – EBSD map (IPF colouring) showing a sample of alloy 94 deformed at 450 ºC with a strain rate of 0.5/s. Subgrain boundaries are superimposed in white.

At the highest Z value (see Figure 4.30) the form of DRX changes again. At these conditions the microstructure is dominated by dynamically recrystallised twins. This type of recrystallisation occurs with the same mechanism as CDRX, but the dislocation pile-up

occurs in and around twinned material. The twin boundaries act as stress concentration zones, allowing further slip systems to activate. As the dislocation density increases, cell structure and subgrains start to form. As with standard CDRX, these subgrains will eventually develop into fully recrystallised grains. Although less common, some previous workers have examined the effect of twinning on the DRX behaviour of magnesium alloys[106-108]. Park et al.[108] successfully exploited the twin-induced CDRX phenomenon to improve the tensile properties of extruded AZ31 with a cold pre-forging process while observing a slight weakening of the basal texture. It is generally accepted that high strain rates and low temperatures (high Z) favour the development of twinning in HCP metals due to the limited number of available slip systems. By extension, at higher strains, these conditions promote the development of twinning-induced CDRX grains. Twinning-induced CDRX is commonly observed to occur by primary twins being intersected by low angle grain boundaries and double twinning[104, 113]. Another observation is that the intersection of primary twins can create a new crystallite, bordered by the twin boundaries. This crystallite acts a nucleation point for further DRX[107, 113]. However, this intersection of primary twins was not observed in the current work.

As there is little in the way of texture randomisation with the CDRX mechanism, it is possible to identify the type of twin that twinning-induced CDRX grains originate from. It is common to identify twins by measuring their characteristic misorientation angle with the grain matrix[72]. By looking for specific peaks in a misorientation distribution plot, common twin types can be identified. As the randomisation of texture is weak in CDRX the same technique can be employed. Figure 4.50 shows misorientation angle plot of the twin-induced CDRX grains observed in Figure 4.30. The notable peaks are clustered around 35–45º, 50–60º and 80–90º. The first peak corresponds with a $\{10\bar{1}1\}$-$\{10\bar{1}2\}$ double twin parent that would have a misorientation with the matrix of 38º. The second peak would fit with a $\{10\bar{1}1\}$ primary twin parent that would have a misorientation of 56º with the matrix. Finally, a peak around 80–90º would suggest the recrystallisation of a $\{10\bar{1}2\}$ type parent twin that would have originally had an 86º angle of misorientation. Although there is another narrow peak at approximately 72º, this could not be identified with any particular type of parent twin reported in the literature.

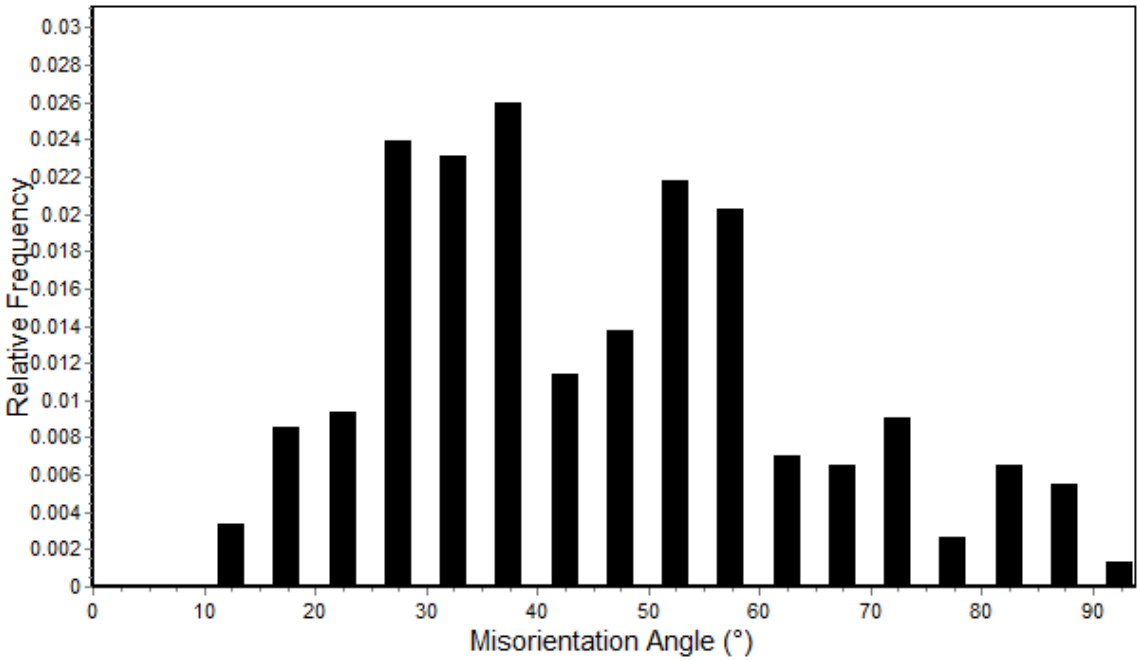

Figure 4.50 – Misorientation angle plot of twin-induced CDRX grains in a sample of alloy 94 deformed at 425 ºC with a strain rate of 5/s.

It is interesting to note that as well as twinning induced CDRX, there is significant evidence of recovery and standard CDRX occurring in the twinned regions. Figure 4.33 shows the sub-structure existing in the sample. Subgrains started to form along the recrystallised twins. Upon further straining, these subgrains would have developed into fully recrystallised grains. Eventually, by further CDRX, the entire grain would be consumed. Many of the CDRX twins exhibit a single DRX grain across their width at this strain. This would suggest that the environment within the twin favours CDRX development. That is, grains will recrystallise preferentially within the twin boundaries. It is believed that the narrow morphology of twins leads to a higher build-up and entanglement of dislocations than in the grain matrix. Further strain is required to provide the driving force for further CDRX outside of the twin boundaries.

For the three alloys studied in the current work there seems to be a correlation between the Zener-Hollomon parameter and the dominant mechanism of dynamic recrystallisation. At low values of Z a significant amount of grain serration and bulging was observed. This would

point to DDRX being active at these processing conditions. At the middle of the test matrix, in terms of Z, there is little evidence of DDRX being active. At these conditions it is believed that CDRRX is the dominant mechanism of DRX. This mechanism weakens the texture of the material considerably through large rotations of the crystal lattice around grain boundaries. Finally, at the highest Z values, twinning induced CDRX occurs. It stands to reason that these processing conditions favour the development of twins early on in the deformation due to limited slip systems being active at the lower temperature. Twin boundaries act as barriers to dislocation motion in the same way as grain boundaries. By dislocation pile-up, the substructure begins to develop leading to subgrain formation and finally, fully recrystallised grains form. Observations in the current work indicate that twinning induced CDRX occurs preferentially within the twin boundaries with further strain being necessary for DRX to occur outside of the twin. Further activity was observed in the form of CDRX occurring around the DRX twins. It should be stated that, although certain types of DRX may be dominant at a given value of Z, other mechanisms may still be active. When one mechanism dominates it often masks any other mechanisms that may be active. Hence, even if a particular mechanism of DRX is not observed, its activity cannot, conclusively, be ruled out entirely. The DRX mechanisms observed in the novel alloys at different levels of Z are summarised in Table 4.13.

Table 4.13 – Dominant DRX mechanisms observed in terms of Z value.

Z Value	**Major Observed DRX Mechanisms**
Low	DDRX
Middle	CDRRX
High	Twin-CDRX + CDRX

4.6.3.2 Recrystallised Fraction

The recrystallised fraction was analysed in section 4.5.3. Figure 4.31 shows the relationship of the recrystallised fraction with Z. It can be seen that there is not a direct relationship with Z alone. When the tests are grouped into temperature a clearer trend emerges. Within each individual temperature group the recrystallised fraction increases linearly with increasing strain rate. This contrasts with some previous studies where the recrystallised fraction generally decreased with increasing Z[109, 173, 174], whereas other work has shown an general increase in recrystallised fraction with an increase in Z[175, 176]. The large amount of scatter is common in these studies when comparing recrystallised fraction directly with Z. This suggests that a direct relationship between Z and the recrystallised fraction is difficult to demonstrate. From the current work, when referring to Figure 4.31, it appears that temperature is the dominant, rate-controlling factor, in terms of the recrystallised fraction.

It will be recalled from section 4.6.3.1 that a distinct change in the DRX mechanism occurs on changing Z value. It is unclear at this time which mechanism of DRX causes the highest recrystallised fraction. In the current work, the highest recrystallised fraction observed was during tests at 450 ºC with a strain rate of 5/s. At these conditions CDRRX appears to be the dominant DRX mechanism. However, as previously discussed, other DRX mechanisms may still be active, but less apparent. Therefore the highest levels of DRX cannot be attributed to a single recrystallisation mechanism.

Table 4.9 shows the maximum achievable recrystallised fraction for the three novel alloys with the testing regime used. Alloy 95 exhibited the greatest volume fraction of DRX grains at 0.64, with alloys 93 and 94 exhibiting DRX volume fractions of 0.25 and 0.19 respectively. It is tempting to compare the recrystallised fraction to the activation energy of deformation (Q_{def}) in respect to each alloy. That is, for the three alloys tested, the maximum recrystallised fraction achievable is higher with a lower value of Q_{def}. It is plausible that the onset of DRX would occur earlier in the test for alloys with a lower Q_{def}, allowing longer for the microstructure to recrystallise. However, as discussed in section 4.6.2.3, the current values of Q_{def} cannot be accepted as truly accurate. While questions remain over the involvement of the

second phase during deformation, direct comparisons between Q_{def} and the microstructural development must be withheld.

4.6.3.2.1 Recrystallised Grain Size

Section 4.5.3.1 examined the recrystallised grain size of the three alloys after deformation. The general trend observed in all of the alloys was a decrease in the final recrystallised grain size with increasing Z value. The trend is in keeping with most studies into the recrystallisation behaviour of magnesium alloys[60, 100, 102, 109, 113-115, 165, 170]. At lower values of Z the high temperatures ease grain boundary mobility and the low strain rates allow time for the grains to coarsen. As the value of Z increases, grain boundary mobility is drastically reduced and the faster strain rates limit the time in which grains can grow. The deformation tests carried out in this work included a water quench immediately after the test to freeze the post deformation microstructure. Future work could investigate the effect of a post deformation anneal on the final DRX grain size.

Once again, the mechanism of DRX will affect the final recrystallised grain size. Referring to section 4.6.3.1, tests at the lower values of Z exhibited DDRX. This form of DRX causes the nucleation of entirely new grains, typically at grain boundaries, followed by a prolonged period of grain growth. Therefore, a larger final DRX grain size would be expected. As Z increases, the active mode of DRX changes to a continuous mechanism. CDRX mechanisms rely on the development of subgrain boundaries. For this reason, the initial subgrain size controls the final DRX grain size. Once the new grains have formed, further CDRX occurs by the continuous movement of dislocations forming new substructure. The mobility of the grain boundaries is restricted in this situation and grain growth is minimal. Again this correlates well with the reduction in final recrystallised grain size with increasing Z value observed in this work and the work referenced above.

Tables 4.10 and 4.11 list the average DRX grain sizes for each alloy at the lowest value of Z and the highest value of Z respectively. It can be seen that there is little difference in grain size between the different alloys. The slight differences that exist are within the 95% confidence limits and can therefore be classed as negligible.

4.6.3.3 Texture

Section 4.5.5 investigated the variation in texture with different processing conditions. When referring to the pole figures displayed in Figure 4.36, it can be seen that the global texture of the samples deformed through a range of Z values was reasonably constant. The deformed samples from all three alloys exhibited strong basal textures with all processing conditions. The strong basal texture after hot compression is common in all HCP metals with magnesium being no exception[68, 87, 109, 127, 177]. The basal texture is caused by mechanical twining in the early stages of deformation[60, 100, 117, 143, 177]. There is a distinct split in the basal texture. The split is highest (34º) at the lowest value of Z and decreases to 22º at the highest value of Z. This split in the basal texture is commonly observed in magnesium alloys that have undergone deformation[117, 166, 178]. However, the split is usually less pronounced (lower than 20º) than observed in the current work. It is believed that the activation of <c+a> slip causes the split in texture observed, occurring after the grains have reordered into a purely basal texture in the early stages of deformation[112, 117, 166, 178-181].

Figure 4.37 shows pole figures of the DRX grains only within the same three samples deformed at different Z conditions. All three pole figures display a distinctly weaker basal texture than the global pole figures in 4.36. This contradicts the discussion in section 4.6.31 which suggests that significant randomisation in texture only occurs when CDRRX is the dominant recrystallisation mechanism. In that case, only Figure 4.36b would be expected to show the weaker basal texture as this represents the correct processing conditions for CDRRX to dominate (450 ºC with a strain rate of 5/s). However several other occurrences can weaken the basal texture, such as: grain boundary sliding, shear band formation and reduced twining in the early stages of deformation in deformation at low values of Z[100, 109, 111, 123, 182]. When investigating the misorientation distribution of the DRX grains, only the tests carried out at 450 ºC with strain rate of 5/s closely matched the Mackenzie[141] plot of theoretical random orientation (see Figure 4.41). In this instance, there is a good correlation with CDRRX having a strong effect on the randomisation of texture as it was only with these testing conditions that it was observed to be active.

4.7 Summary

This chapter has given an in depth analysis of the deformation behaviour of the three novel magnesium alloys. The general flow behaviour shows a similar trend to previous work in that it rises to a peak stress upon deformation, followed by a prolonged period of flow softening due to dynamic recrystallisation. The process window is disappointingly narrow for these alloys when compared to other, base-level alloys, such as AZ31. The likely culprit for this is a significant eutectic second phase existing at grain boundaries and triple points in each of the alloys, to varying degrees. Further work is required to fully understand the impact of this second phase in order to develop full, reliable constitutive behaviour.

The post-deformation microstructures were examined and it was revealed that the alloys have a strong basal texture, in line with the majority of previous magnesium alloy deformation studies. The change in recrystallisation mode was investigated as a function of the Zener-Hollomon parameter (Z). It was discovered that several forms of dynamic recrystallisation are active (continuous and discontinuous), dependant on the deformation conditions. The particular form that is active at any one time can be linked directly to the Z value. The resultant recrystallised fraction could not be linked to Z in such a direct way. Temperature appears to be the largest rate-controlling variable during deformation. However, strain rate also has an effect. The largest recrystallised fraction occurred when deformation was carried out at the highest temperature and highest strain rate (equivalent of a Z value in the middle of the tested range). The final recrystallised grain size is directly dependant on Z with finer grain sizes being developed at higher values of Z. It is believed that a combination of recrystallisation mode and temperature cause the coarser grain sizes at low Z values. The higher temperatures at low Z values allow for improved mobility of grain boundaries which assists with grain growth. Although largely basal, the change in recrystallisation mode also affected the final texture of the alloys to varying degrees. The recrystallisation mechanisms active when both temperature and strain rate are highest develop the largest randomisation of texture observed in each of the alloys.

Throughout this chapter a common theme has been the unknown effect of the second phase on the performance of the alloys. To broaden the prospective process window the second

phase needs to be further understood. The following chapter will briefly analyse the chemistry of the three alloys and examine their thermal behaviour. By further understanding the thermal behaviour of the alloys, a recommendation can be made in respect of maximising the process window.

5. Results and Discussion II

5.1 Analysis of the Second Phase

5.1.1 Introduction

Throughout Chapter 4 the second phase appearing at grain boundaries and triple points was highlighted as having a detrimental effect on the deformation behaviour of the three novel alloys. This eutectic phase has a low melting point and is brittle when solid. It is believed that the phase causes two major failures to occur during hot deformation of the alloys. Firstly, at the lower end of the process window in terms of temperature, the phase shears readily, causing brittle fracture to occur. This causes intergranular fracture across the sample, as documented during the rolling trial in section 4.4.5. At slightly elevated processing temperatures, taking into account adiabatic heating, incipient meting occurs as the phase reaches its solidus, causing the type of failure observed in Figure 4.19. It appears that the phase remains after the solution heat treatment of the alloys with negligible change after prolonged treatments (see table 4.5).

For the alloys to be viable in an industrial setting, all efforts must be made to reduce the volume fraction of the second phase, thereby reducing the detrimental impact during deformation. First it must be ascertained why the phase exists after the solution heat treatment. This section aims to provide further insight into the composition of the second phase and its effect on the alloys as a whole. Energy dispersive X-ray (EDX) spectroscopy is used to qualitatively assess the composition of phase. The solidus of the phase is measured using differential scanning calorimetry (DSC). Further on, thermodynamic modelling software (Thermo-Calc) is used to model the phase behaviour of the current alloys as well as making recommendations for adjustments to their compositions.

5.1.2 Energy Dispersive X-ray Spectroscopy

A JEOL 6400 SEM operating at 20 kV was used for chemical analysis. An Oxford Instruments ISIS EDX detector with the INCA software package was used for compositional information. To maintain an acceptable level of accuracy, a cobalt standard was used to calibrate the machine. Although EDX is reasonably accurate when using a known standard for calibration, there is still a level of error introduced by variables in the sample preparation, oxidation and data collection of the detector. For this reason, the EDX data quoted in this work is for qualitative assessment only. For each measurement, three areas were used with the average being recorded, along with the standard deviation of the solute additions.

Firstly, bulk analysis was carried out on each of the alloys to compare to the compositions reported in Table 4.1. The SEM was set at 200x magnification and the ISIS software was used to scan the full area. For each alloy, the recorded composition of the bulk scan was within 6% of the quoted composition (see Table 4.1). The software was then set to scan a large area of the second phase. Table 5.1 shows the composition of the second phase in each alloy in weight per cent terms. Zirconium was not detected in the second phase. It is likely that, due to the very dilute amount present in the alloys, any detected zirconium was masked by the background noise in the EDX spectra.

Table 5.1 – Weight percentage of major alloying additions present in the second phase. Standard deviation of solute additions in brackets.

	Composition of Second Phase Area (Weight %)			
Alloy	**Mg**	**Zn**	**Y**	**Nd**
93	65.12	13.18 (±1.08)	3.40 (±0.51)	18.29 (±2.38)
94	60.67	13.61 (±2.01)	3.68 (±0.42)	22.03 (±3.10)
95	56.61	15.23 (±2.36)	5.51 (±0.92)	22.64 (±2.82)

As a comparison, another EDX scan was taken from a selected area within the grain matrix of each alloy, away from the second phase. The composition of the matrix area of the alloys is displayed in table 5.2.

Table 5.2 – Weight percentage of major alloying additions present in the matrix. Standard deviation of solute additions in brackets.

	Composition of Matrix Area (Weight %)			
Alloy	**Mg**	**Zn**	**Y**	**Nd**
93	97.61	1.08 (±0.16)	0.52 (±0.05)	0.78 (±0.06)
94	96.97	0.90 (±0.21)	0.68 (±0.04)	1.44 (±0.23)
95	95.87	1.11 (±0.20)	1.39 (±0.32)	1.62 (±0.09)

5.1.3 Differential Scanning Calorimetry

A Perkin-Elmer twin furnace differential scanning calorimeter (DSC) with the Pyris Software package was used to assess the solidus temperature of each alloy. Small samples, weighing ~3 mg, were used for each analysis. The sample was placed within an alumina pan into one of the furnaces. An empty pan was placed into the remaining furnace as a reference. The sample and reference pan were heated at a rate of 10 ºC/min up to 650 ºC. The Pyris software monitored the heat flow in mW into the furnaces and recorded any variations. Changes in state due to a phase melting were recorded on a temperature vs heat flow curve. Figure 5.1 shows an example of a DSC trace for alloy 93. A clear peak in the trace occurs as the second phase melts. The start of this curve marks the onset of melting for the phase. The onset of melting is important in understanding the behaviour of the alloy during the solution heat treatment. Each DSC scan was repeated in triplicate with the average value being recorded. The temperatures at which the onset of melting occurred in the second phase for each alloy are listed in Table 5.3.

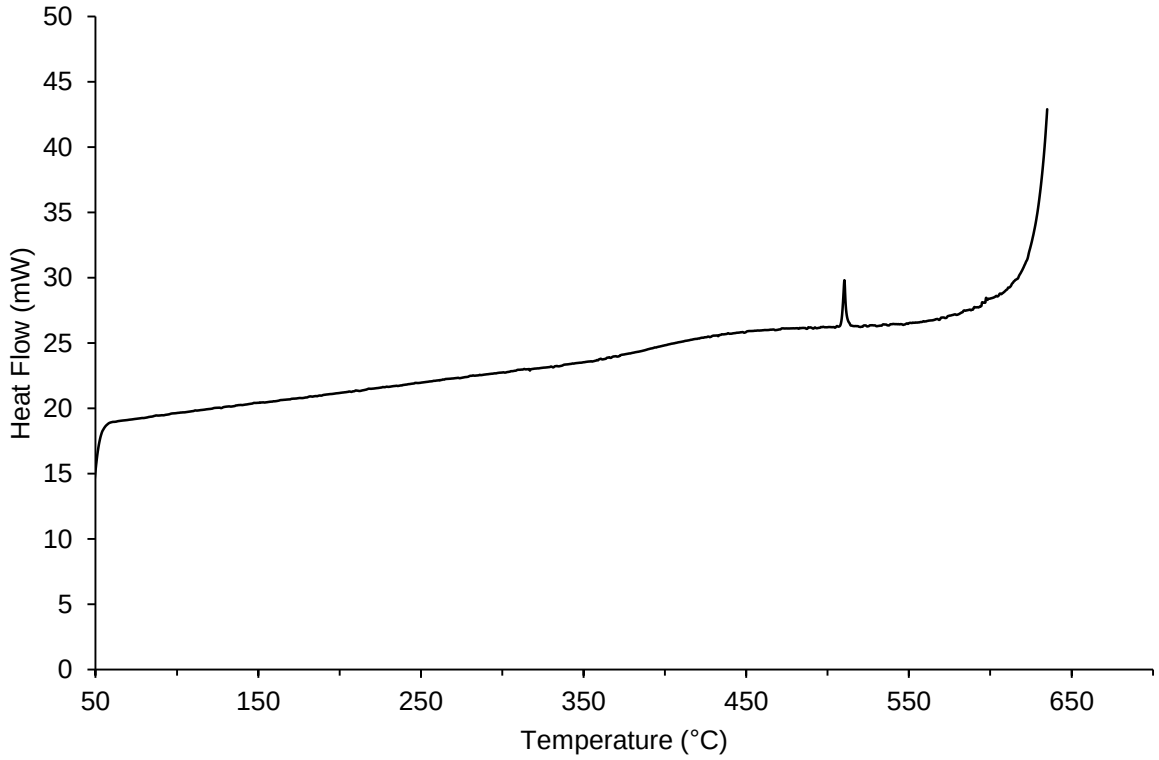

Figure 5.1 – DSC trace of alloy 93 heated to 650 ºC at a rate of 10 ºC/min.

Table 5.3 – Onset of melting for the second phase in each novel alloy.
Standard deviation in brackets.

Alloy	Onset of Melting in Second Phase (ºC)
93	509.2 (±1.1)
94	510.5 (±1.0)
95	510.1 (±1.3)

To investigate the effect of the heating rate on the onset of melting, the experiments were repeated at a rate of 1 ºC/min. No statistically significant variation in the melting behaviour of the second phase or of the bulk material was observed.

5.1.4 Software-based Analysis of Phase Transformations

Thermo-Calc is a software package that employs a broad database of thermodynamic reactions to accurately calculate phase changes within an alloy of nearly any composition. By inputting the composition of a material, various predictions about its reaction at different temperatures can be forecast. In the context of the current work, the low melting point second phase is of particular interest. Thermo-Calc was used to corroborate the DSC findings reported in section 5.1.3. For the analysis, the nominal composition was entered for each alloy and an equilibrium step diagram was produced. Figure 5.2 shows an example step diagram for alloy 94. The diagram shows the volume fraction of a predicted phase present (y-axis) at a given temperature in ºC (x-axis). The phase of interest for the novel alloys is the liquid phase, marked in green and labelled with number 3. The point where this line crosses the x-axis effectively shows the onset of melting for the phase. The software can be used to pinpoint the temperature where this phase transformation occurs. Table 5.4 shows the predictions for the onset of melting of the second phase from the Thermo-Calc software. There is a very close correlation between the onset of melting calculated by DSC in section 5.1.3 and the predicted figures from the software.

Table 5.3 – Onset of melting predicted by Thermo-Calc for the second phase in each novel alloy.

Alloy	Onset of Melting in Second Phase (ºC)
93	507.4
94	509.5
95	509.9

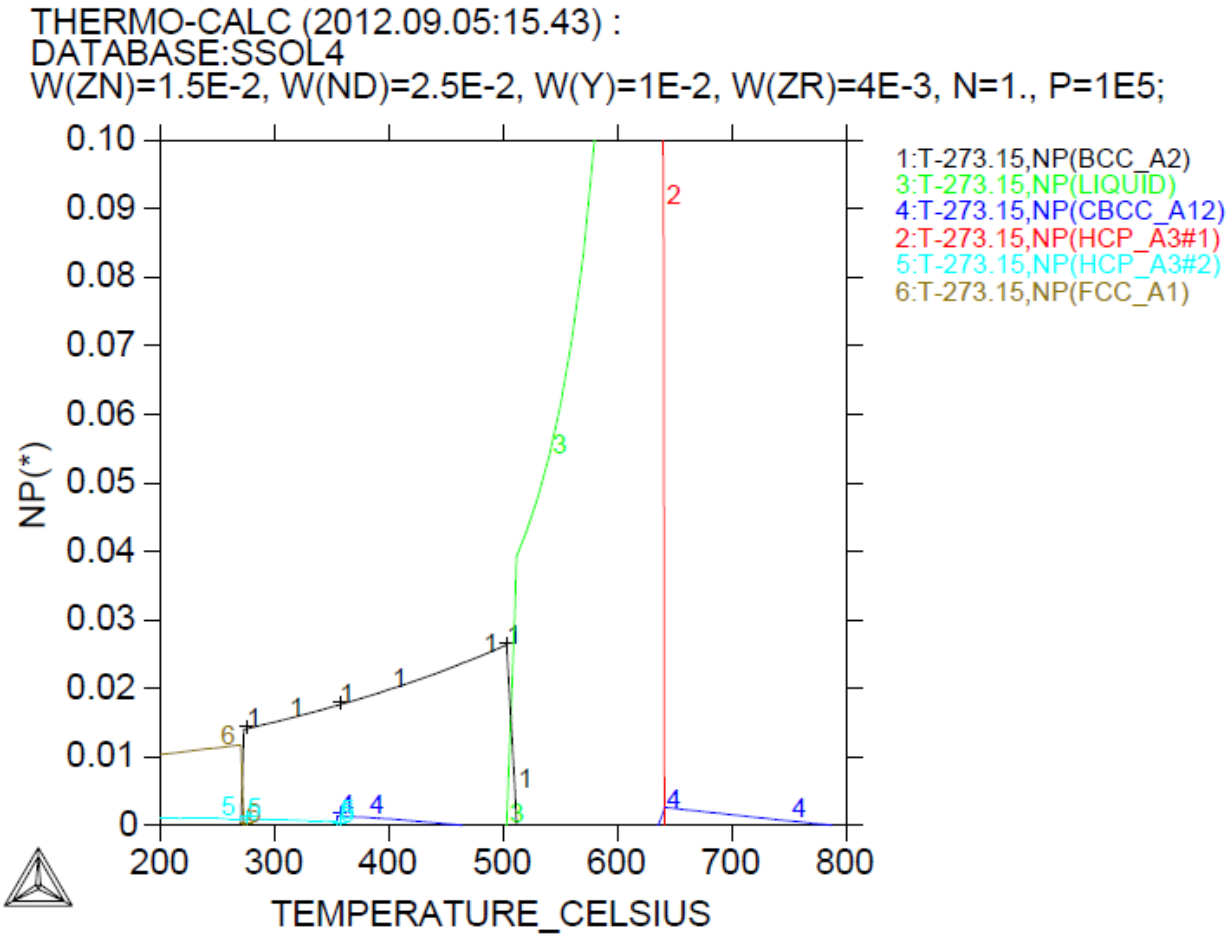

Figure 5.2 – Equilibrium step diagram for alloy 94.

5.1.5 Discussion

Table 5.1 shows that there is a significant amount of the solute additions tied up in the second phase. The effect of this can be seen in Table 5.2 where a distinct weakening of the solute additions in the matrix can be seen when compared to the nominal compositions for the alloys quoted in Table 4.1. It has been mentioned several times that the second phase has a deleterious effect on the mechanical properties of the three alloys. It was reported in sections 5.1.3 and 5.1.4 that the solidus of the second phase is between 508.4–510.5 ºC depending on alloy composition. As the solution heat treatment is carried out at 525 ºC, the second phase is completely liquid while the remaining material is in a solid solution. This causes the phase to segregate to grain boundaries and triple points, as has been observed throughout the project. As the alloys cool from the solution heat treatment the liquid phase solidifies into a brittle eutectic compound. The main solution heat treatments used were reported in section 4.2. However, in the earlier stages of this work, several solution heat treatments were trialled in an attempt to minimise the volume fraction of the second phase present after cooling. Initially various cooling methods were attempted, including: oil quenching, air cooling and furnace cooling. The cooling rate did not have an observable effect on the volume fraction of the residual second phase. Further solution heat treatments were carried out at 505 ºC, below the solidus of the second phase. However, the alloys failed to fully homogenise at this temperature, even with longer heating times of 12 hours.

5.1.5.1 Phase Reactions in Mg-Zn-Y Alloys

It has been reported in previous studies[9, 33, 183] that increasing the zinc content, in similar rare earth-based magnesium alloys, increases the remaining volume fraction of residual second phase after the solution heat treatment. More recent work with Mg-Zn-Y alloys[23-25] has indicated that the Zn/Y ratio (in weight terms) controls not only the volume fraction of second phase but also the type of compound formed. When looking at the Mg-Zn-Y and Mg-Zn-Y-Zr systems, there are two major phases that are of interest in the current work[23, 27, 184, 185]. The I-phase (Mg_3Zn_6Y) has an icosahedral structure and is considered to be a quasicrystal[186] while the W-phase ($Mg_3Zn_3Y_2$) forms as a face centred cubic (FCC) structure. It has been suggested that when the Zn/Y ratio is above 4.38, the primary phase

present in the alloys is the I-phase[187]. While the ratio of Zn/Y is between 1.10 and 4.38, both the I and W-phases exist[187]. For alloys having a Zn/Y ratio of lower than 1.10, the major phase present is the W-phase[23]. The presence of zirconium in the alloys does not seem to affect the second phase development[188]. The I-phase is considered to be beneficial to the properties of Mg-Zn-Y based alloys[189, 190] with high hardness, good thermal stability and high corrosion resistance. In addition, the I-phase has a good orientation relationship with the α-Mg matrix, forming a strong bond and resists dislocation slip[27]. Conversely, the W-phase has little benefit to the material properties[184, 191, 192]. The W-phase has a poor orientation relationship with the α-Mg matrix and very weak atomic bonding[24]. Due to the brittleness of the phase and the ease of decohesion from the α-Mg, Ji et al.[24] concluded that the ultimate tensile strength (UTS) and elongation of Mg-Zn-Y-Zr alloys strongly depends on the volume fraction of the eutectic W-phase present. It was noted that increasing the Zn content increased the volume fraction of the W-phase in the alloys[24].

5.1.5.2 Neodymium Additions to the Mg-Zn-Y System

When neodymium is added to Mg-Zn-Y-Zr alloys, it can substitute yttrium atoms in the second phases. Li et al.[192] observed a distinct increase in the lattice parameter of the W-phase present in Mg-Zn-Y alloys, reported by Padezhnova et al.[186], with additions of Nd. The original lattice parameter reported by Padezhnova et al.[186] of a = 0.6848 nm was increased to a = 0.695 nm in a Mg-Zn-Y-Nd-Zr alloy and even further increased to a = 0.711 nm in a Mg-Zn-Nd-Zr alloy[192]. It was suggested that the increase in lattice parameter was caused by the replacement of Y atoms with Nd which has a larger atomic radius[192]. When Zn is present, the W-phase becomes $Mg_3Zn_3(Y,Nd)_2$[193]. In this case, the Zn/(Y, Nd) weight ratio must be considered as the controlling factor in the development of second phases. For the current alloys the Zn/(Y, Nd) weight ratio ranges from 0.33 to 0.6, depending on alloy composition.

5.1.5.3 Characterisation of the Second Phase

Several authors have reported that the W-phase melts at 510 ºC[25, 27, 194] while the I-phase melts between 440–450 ºC[25, 27, 194, 195]. Referring to the DSC carried out in the current work

(section 5.1.3), the melting point of the second phase in the three novel alloys is also ~510 ºC, depending on alloy chemistry. The work carried out using Thermo-Calc (section 5.1.4) corroborates this value. However, there were no observable peaks in the range of 440–450 ºC to suggest that any phase was melting at that temperature. With this information, it is concluded that the second phase occurring in these alloys after solution heat treatment is a form of the W-phase eutectic discussed above. Furthermore, from the DSC results (section 5.1.3), the I-phase does not appear to form after the solution heat treatment. These results are consistent with the previous work carried out on Mg-Zn-Y, Mg-Zn-Y-Zr, Mg-Zn-Nd-Zr and Mg-Zn-Y-Nd-Zr alloys[23, 25, 27, 192, 194-196] which indicate that the I-phase is not present after solidification or solution heat treatment when the Zn/Y(Nd) weight ratio is low (<1.10).

During the current work, the W-phase eutectic was observed to break up under plastic deformation, to some extent. The EBSD maps in section 4.5.2 showed areas of second phase that remained at grain boundaries after deformation. However, evidence of W-phase break-up was observed during investigation of the deformed samples with transmission electron microscopy (TEM). Figures 5.3 and 5.4 show TEM micrographs of alloy 95 after deformation at 435 ºC with a strain rate of 5/s. The micrographs were taken in the vicinity of a triple point where a large area of second phase existed. The first image shows a particle of second phase existing along the grain boundary with further particles that have migrated away from the boundary. The second image shows slightly smaller particles that exist further into the grain matrix. Figure 5.5 shows another example of W-phase break-up in the same sample at a grain boundary. The insert shows a selected area diffraction (SAD) pattern taken with the beam parallel to the $[0001]_{Mg}$ direction. Spots associated with an FCC [111] zone axis are present within the α-Mg matrix pattern. The FCC atomic structure of the second phase is, again, consistent with previous observations of the W-phase[23, 26, 27]. Similar observations of the breakdown of the W-phase have been made in previous work[27, 197, 198]. Generally, the W-phase particles that exist after plastic deformation share the same properties as the eutectic compound. They possess a weak bond with the α-Mg matrix and are easily fractured due to their brittle nature. However, Yang and Guo[198] did report effective grain boundary pinning by the W-phase particles during hot extrusion of a Mg-6%Zn-4%Y alloy.

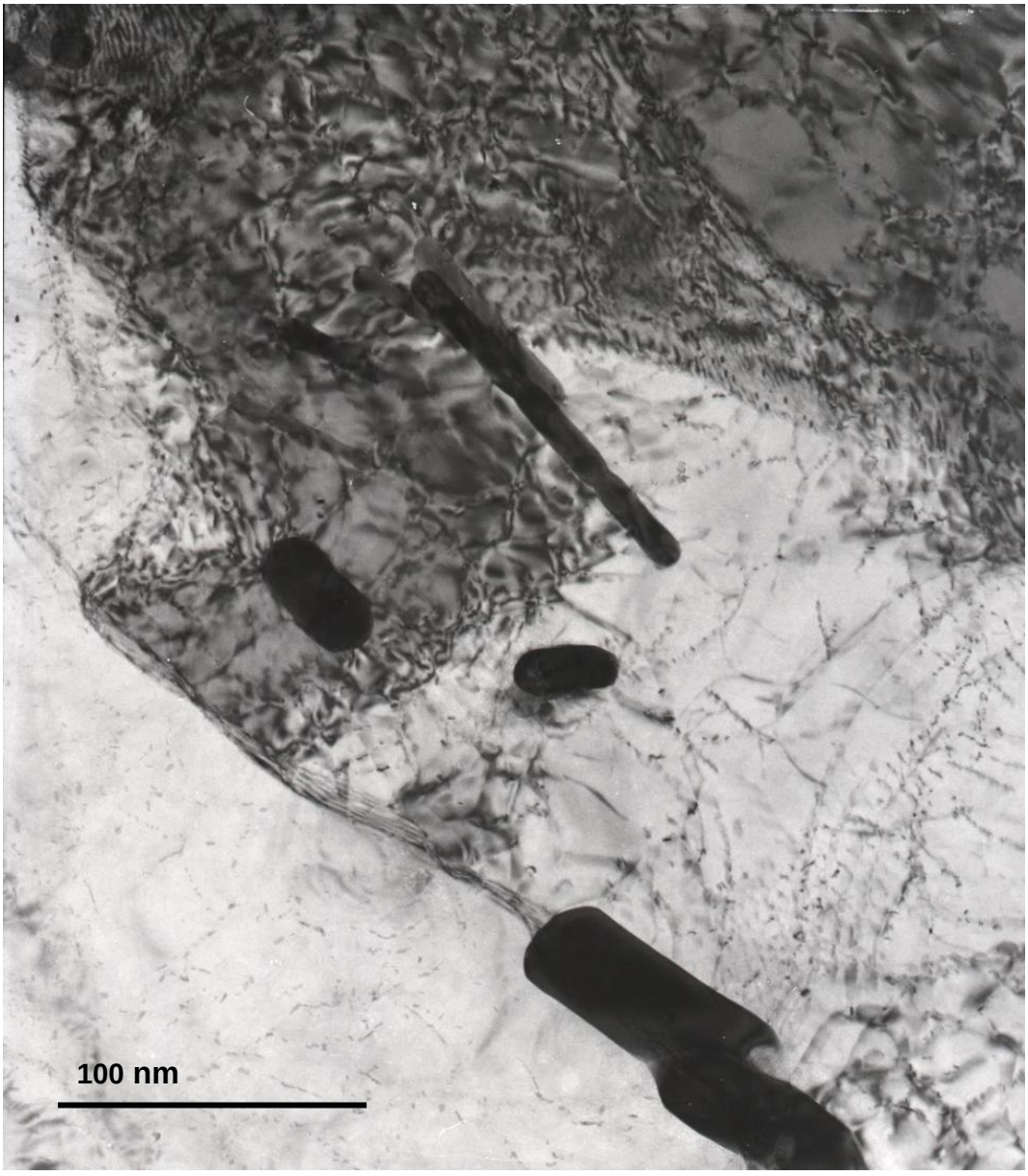

Figure 5.3 – TEM bright field micrograph of alloy 95 after compression at 435 ºC with a strain rate of 5/s. Beam direction is tilted slightly away from the $[0001]_{Mg}$ direction of the upper grain.

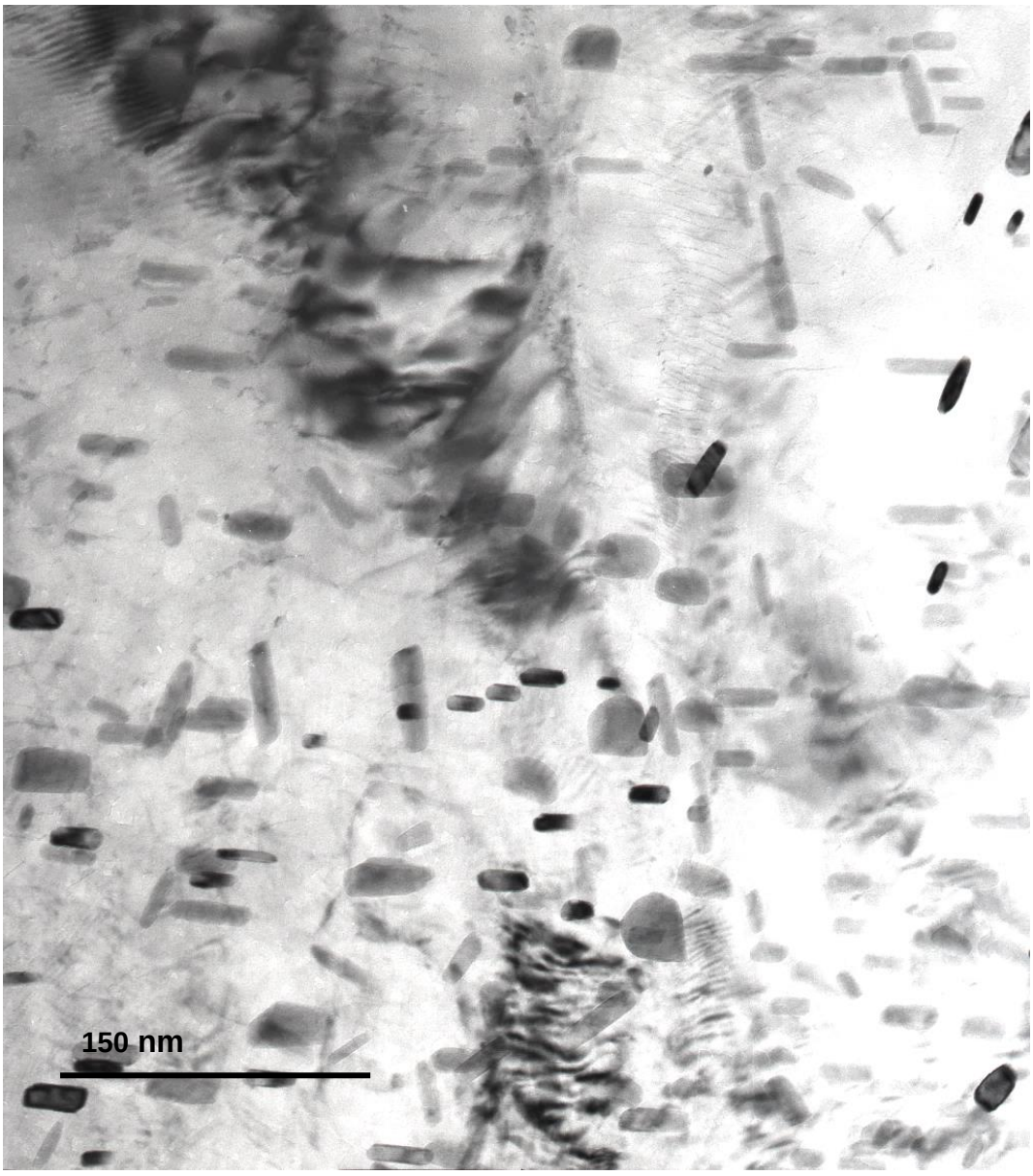

Figure 5.4 – TEM bright field micrograph of alloy 95 after compression at 435 ºC with a strain rate of 5/s. Beam direction is tilted slightly away from the $[0001]_{Mg}$ direction.

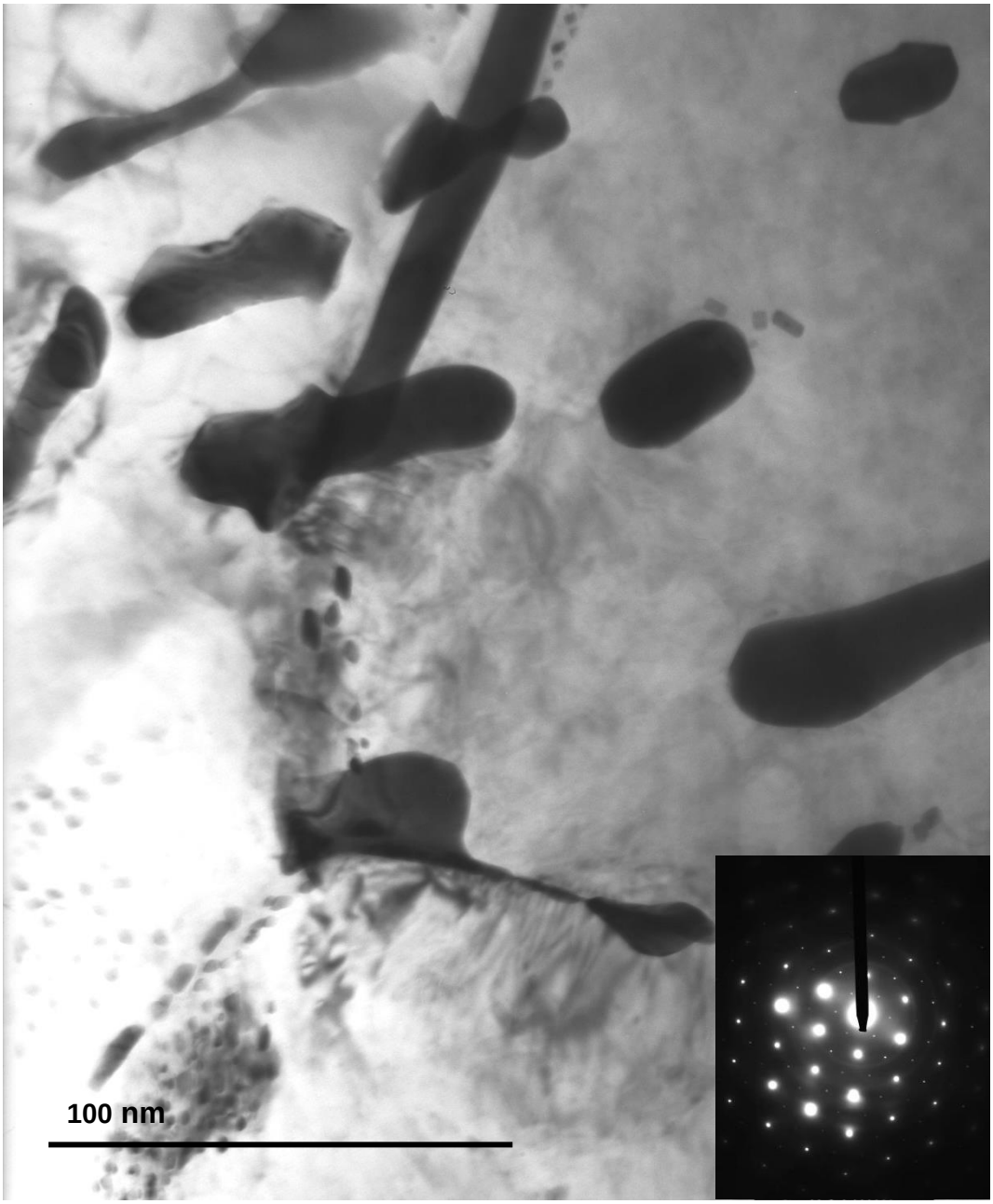

Figure 5.5 – TEM bright field micrograph of alloy 95 after compression at 435 ºC with a strain rate of 5/s. Beam direction is tilted slightly away from the $[0001]_{Mg.}$ direction. Insert of SAD pattern; FCC [111] zone axis spots visible within the α-Mg matrix.

5.1.5.4 Improving the Current Alloys

Although the residual volume fraction of second phase in the current alloys is detrimental to their deformation behaviour, there is potential for improved properties by promoting the formation of the I-phase. The I-phase forms in similar way to the W-phase in that it develops as a eutectic or peritectic, depending on yttrium content, at grain boundaries when cooling from casting or solution heat treatment[28, 196]. However, unlike the W-phase, the I-phase forms a strong atomic bond with the α-Mg matrix and under plastic deformation, breaks down into fine precipitates[27, 196]. These precipitates act to retard dislocation motion, improving the tensile properties of the alloy dramatically[25, 27, 184, 196]. Bae et al.[196] conducted experimental rolling on two Mg-rich Mg-Zn-Y alloys. After rolling, a fine dispersion of I-phase particles existed throughout the α-Mg matrix in the size range of 0.5–2 μm. It was noted that any voids remaining after the I-phase break up were readily healed by thermal processes[196]. An increase in the volume fraction of the I-phase was accompanied by an increase in the yield strength and elongation properties of the alloys[196]. The precipitates are found to have high thermal stability with the α-Mg up to temperatures approaching the melting point of the alloy[196]. Further studies[25-27, 185] have corroborated the fact that the atomic bonding between the I-phase and α-Mg matrix is robust enough to be retained after severe plastic deformation. Furthermore, the I-phase helps pin grain boundaries, refining final grain size and promotes particle stimulated nucleation of dynamically recrystallised grains during deformation[28, 196].

In their current form, the novel alloys studied in the work have very limited industrial appeal. The observed second phase that exists after solution heat treatment severely retards the tensile properties of the alloys. Cleary, further work needs to be carried out if the alloys are to be commercially viable. A change in the composition is required before further work can be carried out. To promote the formation of the I-phase preferentially over the W-phase after the solution heat treatment, the Zn/Y(Nd) weight ratio must be adjusted. Many of the studies cited above[23, 28, 195, 196, 198-201] agree that the Zn/Y(Nd) ratio is a controlling factor in Mg-Zn-Y(Nd)-Zr systems when it comes to phase development. There is general agreement[26, 27, 185, 191, 192, 195, 196, 200, 201] that the Zn/Y(Nd) needs to be ~5–7 for Mg-Zn-Y(Nd) based alloys to form I-phase after casting or after solution heat treatment. Alloys with a Zn/Y(Nd) weight

ratio of ~1.5–5 will form both I-phase and W-phase, while alloys with a Zn/Y(Nd) ratio of less than 1.5 will generally only form W-phase[26, 28].

Alternatively, the composition could be adjusted in such a way that no eutectic phase remained after a solution heat treatment. Higher volumes of zinc in the alloys reduce the melting temperatures of the second phases formed and of the alloy itself, thereby increasing the volume fraction of the eutectic compound remaining after the solution heat treatment. Reducing the zinc content of the alloys would increase the temperature at which any second phase compounds melted. If the melting point of the second phase was above the ideal solution heat treatment temperature for the current alloys (~525 ºC), the homogenisation should take place entirely in the solid solution state. In this case, the segregation of second phases to grain boundaries would be minimal. Thermo-Calc was used to investigate alternative compositions for the current alloys. A variety of compositions were entered into the software to investigate the temperature at which the liquid phase appeared. As an example, a composition of Mg-0.15%Zn-1%Y-1.5%Nd-0.4%Zr was inputted into the Thermo-Calc software. This composition contains much less Zn than the current alloys. However, the rare earth content is still quite dilute, in keeping with cost-effective nature of the design. Figure 5.6 shows the equilibrium step diagram for the hypothetical alloy. There is a clear shift in the occurrence of the liquid phase when compared to Figure 5.2. The onset of melting of second phase in the hypothetical alloy is 538.2 ºC, much higher than the ~510 ºC reported for the current alloys. Although the residual second phase at grain boundaries would effectively be eliminated, the properties of the alloy would be significantly changed, requiring further, in-depth investigation.

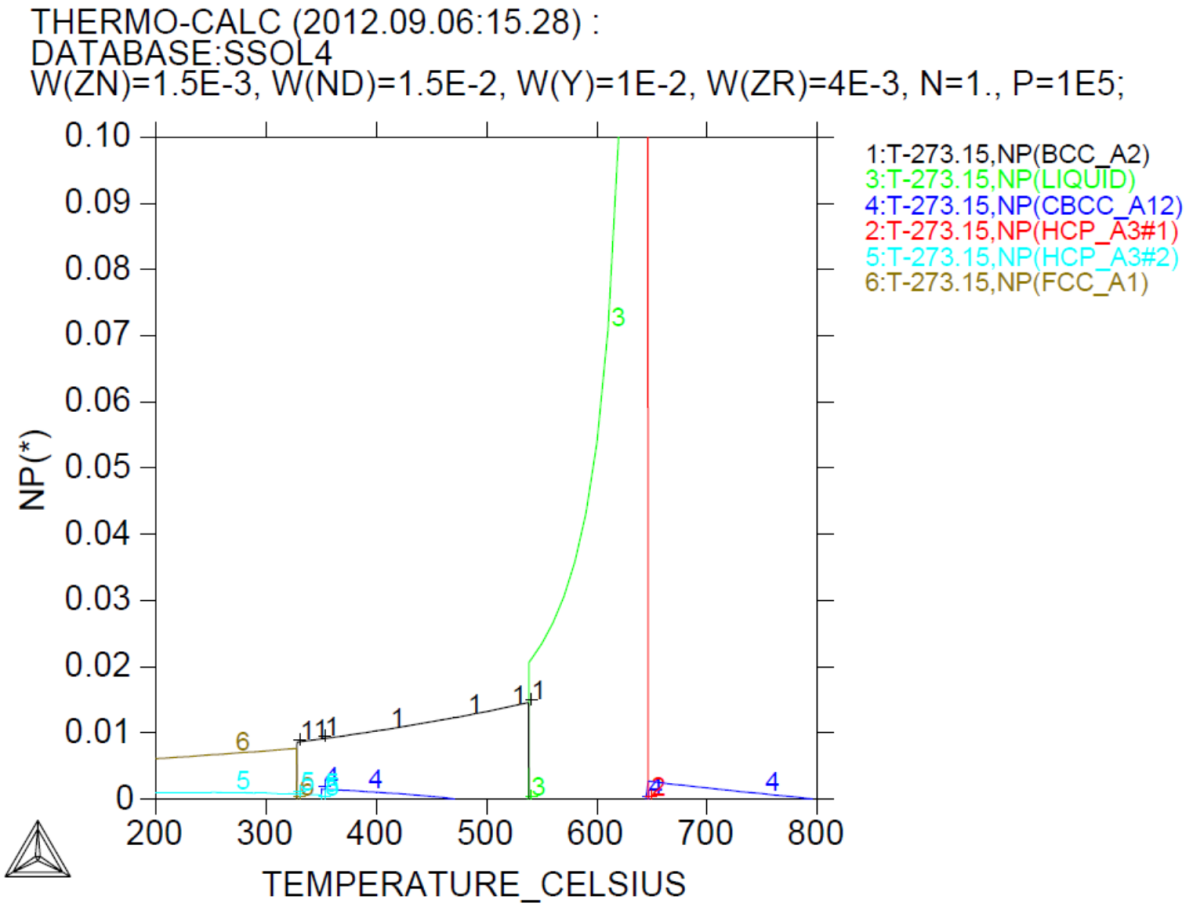

Figure 5.6 – Equilibrium step diagram for a hypothetical alloy (Mg-0.15%Zn-1%Y-1.5%Nd-0.4%Zr).

5.2 Isothermal Age Hardening

5.2.1 Introduction

A brief study on the ageing response of the novel alloys was carried out to complement the current work, as described in section 3.3. After the solution heat treatment, the three alloys were sectioned into small billets measuring approximately 30x20x10 mm. A simple ageing process was carried out at 225 ºC. The billets were removed from the furnace after 1, 2, 4, 8, 10, 12, 24, 48, and 100 hours and allowed to cool in air. Vickers hardness tests were carried out as detailed in section 3.3.2. The purpose of the study was to not only investigate the variation in ageing response between the novel alloys but also to observe any precipitation reactions that occurred, particularly in the peak aged condition.

5.2.2 Isothermal Ageing Response

Table 5.4 shows the peak hardness (Vickers) reached and the time taken to reach the peak for each of the novel alloys at 225 ºC. Figure 5.7 shows the ageing response curves of the three alloys after ageing at 225 ºC. All of the alloys exhibited a modest ageing response. Alloy 93 reached peak hardness after 10 hours, with alloys 94 and 95 reaching a peak after 24 hours. Alloys 94 and 95 exhibited a very similar age hardening response with near identical ageing curves.

Table 5.4 – Peak hardness and time to reach peak hardness for each of the novel alloys at 225 ºC.

Alloy	Peak Hardness (Vickers)	Time to Reach Peak Hardness (Hours)
93	73	10
94	76	24
95	79	24

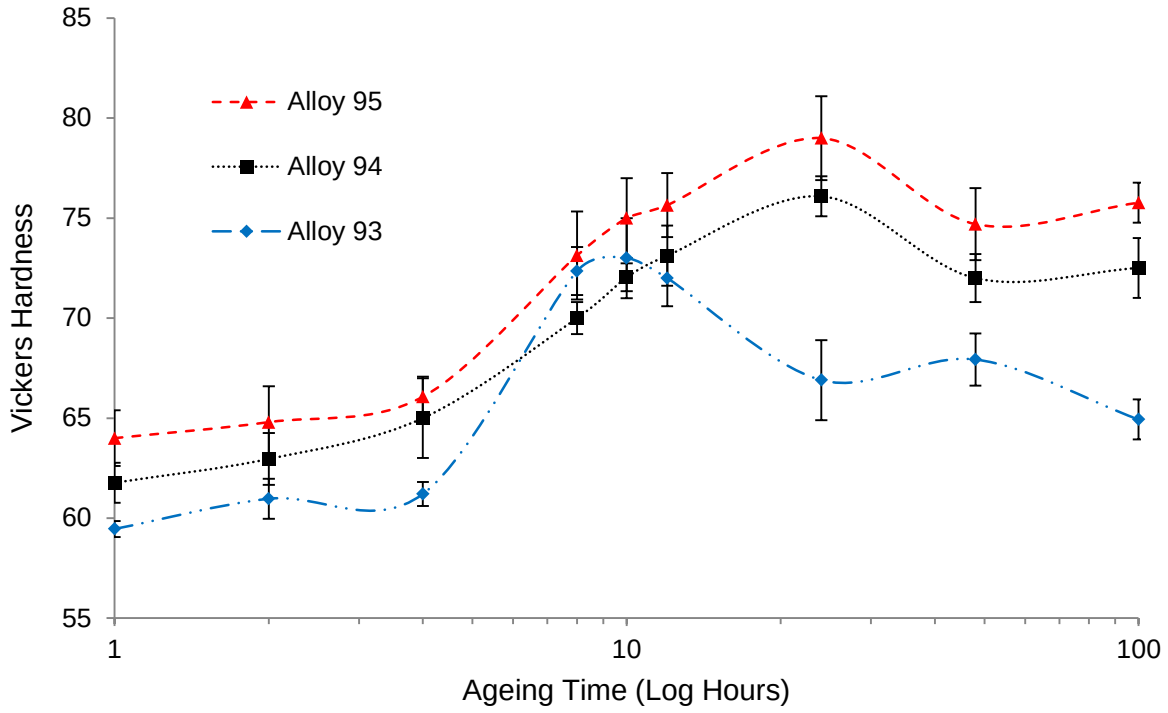

Figure 5.7 – Ageing response of the three novel alloys at 225 ºC. Error bars indicate standard deviation.

5.2.3 Precipitation Reactions in the Peak Aged Condition

Transmission electron microscopy (TEM) was used to study the precipitation after isothermal ageing. Alloy 95 was chosen to investigate precipitation in the peak aged condition. The alloy contained the highest level of solute additions compared to the other two alloys and exhibited the highest peak hardness. For this reason it was expected that a greater density of precipitates would take place in alloy 95 compared to the two other novel alloys. The main precipitates observed in the alloy were long, rod-like structures that existed parallel to the $[10\bar{1}0]_{Mg}$ direction. Images of the precipitates were taken with the beam either normal to or parallel to the basal plane. The occurrence of precipitates seemed rather random. Some grains would exhibit a fine dispersion of precipitates throughout while other grains appeared to be completely precipitate free. Figure 5.7 shows an example of the precipitation observed in the peak aged condition. In the upper grain there is a fine dispersion of rod-like precipitates growing along the $[10\bar{1}0]$ direction in the grain matrix.

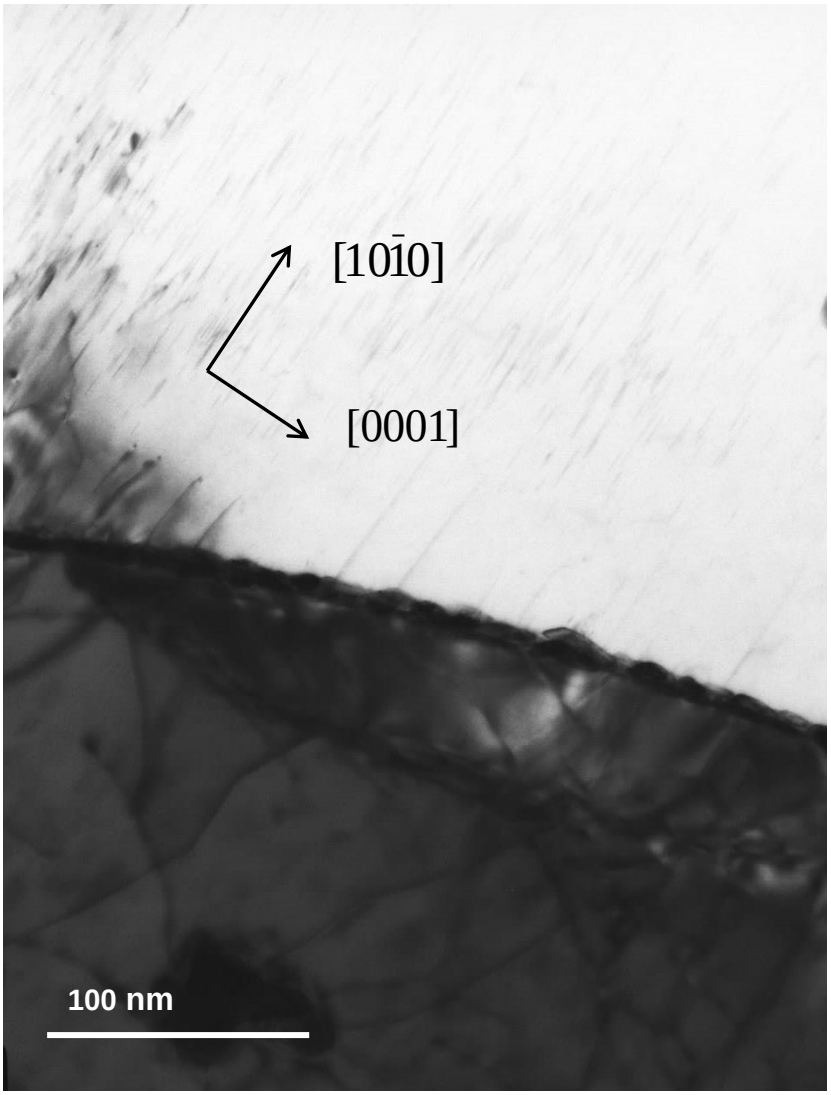

Figure 5.7 – TEM bright field micrograph of alloy 95 after ageing at 225 ºC for 24 hours. Beam direction is tilted slightly away from the $[1\bar{2}10]_{Mg}$ direction of the upper grain.

Figure 5.8 shows another image in the centre of a grain with the bean parallel to the $[1\bar{2}10]_{Mg}$ direction. Again a fine dispersion of needle-like precipitates can be seen growing parallel to the $[1\bar{2}10]_{Mg}$ direction. A selected area diffraction pattern has been added to the image to show streaking in the $[0001]_{Mg}$ direction associated with the precipitates.

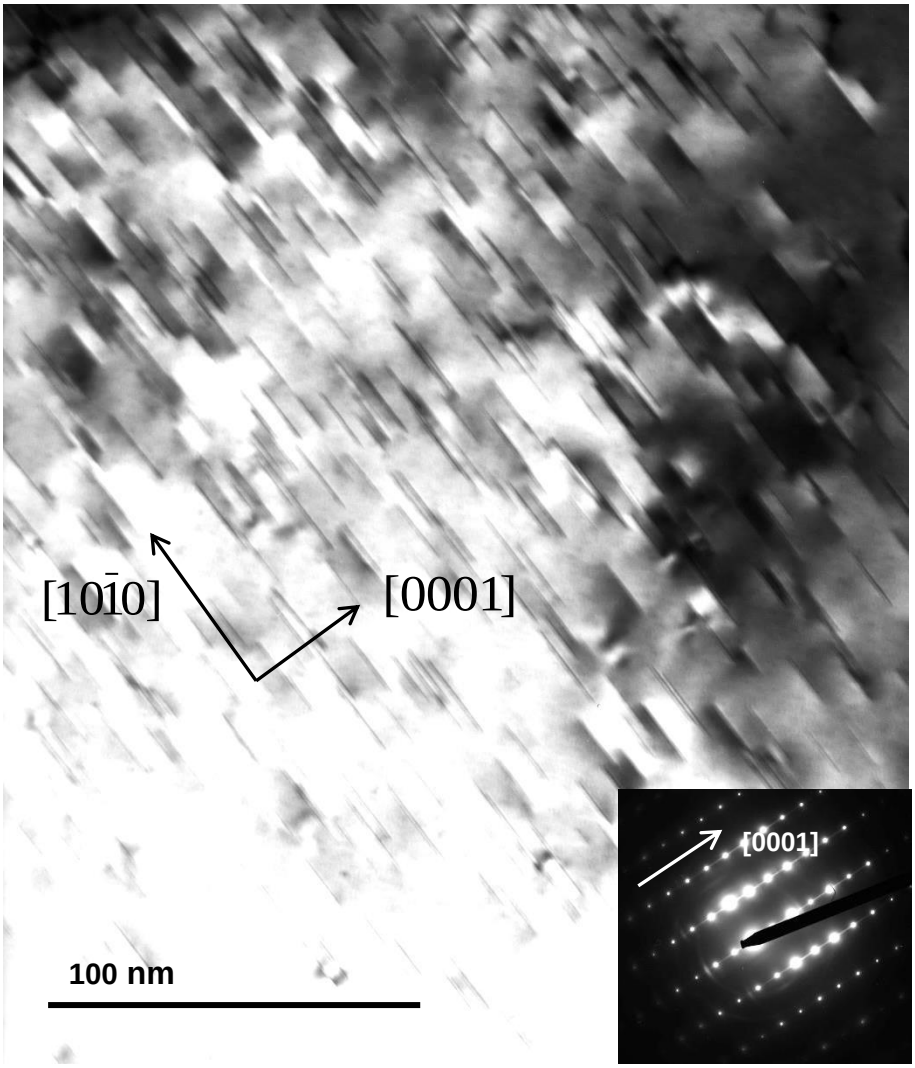

Figure 5.8 – TEM bright field micrograph of alloy 95 after ageing at 225 ºC for 24 hours. Beam direction is tilted slightly away from the $[1\bar{2}10]_{Mg}$.

Figure 5.9 depicts a bright field micrograph of a sample with the beam parallel to the $[0001]_{Mg}$ direction. In this image, examples of precipitates are indicated with black arrows. In this direction, the precipitates are 'end-on' with their long axis extending along the $[0001]_{Mg}$ direction. Arrays of dislocations can be seen to interact with the precipitates from this angle.

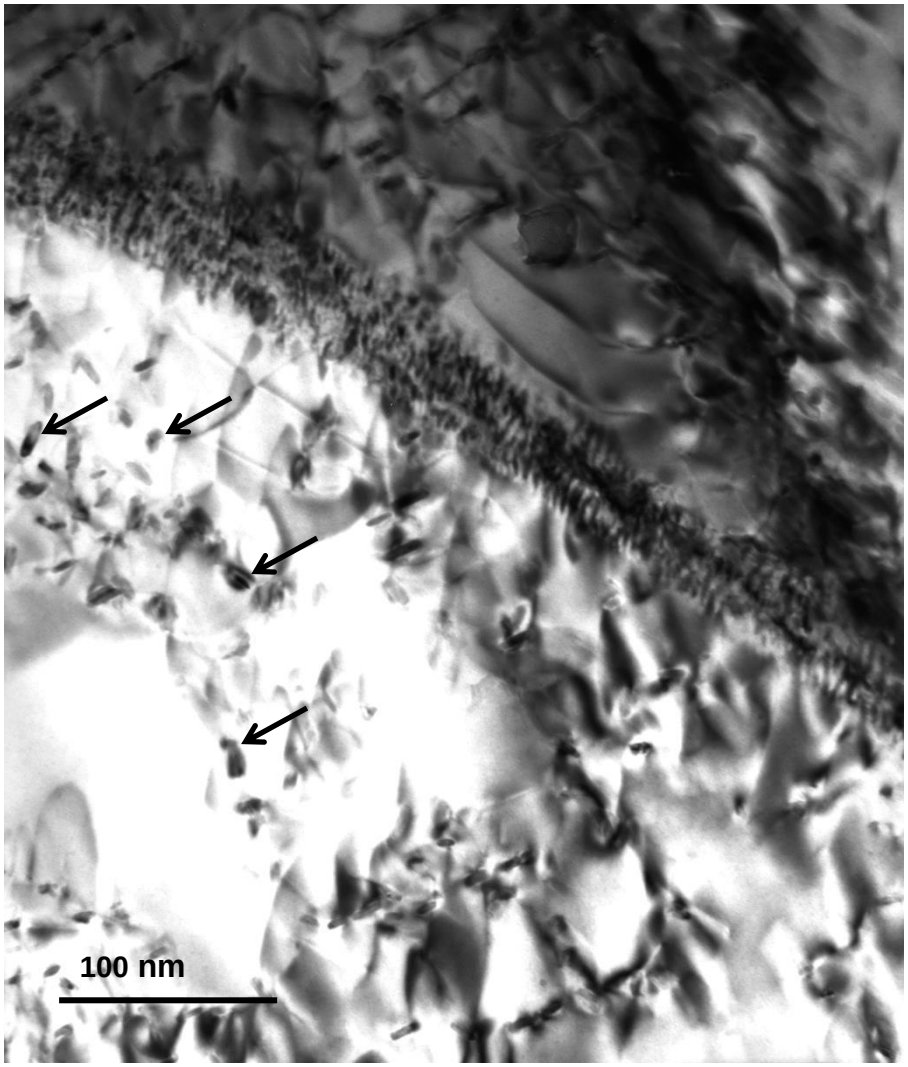

Figure 5.9 – TEM bright field micrograph of alloy 95 after ageing at 225 ºC for 24 hours. Beam direction is tilted slightly away from the $[0001]_{Mg}$ direction of the lower grain. Black arrows indicate examples of 'end-on' precipitates.

5.2.4 Discussion

5.2.4.1 Age Hardening Response

The three alloys were solution heat treated and artificially aged in accordance with a T6 temper regime. Each of the alloys exhibited a 19% increase in hardness after isothermal ageing at 225 ºC. Alloy 93 reached peak hardness after 10 hours, with alloys 94 and 95 reaching a peak after 24 hours. When examining the ageing curves in Figure 5.7, there is a distinct drop in the hardness after the peak followed by a slight increase in the severely over aged condition. It must be stated that the apparent rise is somewhat exaggerated by the log scale and is within the range of standard deviation for each alloy. However, all three alloys do exhibit a similar shape ageing curve. The ageing response in the current alloys is consistent with previous ageing studies on Mg-Zn and Mg-Zn-RE alloys[33, 47, 50-52, 55, 202]. However, Rosalie et al.[52] found that the hardness could be further developed by a T8 treatment (solution heat treatment, cold working and age hardening). The peak hardness seems to increase in the alloys with increased rare earth additions. The logical conclusion being that the increased rare earths provide a higher level of solute for strengthening precipitation upon ageing. Although, as reported in section 5.1, the Zn/RE ratio also affects the volume fraction of the W-phase eutectic after solution heat treatment. The increased volume fraction of W-phase at grain boundaries will reduce the solute available for precipitation reactions within the matrix.

5.2.4.2 Precipitation Reactions

Only a brief analysis of the precipitation reactions has been carried out on alloy 95. To fully understand the development and effect of strengthening precipitation with the current alloys, further work is required. Full diffraction data is needed for the precipitate characterisation. Also, the under age and over aged samples need to be analysed in order to document the precipitation sequence in full. With that in mind, the observations made during the current work are useful for comparing the behaviour of the alloys to other alloys with similar compositions.

Figure 5.7 shows a dispersion of fine precipitates throughout the upper grain matrix. The beam is tilted slightly away from the $[1\bar{2}10]_{Mg}$ direction. The particles appear to have a needle-like and slightly lenticular morphology, growing along the $[10\bar{1}0]_{Mg}$ direction. The length of the precipitates is approximately 15–45 nm. Approaching the boundary there appears to be a precipitate free zone, possibly indicating solute depletion in the grain boundary region. A couple of precipitate-like features are visible, touching the grain boundary at the centre of the image. On closer inspection, these features are distinctly longer than the grain matrix precipitates and completely straight (non-lenticular). These features are possibly crystal defects such as stacking faults also growing along the $[10\bar{1}0]_{Mg}$ direction.

Figure 5.8 shows another grain with a fine dispersion of similar precipitates with the beam tilted slightly away from the $[1\bar{2}10]_{Mg}$ direction. Once again, the precipitates grow along the $[10\bar{1}0]_{Mg}$ direction. The diffraction pattern insert shows distinct streaking along the $[0001]_{Mg}$ direction. This suggests that the precipitate exists on the basal plane of the α-Mg matrix and has an HCP structure. Referring to the literature[33, 55, 203], the type of precipitate that matches the morphology, habit plane and structure in similar alloys is the β_1 precipitate. The β_1 precipitate is known to strengthen Mg-Zn-RE alloys by creating a barrier against dislocation motion[33, 55, 203].

Figure 5.9 presents a different type of precipitate that occurred after peak ageing in the alloy. The beam is tilted slightly away from the $[0001]_{Mg}$ direction so that an acceptable level of contrast existed between the grain matrix and precipitates. Black arrows have been used to highlight some of the visible precipitates, although there are many more apparent within the grain. By tilting the sample further away from the zone axis, it appeared that the precipitates were rod-like in nature with the long axis existing parallel to the $[0001]_{Mg}$ direction. From the $[0001]_{Mg}$ direction in the image, they appear 'end-on'. Many dislocations can be observed interacting with the precipitates within the matrix suggesting that these precipitates also act as barriers to dislocation motion. Unfortunately, quality diffraction data was unobtainable to examine the precipitates further. However, the morphology and habit plane of the precipitates is similar to those observed in other Mg-Zn-RE alloys. The β_1' precipitate has been reported

by several authors[11, 20, 47, 50-52, 202] to grow as rod shapes, along the $[0001]_{Mg}$ axis of Mg-Zn and Mg-Zn-RE alloys. Similar interactions between the precipitates and dislocations have been observed by several authors who state that, rod-like precipitates, parallel to the $[0001]_{Mg}$ axis, are more effective at obstructing slip along the basal and prismatic planes than spherical or plate-like precipitates[52-54]. This is simply because the rod-like morphology intersects more basal planes. Although the precipitates in the current work appear very similar to the β_1' precipitate described, further diffraction data is required to fully characterise the precipitate phase.

This preliminary ageing work has shown that the current alloys are treatable with a T6 tempering regime (solution heat treatment and artificial ageing) showing a reasonable increase in hardness. It is quite probable, that after deformation, a further increase in hardness could be achieved due to the increased density of dislocations providing nucleation sites for strengthening precipitation. This effect has previously been observed by Rosalie et al.[52] in Mg-Zn alloys.

5.3 Summary

This chapter has expanded on some of the concerns raised in Chapter 4. Further insight into the residual second has been provided. Energy dispersive X-ray (EDX) spectroscopy showed that the second phase contained a significant volume of the solute additions for the alloys as a whole. The effect of this was to reduce solute available within the matrix for solid solution strengthening and precipitate reactions. It has been noted that the increase of zinc in Mg-RE alloys decreases the melting point of the second phase and the alloys as a whole. It has more recently been demonstrated that the Zn/RE weight ratio controls the volume fraction of the residual second phase after the solution heat treatment as well as defining the type of phase formed. Alloys with a low Zn/RE weight ratio (<1.5), like the current novel alloys, will generally only develop the W-phase eutectic after solution heat treatment. The W-phase was identified in the current alloys by its characteristic melting point of 510 ºC, measured by differential scanning calorimetry (DSC), and its FCC atomic structure observed with selected area diffraction (SAD). The W-phase is generally deleterious to Mg-Zn-RE alloys due to its brittle nature and low melting point. With an increased Zn/RE weight ratio (>5), the I-phase forms within Mg-Zn-RE alloys. The I-phase breaks down upon deformation, forming stable, strengthening precipitates throughout the matrix. It was suggested that to improve the current alloys, the Zn/Y(Nd) weight ratio should be increased. This would promote the formation of the beneficial I-phase in place of the W-phase, thereby widening the limited process window. Alternatively, the Zn/Y(Nd) ratio could be reduced so that the eutectic second phase doesn't melt below the solution temperature of the alloys. This would eliminate the residual eutectic, but would also lose any beneficial effects that the I-phase offers.

Finally, it has been shown that all the alloys harden upon isothermal ageing. A brief transmission electron microscopy (TEM) study was carried out to investigate precipitation reactions in one of the novel alloys (alloy 95). Two types of strengthening precipitate were qualitatively identified. The β^1 type precipitate was observed growing along the $[10\bar{1}0]_{Mg}$ axis. Streaking in the SAD pattern parallel with the $[0001]_{Mg}$ direction indicated that the precipitates were growing on the basal plane and had an hexagonal close packed (HCP) atomic structure. A further type of precipitate was identified as being the β_1' precipitate. This rod-like structure, grows parallel to the $[0001]_{Mg}$ direction and acts as a potent obstruction to

dislocation motion. The ageing work carried out indicates that a full analysis of the precipitation and ageing behaviour of these alloys would make for a fascinating project in itself.

6. Conclusions

The three novel alloys have been tested with hot axisymmetric compression through a standard test matrix with temperatures in the range of 425–450 ºC and strain rates ranging from 0.5 to 5/s. The flow behaviour has been analysed and the resultant microstructures have been examined with electron backscattered diffraction (EBSD). A significant volume of a eutectic phase has been identified in the alloys. Analysis of the phase has been carried out and discussed. Finally, a brief ageing study was conducted to complement the current work.

From the work carried during this project, the following conclusions have been made:

6.1 Initial Microstructure

- The starting material exhibited large, equiaxed grains with a random texture.

- The optimal solution heat treatment was found to be heating to 525 ºC for 8 hours. However, a significant volume fraction of a eutectic phase existed in each of the alloys with no reduction observed after extended heat treatments.

- The approximate volume fraction of the eutectic remaining in alloys 93, 94 and 95 after solution heat treatment was 0.005, 0.0127 and 0.0381 respectively.

6.2 Flow Behaviour

- Each of the alloys exhibited a similar shaped flow curve, with a work hardening region rising to a peak stress, followed by a prolonged period of flow softening. No steady state was reached up to a strain of 0.6.

- Mechanical twinning and slip are active during work hardening. Dynamic recrystallisation (DRX) is accepted as being the dominant mechanism of flow softening.

- The coefficient of friction for the three alloy during deformation was calculated to be 0.2

- The activation energy of deformation (Q_{def}) for alloys 93, 94 and 95 was calculated to be 196.8, 250.5 and 150.8 MPa respectively.

- Q_{def} was observed to vary considerably throughout the deformation test. Such variation suggests that more than one deformation mechanism was at work. While questions remain over the mechanisms operating during deformation, the values calculated for Q_{def} cannot be considered reliable.

- The strain at which peak stress was achieved during deformation of the three alloys increased as the Zener-Hollomon parameter (Z) increased. This relationship was linear.

- The process window of each of the alloys was very narrow. Samples tested above 450 ºC at strain rates above 1/s failed due to incipient melting. Samples tested at temperatures of 425 ºC or lower with strain rates over 1/s failed due to shear fracture.

- The eutectic, existing at grain boundaries and triple points, had a deleterious effect on the deformation behaviour of the alloys. At high temperatures the phase melted and at low temperatures its brittle nature promoted fracture at grain boundaries.

- Rolling the alloys, preheated to ~450ºC with rolls at ~70 ºC, led to catastrophic failure. The rolling samples either crumbled or exhibited a classic ‘alligator’ separation. The failure was bimodal, with incipient melting occurring at the centre and brittle fracture occurring at the outer edges.

6.3 Post-deformation Microstructure

- The deformed samples exhibited a strong basal texture.

- Several mechanisms of DRX were observed after deformation. A relationship existed between the dominant mode of DRX and the Zener-Hollomon Parameter. At low values of Z, discontinuous DRX (DDRX) was prevalent. At medium values of Z, continuous dynamic rotation recrystallisation (CDRRX) dominated. At high values of Z both continuous DRX (CDRX) and twin-induced CDRX were observed.

- Significant randomisation of the final texture was only through CDRRX. The most random textures were observed after deformations at 450 ºC with a strain rate of 5/s (middle of the test matrix in terms of Z). CDRRX was observed to be the dominant DRX mechanism at those test conditions.

- When twinning-induced CDRX occurred it was possible to identify the type of twin that the DRX grains originated from by measuring the misorientation with the unrecrystallised grain matrix. $\{10\bar{1}1\}$-$\{10\bar{1}2\}$ double twins, $\{10\bar{1}1\}$ and $\{10\bar{1}2\}$ primary twins were identified from the CDRX grains.

- CRDX was observed to nucleate preferentially within twin boundaries before spreading to the surrounding grain matrix.

- The average DRX grain size increased linearly as Z decreased. The higher temperatures allowed for greater grain boundary mobility while the slow strain rates provided more time for grains to coarsen.

- The DRX fraction was not directly related to Z in the current work. Temperature is the rate-controlling factor in terms of DRX fraction.

6.4 Analysis of the Second Phase

- Qualitative energy dispersive X-ray analysis (EDX) showed that a significant amounts of the solute additions in each of the alloys existed in the second phase. This had the effect of reducing the available solute in the matrix.

- Differential scanning calorimetry was used to measure the melting point of the second phase in the three alloys. The phase melted at approximately 510 ºC in each alloy, below the ideal solution heat treatment temperature of 525 ºC.

- The 510 ºC melting point is characteristic of the W-phase that occurs in magnesium alloys containing zinc and rare earths metals. Selected area diffraction (SAD) data showed that the phase observed in the current alloys had a face centre cubic (FCC) atomic structure matching that of the W-phase reported in the literature.

- The W-phase is a brittle eutectic phase that retards the tensile properties of magnesium alloys.

- Increasing the Zn/RE ratio to over ~5 will promote the formation of the I-phase. The I-phase improves the tensile properties of the alloy by forming strengthening precipitates upon deformation.

- Alternatively, the Z/RE could be reduced in order to raise the melting point of the second phase to above the solution heat treatment temperature of 525 ºC. However, this approach would sacrifice the favourable tensile properties of the I-phase.

6.5 Artificial Age Hardening

- Each of the alloys exhibited modest increases in hardness, of approximately 19%, when aged at 225 ºC.

- Peak hardness was reached after 10 hours for alloy 93 and after 24 hours for alloys 94 and 95.

- Two types of precipitate were identified in the peak aged sample of alloy 95.

- Firstly, a fine dispersion of needle-like precipitates was observed to grow along the $[10\bar{1}0]_{Mg}$ direction. A SAD pattern of this precipitate exhibited streaks in the $[0001]_{Mg}$ direction. This type of pattern would be indicative of a hexagonally close packed (HCP) precipitate growing on the basal plane of the α-Mg matrix. The structure and morphology matches that of the β^1 type precipitate observed in other Mg-Zn-RE alloys reported in the literature. The β^1 precipitate is known to be a strengthening precipitate.

- Another precipitate, with a rod-like morphology, was observed to grow along the $[0001]_{Mg}$ direction. Networks of dislocations were visible being impeded by the structures. The precipitates are similar in morphology and habit plane to the β_1' precipitate that exists in other Mg-Zn-RE alloys reported in the literature. Again, β_1' is classed as a strengthening precipitate.

7. Future Work

The current project has provided a firm foundation for further investigation into three new alloys. However, there are still aspects of the current work that remain incomplete. This chapter will address the shortcomings in the current work and highlight potential avenues of further investigation.

Originally it was planned to carry out a range of lower strain tests with the alloys. Unfortunately, a series of severe failures with the TMC machine, while testing, consumed the remaining material that had been kept for variable strain study. Investigating the earlier stages of deformation is an essential step in understanding the modes of deformation that a material goes through. Should further material be made available, then a series of deformation tests would be carried out to strains of 0.05, 0.1, 0.2, and 0.3. This range should provide detailed information on the work hardening region of the test and the change in deformation mode as peak stress is reached. EBSD would be used to analyse the deformation modes at lower strains. Particular interest would be given to the effect of mechanical twinning and slip during the early stages of deformation.

The validity of Q_{def} has been called into question in the current work. The primary concern for the current alloys is the unknown effect of the eutectic W-phase. While the grain matrix undergoes plastic deformation, the grain boundaries and triple points can give way due to the brittle nature of the eutectic. To produce a more reliable figure for Q_{def}, further investigation of the second phase is required. One possibility would be to conduct localised deformation testing on the second phase regions. With further knowledge of the tensile properties of the second phase, an adaptation of the classic Q_{def} calculation could be made. By incorporating both phases into the calculation, a more robust value of Q_{def} could be achieved for the material as a whole.

It is disappointing that constitutive behaviour for the alloys could not be realised. The method of developing constitutive behaviour depends of having a broad range of data over a wide range of testing conditions. Unfortunately, the current alloys exhibit an extremely narrow

process window. As such, the reliability of any constitutive behaviour would be questionable. In order to achieve a broader set of data, slower strain rates could be investigated. It was observed that, when testing with the TMC machine at lower strain rates (<0.5/s), the data became unreliable due to noise. It would be prudent to either use alternative equipment or improve the TMC control systems to test strain rates that are within the creep regime. This way, a wider set of temperatures could be assessed. If combined with a reliable value for Q_{def} full constitutive behaviour would be possible. If a reliable mathematical model was produced, finite element modelling could be used to fully predict the behaviour of the alloys during various deformation conditions.

The method for calculating the coefficient of friction for the current project was rather rudimentary. Although a friction coefficient of 0.2 was deemed reasonable in the current work, a more accurate method of assessment would be needed when deforming larger sections of material in an industrial setting. A secondary assessment method could be used to confirm the coefficient of friction. The ring test uses a ring of the material with known inner and outer diameters. Under deformation the inner diameter will change at a different rate to the outer diameter. The variation in these diameters can be used to accurately calculate the coefficient of friction using a calibration chart.

Another issue that was encountered during the deformation study was that the lubricant used became unreliable at greater strains. The graphite was applied to the samples in an aqueous solution with a high viscosity. When the sample was heated prior to deformation, the solution solidified. When the compression test reached strains of over 0.6 the lubricant started to crack, leaving areas of the interface surface un-lubricated. To carry out tests to higher strains, a different form of lubricant would be required. Several types of lubricant could be tested to assess their suitability at higher strains.

The current work has shown that the three alloys harden when artificially aged. Preliminary TEM analysis of the alloys showed that a range of precipitation reactions occurred. To fully document this phenomenon, a broader range of analyses would be required. Full diffraction data would be needed of the observed precipitate phases to fully characterise them. To document the full precipitation sequence, the under and over aged alloys would also need to

be investigated. The study could investigate the effect of different ageing temperatures on the age hardening response and the precipitation sequence. A further study could be conducted to investigate the effect of prior deformation to the ageing response. It has been noted in the current work that dislocation density plays an important role in the nucleation of strengthening precipitates. Prior deformation would introduce a greater number of nucleation sites and therefore greatly affect the precipitation reactions and by extension the age hardening response.

It was observed in the current work that precipitate free zones (PFZ) existed at some of the grain boundaries. A PFZ is usually caused by solute depletion in the grain boundary region. Any such depletion can set up an electrochemical framework for occurrence of corrosion. In particular, stress corrosion cracking (SCC) would be possible. The electrochemical activity of the alloys could be tested as a function of ageing time. Susceptibility to SCC often varies according to ageing time and grain misorientation within the alloy. TEM analysis could be used to investigate the occurrence of PFZs as a function of ageing time and grain misorientation. TEM work is time-consuming and as such, the combined ageing and SCC study would make for a substantial research project in its own right.

For the current alloys to be commercially viable, a change in chemistry is required. Although casting new alloys is beyond the scope of this project, it would be important work in respect of creating alloys that are commercially attractive for wrought application. A range of alloys could be produced with various Zn/RE ratios. It has been previously discussed that increasing the Zn/RE ratio would promote the formation of the desirable I-phase. If the I-phase was introduced to the alloys, the effect on the deformation characteristics and process window could be explored. An alternative route would be to produce an alloy with a low Zn/RE ratio that would raise the melting point of the second phase to above the solution heat treatment temperature. This would eliminate the residual second phase but lose the potential positive influence of the I-phase.

8. References

[1] **Emley, E.F.**, *Principles of Magnesium Technology*. 1966, Oxford: Pergamon.

[2] **Raynor, G.V.**, *The Physical Metallurgy of Magnesium and Its Alloys*. 1959: London.

[3] **Friedrich, H.E. and Mordike, B.L.**, *Magnesium Technology : Metallurgy, Design Data, Automotive Applications*. 2006, Berlin ; [Great Britain]: Springer.

[4] **Mordike, B.L. and Hehmann, F.E.**, *Magnesium Alloys and Their Applications : Symposium : Conference : Papers*. 1992: DGM Informationsgesellschaft Verlag.

[5] **Polmear, I.J.**, *Light Alloys : From Traditional Alloys to Nanocrystals*. 4th ed. ed. 2006, Amsterdam ; London: Elsevier Butterworth-Heinemann.

[6] **Furuya, H., Matunaga, S., and Kogizo, N.**, *Requirements and Feasibility of Magnesium Alloys for Aerospace Applications*, in *Magnesium Alloys 2003, Pts 1 and 2*, Kojima, Y., et al., Editors. 2003. p. 261-63.

[7] **Avedesian, M.M. and Baker, H.**, *Magnesium and Magnesium Alloys*. 1999, Materials Park, Ohio: ASM International.

[8] **Mordike, B.L.**, *Creep-Resistant Magnesium Alloys.* Materials Science and Engineering A, 2002. **324**(1-2): p. 103-12.

[9] **Rokhlin, L.L.**, *Magnesium Alloys Containing Rare Earth Metals : Structure and Properties*. 2003, London: Taylor & Francis.

[10] **Mordike, B.L.** *Development of Highly Creep Resistant Magnesium Alloys*. 2001. Switzerland: Elsevier.

[11] **Polmear, I.J.**, *Magnesium Alloys and Applications.* Materials Science and Technology, 1994. **10**(1): p. 1-16.

[12] **Nie, J.F. and Muddle, B.C.**, *Precipitation in Magnesium Alloy WE54 During Isothermal Ageing at 250 ºC.* Scripta Materialia, 1999. **40**(10): p. 1089-94.

[13] **Nie, J.F. and Muddle, B.C.**, *Characterisation of Strengthening Precipitate Phases in a Mg-Y-Nd Alloy.* Acta Materialia, 2000. **48**(8): p. 1691-703.

[14] **Nie, J.F., Xiao, X.L., Luo, C.P., and Muddle, B.C.**, *Characterisation of Precipitate Phases in Magnesium Alloys Using Electron Microdiffraction.* Micron, 2001. **32**(8): p. 857-63.

[15] **Leontis, T.E.**, *Effect of Rare-Earth Metals on the Properties of Extruded Magnesium.* Journal of Metals, 1951. **3**(11): p. 987-93.

[16] **Leontis, T.E.**, *Properties of Magnesium-Thorium and Magnesium-Thorium-Cerium Alloys.* Journal of Metals, 1952. **4**(3): p. 287-94.

[17] **Leontis, T.E.**, *The Room and Elevated Temperature Properties of Some Sand Cast Magnesium-Base Alloys Containing Zinc.* Transactions of the American Institute of Mining and Metallurgical Engineers, 1949. **180**: p. 287-321.

[18] **Leontis, T.E.**, *The Properties of Sand Cast Magnesium-Rare Earth Alloys.* Transactions of the American Institute of Mining and Metallurgical Engineers, 1949. **185**(12): p. 968-83.

[19] **Okamoto, H.**, *Supplemental Literature Review of Binary Phase Diagrams: Cs-in, Cs-K, Cs-Rb, Eu-in, Ho-Mn, K-Rb, Li-Mg, Mg-Nd, Mg-Zn, Mn-Sm, O-Sb, and Si-Sr.* Journal of Phase Equilibria and Diffusion, 2013. **34**(3): p. 251-63.

[20] **Clark, J.B.**, *Transmission Electron Microscopy Study of Age Hardening in a Mg-5 Wt Per Cent Zn Alloy.* Acta Metallurgica, 1965. **13**(12): p. 1281.

[21] **Nie, J.F., Gao, X., and Zhu, S.M.**, *Enhanced Age Hardening Response and Creep Resistance of Mg-Gd Alloys Containing Zn.* Scripta Materialia, 2005. **53**(9): p. 1049-53.

[22] **Honma, T., Ohkubo, T., Kamado, S., and Hono, K.**, *Effect of Zn Additions on the Age-Hardening of Mg-2.0gd-1.2y-0.2zr Alloys.* Acta Materialia, 2007. **55**(12): p. 4137-50.

[23] **Xu, D.K., Tang, W.N., Liu, L., Xu, Y.B., and Han, E.H.**, *Effect of W-Phase on the Mechanical Properties of as-Cast Mg-Zn-Y-Zr Alloys.* Journal of Alloys and Compounds, 2008. **461**(1-2): p. 248-52.

[24] **Ji, D.W., Liu, C.M., Chen, Z.Y., Wang, H.H., and Wang, B.**, *Effects of Zn Content on Microstructures and Mechanical Properties of as Cast Mg-Zn-Y-Zr Alloys.* Materials Science and Technology, 2013. **29**(4): p. 480-86.

[25] **Xu, D.K., Han, E.H., Liu, L., and Xu, Y.B.**, *Influence of Higher Zn/Y Ratio on the Microstructure and Mechanical Properties of Mg-Zn-Y-Zr Alloys.* Metallurgical and Materials Transactions a-Physical Metallurgy and Materials Science, 2009. **40A**(7): p. 1727-40.

[26] **Lee, J.Y., Do, H.K., Lim, H.K., and Kim, D.H.**, *Effects of Zn/Y Ratio on Microstructure and Mechanical Properties of Mg-Zn-Y Alloys.* Materials Letters, 2005. **59**(29-30): p. 3801-05.

[27] **Zeng, X.Q., Zhang, Y., Lu, C., Ding, W.J., Wang, Y.X., and Zhu, Y.P.**, *Precipitation Behavior and Mechanical Properties of a Mg-Zn-Y-Zr Alloy Processed by Thermo-Mechanical Treatment.* Journal of Alloys and Compounds, 2005. **395**(1-2): p. 213-19.

[28] **Xu, D.K. and Han, E.H.**, *Effects of Icosahedral Phase Formation on the Microstructure and Mechanical Improvement of Mg Alloys: A Review.* Progress in Natural Science-Materials International, 2012. **22**(5): p. 364-85.

[29] **Sauerwald, F.**, **Uber Die Beeinflussung Der Erstarrungskristallisation Von Magnesiumlegierungen Durch Zirkonium Und Einige Eigenschaften Von Gegossenen Magnesium-Legierungen Mit Zirkonium.* Zeitschrift Fur Metallkunde, 1949. **40**(2): p. 41-46.

[30] **Lee, Y.C., Dahle, A.K., and StJohn, D.H.**, *The Role of Solute in Grain Refinement of Magnesium.* Metallurgical and Materials Transactions a-Physical Metallurgy and Materials Science, 2000. **31**(11): p. 2895-906.

[31] **Lee, Y.C., Dahle, A.K., and StJohn, D.H.**, *Grain Refinement of Magnesium*. Magnesium Technology 2000, ed. Kaplan, H.L., Hryn, J.N., and Clow, B.B. 2000.

[32] **Qian, M., St John, D.H., and Frost, M.T.**, *Characteristic Zirconium-Rich Coring Structures in Mg-Zr Alloys.* Scripta Materialia, 2002. **46**(9): p. 649-54.

[33] **Gill, L.R.**, *Microstructure/Property Relationships of Four Mg-RE-Zn-Zr Alloys [Electronic Resource]*. 2005.

[34] **Kelly, A., Groves, G.W., and Kidd, P.**, *Crystallography and Crystal Defects*. Rev. ed. / A. Kelly, G.W. Groves and P. Kidd. ed. 2000, Chichester: Wiley.

[35] **Agnew, S.R. and Duygulu, O.**, *Plastic Anisotropy and the Role of Non-Basal Slip in Magnesium Alloy AZ31b.* International Journal of Plasticity, 2005. **21**(6): p. 1161-93.

[36] **Li, D.H., Dong, J., Zeng, X.Q., Lu, C., and Ding, W.J.**, *Characterization of β'' Precipitate Phase in a Mg-Dy-Gd-Nd Alloy.* Materials Characterization, 2007. **58**: p. 1025-28.

[37] **Ahmed, M., Lorimer, G.W., Lyon, P., and Pilkington, R.**, *The Effect of Heat-Treatment and Composition on the Microstructure and Properties of Cast Mg-Y-Re Alloys.* Magnesium Alloys and Their Applications, 1992: p. 301-08.

[38] **Lorimer, G., Azari-Khosroshahi, R., and Ahmed, M.**, *Precipitation Reactions in Two Magnesium Alloys Containing Rare Earths.* Japan Institute of Metals, Proceedings, Vol 12, (Jimic-3), Pts 1 and 2, 1999: p. 185-92.

[39] **Pike, T.J. and Noble, B.**, *Formation and Structure of Precipitates in a Dilute Magnesium-Neodymium Alloy.* Journal of the Less-Common Metals, 1973. **30**(1): p. 63-74.

[40] **Hisa, M., Barry, J.C., and Dunlop, G.L.**, *Precipitation During Age Hardening of Mg Rare Earth Alloys*. Proceedings of the Third International Magnesium Conference, ed. Lorimer, G.W. 1997.

[41] **Karimzadeh, H**. *The Microstructure and Mechanical Properties of Some Magnesium Alloys Containing Yttrium and Heavy Rare Earths. [Electronic Resource]*. 1985.

[42] **Mizer, D. and Peters, B.C.**, *Study of Precipitation at Elevated-Temperatures in a Mg-8.7 Pct Y Alloy.* Metallurgical Transactions, 1972. **3**(12): p. 3262-64.

[43] **Sturkey, L. and Clark, J.B.**, *Mechanism of Age-Hardening in Magnesium Zinc Alloys.* Journal of the Institute of Metals, 1959. **88**(4): p. 177-81.

[44] **Umezurike, C**. *Age-Hardening in H.C.P. Magnesium Alloys. [Electronic Resource]*. 1976.

[45] **Gallot, J. and Graf, R.**, *Nouvelles Observations Aux Rayons X Et Au Microscope Electronique Sur La Phase Transitoire Appraissant Dans Lalliage Magnesiumzinc a 6(De Zinc.* Comptes Rendus Hebdomadaires Des Seances De L Academie Des Sciences, 1965. **261**(3): p. 728.

[46] **Chun, J.S. and Byrne, J.G.**, *Precipitate Strengthening Mechanisms in Magnesium Zinc Alloy Single Crystals.* Journal of Materials Science, 1969. **4**(10): p. 861-72.

[47] **Wei, L.Y., Dunlop, G.L., and Westengen, H.**, *Precipitation Hardening of Mg-Zn and Mg-Zn-Re Alloys.* Metallurgical and Materials Transactions a-Physical Metallurgy and Materials Science, 1995. **26**(7): p. 1705-16.

[48] **Hall, E.O.**, *Age-Hardening Characteristics of 2 Magnesium-Zinc Alloys.* Journal of the Institute of Metals, 1968. **96**: p. 21.

[49] **Gao, X. and Nie, J.F.**, *Characterization of Strengthening Precipitate Phases in a Mg-Zn Alloy.* Scripta Materialia, 2007. **56**(8): p. 645-48.

[50] **Singh, A. and Tsai, A.P.**, *Structural Characteristics of β_1' Precipitates in Mg-Zn-Based Alloys.* Scripta Materialia, 2007. **57**(10): p. 941-44.

[51] **Singh, A., Rosalie, J.M., Somekawa, H., and Mukai, T.**, *The Structure of β_1' Precipitates in Mg-Zn-Y Alloys.* Philosophical Magazine Letters, 2010. **90**(9): p. 641-51.

[52] **Rosalie, J.M., Somekawa, H., Singh, A., and Mukai, T.**, *The Effect of Size and Distribution of Rod-Shaped β_1' Precipitates on the Strength and Ductility of a Mg-Zn Alloy.* Materials Science and Engineering a-Structural Materials Properties Microstructure and Processing, 2012. **539**: p. 230-37.

[53] **Nie, J.F.**, *Effects of Precipitate Shape and Orientation on Dispersion Strengthening in Magnesium Alloys.* Scripta Materialia, 2003. **48**(8): p. 1009-15.

[54] **Robson, J.D., Stanford, N., and Barnett, M.R.**, *Effect of Precipitate Shape on Slip and Twinning in Magnesium Alloys.* Acta Materialia, 2011. **59**(5): p. 1945-56.

[55] **Wilson, R., Bettles, C.J., Muddle, B.C., and Nie, J.F.**, *Precipitation Hardening in Mg-3 Wt.% Nd(-Zn) Casting Alloys*, in *Magnesium Alloys 2003, Pts 1 and 2*, Kojima, Y., et al., Editors. 2003. p. 267-72.

[56] **Humphreys, F.J. and Hatherly, M.**, *Recrystallization and Related Annealing Phenomena*. 2nd ed. ed. 2004, London: Elsevier Science Ltd.

[57] **von Mises, R.**, *Mechanics of the Ductile Form Changes of Crystals.* Zeitschrift Fur Angewandte Mathematik Und Mechanik, 1928. **8**: p. 161-85.

[58] **Groves, G.W. and Kelly, A.**, *Independent Slip Systems in Crystals.* Philosophical Magazine, 1963. **8**(89): p. 877.

[59] **Barnett, M.R.**, *A Taylor Model Based Description of the Proof Stress of Magnesium AZ31 During Hot Working.* Metallurgical and Materials Transactions a-Physical Metallurgy and Materials Science, 2003. **34A**(9): p. 1799-806.

[60] **Ion, S.E., Humphreys, F.J., and White, S.H.**, *Dynamic Recrystallization and the Development of Microstructure During the High-Temperature Deformation of Magnesium.* Acta Metallurgica, 1982. **30**(10): p. 1909-19.

[61] **Staroselsky, A. and Anand, L.**, *A Constitutive Model for HCP Materials Deforming by Slip and Twinning: Application to Magnesium Alloy AZ31b.* International Journal of Plasticity, 2003. **19**(10): p. 1843-64.

[62] **Kocks, U.F. and Westlake, D.G.**, *Importance of Twinning for Ductility of CPH Polycrystals.* Transactions of the Metallurgical Society of Aime, 1967. **239**(7): p. 1107.

[63] **Hall, E.O.**, *Twinning and Diffusionless Transformations in Metals*. 1954, [S.l.]: Butterworths.

[64] **Barnett, M.R.**, *Twinning and the Ductility of Magnesium Alloys Part Ii. "Contraction" Twins.* Materials Science and Engineering a-Structural Materials Properties Microstructure and Processing, 2007. **464**(1-2): p. 8-16.

[65] **Christian, J.W. and Mahajan, S.**, *Deformation Twinning.* Progress in Materials Science, 1995. **39**(1-2): p. 1-157.

[66] **Cahn, R.W.**, *Twinned Crystals.* Advances in Physics, 1954. **3**(12): p. 363-445.

[67] **Bingert, J.F., Mason, T.A., Kaschner, G.C., Maudlin, P.J., and Gray, G.T.**, *Deformation Twinning in Polycrystalline Zr: Insights from Electron Backscattered Diffraction Characterization.* Metallurgical and Materials Transactions a-Physical Metallurgy and Materials Science, 2002. **33**(3): p. 955-63.

[68] **Barnett, M.R.**, *Influence of Deformation Conditions and Texture on the High Temperature Flow Stress of Magnesium AZ31*. Journal of Light Metals, 2001. **1**(3): p. 167-77.

[69] **Fundenberger, J.J., Philippe, M.J., and Esling, C.**, *Mechanical Twinning at High-Temperatures in Some Hexagonal Alloys.* Scripta Metallurgica Et Materialia, 1990. **24**(7): p. 1215-20.

[70] **Barnett, M.R.**, *Twinning and the Ductility of Magnesium Alloys Part I: "Tension" Twins.* Materials Science and Engineering a-Structural Materials Properties Microstructure and Processing, 2007. **464**(1-2): p. 1-7.

[71] **Wonsiewi.Bc and Backofen, W.A.**, *Plasticity of Magnesium Crystals.* Transactions of the Metallurgical Society of Aime, 1967. **239**(9): p. 1422.

[72] **Nave, M.D. and Barnett, M.R.**, *Microstructures and Textures of Pure Magnesium Deformed in Plane-Strain Compression.* Scripta Materialia, 2004. **51**(9): p. 881-85.

[73] **Koike, J.**, *Enhanced Deformation Mechanisms by Anisotropic Plasticity in Polycrystalline Mg Alloys at Room Temperature.* Metallurgical and Materials Transactions a-Physical Metallurgy and Materials Science, 2005. **36A**(7): p. 1689-96.
[74] **Barnett, M.R., Beer, A.G., Atwell, D., and Oudin, A.**, *Influence of Grain Size on Hot Working Stresses and Microstructures in Mg-3Al-1Zn.* Scripta Materialia, 2004. **51**(1): p. 19-24.
[75] **Lahaie, D., Embury, J.D., Chadwick, M.M., and Gray, G.T.**, *A Note on the Deformation of Fine-Grained Magnesium Alloys.* Scripta Metallurgica Et Materialia, 1992. **27**(2): p. 139-42.
[76] **Kaibyshev, R., Galiev, A., and Sitdikov, O.**, *On the Possibility of Producing a Nanocrystalline Structure in Magnesium and Magnesium Alloys.* Nanostructured Materials, 1995. **6**(5-8): p. 621-24.
[77] **Meyers, M.A., Vohringer, O., and Lubarda, V.A.**, *The Onset of Twinning in Metals: A Constitutive Description.* Acta Materialia, 2001. **49**(19): p. 4025-39.
[78] **Koike, J., Kobayashi, T., Mukai, T., Watanabe, H., Suzuki, M., Maruyama, K., and Higashi, K.**, *The Activity of Non-Basal Slip Systems and Dynamic Recovery at Room Temperature in Fine-Grained AZ31b Magnesium Alloys.* Acta Materialia, 2003. **51**(7): p. 2055-65.
[79] **Koike, J., Ohyama, R., Kobayashi, T., Suzuki, M., and Maruyama, K.**, *Grain-Boundary Sliding in AZ31 Magnesium Alloys at Room Temperature to 523 K.* Materials Transactions, 2003. **44**(4): p. 445-51.
[80] **Ohyama, R., Koike, J., Kobayashi, T., Suzuki, M., and Maruyama, K.**, *Enhanced Grain-Boundary Sliding at Room Temperature in AZ31 Magnesium Alloy*, in *Magnesium Alloys 2003, Pts 1 and 2*, Kojima, Y., et al., Editors. 2003. p. 237-41.
[81] **Tan, J.C. and Tan, M.J.**, *Dynamic Continuous Recrystallization Characteristics in Two Stage Deformation of Mg-3A1-1Zn Alloy Sheet.* Materials Science and Engineering a-Structural Materials Properties Microstructure and Processing, 2003. **339**(1-2): p. 124-32.
[82] **Huang, X., Suzuki, K., Watazu, A., Shigematsu, I., and Saito, N.**, *Microstructural and Textural Evolution of AZ31 Magnesium Alloy During Differential Speed Rolling.* Journal of Alloys and Compounds, 2009. **479**(1-2): p. 726-31.
[83] **Mabuchi, M., Ameyama, K., Iwasaki, H., and Higashi, K.**, *Low Temperature Superplasticity of AZ91 Magnesium Alloy with Non-Equilibrium Grain Boundaries.* Acta Materialia, 1999. **47**(7): p. 2047-57.
[84] **Kumar, N.V.R., Blandin, J.J., Desrayaud, C., Montheillet, F., and Suery, M.**, *Grain Refinement in AZ91 Magnesium Alloy During Thermomechanical Processing.* Materials Science and Engineering a-Structural Materials Properties Microstructure and Processing, 2003. **359**(1-2): p. 150-57.
[85] **Gottstein, G.**, *Physical Foundations of Materials Science*. 2004, Berlin ; London: Springer.
[86] **Zener, C. and Hollomon, J.H.**, *Effect of Strain Rate Upon Plastic Flow of Steel.* Journal of Applied Physics, 1944. **15**(1): p. 22-32.
[87] **Philippe, M.J., Serghat, M., Vanhoutte, P., and Esling, C.**, *Modeling of Texture Evolution for Materials of Hexagonal Symmetry .2. Application to Zirconium and Titanium Alpha-Alloys or near-Alpha-Alloys.* Acta Metallurgica Et Materialia, 1995. **43**(4): p. 1619-30.

[88] **Philippe, M.J., Wagner, F., Mellab, F.E., Esling, C., and Wegria, J.**, *Modeling of Texture Evolution for Materials of Hexagonal Symmetry .1. Application to Zinc-Alloys.* Acta Metallurgica Et Materialia, 1994. **42**(1): p. 239-50.

[89] **Akhtar, A. and Teghtsoo.E**, *Solid Solution Strengthening of Magnesium Single Crystals .I. Alloying Behaviour in Basal Slip.* Acta Metallurgica, 1969. **17**(11): p. 1339.

[90] **Akhtar, A. and Teghtsoo.E**, *Solid Solution Strengthening of Magnesium Single Crystals .2. Effect of Solute on Ease of Prismatic Slip.* Acta Metallurgica, 1969. **17**(11): p. 1351.

[91] **Obara, T., Yoshinga, H., and Morozumi, S.**, *112bar2 (11bar23) Slip System in Magnesium.* Acta Metallurgica, 1973. **21**(7): p. 845-53.

[92] **Flynn, P.W., Mote, J., and Dorn, J.E.**, *On the Thermally Activated Mechanism of Prismatic Slip in Magnesium Single Crystals.* Transactions of the Metallurgical Society of Aime, 1961. **221**(6): p. 1148-54.

[93] **Reedhill, R.E. and Robertson, W.D.**, *The Crystallographic Characteristics of Fracture in Magnesium Single Crystals.* Acta Metallurgica, 1957. **5**(12): p. 728-37.

[94] **Ando, S. and Tonda, H.**, *Non-Basal Slips in Magnesium and Magnesium-Lithium Alloy Single Crystals*, in *Magnesium Alloys 2000*, Kojima, Y., Aizawa, T., and Kamado, S., Editors. 2000. p. 43-48.

[95] **Yoshinaga, B.H. and Horiuchi, R.**, *Deformation Mechanisms in Magnesium Single Crystals Compressed in the Direction Parallel to Hexagonal Axis.* Trans JIM, 1963. **4**: p. 1-8.

[96] **Hardwick, D. and Tegart, W.J.M.**, *Structural Changes During the Deformation of Copper, Aluminium and Nickel at High Temperatures and High Strain Rates.* Journal of the Institute of Metals, 1961. **90**(1): p. 17-21.

[97] **Sastry, D.H., Prasad, Y.V.R., and Vasu, K.I.**, *Comments on Stacking Fault Energies of Close-Packed Hexagonal Metals - Reply.* Scripta Metallurgica, 1970. **4**(5): p. 347.

[98] **Murr, L.E.**, *Interfacial Phenomena in Metals and Alloys*. 1975, Reading, Mass. ; London: Addison-Wesley.

[99] **Somekawa, H., Hirai, K., Watanabe, H., Takigawa, Y., and Higashi, K.**, *Dislocation Creep Behavior in Mg-Al-Zn Alloys.* Materials Science and Engineering a-Structural Materials Properties Microstructure and Processing, 2005. **407**(1-2): p. 53-61.

[100] **Al-Samman, T. and Gottstein, G.**, *Dynamic Recrystallization During High Temperature Deformation of Magnesium.* Materials Science and Engineering a-Structural Materials Properties Microstructure and Processing, 2008. **490**(1-2): p. 411-20.

[101] **Spigarelli, S., El Mehtedi, M., Cabibbo, M., Evangelista, E., Kaneko, J., Jager, A., and Gartnerova, V.**, *Analysis of High-Temperature Deformation and Microstructure of an AZ31 Magnesium Alloy.* Materials Science and Engineering a-Structural Materials Properties Microstructure and Processing, 2007. **462**(1-2): p. 197-201.

[102] **Galiyev, A., Kaibyshev, R., and Gottstein, G.**, *Correlation of Plastic Deformation and Dynamic Recrystallization in Magnesium Alloy ZK60.* Acta Materialia, 2001. **49**(7): p. 1199-207.

[103] **Barnett, M.R.**, *Quenched and Annealed Microstructures of Hot Worked Magnesium AZ31.* Materials Transactions, 2003. **44**(4): p. 571-77.

[104] **Galiyev, A., Sitdikov, O., and Kaibyshev, R.**, *Deformation Behavior and Controlling Mechanisms for Plastic Flow of Magnesium and Magnesium Alloy*. Materials Transactions, 2003. **44**(4): p. 426-35.
[105] **McQueen, H.J. and Konopleva, E.V.**, *Creep and Hot Working of Mg Alloy AZ91*. Magnesium Technology 2001, ed. Hryn, J.N. 2001, Warrendale: Minerals, Metals & Materials Soc.
[106] **Beer, A.G. and Barnett, M.R.**, *Microstructural Development During Hot Working of Mg-3Al-1Zn.* Metallurgical and Materials Transactions a-Physical Metallurgy and Materials Science, 2007. **38A**(8): p. 1856-67.
[107] **Xu, S.W., Kamado, S., Matsumoto, N., Honma, T., and Kojima, Y.**, *Recrystallization Mechanism of as-Cast AZ91 Magnesium Alloy During Hot Compressive Deformation.* Materials Science and Engineering a-Structural Materials Properties Microstructure and Processing, 2009. **527**(1-2): p. 52-60.
[108] **Park, S.H., Kim, H.S., Bae, J.H., Yim, C.D., and You, B.S.**, *Improving the Mechanical Properties of Extruded Mg-3Al-1Zn Alloy by Cold Pre-Forging.* Scripta Materialia, 2013. **69**(3): p. 250-53.
[109] **Randman, D.**, *Deformation Mechanisms in Magnesium Alloy Elektron 675*, in *Department of Engineering and Materials*.Ph.D. 2010, University of Sheffield: Sheffield, UK.
[110] **Humphreys, F**., (1981) *Dynamic Recrystallisation - the Influence of Crystal Structure*. Deformation of polycrystals: mechanisms and microstructures : proceedings of the 2nd Risø International Symposium on Metallurgy and Materials Science, September 14-18, 1981, 305-10.
[111] **del Valle, J.A., Perez-Prado, M.T., and Ruano, O.A.**, *Texture Evolution During Large-Strain Hot Rolling of the Mg AZ61 Alloy*. Materials Science and Engineering a-Structural Materials Properties Microstructure and Processing, 2003. **355**(1-2): p. 68-78.
[112] **Yi, S.B., Zaefferer, S., and Brokmeier, H.G.**, *Mechanical Behaviour and Microstructural Evolution of Magnesium Alloy AZ31 in Tension at Different Temperatures.* Materials Science and Engineering a-Structural Materials Properties Microstructure and Processing, 2006. **424**(1-2): p. 275-81.
[113] **Sitdikov, O. and Kaibyshev, R.**, *Dynamic Recrystallization in Pure Magnesium.* Materials Transactions, 2001. **42**(9): p. 1928-37.
[114] **Kaibyshev, R., Sakai, T., Miura, H., Sitdikov, O., and Galiyev, A.**, *Plastic Deformation of Magnesium and Magnesium Alloy at Low to High Temperature*. Pricm 4: Forth Pacific Rim International Conference on Advanced Materials and Processing, Vols I and Ii, ed. Hanada, S., et al. 2001.
[115] **Hakamada, M., Watazu, A., Saito, N., and Iwasaki, H.**, *Effects of Homogenization Annealing on Dynamic Recrystallization in Mg-Al-Ca-Re (Rare Earth) Alloy.* Materials Transactions, 2008. **49**(5): p. 1032-37.
[116] **Watanabe, H., Tsutsui, H., Mukai, T., Ishikawa, K., Okanda, Y., Kohzu, M., and Higashi, K.**, *Grain Size Control of Commercial Wrought Mg-Al-Zn Alloys Utilizing Dynamic Recrystallization.* Materials Transactions, 2001. **42**(7): p. 1200-05.
[117] **Agnew, S.R., Yoo, M.H., and Tome, C.N.**, *Application of Texture Simulation to Understanding Mechanical Behavior of Mg and Solid Solution Alloys Containing Li or Y.* Acta Materialia, 2001. **49**(20): p. 4277-89.
[118] **Roberts, C.S.**, *Magnesium and Its Alloys*. 1960, New York ; London: Wiley.

[119] **Yukutake, E., Kaneko, J., and Sugamata, M.**, *Anisotropy and Non-Uniformity in Plastic Behavior of AZ31 Magnesium Alloy Plates.* Materials Transactions, 2003. **44**(4): p. 452-57.
[120] **Senn, J.W. and Agnew, S.R.**, *Texture Randomization of Magnesium Alloys Containing Rare Earth Elements*, in *Magnesium Technology 2008*, Pekguleryuz, M.O., et al., Editors. 2008, Minerals, Metals & Materials Soc: Warrendale. p. 153-58.
[121] **Bohlen, J., Agnew, S.R., Nurnberg, M.R., Senn, J.W., and Letzig, D.**, *The Texture and Anisotropy of Magnesium-Zinc-Rare Earth Alloy Sheets.* Acta Materialia, 2007. **55**(6): p. 2101-12.
[122] **Ball, E.A. and Prangnell, P.B.**, *Tensile-Compressive Yield Asymmetries in High-Strength Wrought Magnesium Alloys.* Scripta Metallurgica Et Materialia, 1994. **31**(2): p. 111-16.
[123] **Stanford, N. and Barnett, M.R.**, *The Origin of "Rare Earth" Texture Development in Extruded Mg-Based Alloys and Its Effect on Tensile Ductility.* Materials Science and Engineering a-Structural Materials Properties Microstructure and Processing, 2008. **496**(1-2): p. 399-408.
[124] **Robson, J.D., Henry, D.T., and Davis, B.**, *Particle Effects on Recrystallization in Magnesium-Manganese Alloys: Particle-Stimulated Nucleation.* Acta Materialia, 2009. **57**(9): p. 2739-47.
[125] **Davenport, S.B., Silk, N.J., Sparks, C.N., and Sellars, C.M.**, *Development of Constitutive Equations for Modelling of Hot Rolling.* Materials Science and Technology, 2000. **16**(5): p. 539-46.
[126] **Roebuck, B., Lord, J.D., Brooks, M., Loveday, M.S., Sellars, C.M., and Evans, R.W.**, *Measurement of Flow Stress in Hot Axisymmetric Compression Tests.* Materials at High Temperatures, 2006. **23**(2): p. 59-83.
[127] **Prasad, Y. and Rao, K.P.**, *Processing Maps for Hot Deformation of Rolled AZ31 Magnesium Alloy Plate: Anisotropy of Hot Workability.* Materials Science and Engineering a-Structural Materials Properties Microstructure and Processing, 2008. **487**(1-2): p. 316-27.
[128] **Beladi, H. and Barnett, M.R.**, *Influence of Aging Pre-Treatment on the Compressive Deformation of WE54 Alloy.* Materials Science and Engineering a-Structural Materials Properties Microstructure and Processing, 2007. **452**: p. 306-12.
[129] **Bhattacharya, R., Wynne, B.P., Rainforth, W.M., and Davies, B.**, *Flow Stress Modelling of Magnesium AZ31 Alloy Based on High Strain Plane Strain Compression Data*, in *Magnesium Technology 2008*, Pekguleryuz, M.O., et al., Editors. 2008. p. 75-80.
[130] **Randman, D., Rainforth, W.M., Wynne, B.P., and Davis, B.**, *Deformation Mechanisms in Magnesium Alloy Elektron 675*, in *Magnesium Technology 2009*, Nyberg, E.A., et al., Editors. 2009, Minerals, Metals & Materials Soc: Warrendale. p. 497-502.
[131] **Thomas, M.J.**, *The Effect of Thermomechanical Process Parameters on the Mictrostructure and Crystallographic Texture Evolution of near-A Aerospace Alloy Timetal®834* Ph.D. 2007, University of Sheffield: Sheffield.
[132] **Hinton, J.S.**, *Laboratory Simulation of Microstructural Evolution in AISI 430 Ferritic Stainless Steel During the Steckel Mill Process*. 2006.
[133] **Alexander, J.M.**, *The Effect of Coulomb Friction in the Plane-Strain Compression of a Plastic-Rigid Material.* Journal of the Mechanics and Physics of Solids, 1955. **3**(4): p. 233-45.

[134] **Dieter, G.E. and Bacon, D.**, *Mechanical Metallurgy*. SI metric ed. 1988: McGraw-Hill.
[135] **Tukey, J.W.**, *Exploratory Data Analysis*. 1977, [S.l.]: Addison Wesley.
[136] **Blackmore, M.**, *Strain Path Effects on Timetal 834 under Hot Working Conditions [Electronic Resource]*, 2009, University of Sheffield.
[137] **Humphreys, F.J.**, *Review - Grain and Subgrain Characterisation by Electron Backscatter Diffraction.* Journal of Materials Science, 2001. **36**(16): p. 3833-54.
[138] **Vaudin, M.D.**, *Pseudosymmetry in EBSD Patterns.* Microscopy and Microanalysis, 2005. **11**(SupplementS02): p. 510-11.
[139] **ASTM International**, *E112: Standard Test Methods for Determining Average Grain Size*, 1996, ASTM International: West Conshocken, PA.
[140] **ASTM International**, *E562: Standard Test Method for Determining Volume Fraction by Systematic Manual Point Count*, 2011, ASTM International: West Conshohocken, PA.
[141] **MACKENZIE, J.K.**, *Second Paper on Statistics Associated with the Random Disorientation of Cubes.* Biometrika, 1958. **45**(1-2): p. 229-40.
[142] **Kelley, E.W. and Hosford, W.F.**, *Plane-Strain Compression of Magnesium and Magnesium Alloy Crystals.* Transactions of the Metallurgical Society of AIME, 1968. **242**(1): p. 5.
[143] **Gehrmann, R., Frommert, M.M., and Gottstein, G.**, *Texture Effects on Plastic Deformation of Magnesium.* Materials Science and Engineering a-Structural Materials Properties Microstructure and Processing, 2005. **395**(1-2): p. 338-49.
[144] **Klimanek, P. and Potzsch, A.**, *Microstructure Evolution under Compressive Plastic Deformation of Magnesium at Different Temperatures and Strain Rates.* Materials Science and Engineering a-Structural Materials Properties Microstructure and Processing, 2002. **324**(1-2): p. 145-50.
[145] **Barnett, M.R., Keshavarz, Z., Beer, A.G., and Atwell, D.**, *Influence of Grain Size on the Compressive Deformation of Wrought Mg-3Al-1Zn.* Acta Materialia, 2004. **52**(17): p. 5093-103.
[146] **Jiang, L., Jonas, J.J., Luo, A.A., Sachdev, A.K., and Godet, S.**, *Influence of {10-12} Extension Twinning on the Flow Behavior of AZ31 Mg Alloy.* Materials Science and Engineering a-Structural Materials Properties Microstructure and Processing, 2007. **445**: p. 302-09.
[147] **Karaman, I., Sehitoglu, H., Beaudoin, A.J., Chumlyakov, Y.I., Maier, H.J., and Tome, C.N.**, *Modeling the Deformation Behavior of Hadfield Steel Single and Polycrystals Due to Twinning and Slip.* Acta Materialia, 2000. **48**(9): p. 2031-47.
[148] **Shamsi, M., Sanjari, M., and Hanzaki, A.Z.**, *Study of Fractional Softening of AZ31 Magnesium Alloy under Multistage Hot Deformation.* Materials Science and Technology, 2009. **25**(8): p. 1039-45.
[149] **Slooff, F.A., Dzwonczyk, J.S., Zhou, J., Duszczyk, J., and Katgerman, L.**, *Hot Workability Analysis of Extruded Magnesium Alloys with Processing Maps.* Materials Science and Engineering a-Structural Materials Properties Microstructure and Processing, 2010. **527**(3): p. 735-44.
[150] **Srinivasan, N., Prasad, Y., and Rao, P.R.**, *Hot Deformation Behaviour of Mg-3Al Alloy - a Study Using Processing Map.* Materials Science and Engineering a-Structural Materials Properties Microstructure and Processing, 2008. **476**(1-2): p. 146-56.

[151] **Zinov'ev, A.V., Ionov, A.M., Kaputkina, L.M., Mironov, P.V., Kaputkin, E.Y., Sigalov, Y.M., and Solomonik, Y.L.**, *A Study of the Process of Hot Deformation of Magnesium Alloy AZ31.* Metal Science and Heat Treatment, 2006. **48**(11-12): p. 494-98.

[152] **Farzadfar, S.A., Sanjari, M., Jung, I.H., Essadiqi, E., and Yue, S.**, *Role of Yttrium in the Microstructure and Texture Evolution of Mg.* Materials Science and Engineering a-Structural Materials Properties Microstructure and Processing, 2011. **528**(22-23): p. 6742-53.

[153] **Poliak, E.I. and Jonas, J.J.**, *A One-Parmenter Approach to Determining the Critical Conditions for the Initiation of Dynamic Recrystallization.* Acta Materialia, 1996. **44**(1): p. 127-36.

[154] **Zhou, H.T., Liu, C.M., and Chen, M.A.**, *Constitutive Model Development and Hot Extrusion Simulation for AZ61 Magnesium Alloy.* Materials Science and Technology, 2006. **22**(5): p. 597-603.

[155] **Yang, Z., Li, J.P., Zhang, J.X., Guo, Y.C., Wang, B.W., Xia, F., and Liang, M.X.**, *Effect of Homogenization on the Hot-Deformation Ability and Dynamic Recrystallization of Mg-9Gd-3Y-0.5Zr Alloy.* Materials Science and Engineering a-Structural Materials Properties Microstructure and Processing, 2009. **515**(1-2): p. 102-07.

[156] **He, Y.B., Pan, Q.L., Qin, Y.J., Liu, X.Y., Li, W.B., Chiu, Y.L., and Chen, J.J.J.**, *Microstructure and Mechanical Properties of ZK60 Alloy Processed by Two-Step Equal Channel Angular Pressing.* Journal of Alloys and Compounds, 2010. **492**(1-2): p. 605-10.

[157] **Yu, K., Li, W.X., Zhao, J., Ma, Z.Q., and Wang, R.C.**, *Plastic Deformation Behaviors of a Mg-Ce-Zn-Zr Alloy.* Scripta Materialia, 2003. **48**(9): p. 1319-23.

[158] **Slooff, F.A., Duszczyk, J., and Katgerman, L.**, *Constitutive Analysis of Wrought Magnesium Alloy Mg-Al4-Zn1.* Scripta Materialia, 2007. **57**(8): p. 759-62.

[159] **Slooff, F.A., Zhou, J., Duszczyk, J., and Katgerman, L.**, *Strain-Dependent Constitutive Analysis of Three Wrought Mg-Al-Zn Alloys.* Journal of Materials Science, 2008. **43**(22): p. 7165-70.

[160] **Mwembela, A., Konopleva, E.B., and McQueen, H.J.**, *Microstructural Development in Mg Alloy AZ31 During Hot Working.* Scripta Materialia, 1997. **37**(11): p. 1789-95.

[161] **Guo, Q., Yan, H.G., Zhang, H., Chen, Z.H., and Wang, Z.F.**, *Behaviour of AZ(31) Magnesium Alloy During Compression at Elevated Temperatures.* Materials Science and Technology, 2005. **21**(11): p. 1349-54.

[162] **Guo, Q., Yan, H.G., Chen, Z.H., and Zhang, H.**, *Elevated Temperature Compression Behaviour of Mg-Al-Zn Alloys.* Materials Science and Technology, 2006. **22**(6): p. 725-29.

[163] **Zhou, H.T., Zeng, X.Q., Liu, L.L., Dong, J., Wang, Q.D., Ding, W.J., and Zhu, Y.P.**, *Microstructural Evolution of AZ61 Magnesium Alloy During Hot Deformation.* Materials Science and Technology, 2004. **20**(11): p. 1397-402.

[164] **Myshlyaev, M.M., McQueen, H.J., Mwembela, A., and Konopleva, E.**, *Twinning, Dynamic Recovery and Recrystallization in Hot Worked Mg-Al-Zn Alloy.* Materials Science and Engineering A, 2002. **337**(1-2): p. 121-33.

[165] **Kaibyshev, R.O., Sitdikov, O.S., and Galiyev, A.M.**, *Mechanisms of Plastic Deformation of Magnesium .1. Deformation Behaviour of Coarse-Grain Magnesium.* Fizika Metallov I Metallovedenie, 1995. **80**(3): p. 174-84.

[166] **Perez-Prado, M.T., del Valle, J.A., Contreras, J.M., and Ruano, O.A.**, *Microstructural Evolution During Large Strain Hot Rolling of an AM60 Mg Alloy.* Scripta Materialia, 2004. **50**(5): p. 661-65.
[167] **Helis, L., Okayasu, K., and Fukutomi, H.**, *Microstructure Evolution and Texture Development During High-Temperature Uniaxial Compression of Magnesium Alloy AZ31*. Materials Science and Engineering a-Structural Materials Properties Microstructure and Processing, 2006. **430**(1-2): p. 98-103.
[168] **Li, H.L., Hsu, E., Szpunar, J., Utsunomiya, H., and Sakai, T.**, *Deformation Mechanism and Texture and Microstructure Evolution During High-Speed Rolling of AZ31B Mg Sheets.* Journal of Materials Science, 2008. **43**(22): p. 7148-56.
[169] **Beausir, B., Biswas, S., Kim, D.I., Toth, L.S., and Suwas, S.**, *Analysis of Microstructure and Texture Evolution in Pure Magnesium During Symmetric and Asymmetric Rolling.* Acta Materialia, 2009. **57**(17): p. 5061-77.
[170] **Beer, A.G. and Barnett, M.R.**, *Microstructure Evolution in Hot Worked and Annealed Magnesium Alloy AZ31*. Materials Science and Engineering a-Structural Materials Properties Microstructure and Processing, 2008. **485**(1-2): p. 318-24.
[171] **Beladi, H., Fatemi-Varzaneh, S.M., and Zarei-Hanzaki, A.**, *Dynamic Recrystallization in AZ31 Magnesium Alloy.* Materials Science and Engineering A (Structural Materials: Properties, Microstructure and Processing), 2007. **456**(1-2): p. 52-7.
[172] **Fatemi-Varzaneh, S.M., Zarei-Hanzaki, A., and Beladi, H.**, *Dynamic Recrystallization in AZ31 Magnesium Alloy.* Materials Science and Engineering a-Structural Materials Properties Microstructure and Processing, 2007. **456**(1-2): p. 52-57.
[173] **Liu, L.F. and Ding, H.L.**, *Study of the Plastic Flow Behaviors of AZ91 Magnesium Alloy During Thermomechanical Processes.* Journal of Alloys and Compounds, 2009. **484**(1-2): p. 949-56.
[174] **Zhang, Y., Zeng, X.Q., Lu, C., and Ding, W.J.**, *Deformation Behavior and Dynamic Recrystallization of a Mg-Zn-Y-Zr Alloy.* Materials Science and Engineering a-Structural Materials Properties Microstructure and Processing, 2006. **428**(1-2): p. 91-97.
[175] **Sanjari, M., Farzadfar, S.A., Jung, I.H., Essadiqi, E., and Yue, S.**, *Influence of Strain Rate on Hot Deformation Behaviour and Texture Evolution of AZ31B.* Materials Science and Technology, 2012. **28**(4): p. 437-47.
[176] **Yang, Z., Guo, Y.C., Li, J.P., He, F., Xia, F., and Liang, M.X.**, *Plastic Deformation and Dynamic Recrystallization Behaviors of Mg-5Gd-4Y-0.5Zn-0.5Zr Alloy*. Materials Science and Engineering a-Structural Materials Properties Microstructure and Processing, 2008. **485**(1-2): p. 487-91.
[177] **Calnan, E.A. and Clews, C.J.B.**, *The Development of Deformation Textures in Metals - .3. Hexagonal Structures.* Philosophical Magazine, 1951. **42**(331): p. 919-31.
[178] **Styczynski, A., Hartig, C., Bohlen, J., and Letzig, D.**, *Cold Rolling Textures in AZ31 Wrought Magnesium Alloy.* Scripta Materialia, 2004. **50**(7): p. 943-47.
[179] **Kocks, U.F., Tome, C.N., and Wenk, H.-R.**, *Texture and Anisotropy : Preferred Orientations in Polycrystals and Their Effect on Materials Properties*. 1998, New York ; Cambridge: Cambridge University Press.
[180] **Tenckhoff, E.**, *Development of Deformation Texture in Zirconium During Rolling in Sequential Passes.* Metallurgical Transactions a-Physical Metallurgy and Materials Science, 1978. **9**(10): p. 1401-12.

[181] **Li, H.L., Hsu, E., Szpunar, J., Verma, R., and Carter, J.T.**, *Determination of Active Slip/Twinning Modes in AZ31 Mg Alloy near Room Temperature.* Journal of Materials Engineering and Performance, 2007. **16**(3): p. 321-26.

[182] **Liu, Y. and Wu, X.**, *An Electron-Backscattered Diffraction Study of the Texture Evolution in a Coarse-Grained AZ31 Magnesium Alloy Deformed in Tension at Elevated Temperatures.* Metallurgical and Materials Transactions a-Physical Metallurgy and Materials Science, 2006. **37A**(1): p. 7-17.

[183] **Tikhova, N.M., Blokhina, V.A., and Antipova, A.P.**, *Effect of Heat-Treatment on Dimensional Stability of Castings and Mechanical-Properties of Alloy-Ml19.* Metal Science and Heat Treatment, 1977. **19**(3-4): p. 239-40.

[184] **Xu, D.K., Tang, W.N., Liu, L., Xu, Y.B., and Han, E.H.**, *Effect of Y Concentration on the Microstructure and Mechanical Properties of as-Cast Mg-Zn-Y-Zr Alloys.* Journal of Alloys and Compounds, 2007. **432**(1-2): p. 129-34.

[185] **Lee, J.Y., Lim, H.K., Kim, D.H., Kim, W.T., and Kim, D.H.**, *Effect of Volume Fraction of Qusicrystal on the Mechanical Properties of Quasicrystal-Reinforced Mg-Zn-Y Alloys.* Materials Science and Engineering a-Structural Materials Properties Microstructure and Processing, 2007. **449**: p. 987-90.

[186] **Padezhnova, E.M., Melnik, E.V., Miliyevskiy, R.A., Dobatkina, T.V., and Kinzhibalo, V.V.**, *Investigation of the Mg-Zn-Y System.* Russian Metallurgy, 1982(4): p. 185-88.

[187] **Xu, D.K., Liu, L., Xu, Y.B., and Han, E.H.**, *The Influence of Element Y on the Mechanical Properties of the as-Extruded Mg-Zn-Y-Zr Alloys.* Journal of Alloys and Compounds, 2006. **426**(1-2): p. 155-61.

[188] **Smith, W.F.**, *Structure and Properties of Engineering Alloys*. 2nd ed. ed. 1993, New York ; London: McGraw-Hill.

[189] **Pierce, F.S., Poon, S.J., and Guo, Q.**, *Electron Localization in Metallic Quasi-Crystals.* Science, 1993. **261**(5122): p. 737-39.

[190] **Hagihara, K., Yokotani, N., and Umakoshi, Y.**, *Plastic Deformation Behavior of Mg12YZn with 18r Long-Period Stacking Ordered Structure.* Intermetallics, 2010. **18**(2): p. 267-76.

[191] **Wang, J.F., Song, P.F., Gao, S., Huang, X.F., Shi, Z.Z., and Pan, F.S.**, *Effects of Zn on the Microstructure, Mechanical Properties, and Damping Capacity of Mg-Zn-Y-Zr Alloys.* Materials Science and Engineering a-Structural Materials Properties Microstructure and Processing, 2011. **528**(18): p. 5914-20.

[192] **Li, Q., Wang, Q.D., Wang, Y.X., Zeng, X.Q., and Ding, W.J.**, *Effect of Nd and Y Addition on Microstructure and Mechanical Properties of as-Cast Mg-Zn-Zr Alloy.* Journal of Alloys and Compounds, 2007. **427**(1-2): p. 115-23.

[193] **Chen, T.J., Wang, W., Zhang, D.H., Ma, Y., and Hao, Y.**, *Development of a New Magnesium Alloy ZW21.* Materials & Design, 2013. **44**: p. 555-65.

[194] **Zhang, Y., Zeng, X.Q., Liu, L.F., Lu, C., Zhou, H.T., Li, Q., and Zhu, Y.P.**, *Effects of Yttrium on Microstructure and Mechanical Properties of Hot-Extruded Mg-Zn-Y-Zr Alloys.* Materials Science and Engineering a-Structural Materials Properties Microstructure and Processing, 2004. **373**(1-2): p. 320-27.

[195] **Bae, D.H., Kim, Y., and Kim, I.J.**, *Thermally Stable Quasicrystalline Phase in a Superplastic Mg-Zn-Y-Zr Alloy.* Materials Letters, 2006. **60**(17-18): p. 2190-93.

[196] **Bae, D.H., Kim, S.H., Kim, D.H., and Kim, W.T.**, *Deformation Behavior of Mg-Zn-Y Alloys Reinforced by Icosahedral Quasicrystalline Particles.* Acta Materialia, 2002. **50**(9): p. 2343-56.

[197] **Li, J.H., Du, W.B., Li, S.B., and Wang, Z.H.**, *Icosahedral Quasicrystalline Phase in an as-Cast Mg-Zn-Er Alloy.* Rare Metals, 2009. **28**(3): p. 297-301.
[198] **Yang, W.-p. and Guo, X.-f.**, *High Strength Magnesium Alloy with A-Mg and W-Phase Processed by Hot Extrusion.* Transactions of Nonferrous Metals Society of China, 2011. **21**(11): p. 2358-64.
[199] **Li, J., Du, W., Li, S., and Wang, Z.**, *Icosahedral Quasicrystalline Phase in an as-Cast Mg-Zn-Er Alloy.* Rare Metals, 2009. **28**(3): p. 297-301.
[200] **Meng, F.G., Wang, J., Liu, H.S., Liu, L.B., and Jin, Z.P.**, *Experimental Investigation and Thermodynamic Calculation of Phase Relations in the Mg-Nd-Y Ternary System.* Materials Science and Engineering a-Structural Materials Properties Microstructure and Processing, 2007. **454**: p. 266-73.
[201] **Wang, J., Song, P., Gao, S., Wei, Y., and Pan, F.**, *Influence of Y on the Phase Composition and Mechanical Properties of as-Extruded Mg–Zn–Y–Zr Magnesium Alloys.* Journal of Materials Science, 2012. **47**(4): p. 2005-10.
[202] **Rosalie, J.M., Somekawa, H., Singh, A., and Mukai, T.**, *Effect of Precipitation on Strength and Ductility in a Mg-Zn-Y Alloy.* Journal of Alloys and Compounds, 2013. **550**: p. 114-23.
[203] **Ping, D.H., Hono, K., and Nie, J.F.**, *Atom Probe Characterization of Plate-Like Precipitates in a Mg-Re-Zn-Zr Casting Alloy.* Scripta Materialia, 2003. **48**(8): p. 1017-22.